Unraveling Stochastic Transport in Complex Systems: Analytical and Computational Frameworks

Ph.D. Thesis

by

Nikhil Bhatia



Department of Mathematics
Indian Institute of Technology Ropar
Rupnagar, Punjab, India - 140001

February, 2025

Unraveling Stochastic Transport in Complex Systems: Analytical and Computational Frameworks

A Thesis

Submitted in partial fulfillment of the requirements for the degree of

DOCTOR OF PHILOSOPHY

by

Nikhil Bhatia

(Entry Number: 2019MAZ0007)

Under the guidance of

Dr. Arvind Kumar Gupta



to the

Department of Mathematics
Indian Institute of Technology Ropar
Rupnagar, Punjab, India - 140001

February, 2025

©Indian Institute of Technology Ropar - 2021 All rights reserved.

Declaration of Originality

I hereby declare that the work which is being presented in the thesis entitled **Unraveling Stochastic Transport in Complex Systems: Analytical and Computational Frameworks** has been solely authored by me. It presents the result of my own independent investigation/research conducted during the time period from December 2019 to March 2025 under the supervision of Dr. Arvind Kumar Gupta, Associate Professor at the Department of Mathematics, IIT Ropar.

To the best of my knowledge, it is an original work, both in terms of research content and narrative, and has not been submitted or accepted elsewhere, in part or in full, for the award of any degree, diploma, fellowship, associateship, or similar title of any university or institution. Further, due credit has been attributed to the relevant state-of-the-art and collaborations (if any) with appropriate citations and acknowledgments, in line with established ethical norms and practices. I also declare that any idea/data/fact/source stated in my thesis has not been fabricated/ falsified/ misrepresented. All the principles of academic honesty and integrity have been followed. I fully understand that if the thesis is found to be unoriginal, fabricated, or plagiarized, the Institute reserves the right to withdraw the thesis from its archive and revoke the associated Degree conferred. Additionally, the Institute also reserves the right to appraise all concerned sections of society of the matter for their information and necessary action (if any). If accepted, I hereby consent for my thesis to be available online in the Institute's Open Access repository, inter-library loan, and the title & abstract to be made available to outside organizations.

Signature

Name: Nikhil Bhatia

Entry Number: 2019MAZ0007

Program: PhD

Department: Mathematics

Indian Institute of Technology Ropar

Rupnagar, Punjab 140001

Date: 19/05 \2015

Certificate

This is to certify that the thesis entitled **Unraveling Stochastic Transport in Complex Systems: Analytical and Computational Frameworks**, submitted by **Nikhil Bhatia** (2019MAZ0007) for the award of the degree of **Doctor of Philosophy** of Indian Institute of Technology Ropar, is a record of bonafide research work carried out under my (our) guidance and supervision. To the best of my knowledge and belief, the work presented in this thesis is original and has not been submitted, either in part or full, for the award of any other degree, diploma, fellowship, associateship, or similar title of any university or institution.

In my (our) opinion, the thesis has reached the standard of fulfilling the requirements of the regulations relating to the Degree.

Aril What Signature

Dr. Arvind Kumar Gupta
Department of Mathematics
Indian Institute of Technology Ropar
Rupnagar, Punjab 140001

Date: 19.05.2025

This thesis is dedicated to my beloved parents whose endless support, wisdom, and sacrifices have shaped my journey.

Your faith in me has been my greatest strength.

Acknowledgement

I want to express my profound gratitude to God for granting me patience and perseverance throughout this journey.

I sincerely thank my supervisor, Dr. Arvind Kumar Gupta, for his invaluable guidance and support. I am also grateful to my doctoral committee members—Dr. M. Prabhakar, Dr. S. C. Martha, Dr. P. S. Dutta from the Mathematics department, and Dr. Somdev Kar from the HSS department—for their constant evaluation and insightful comments shaping this research.

I appreciate Mr. Neeraj, Senior Lab Assistant, Mr. Pankaj Kumar, Junior Technical Superintendent, and Ms. Jaspreet Kaur from the department office for their assistance over the years.

I am deeply indebted to my dear friends, Ms. Priya Koundle and Mr. Divas Dagur, for their unwavering support and selfless help and for being like a family away from home during these five years. Their presence during both the highs and lows of this journey has been invaluable. I also appreciate my seniors Bipasha, Ankita, and Aditi, and juniors Naman, Shankha, Ashish, and Nisha for our fruitful discussions.

I owe everything to my family—my father, Mr. Uttam Prakash Bhatia; my mother, Krishna Bhatia; and my brothers, Yash and Mayank. Their patience, faith, and support have been my strength. They have cherished every milestone I've achieved as their own.

I am extremely grateful to IIT Ropar for providing the necessary resources for my research and financial support to present my work at various conferences. Finally, I would like to thank CSIR for granting the fellowship that made this research possible.

Abstract

Movement is a fundamental aspect of life, occurring across all scales from microscopic to macroscopic levels. At the cellular level, essential processes such as gene expression rely on the movement of RNA polymerases along DNA strands to produce messenger RNA (mRNA), followed by ribosomes traversing the mRNA to synthesize proteins. On a larger scale, vehicular flow in urban environments exemplifies a ubiquitous transport process that impacts daily life, facilitating access to workplaces, services, and institutions. These diverse examples represent non-equilibrium complex systems, unified by their inherent complexity and categorized as driven-diffusive systems. This classification is crucial because non-equilibrium transport processes lack a unified theory for describing their steady-state properties. Grouping similar complex transport phenomena enhances our understanding and aids in developing solution strategies, making it a significant area of research across multiple disciplines, including mathematics, biology, and physics.

To effectively study these systems, it is necessary to develop appropriate mathematical and computational models that can accurately analyze particle flow dynamics. The Totally Asymmetric Simple Exclusion Process (TASEP) has emerged as a preeminent model for studying driven diffusive systems. Over time, this exclusion model has established itself as a paradigmatic framework, offering a streamlined mathematical approach to capture the intricate stochastic transport dynamics on a one-dimensional discrete lattice. This lattice effectively represents pathways for the unidirectional flow of particles, which can be analogous to vehicles in traffic flow scenarios. The TASEP model's strength lies in its ability to distill complex transport phenomena into a tractable form, enabling researchers to gain insights into fundamental principles governing non-equilibrium systems.

Building upon this foundation, our research contributes to a more comprehensive understanding of the collective behavior of particles in various single-lane TASEP model adaptations. Inspired by the presence of obstacles in vehicular and molecular motor transport, we investigate the impact of stochastic defects on system inhomogeneity. This research proposes a TASEP model where particle entry and exit on an inhomogeneous lattice are governed by the occupancy of a finite reservoir connected to both ends, reflecting real-world resource limitations. We examine the collective effects of these dynamics on system properties. Furthermore, we extend our analysis to non-conserving TASEP models, exploring the non-trivial effects of defect dynamics and non-conserving kinetics on density profiles and phase diagrams. Our research also delves into biological and physical systems exhibiting stochastic local resetting phenomena. We scrutinize the stationary properties of systems where entities enter the lattice from a limited resource pool and either move horizontally or

reset to specific lattice positions. Advancing our investigation, we study the impact of local stochastic resetting in bidirectional TASEP models, where particles of distinct species move in opposite directions. Additionally, motivated by entity flow in narrow channels and the goal of separating colloidal particles of different sizes, we examine a geometrically adapted TASEP model. In this model, each lattice site connects to a pocket-like structure with a defined particle capacity, mimicking the asymmetric geometry of narrow channels. We analyze the system's stationary characteristics under both finite and infinite particle availability.

In essence, our research employs mathematical modeling to elucidate previously unexplored complexities in transport processes. These findings, corroborated by simulations, underscore the importance of understanding the collective dynamics of moving entities in various contexts.

Keywords: Complex systems; Stochastic transport processes; Driven diffusive system; Mathematical Modeling; Exclusion process; Monte Carlo simulations; Mean-field theory;

Contents

Fr	ont C	Cover		i
Ti	tle Pa	ıge		iii
De	eclara	tion		vii
Ce	ertific	ate		ix
A	cknov	vledgem	ents	xiii
Al	ostrac	et		XV
Ta	ble of	f conten	ts	xvii
Li	st of l	Figures		xxiii
Li	st of '	Fables		xxxi
1	Intr	oductio	n to Complex Systems & Transport Phenomena	1
	1.1	Systen	ns in statistical mechanics	. 2
		1.1.1	Equilibrium Systems	. 2
		1.1.2	Non-Equilibrium Systems	. 3
		1.1.3	Transport mechanisms	. 5
	1.2	TASEI	P: a Stochastic Model for Far from Equilibrium Transport Processes	. 6
	1.3	Metho	ds for the Description of Stochastic Models	. 9
		1.3.1	Mean-Field Approximation Method	. 10

		1.3.2	Numerical	tools	12	
			1.3.2.1 N	Monte Carlo simulations	13	
			1.3.2.2	Convergence of simulations	15	
			1.3.2.3	Numerical Differentiation	16	
	1.4	Genera	alizations of	TASEP Model	17	
		1.4.1	Langmuir l	kinetics	17	
		1.4.2	Stochastic	local resetting	18	
		1.4.3	Dynamic d	lisorder	19	
		1.4.4	Finite reso	urces	20	
		1.4.5	Bidirection	nal transport	21	
	1.5	Aims d	& Objectives	3	22	
	1.6	Outline	e of the thesi	is	24	
2	Role	of site-	wise dynam	nic defects in a resource-constrained exclusion process	29	
	2.1	Backg	round		30	
	2.2	Model	description		31	
	2.3	Theore	Theoretical analysis			
	2.4	Naive	mean-field f	ramework	35	
		2.4.1	Defect-par	ticle interplay in the presence of finite resources	39	
		2.4.2	Theoretical	l calculations for phase existence and phase boundaries .	41	
		2.4.3	Phase plan	e analysis for faster defect dynamics	43	
	2.5	Failure	of naive me	ean-field theory	46	
	2.6	Enhan	ced mean-fie	eld framework	48	
		2.6.1	Theoretical	l calculations of phase existence and phase boundaries		
			for $k^+, k^-,$	$p_d \ll 1$ in the presence of finite resources	51	
		2.6.2	Phase plan	ne analysis for slower defect dynamics with $p_d \ll 1$	54	
	2.7	Conclu	ision		57	
3	Site-	wise dy	namic defe	cts in a non-conserving exclusion process	59	
	3.1	Backg	round		60	
	3.2	Mode	overview		62	
	3.3	Maste	r equations		64	

	3.4	Continuum mean-field approximations	65		
	3.5	Analytical solution at stationary state	68		
		3.5.1 Analysis for $K^* = 1$	69		
		3.5.1.1 Existence of stationary phases	71		
		3.5.2 $K^* \neq 1$	74		
	3.6	Results & Discussion	78		
		3.6.1 System behavior for $K = 1$	79		
		3.6.2 System behavior for $K > 1$	83		
		3.6.3 System behavior for $K < 1$	86		
	3.7	Shock analysis & Finite-size effect	88		
	3.8	Conclusion	90		
	TD 4				
4		ally asymmetric simple exclusion process with local resetting in a resource			
		strained environment	93		
	4.1	Background	94 95		
	4.2	1			
	4.3	, , , , , , , , , , , , , , , , , , , ,			
	4.4				
	4.7	of finite resources			
	4.5	Simulations			
		4.5.1 Direct simulation			
		4.5.2 Monte Carlo simulations			
	4.6	Results & discussion			
		4.6.1 Phase diagram: Role of Filling factor& Resetting rate			
		4.6.2 Influence of R and μ on stationary state density & current	111		
		4.6.3 Comparison of the proposed model with TASEP-LK with detach-			
		ment only			
	, -	4.6.4 Shock dynamics & Finite-size effect			
	4.7	Conclusion	117		
5	Loca	al Resetting in a Bidirectional Transport System	119		
	5.1	Background	120		

	5.2	Model definition					
	5.3	Theore	etical analysis under mean-field framework	122			
	5.4	Direct simulation					
	5.5	Station	nary phases for bidirectional model	130			
		5.5.1	Symmetric phases	130			
		5.5.2	Asymmetric phases	131			
	5.6	Results	s and discussion	132			
		5.6.1	Role of resetting rate on phase diagrams	134			
		5.6.2	Spontaneous symmetry-breaking phenomena (SSB)	137			
		5.6.3	Influence of R on Entry & Exit	139			
		5.6.4	Shock dynamics	141			
	5.7	Conclu	asion	143			
6	Loca	al resett	ing in a dynamically disordered exclusion process	147			
	6.1	Backg	round	148			
	6.2	Model	dynamics	149			
	6.3	Mathe	matical framework employing mean-field approximation	152			
	6.4	Theore	etical Analysis	154			
	6.5	Numer	rical solution	157			
	6.6	Results	s and discussion: Stationary-state characteristics	159			
		6.6.1	Phase diagrams: Role of obstruction factor & resetting rate	161			
		6.6.2	Influence of Obstruction Factor and Resetting Rate on Entry and				
			Exit Densities	164			
		6.6.3	Transition of stationary phases and steady-state current	166			
		6.6.4	Domain Wall and Finite-size effect	169			
	6.7	Conclu	asion	170			
7	Far	from eq	uilibrium transport on TASEP with pockets	173			
	7.1	Backg	round	174			
	7.2	Model		175			
	7.3	Maste	er equations and mean-field analysis of lattice with single-capacity				
		nocket		177			

		7.3.1	Phase pl	ane analysis for infinite resources	181
		7.3.2	Lattice a	and pocket compete for finite resources	184
			7.3.2.1	Theoretical calculations for phase existence and phase	
				boundaries ($\Omega_c = \Omega_d$)	185
			7.3.2.2	Theoretical calculations for phase existence and phase	
				boundaries ($\Omega_c eq \Omega_d$)	189
	7.4	Maste	r equation	s and mean-field analysis of lattice with multiple-capacity	
		pocket			195
		7.4.1	Phase pl	ane analysis for infinite resources	198
		7.4.2	Lattice a	and multiple-capacity pockets compete for finite resources .	200
		7.4.3	Phase pl	ane analysis	201
	7.5	Conclu	ision		203
8	Con	clusion	and Futu	re work	207
	8.1	Future	Scope .		208
Re	eferen	ces			211
Ρυ	ıblica	tions			223

List of Figures

1.1	A Venn diagram illustrating the classification of systems in statistical me-	
	chanics	2
1.2	Illustration of stochastic transport in (a) automobile traffic on a road and (b)	
	intracellular transport by motor proteins within a biological cell	5
1.3	Schematic representation of a one-dimensional open TASEP model, where	
	circles denote particles, illustrating (a) open boundary conditions (OBC)	
	and (b) periodic boundary conditions (PBC)	7
1.4	(a) Phase diagram of the one-dimensional open TASEP model in the $(lpha,eta)$	
	parameter space, where $lpha$ and eta represent the boundary control parameters.	
	(b) A fundamental diagram illustrating the relationship between the average	
	particle density and the current in the system	10
1.5	Flowchart of the Gillespie algorithm during Monte Carlo simulation utiliz-	
	ing random sequential updating for a TASEP with open boundaries	13
1.6	Schematic representation of Langmuir Kinetics (LK) dynamics on a TASEP	
	with OBC	17
1.7	Schematic representation of Local-resetting (LR) dynamics on a TASEP	
	with OBC	18
1.8	Schematic representation of dynamic disorder dynamics on a TASEP with	
	OBC	20
1.9	Schematic representation of a particle coming from a finite reservoir on a	
	TASEP with OBC	21

1.10	transport dynamics on a TASEP with OBC	22
2.1	A schematic diagram of the proposed model, where the particles (in red) enter the first site of the lattice $(j=1)$ from a finite reservoir (R_1) with the rate $\alpha_{\rm eff}$ or $\alpha_{\rm eff}p_d$, depending upon the defect occupancy at the first site. The particles hop horizontally on the lattice with rate 1 or p_d depending upon the defect occupancy at the arrival site. Particles exit the lattice from its last site $(j=L)$ with the rate β . The defects or obstacles (in blue) binds and unbinds vertically on the lattice site from another finite reservoir (R_2) with rate $k_{\rm eff}^+$ and k^- , respectively	322
2.2	The effect of the obstruction factor $\left(z = \rho_d (1 - p_d)\right)$ on the phase diagrams obtained through naive mean-field approach for the following choices of the filling factor: (a) $\mu = 0.5$, (b) $\mu = 0.7$, (c) $\mu = 1$, and (d) $\mu = 5$	44
2.3	a) The phase diagram obtained for $\mu=5$ shows the breakdown of the naive mean-field for slow defects with $p_d=0$, here the binding and unbinding rates are chosen as $k^+=0.02$, and $k^-=0.1$, respectively. Maximum current J_{max} as a function of the affected hopping rate p_d for the following binding/un-binding rates (b) $k^+=5$, $k^-=1$, (c) $k^+=0.005$, $k^-=0.01$	46
2.4	Correlations between (a) particle-defect residing on neighboring sites and (b) particle-particle residing on neighboring sites obtained through simulations	48
2.5	The effect of the modified obstruction factor on the phase diagrams obtained through enhanced mean-field approach the following choices of the filling factor (μ): (a) $\mu=0.5$, (b) $\mu=0.7$, (c) $\mu=1$, and (d) $\mu=5$	55
2.6	(a) Re-normalized current J/J_{max} as a function of $\widehat{\alpha}_{eff}$ for $\beta=1, \ \mu=1$. Maximum current J_{max} as a function of (b) z and (c) z_E for $L=1000, \mu=1$.	56

3.1	A diagrammatic representation of a non-conserving TASEP model depict-	
	ing the dynamics of particles (highlighted in pink) and defects or obstacles	
	(illustrated in a blue mesh). (a) Depicts different particle dynamics, includ-	
	ing entry, exit, hopping, and attachment/detachment, along with the cor-	
	responding rates at which these events occur in the presence and absence	
	of defects. (b) Illustrates the dynamics of defects on the lattice, including	
	defect binding/unbinding and their corresponding rates	62
3.2	(a)-(e) demonstrates how the phase diagram is influenced by z and Ω when	
	K = 1. Solid and dashed lines represent theoretical predictions derived from	
	mean-field theory, while Monte Carlo simulation results are depicted with	
	diamonds. The presence of boundary layers at the left or right end of the sys-	
	tem is highlighted by "(l)" and "(r)" respectively. In (f), the plot illustrates	
	Ω^c as a function of z, with different symbols (stars, circles, and squares)	
	distinguishing the two critical values Ω^{c_1} and Ω^{c_2} obtained for $z=0$	80
3.3	(a)-(g) shows the effect of z and Ω_d on the phase diagram for $K=3$. Solid	
	and dashed lines denote the theoretical outcomes through mean-field the-	
	ory, whereas diamonds denote the Monte Carlo simulation results. In (h),	
	the plot shows Ω_d^c as a function of z and K. Here, the symbol star, circle,	
	and square distinguish the two critical values Ω^{c_1} and Ω^{c_2} obtained corre-	
	sponding to $z = \frac{K-1}{K}$	82
3.4	Average density profiles: (a) LD, (b) MC, (c) HD, (d) LD-MC, (e) LD-	
	HD, (f) MC-HD, and (g) LD-MC-HD phases. Mean-field solutions (solid	
	curves) contrasted with Monte Carlo simulations (markers). Parameters:	
	$K = 3$, $\Omega_d = 0.1$, $z = \frac{K-1}{K}$. Sub-captions detail (α, β) configurations	85
3.5	(a)-(b) shows the effect of z and Ω_d on the phase diagram for $K=0.3$.	
	Solid and dashed lines denote the theoretical outcomes through mean-field	
	theory, whereas diamonds denote the Monte Carlo simulation results. In (c),	
	the graph depicts Ω_d^c varying with z and K	86
3.6	(a) Examining shock profiles under varying z for $\alpha = 0.1$, $\beta = 0.05$, $\Omega_d =$	
	0.1, and $K = 1$. (b) Finite-size effects on shock profiles at $z = 0$. Investigat-	
	ing (c) shock displacement and (d) shock amplitude across z	89

4.1	Schematic diagram of the TASEP with local resetting at the entry site. The rate of each process is represented by a matching symbol, and it is believed that lattice sites are arranged from left to right. If the arrival site is unoccupied, the hopping process has a unit rate; otherwise, it is prohibited (zero rate)
4.2	Stationary state phase diagrams for $\mu=0.1$ and different values of R . The markers are results from Monte Carlo simulations (MCS) and the solid lines are results from a continuum mean-field (CMF) approximation. The transition from LD to the LD-HD phase is discontinuous, resulting in a first-order transition. The transition from LD to the MC phase displays a continuous transition and hence is a second-order phase transition
4.3	Stationary state phase diagrams for $\mu=0.3$ and different values of R . The markers are results from Monte Carlo simulations (MCS) and the solid lines are results from a continuum mean-field (CMF) approximation. The transition from MC to the MC-HD phase is discontinuous, whereas in (c), the transition from LD-HD to the MC-HD phase displays a continuous transition. 107
4.4	Stationary state phase diagrams for $\mu=1$ and different values of R . The markers are results from Monte Carlo simulations (MCS) and the solid lines are results from a continuum mean-field (CMF) approximation. The transition from LD-HD as well as the MC-HD phase to the HD phase is discontinuous
4.5	Stationary state phase diagrams for $\mu=10$ and different value of R . The markers are results from Monte Carlo simulations (MCS) and the solid lines are results from continuum mean-field (CMF) approximation 109
4.6	(a) Transition of the stationary state density profile from the LD-HD phase to the LD phase and thereafter to the MC phase for $\mu=0.3$, $R=1.5$. The black dotted line is marked to show $\rho=0.5$. (b) Stationary density profile as a function of the scaled position variable $\xi\equiv\lambda i/L$, in the large resetting regime: $r=R/L=0.1$ and $\mu=1$. The solid lines denote the mean-field continuum profile and the markers denote Monte Carlo results

4.7	Stationary state density and current displaying (a) the effect of R , (b) the effect of μ . The markers represent outcomes obtained through Monte Carlo	
	simulations (MCS), while the solid lines depict results derived from the con-	
	tinuum mean-field (CMF) approximation	112
4.8	Fixed-point diagram	
4.9	Effect of R on the (a) LD-HD shock profile and (b) its height and position for $\mu=1$ and $\alpha=0.2, \beta=0.1$. The markers represent outcomes obtained through Monte Carlo simulations (MCS), while the solid lines depict results derived from the continuum mean-field (CMF) approximation	
4.10	Effect of R on the (a) MC-HD shock profile and (b) its height and position for $\mu=1$ and $\alpha=0.9, \beta=0.2$. The markers represent outcomes obtained through Monte Carlo simulations (MCS), while the solid lines depict results derived from the continuum mean-field (CMF) approximation	115
4.11	Finite size effect on (a) the LD-HD density profile as well as (b) the MC-HD density profile for $\mu=1$ and $R=0.25$. The markers represent outcomes obtained through Monte Carlo simulations (MCS), while the solid lines depict results derived from the continuum mean-field (CMF) approximation	116
5.1	Schematic diagram illustrating the bidirectional transport with local resetting along a one-dimensional channel. The channel accommodates two oppositely directed species of particles: plus particles (in red) and minus particles (in yellow) move from left to right and vice versa, respectively. Allowed transitions are shown by arrows, and their corresponding rates are represented by a matching symbol. Entrance rates of both species of particles are equal to α if there is no particle at their corresponding entry site. Exit rates for both species are β . Each species undergoes hopping with a unit rate when the arrival site is unoccupied, or they swap positions at a rate of q when they encounter each other on adjacent sites	123
5.2	The stationary state phase diagrams for (a) $R = 0.03$, (b) $R = 0.25$, (c) $R = 1$ and (d) $R = 5$ with $q = 1$. The asymmetric <i>LD/LD</i> phase has been written in	
	italic fonts to distinguish it from the symmetric LD/LD phase	133

5.3	The stationary state phase transition in ρ^+ and ρ^- for a fixed α while varying β , where $R = 1, \dots, \dots$	135
5.4	Particle density histogram for the asymmetric phases: (a) <i>LD/LD</i> , (b) (LD-HD)/LD, (c) (MC-HD)/LD (d) HD/LD with the parameters defined in the captions of the figures, respectively	136
5.5	Impact of the resetting phenomena on the stationary state entry and exit densities for a fixed choice of entry and exit rate for both species	137
5.6	In the fixed-point diagram of the boundary-layer differential equation, the solid and dashed lines represent the two fixed-point branches. The vertical arrows signify that the upper and lower fixed-point branches are stable and unstable, respectively. These arrows indicate the direction of the boundary-layer solution flow as x increases. The coordinates (-0.25, 0.5) correspond to the bifurcation point. The flow toward or away from this particular point is depicted by vertical downward arrows on the y -axis	138
5.7	The influence of the resetting dynamics is depicted on (a) the (LD-HD)/LD phase and (b) the domain wall's position and height for $\alpha=0.1$ and $\beta=0.07$. The solid lines represent mean-field results, whereas the markers ("circles") represent the Monte Carlo results	139
5.8	The influence of the resetting dynamics is depicted on (a) the (MC-HD)/LD phase and (b) the domain wall's position and height and position for $\alpha = 0.2, \beta = 0.07$. The solid lines represent mean-field results, whereas the markers ("circles") represent the Monte Carlo results	140
5.9	Finite size effect on (a) the LD-HD density profile as well as (b) the MC-HD density profile for $R=1$. The solid lines represent mean-field results, whereas the markers ("circles") represent the Monte Carlo results	141
6.1	Schematic picture of the TASEP model with dynamics defects and local resetting	150
6.2	Role of the obstruction factor on the stationary state phase diagrams for different choices of the resetting rate	162

6.3	(a) Effect of R and z on stationary-state density at entry site and exit site.(b) The MC phase density profile as a function of the re-scaled variable	
	$\xi = \lambda i/L$, where the dotted curve represents the analytical expression of	
	$\rho(\xi,z) = -1/2W_0(-\exp(-1-\xi/(1-z)))$ obtained through the mean-field	
	approach.	163
6.4	Transition in the stationary state density profile and current with respect to	
	$R \text{ for } z = 0.5. \dots $	164
6.5	Transition in the stationary state density profile and current with respect to z for $R = 0.5$	165
6.6	(a) Propagation and (b) change in the position and the height of the LD-HD shock profile with respect to R for $z = 0.5.$	168
6.7	(a) Propagation and (b) change in the position and the height of the LD-HD shock profile with respect to z for $R = 0.5$	168
6.8	Finite-size effect on the LD-HD shock profile and (b) particle-particle correlations in the lattice with respect to R for $\alpha = 0.01, \beta = 0.004, R = 0.2,$ and $z = 0.5, \ldots$	169
7 1		
7.1	A schematic perspective of the pocket model, in which each pocket has the	
	same capacity, say q . Particles (red) enter the first site of the lattice ($j = 1$) from the reservoir with the rate α_{eff} and depart the lattice from the last site	
	$(j = L)$ with the rate β . The particles migrate from various lattice sites to	
	pockets or vice versa with rates c and d , respectively	175
7.2	The phase diagram of lattice and pocket of any capacity q with infinite re-	
	sources for $\Omega_c=\Omega_d$, where the first phase refers to the density phase in	
	lattice and the second phase refers to the density phase in the pocket	181
7.3	The phase diagram of lattice and pocket of any capacity q with infinite re-	
	sources for $\Omega_c eq \Omega_d$. (a) The phase diagram (on left) is for $\Omega_c = 0.35$ and	
	$\Omega_d=0.65$. (b) The phase diagram (on right) is for $\Omega_c=0.65$ and $\Omega_d=0.35$.	182
7.4	The effect of μ on the phase diagram of lattice and single-capacity pocket	
	phase for the case $\Omega_c = \Omega_d$. (a) $\mu = 0.7$, (b) $\mu = 1.55$, (c) $\mu = 2$, (d) $\mu = 5$.	189

7.5	The effect of μ on phase diagrams of lattice and single-capacity pockets for	
	the case $\Omega_c > \Omega_d$, where $\Omega_c = 0.3$ and $\Omega_d = 0.1$ (a) μ = 0.7, (b) μ = 1.1,	
	(c) μ = 2.01, (d) μ = 2.5. The arrow (in black) refers to the region occupied	
	by the corresponding density phase. The dotted arrow (in red) refers to the	
	back and forth (reentrant) transition	194
7.6	(a) Pocket density vs lattice density for different choices of q and $\Omega_c = \Omega_d$.	
	(b) Pocket density vs lattice density for different choices of q and $\Omega_c \neq \Omega_d$,	
	where $\Omega_c, \Omega_d \in \{0.35, 0.65\}$. The dashed arrow (in red) refers to the shift	
	in the density profiles with increasing q . (c) The density profile in the LD	
	phase (in pocket) approaches toward 0 in the limit $q \rightarrow \infty$. (d) The density	
	profile in the HD phase (in pocket) approaches towards 1 in the limit $q \to \infty$.	199
7.7	The effect of q on phase diagrams obtained for lattice and multiple-capacity	
	pockets under finite resources. The phase boundaries with white circles	
	remain intact with an increase in q . (a) $\mu=1.55$ and $\Omega_c=\Omega_d$. (b) $\mu=1.8$	
	and $\Omega_c=0.1,\Omega_d=0.3.$ (c) $\mu=2.01$ and $\Omega_c=0.3,\Omega_d=0.1.$ The dotted	
	arrows (in red) refer to the back-and-forth (reentrant) transition for larger	
	choices of q . The arrows (in black) refer to the region occupied by the	
	corresponding density phase	202

List of Tables

1.1	Comparison between Open and Closed Boundary Conditions in TASEP	8
2.1	Expressions for the existence conditions of the density phases in the lattice	
	with infinite resources through naive mean-field theory	38
2.2	Bounds on μ for the existence of the LD phase	39
2.3	Expressions for the existence conditions of the density phases in the lattice	
	with infinite resources through enhanced mean-field theory	49
2.4	Bounds on μ for the existence of LD phase through enhanced mean-field	
	theory	52
4 1		
4.1	Expressions for the existence conditions of the density phases in the lattice	
	with finite resources through mean-field theory	98
5.1	Expressions for both species' existence conditions, stationary state phases,	
	and densities using a mean-field technique	128
6.1	Formulations outlining the conditions for the presence of stationary phases	
	within a lattice via mean-field theory. Here, $Y = \frac{R}{1-z}$	160
7.1	Expressions for the existence conditions of the density phases in lattice and	
	pocket for $\Omega_c=\Omega_d$	180
7.2	Expressions for the existence conditions of the density phases in pocket for	
	$\Omega_c eq \Omega_d$	183
	a = c + a.	105

1	
Chapter L	

Introduction to Complex Systems & Transport Phenomena

Movement is a fundamental aspect of life, playing a vital role in shaping our daily experiences through a variety of intricate biological and physical processes. In our world, we encounter numerous natural and artificial systems that exhibit inherent complexity. These systems are characterized by interactions and interdependencies among their components, as well as with their surrounding environments. For instance, an amoeba represents a complex dynamical system, containing a solution of various chemical species where countless biological processes occur simultaneously. Interestingly, the internal dynamics of an amoeba can be compared to the bustling energy of public transit systems in large urban areas [121]. In all such systems, movement occurs along defined paths or tracks. What distinguishes the study of these systems is the remarkable way their components interact collectively to generate unexpected patterns and structured movements. This organization, resembling trains on tracks or vehicles on roads, facilitates the study of how entities interact and move collectively along guided pathways. Over time, this has become a key area of focus for scientists from diverse disciplines, aiming to understand the mechanisms that drive these transport processes and analyze their dynamics across different scales. At the macroscopic level, examples include highways for vehicles [28, 12, 96] and pedestrian walkways [64], while at the microscopic level, transport occurs along intracellular pathways utilized by molecular motors [28, 12, 96, 97, 135, 60, 27, 3].

Around 1902, in the early twentieth century, the combined efforts of Gibbs, Maxwell, and Boltzmann laid the groundwork for the field of statistical mechanics [20, 52, 67]. This discipline emerged as a robust and versatile tool for studying evolutionary models involving large numbers of particles, bridging microscopic and macroscopic properties to address

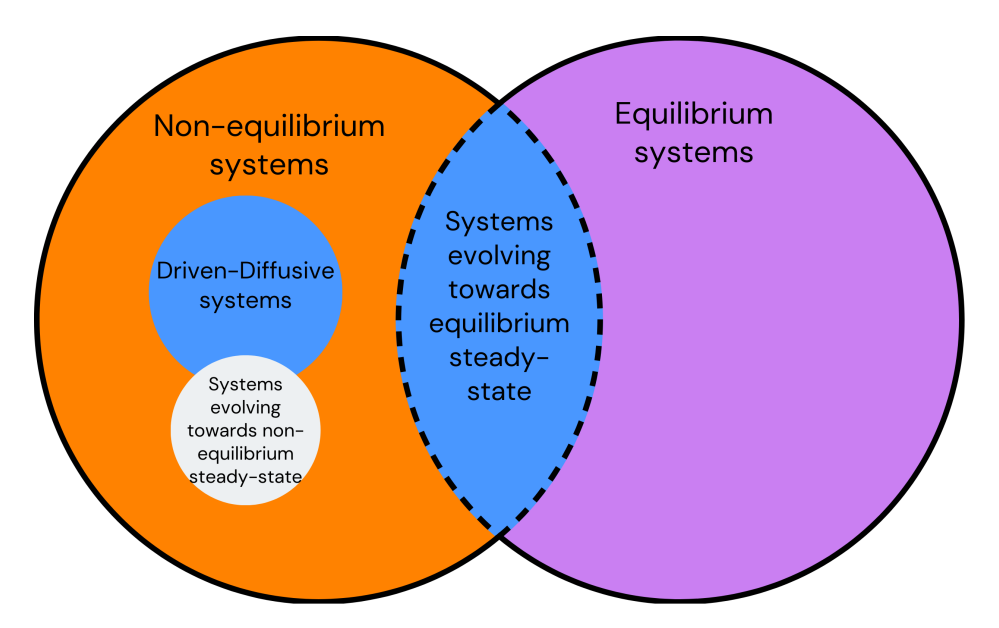


Figure 1.1: A Venn diagram illustrating the classification of systems in statistical mechanics.

uncertainties in their behavior. Josiah Willard Gibbs provided the mathematical framework, while James Clerk Maxwell and Ludwig E. Boltzmann significantly advanced its development, particularly in the realm of thermodynamics [20, 52, 67]. All natural systems display essential differences in their behavior, interactions, and governing principles. To facilitate their analysis and modeling, their categorization is required focusing on their distinct characteristics and dynamics which we will discuss in the upcoming section.

1.1 Systems in statistical mechanics

All natural systems exhibit unique real-world behaviors and display essential differences in their interactions, and governing principles. This necessitates the development of distinct theoretical frameworks to streamline their analysis and modeling. Therefore, the field of statistical mechanics categorizes them into two primary types: equilibrium and non-equilibrium systems, focusing on their distinct characteristics and dynamics [121]. FIG.1.1 illustrates a Venn diagram based on this categorization. We will now provide a brief overview of both equilibrium and non-equilibrium systems.

1.1.1 Equilibrium Systems

In everyday life, we encounter various complex systems, such as a parked car, a metal rod reaching thermal equilibrium with a hot liquid, a reversible chemical reaction $(H_2 + I_2 \leftrightarrow$

2HI), and a seesaw balanced at its fulcrum by two individuals of equal weight. These are examples of equilibrium systems, some of which do not interact with their surroundings, or if they do, the net force and/or net energy exchange is zero, resulting in a steady state [83]. In such systems, internal processes like energy exchanges between particles are balanced, causing their macroscopic properties (e.g., temperature, pressure, and energy) to remain constant over time, provided external conditions are unchanged. A key feature of equilibrium systems is the absence of any net flow of energy, matter, or momentum within the system [121].

Before the 19th century, there was no established framework to study such systems. However, in the early 19th century, the Ising model introduced by Ernst Ising [11], together with foundational principles like the Maxwell-Boltzmann distribution and the laws of thermodynamic equilibrium, became essential tools for analyzing these systems. To examine equilibrium systems, the probability of the system being in a particular configuration is calculated using its Hamiltonian. This information is then used to derive the Gibbs distribution and the partition function. With these two quantities, the average behavior of the system's physical properties can be systematically analyzed.

The time-independent nature of equilibrium systems simplifies their mathematical treatment, and the availability of well-developed analytical tools has made them extensively studied and thoroughly documented in scientific literature.

1.1.2 Non-Equilibrium Systems

Just as equilibrium systems are a part of our surroundings, we are also surrounded by systems that are not in stable equilibrium and often undergo continuous changes due to interactions with their environment or internal processes. These systems encompass the majority of real-world situations, such as traffic flow, biological processes, atmospheric dynamics, and stock market fluctuations, etc. Understanding them is essential for applications where dynamic processes play a crucial role. In each of these cases, a net driving force acts on the system, resulting in a constant, nonzero current or flux. The inherent characteristic of these systems is their time-dependent behavior, where the complexities and uncertainties in their evolution make predicting their future behavior challenging [121, 73]. As a result, unlike equilibrium systems, there is no unified theory for analyzing non-equilibrium systems. These systems can be broadly classified into two subgroups based on whether they eventually reach an equilibrium state after sufficient time for spontaneous evolution: those evolving toward equilibrium and those reaching a non-equilibrium steady state.

Non-equilibrium systems that gradually evolve toward an equilibrium state over time are

categorized as equilibrium steady-state systems or systems near equilibrium, see FIG.1.1. To analyze fluctuations in such systems, various approaches have been developed, including macroscopic theories proposed by Onsager and Machlup [24], which address gaps in understanding non-equilibrium dynamics. Onsager's regression hypothesis asserts that the relaxation of macroscopic non-equilibrium disturbances follows the same laws that govern the regression of spontaneous microscopic fluctuations in an equilibrium system. While the relaxation of macroscopic disturbances out of equilibrium may initially appear unrelated to the regression of microscopic fluctuations in the corresponding equilibrium system, linear response theory provides a crucial connection [65]. The fluctuation-dissipation theorem links the system's response and dissipation to the correlations of its fluctuations. In essence, by employing Onsager's theory alongside linear response theory, one can calculate the Hamiltonian, which serves as a basis for understanding systems near equilibrium. For further details, readers are encouraged to consult references [121, 24].

On the other hand, there exists a category of non-equilibrium systems that progressively transition to a non-equilibrium steady state (NESS) over time, leading to dynamics that do not change with time. For example, consider a metallic rod with heat sources at varying temperatures at each end; the heat flux continues to be non-zero even when the system reaches a steady state. Systems that are significantly out of equilibrium and attain a NESS do not have a counterpart to the time-independent Boltzmann distribution. While considerable advancements have been made in the analytical and theoretical examination of these systems, a comprehensive framework for studying non-equilibrium systems remains lacking.

Additionally, another prevalent category of non-equilibrium systems is driven diffusive systems, where particle transport or movement occurs due to an internal or external driving force, such as an applied electric field, pressure gradient, or concentration gradient. In these systems, the driving force is the primary factor that directs particle flow and governs the overall dynamics. They can be further categorized as field-driven or self-driven, depending on whether the driving energy is external or internal, respectively [123]. These systems are characterized by a continuous flow of particles, momentum, or energy, which prevents them from reaching equilibrium. However, they typically achieve a steady state where macroscopic properties remain constant over time, while still being far from equilibrium due to the ongoing flux. Generally, all types of transport processes fall under self-driven diffusive systems, making them common in real-world scenarios, as discussed in the following sections. Driven diffusive systems play a crucial role in bridging our understanding of the behavior of real-world systems that are far from equilibrium. Next, we will explain certain transport mechanisms that motivate this thesis. It is important to emphasize that this study

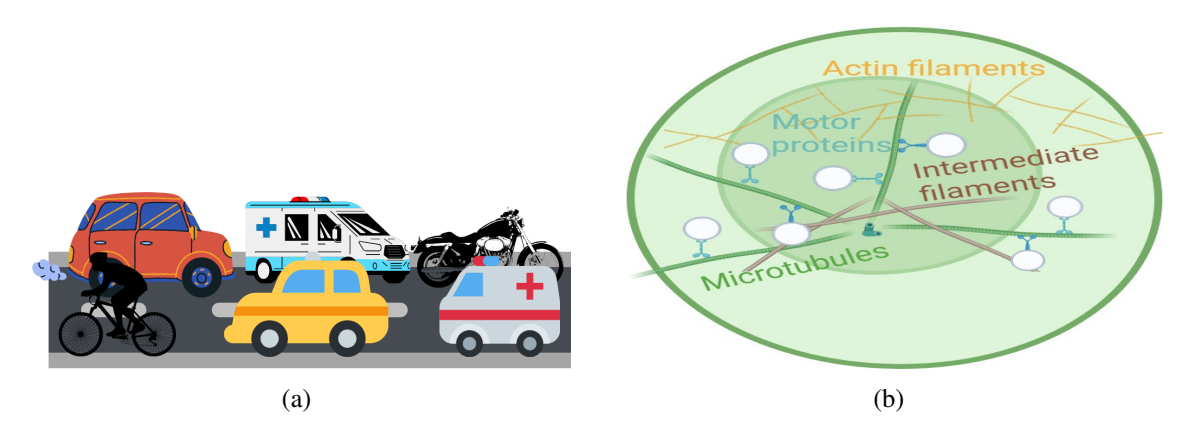


Figure 1.2: Illustration of stochastic transport in (a) automobile traffic on a road and (b) intracellular transport by motor proteins within a biological cell.

extends beyond the limitations imposed by the specific phenomena discussed.

1.1.3 Transport mechanisms

We now explore some real physical and biological stochastic transport processes, which serve as examples of significant self-driven diffusive systems.

1. **Physical systems:** Vehicles traveling on highways display self-driven dynamics, where interactions such as lane changes and speed adjustments give rise to patterns similar to diffusive transport. Vehicular traffic, as shown in FIG.1.2(a) resulting from the growing population has become one of the most pressing challenges of our time. Traffic control theory has emerged as a highly interdisciplinary field of research, with engineers and scientists from diverse disciplines, including nonlinear dynamics, stochastic processes, and statistical mechanics, collaborating to better understand phenomena like traffic jams, lane formation, and other collective flow patterns. Their efforts aim to devise strategies to manage and optimize traffic flow on increasingly congested roads. Other examples include granular flow, where grains in systems such as sand piles or vibrated granular beds exhibit collective motion influenced by external driving forces (e.g., vibration) and local interactions, resembling stochastic transport. Similarly, microscopic particles in fluids driven by external forces, such as electric or magnetic fields, demonstrate behaviors analogous to self-driven diffusive systems. While numerous large-scale physical systems exemplify driven-diffusive processes, we have chosen to focus on a select few widely recognized examples.

2. **Biological systems:** Examples of self-driven stochastic transport at the microscopic level include intracellular transport, where molecular motors such as kinesin and dynein move along microtubules to transport organelles and vesicles within the crowded, diffusive cytoplasmic environment, as illustrated in FIG.1.2(b). This transport is essential for delivering vital substances like water, hormones, gases, minerals, and organic materials necessary to sustain life. These motor proteins are powered by the hydrolysis of adenosine triphosphate (ATP). While significant progress has been made in studying single motor proteins both theoretically and experimentally, motor proteins often operate in large groups, and their collective behavior is critical for proper cellular function. Malfunctions in motor protein activity can result in severe diseases, including Alzheimer's, respiratory disorders, and others [90, 115].

Other examples include blood flow in capillaries, where red blood cells move through narrow vessels in a coordinated, self-driven manner influenced by their deformation and interactions with vessel walls. Similarly, animal group behaviors, such as the flocking of birds, schooling of fish, and herding of animals, exhibit self-organized motion driven by local interactions and collective decision-making.

These systems underscore the universality of self-driven diffusive dynamics across a wide range of fields, providing rich opportunities for both theoretical modeling and experimental investigation.

1.2 TASEP: a Stochastic Model for Far from Equilibrium Transport Processes

In this section, we outline the methodology, grounded in the key characteristics of non-equilibrium transport processes, that will be employed to examine their stationary properties. These systems are inherently stochastic and consist of two primary components: the road, representing space, and the vehicles, representing particles. Typically, their long-term behavior is independent of initial conditions. However, the presence of a large number of particles in these traffic phenomena adds complexity to the analysis. This underscores the need for a population-based stochastic model capable of incorporating randomness and managing a substantial number of particles to provide a macroscopic view of the system under study.

In our daily lives, we encounter various traffic scenarios, such as vehicular traffic on roads or molecular traffic along cytoskeletal filaments inside cells. These systems involve

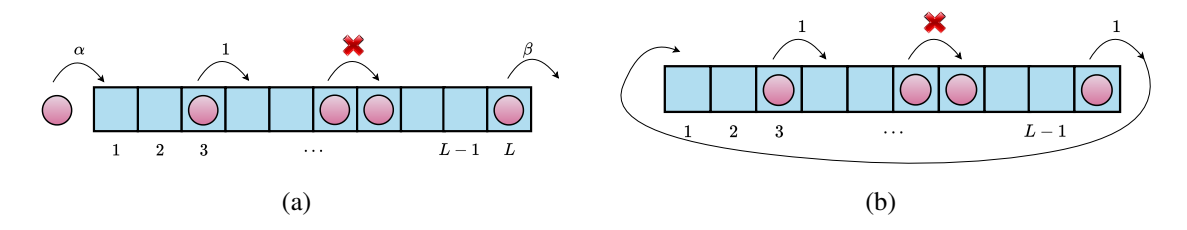


Figure 1.3: Schematic representation of a one-dimensional open TASEP model, where circles denote particles, illustrating (a) open boundary conditions (OBC) and (b) periodic boundary conditions (PBC).

objects—vehicles or molecular particles—moving along a lane, constrained by the presence of others ahead or behind. Building on this idea, Totally Asymmetric Simple Exclusion Process (TASEP)—a fundamental and effective lattice-gas model—was developed to mathematically analyze the complicated traffic dynamics for a large-particle system. TASEP models this behavior using a one-dimensional discrete lattice, which acts as a lane for the movement of particles. The foundation for this approach dates back to 1968 when Macdonald, Gibbs and Pipkin introduced a concept to study the kinetics of biopolymerization [88, 87]. In this framework, particles representing the diffusion of biological entities are allowed to move randomly along a one-dimensional discrete lattice (or lane) in continuous time. "Totally asymmetric" indicates that particles move in only one direction, while "simple" signifies that hopping occurs only between nearest neighbors. The term "exclusion" means that each lattice site can be occupied by no more than one particle at a time. Since their introduction, TASEP has been established as a paradigm tool in enhancing our understanding of molecular transport processes across a range of disciplines. Commonly recognized as stochastic models, they have been thoroughly researched and utilized to explore various transport phenomena, such as vehicular traffic [96], motor protein dynamics [76], protein synthesis [26], pedestrian flow [64], gel electrophoresis [75], and the modeling of ant trails [28]. The dynamics and stationary-state properties of a TASEP are determined by the boundary conditions, which can be either open or closed, as shown in FIG.1.3. Their distinctive features are explicitly mentioned in TABLE 1.1. However, in both cases, the particle within the bulk moves at a constant hopping rate of 1.

Another key aspect of modeling stochastic transport processes is the lattice updating procedure, which plays a pivotal role in shaping the stationary properties and dynamic behavior of the TASEP. The updating rules determine how particles move on the lattice and significantly influence the system's macroscopic characteristics. TASEP has been extensively studied under four primary classes of updating rules [112]:

Aspect	Open Boundary Conditions	Closed Boundary Condi-	
		tions	
Boundary dynamics	The particles enters the first	The particles from the last site	
	site with rate α (injection	moves to the first site with a	
	rate) and exits the last site	unit rate provided the target	
	with rate β .	site is empty.	
Particle Exchange	Total number of particles are	Total number of particles re-	
	not conserved.	main conserved.	
Governing Parameters	Governed by α and β .	Governed by initial density	
		(ρ) .	
Steady-State Phases	Exhibits LD, HD, and MC	Characterized by density-	
	phases as well as the system	dependent phenomena like	
	reveals various counter- shocks or jams [89, 38, 110]		
	intuitive non-equilibrium	n	
	phenomena such as localized	such as localized	
	shock formation, phase tran-		
	sitions, phase separations,		
	symmetry-breaking, etc [82,		
	120, 44, 77, 80, 78, 71, 1].		
Boundary Effects	Strongly influenced by reser-	Dynamics occur purely	
	voir interactions.	within the lattice.	

Table 1.1: Comparison between Open and Closed Boundary Conditions in TASEP.

- 1. Sequential Updating: Particles are updated one at a time in a fixed or random order during each time step.
- 2. Parallel Updating: All particles are updated simultaneously at each time step.
- 3. Random Sequential Updating: Particles are updated randomly, one at a time, during each time step.
- 4. Sub-lattice Parallel Updating: The lattice is divided into sub-lattices, with particles in one sub-lattice updated simultaneously, followed by updates in the next sub-lattice.

The choice of updating procedure affects critical aspects of the system, including the phase diagram, current-density relationship, shock properties, and fluctuations. Selecting an appropriate update rule depends on the characteristics of the transport process being modeled. For instance, the parallel updating rule is typically used to replicate the dynamics of vehicular traffic and pedestrian flow, while the random sequential rule is better suited for biological transport processes.

In this thesis, we will utilize the TASEP model and its extensions that incorporate open boundary conditions and a random-sequential updating procedure. The following sections will provide a comprehensive examination of the mathematical framework of open TASEP, highlighting key results.

Methods for the Description of Stochastic Models 1.3

The modeling of complex transport processes using TASEP can also be understood in terms of a stochastic process, specifically a continuous-time Markov chain, where each lattice configuration represents different state of the system, and each transition corresponding to a particle moving from one site to the next is governed by certain probabilities.

To determine the probability distribution in a Markov chain of TASEP, we need to analyze its long-term behavior, focusing on how the probabilities of different states change over time. For a lattice of length L, let $\mathbf{n}(\mathbf{t}) = (n_1(t), n_2(t), \dots, n_L(t))$ be a binary string of length L that denotes the specific configuration of the system at time t, where each bit corresponds to a site which is either occupied by a particle ($n_i(t) = 1$) or empty ($n_i(t) = 0$). In contrast to equilibrium systems, non-equilibrium systems do not adhere to detailed balance, which implies that the transition rates between different states need not necessarily the same in both directions. Consequently, a master equation serves as a mathematical tool to describe the temporal evolution of the probability distribution of a system as it experiences random transitions between various states. The time-evolution of probability $P(\mathbf{n})$ to find the system in configuration **n** satisfies the following master equation:

$$\frac{dP(\mathbf{n})}{dt} = \underbrace{\sum_{\mathbf{n}'} \left[W(\mathbf{n}' \to \mathbf{n}) P(\mathbf{n}') \right]}_{\text{gain term}} - \underbrace{\sum_{\mathbf{n}'} \left[W(\mathbf{n} \to \mathbf{n}') P(\mathbf{n}) \right]}_{\text{loss term}},$$
(1.1)

where $W(\mathbf{n} \to \mathbf{n}')$ is the transition rate from configuration \mathbf{n} to \mathbf{n}' . Here, the probability of entering each configuration is balanced by the probability of leaving it.

The time evolution of the expected values of $n_i(t)$ can be determined using the following master equations:

$$\frac{d\langle n_1\rangle}{dt} = J_{\text{enter}} - J_{1,2},\tag{1.2}$$

$$\frac{d\langle n_i \rangle}{dt} = J_{i-1,i} - J_{i,i+1}, \quad 1 < i < L$$
(1.3)

$$\frac{d\langle n_1 \rangle}{dt} = J_{\text{enter}} - J_{1,2},$$

$$\frac{d\langle n_i \rangle}{dt} = J_{i-1,i} - J_{i,i+1}, \quad 1 < i < L$$

$$\frac{d\langle n_L \rangle}{dt} = J_{L-1,L} - J_{\text{exit}}$$
(1.2)

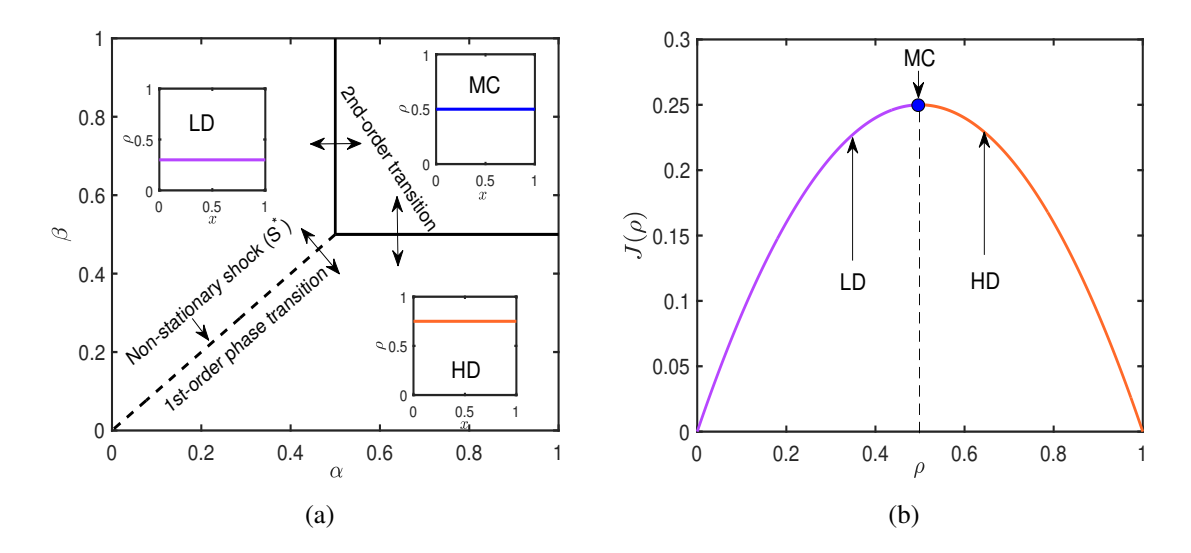


Figure 1.4: (a) Phase diagram of the one-dimensional open TASEP model in the (α, β) parameter space, where α and β represent the boundary control parameters. (b) A fundamental diagram illustrating the relationship between the average particle density and the current in the system.

where $\langle \rangle$ represents the statistical average that is computed with respect to the time-dependent probability distribution of all lattice configuration. Here, $J_{i,i+1}$ represents the average particle flux of particles moving from site i to site i+1 per unit time, and is defined as

$$J_{i,i+1} = \langle n_i (1 - n_{i+1}) \rangle \tag{1.5}$$

The expression of the current entering (exiting) the system at the first (last) sites is given by

$$J_{\text{enter}} = \alpha \langle 1 - n_1 \rangle, \quad \text{and}, J_{\text{exit}} = \beta \langle n_L \rangle$$
 (1.6)

respectively.

In the next section, we will develop the system framework employing an appropriate theoretical approach for the update rule used in the following sections.

1.3.1 Mean-Field Approximation Method

The primary objective of the TASEP model is to examine various key features of transport processes, such as particle distribution, average density, and current (the flow of particles), among others. Although the concept of TASEP was introduced in 1968, it took nearly two to three decades to develop analytical methods, including the matrix-product ansatz [37], recursion methods [36], Bethe ansatz [124], and domain wall theory [80, 118], to

derive its steady-state solution due to the mathematical complexities involved. However, while methods like recursion or Bethe ansatz require solving exponentially large systems of equations (e.g., 2^L equations for a lattice of length L), the matrix-product ansatz (MPA) provides an explicit solution for all L. In MPA, the stationary weights of configurations are expressed as traces of products of non-commuting matrices, enabling direct computation of observables like density and current without solving coupled equations. This makes MPA particularly powerful for studying large systems or arbitrary boundary conditions (α, β) . For example, Derrida et al. (1993) used MPA to derive exact phase diagrams and correlation functions for the TASEP, demonstrating its advantage over other methods. This highlights the challenges of generalizing exact methods to accommodate additional dynamic features when analyzing more realistic models, which will be discussed in the following sections. As a result, the mean-field approximation, an approximate method, has gained significant attention for deriving the steady-state solution of the TASEP model [13]. To support its reliability in specific scenarios, the mean-field approximation has not only provided results consistent with those obtained through exact methods but has also successfully captured the intriguing dynamics of various variants of the TASEP model (discussed in Section. 1.4).

The simplest way to solve Eq. (1.2)-(1.4) is by ignoring all the correlators, i.e. the mean-field approximation, where we factorize the two-point correlators as $\langle n_i n_j \rangle = \langle n_i \rangle \langle n_j \rangle$ and define the average density at the i^{th} site as $\rho_i = \langle n_i \rangle$ where $\langle \cdots \rangle$ denotes the statistical average. To find an explicit solution to these equations, we can simplify the discrete lattice by taking a continuum limit, where the lattice constant $\varepsilon = 1/L$ approaches zero as the system size L increases. By rescaling the position variable x = i/L, we can treat it as quasicontinuous. Utilizing the following Taylor's series expansion of the average density $\rho_{i\pm 1} \equiv \rho(x\pm \varepsilon)$ in powers of ε , and considering the terms accurate to the leading order in ε ,

$$\rho_{i\pm 1} = \rho_i \pm \varepsilon \frac{\partial \rho_i}{\partial x} \pm O(\varepsilon^2)$$
(1.7)

The Eq. (1.3) can be simplified to a nonlinear differential equation that describes the average profile at the stationary state ($\partial_t \rho_i = 0$) as:

$$\frac{\varepsilon}{2}\partial_x^2 \rho - \partial_x J = 0, \tag{1.8}$$

where $J = \rho(1-\rho)$ characterizes the average particle current of the TASEP and the subscript i is dropped by considering the fact that there is no inhomogeneity in the bulk. The boundary densities, $\rho(0)$ and $\rho(1)$, which are directly related to the entry and exit rates, can be determined from the steady-state form of the master equations (Eq. (1.2) and Eq. (1.4)) using the current-continuity principle. This yields $\rho_1 = \alpha$ and $\rho_L = (1 - \beta)$.

In the limit as $(\varepsilon \to 0)$, Eq. (1.8) reduces to a first-order differential equation that has two potential solutions: $\rho(x) = \text{constant}$) and $\rho(x) = 1/2$. It is evident that Eq. (1.8) is overdetermined when combined with two boundary conditions, allowing the constant to be determined by applying one boundary condition at a time. The solution that corresponds to the left boundary condition ($\rho(x=0)=\alpha$) is referred to as the entry-dominated phase or the low-density (LD) phase, while the solution that matches the right boundary condition ($\rho(x=1)=1-\beta$) is known as the exit-dominated phase or the high-density (HD) phase. The second solution, ($\rho(x)=1/2$), which corresponds to the maximum value of (J=1/4), is termed the maximal current phase (MC) [80, 109].

FIG.1.4(a) illustrates the stationary-state phase diagram of the TASEP with open boundary conditions in the $(\alpha-\beta)$ phase plane. Within this parameter space, three types of phase transitions can be identified: the transition from the low-density (LD) phase to the maximal current (MC) phase occurs along $(\alpha=1/2)$, and the transition from the high-density (HD) phase to the MC phase takes place along $(\beta=1/2)$; both of these are continuous (second-order) phase transitions. In contrast, the transition from the LD phase to the HD phase along $(\alpha=\beta<1/2)$ is a discontinuous (first-order) transition. These phase transitions illustrated in the phase diagram are identified with respect to density, which serves as the order parameter.

In addition to the LD, HD, and MC phases, there exists a non-stationary discontinuous coexistence of the LD and HD density profiles, referred to as the de-localized shock (S*) phase, which occurs along the line ($\alpha = \beta < 1/2$). Additionally, the relationship between density and current is a parabolic curve, as shown through the fundamental diagram illustrated in FIG. 1.4(b). Physically, this graph demonstrates that as the density increases, the current in the system also increases, corresponding to the low-density (LD) phase. The current reaches its maximum value at the critical density $\rho = 0.5$ (MC phase). Beyond this point, as the density continues to rise, the particles begin to pack more closely (HD phase), leading to a reduction in the overall particle flow. For further information on phase transitions and the shock phase, we direct the reader to references [82, 80, 55]. A fundamental understanding of the four key phases—LD, HD, MC, and (S*)—is essential for advancing towards generalizations of TASEP-based models.

1.3.2 Numerical tools

Beyond theoretical approaches which utilizes approximation, numerical tools are also available to handle complex stochastic transport processes, which we will explore in this section.

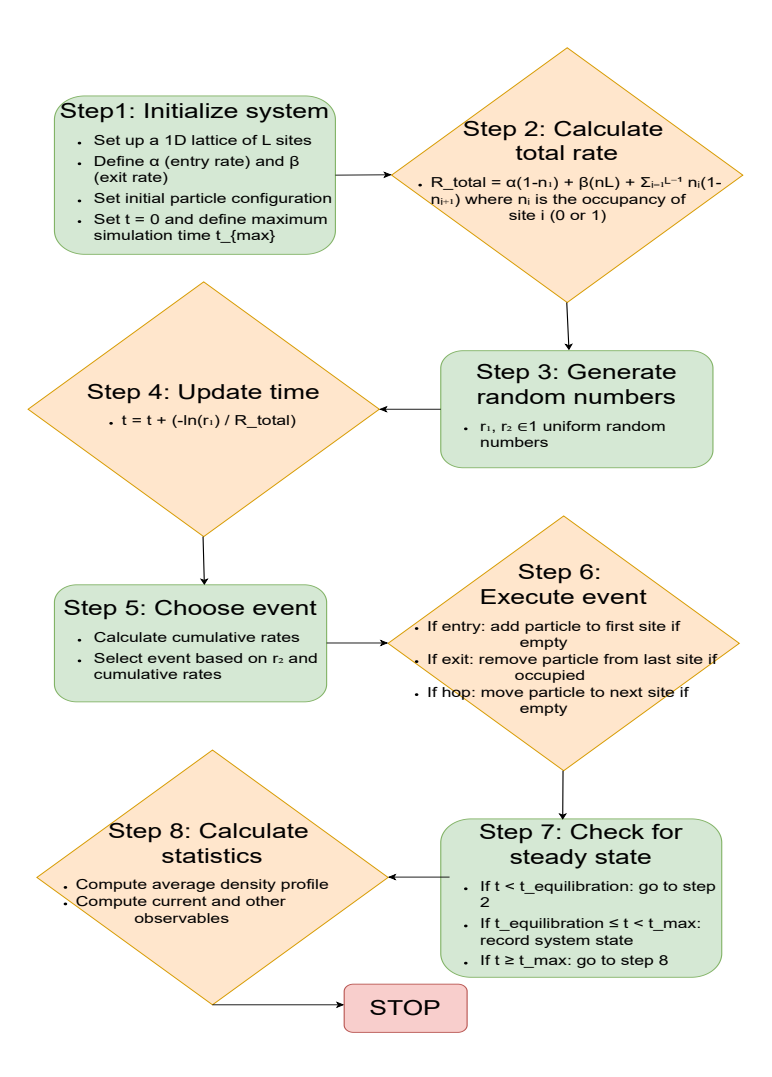


Figure 1.5: Flowchart of the Gillespie algorithm during Monte Carlo simulation utilizing random sequential updating for a TASEP with open boundaries.

1.3.2.1 Monte Carlo simulations

Monte Carlo simulations, named after the Monte Carlo Casino in Monaco, although they are directly not related but share a similar name due to the analogy of randomness. It plays a crucial role in analyzing and understanding the complex dynamics and stationary properties of TASEP-based models using random sampling. Theoretical derivations of a system's physical characteristics often rely on various assumptions and approximations, such as mean-field theory, which may not always accurately represent real-world behavior. Therefore, an alternative approach is needed to validate whether these theoretical predictions hold true. Furthermore, in complex extensions of TASEP—such as multi-lane models,

particle interactions, or site-specific dynamics—obtaining analytical solutions becomes impractical. Monte Carlo simulations [112, 85] provide a powerful numerical tool to explore these scenarios without requiring explicit mathematical solutions. By directly implementing the governing dynamical rules and generating transitions with appropriate probabilities, this method enables researchers to compute key quantities through time averaging. Ultimately, Monte Carlo simulations complement theoretical approaches by capturing random fluctuations and providing deeper insights into the stochastic behavior of TASEP-based models, enhancing their applicability to real-world transport systems. However, this computational tool requires the system to be ergodic, meaning that in configuration space, every accessible state must be reachable from any other state within a finite number of Monte Carlo moves.

For our simulations, we employ a random-sequential update rule. In this approach, each step of the algorithm involves randomly selecting a site and then choosing an event associated with that site. The selection of an event is based on probabilities that are proportional to their respective rates. A limitation of standard Monte Carlo simulations is that they are not rejection-free. In these simulations, events are accepted or rejected based on probabilities proportional to their rates. As a result, events with smaller rates are more likely to be rejected, leading to wasted computational effort without advancing the system's state. This can hinder the ability to obtain the desired results. To address this issue, we also employed the rejection-free Gillespie algorithm [53] in this thesis. This algorithm introduced by Joseph H. Gillespie in 1976, allocates simulation time $\triangle t = -\ln(r)/(\text{sum of all kinetic})$ rates) in a way that ensures every step contributes meaningfully to the system's evolution. It achieves this by directly sampling the next event and its occurrence time based on the current state of the system, eliminating the need for trial-and-error or rejection steps. This approach makes the Gillespie algorithm more efficient for simulations involving rare events or systems with widely varying timescales. However, for simulations requiring large time scales to reach a steady state or for larger lattice sizes, the time distribution of the Gillespie algorithm can become computationally intensive.

In our simulations, we employ a Monte Carlo algorithm utilizing a random sequential update rule [55]. The simulations are run for 10^{10} time steps and several lattice sizes. The initial 5% of time steps are discarded to ensure a steady state is reached, and the average particle density is computed over an interval of 10L, where L represents the lattice size. The phase boundaries through simulations are determined using the bulk density of the lattice as a quantitative criterion to identify phase transition points with an estimated error of less than 2%. The phase boundaries between the stationary phases of the phase diagram are validated through simulations as follows: We fix the value of α and vary β to a precision of up to

two decimal places to identify the values of β at which phase transitions occur. Similarly, we fix β and vary α to determine the values of α where phase transitions take place. The estimated error of less than 2% is primarily due to the step size in the parameter grid for α and β , which was set to 0.01. This limits the precision with which we can resolve the transition points.

However, in addition to the parameter resolution, statistical uncertainties were also considered. These statistical errors either arise due to the finite-size effects or finite sampling errors. To account for finite-size effects, we performed simulations for the control parameters α and β for multiple system sizes $L=100,\,500,\,$ and 1000. For each size, we observed the bulk density profile $\rho(x)$ and identified the transition points $(\alpha_c(L),\beta_c(L))$ by locating the sharp changes in the bulk density for each system size. For the upper bound of an error due to finite-size effects, we computed the difference in the transition points for L=1000 and L=500 system sizes used in the simulation, i.e., $|\alpha_c(L=1000)-\alpha_c(L=500)|$. In addition to errors due to the finite-size effect, we have also taken into account the potential statistical error that may occur during the Monte Carlo simulations. The simulations are stochastic, and the precision of the results depends on the number of samples or iterations. We ensured that the simulations were run long enough to reduce statistical noise. To estimate the statistical uncertainties in the transition point due to fluctuations in the bulk density, we compute the standard error in the bulk density profiles, which are obtained by averaging over multiple Monte Carlo simulations.

A flowchart provided in FIG.1.5 outlines the procedure for simulating a standard TASEP model with open boundaries, assuming particles move from left to right. While Monte Carlo simulations effectively capture the dynamics of the systems being studied, these algorithms tend to be computationally expensive. Additionally, they lack a systematic approach for analyzing multiple dynamics collectively. As a result, the algorithm is mainly used to validate theoretical findings, which in itself demands extensive simulation efforts.

1.3.2.2 Convergence of simulations

The convergence of Monte Carlo simulations is ensured by the ergodicity of the system. This property implies that the Markov chain will ultimately converge to a stationary distribution, irrespective of its initial state.

Moreover, the system exhibits two crucial characteristics:

1. **Irreducibility:** This means that the system can transition from any given configuration to any other possible configuration within the state space. In other words, all states are accessible from any starting point.

2. **Aperiodicity:** This property indicates that the system can return to a specific configuration at irregular intervals. The time required to revisit a particular configuration is not fixed or periodic.

These properties collectively guarantee the robustness and reliability of the Monte Carlo method in exploring the system's state space and converging to the correct stationary distribution.

1.3.2.3 Numerical Differentiation

An alternative approach exists to derive the numerical solution for the second-order continuum mean-field equation (Eq. (1.8)). The primary objective in developing the numerical scheme is to address the challenge of analytically computing the stationary-state particle density using the system of equations (Eq. (1.2) - Eq. (1.4)). This becomes particularly difficult when more complex features of TASEP, as discussed in this thesis, are taken into account.

In this method, we first apply mean-field approximations to these equations to eliminate correlators. The particle density at the i^{th} lattice site is numerically represented as ρ_i^n at the n^{th} time step, with the condition that the stationary-state solution is achieved as $n \to \infty$. Retaining the time derivative within the system, we employ the forward-in-time and central-in-space (FTCS) scheme and derive the finite-difference equation as:

$$\rho_i^{n+1} = \rho_i^n + \triangle t \left(\frac{\varepsilon}{2} \left(\frac{\rho_{i+1}^n - 2\rho_i^n + \rho_{i-1}^n}{\triangle x^2} \right) + \left(\frac{\rho_{i+1}^n - \rho_{i-1}^n}{2\triangle x} \right) (2\rho_i^n - 1) \right). \tag{1.9}$$

Here, the spatial variable $\Delta x = 1/L$ and the temporal variable Δt adhere to the stability criterion of the finite-difference scheme mentioned above, $\Delta t/\Delta x^2 \le 1$. For boundary treatments, we utilize the numerical integration of Eq. (1.2) and Eq. (1.4) which is presented as:

$$\rho_1^{n+1} = \rho_1^n + \Delta t \left(\alpha (1 - \rho_1^n) - \rho_1^n (1 - \rho_2^n) \right), \tag{1.10}$$

and,

$$\rho_{L}^{n} = \rho_{L}^{n} + \triangle t \left(\rho_{L-1}^{n} (1 - \rho_{L}^{n}) - \beta \rho_{L}^{n} \left((1 - \rho_{1}^{n}) \right).$$
 (1.11)

Further, one may also numerically integrate these discrete equations directly but one has to be careful while handling the presence of one-or two-point correlators.

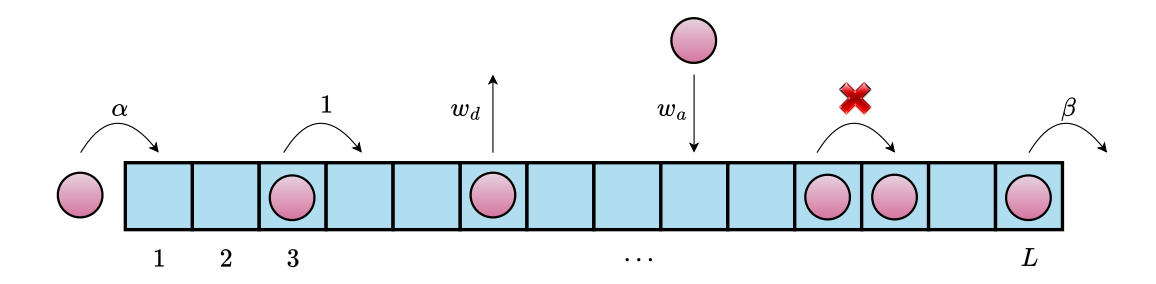


Figure 1.6: Schematic representation of Langmuir Kinetics (LK) dynamics on a TASEP with OBC.

1.4 Generalizations of TASEP Model

There is no question that the one-dimensional structure and straightforward dynamics of TASEP offer a well-established framework for modeling many realistic problems. However, it is equally true that numerous real-world transport systems cannot be accurately represented by this basic model. To overcome this limitation, significant efforts have been made to extend the TASEP framework by incorporating key features such as Langmuir kinetics, stochastic local resetting, dynamic disorder, bidirectional transport, finite resources, and more. In the following section, we will provide a brief overview of each of these generalizations, which are relevant to the problems explored in this thesis.

1.4.1 Langmuir kinetics

In both physical and biological transport processes, situations often arise where moving elements can attach to or detach from their pathways during directional movement due to various factors. In intracellular transport, such situations arise when processive motors, like conventional kinesins and myosins-V, permanently detach from filament tracks after moving several steps. Similarly, in vehicular traffic, this occurs when vehicles enter or exit highways, typically facilitated by on/off-ramps. These phenomena highlight the importance of studying inhomogeneous TASEP models, where particles move along a lattice and are permitted to attach or detach from the bulk of the lattice [61], leading to a non-conserving system. This concept is illustrated in FIG.1.6.

Although TASEP represents a non-equilibrium process, it conserves particles within the bulk of the system. In contrast, TASEP with Langmuir kinetics (LK) allows particles to enter or exit the system from any point in the bulk of the lattice, leading to non-conserving dynamics. If hopping is ignored in TASEP with LK, the steady-state equilibrium density can be expressed as $\rho_{LK} = K/(K+1)$, where $K = w_a/w_d$ represents the binding constant

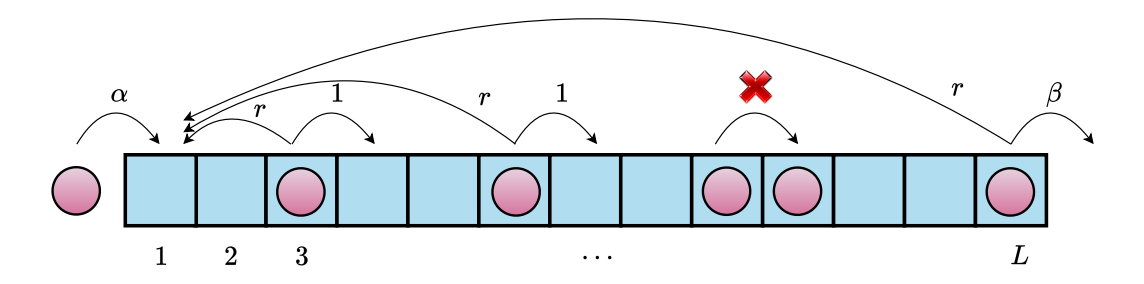


Figure 1.7: Schematic representation of Local-resetting (LR) dynamics on a TASEP with OBC.

[103].

Initially, the LK dynamics were incorporated into TASEP to address a stock market problem [143], and later they were applied to model the dynamics of molecular motors [103, 91, 102]. Mirin and Kolomeisky [91] investigated the effects of particle detachments in a single-lane exclusion process model. Subsequently, Parmeggiani et al. [103] provided a comprehensive analysis of the TASEP model with LK dynamics, revealing numerous intriguing features, including a rich phase diagram with localized shock phases and Meissner phases. They also demonstrated that the topology of the phase diagrams undergoes significant changes with variations in the binding constant, as detailed in references [103, 102]. Over the past decade, extensive research has been conducted on TASEP with LK models, exploring the dynamics of phase coexistence and shock localization [102, 45].

1.4.2 Stochastic local resetting

The concept of resetting emerged within the broader framework of statistical physics and probability theory, inspired by numerous real-world dynamical systems that experience interruptions and subsequent resumptions from particular points in their phase space. A schematic diagram of the local resetting process in a TASEP model is provided in FIG.1.7. It was introduced to study the effects of intermittent interruptions on random walks or diffusion processes. A classic example is the resetting of a Brownian particle to its initial position at a fixed rate [47]. This seemingly straightforward mechanism leads to several intriguing phenomena, such as the emergence of non-trivial stationary states and non-monotonic mean first passage times. In the context of exclusion processes, stochastic local resetting in recent years was incorporated to model microbiological challenges where particles occasionally return to specific locations or states, mimicking real-world phenomena such as molecular motors detaching and reattaching to tracks, or vehicles returning to specific points in traffic flow. Further examples include the interplay between random mRNA degradation and

ribosome loading during translation [136]. Furthermore, this concept has found applications across diverse fields, such as backtrack recovery by RNA polymerases, search and optimization algorithms [93], predator-prey system modeling [131], chemical reaction dynamics [113], and biopolymerization processes [114], among others.

Stochastic resetting typically manifests in two forms: global or local. In global resetting, all particles simultaneously revert to a predefined reference state. In contrast, local resetting involves particles resetting their positions independently to specific sites, which presents greater complexity compared to global resetting. Local resetting has been shown to induce spatially heterogeneous effects, whereas global resetting generally leads to a homogenization of the system. Early research primarily focused on resetting rules from a global perspective, and much of the existing literature has extensively explored this aspect [49, 48, 74, 10].

Local resetting was initially introduced and studied within the framework of a symmetric simple exclusion process featuring periodic boundary conditions [92, 106]. This investigation was later expanded to the Totally Asymmetric Simple Exclusion Process (TASEP) under similar periodic boundary conditions [92, 106]. The resetting mechanism reveals a significant link with Langmuir kinetics (LK) dynamics, illustrating that it can be interpreted as a special case of the LK process where only the detachment of particles from the bulk of the system occurs [92, 106]. These studies demonstrate that resetting introduces a non-equilibrium driving force, which competes with the inherent drift of particles and modifies steady-state density profiles. This can result in the formation of localized traffic jams or, under certain conditions, enhance particle flow. Additionally, resetting influences the conventional phase diagrams of the TASEP, giving rise to new stationary phases. The interaction between particle injection/extraction rates and resetting dynamics can alter the boundaries between high-density, low-density, and shock phases, leading to significant shifts in system behavior.

1.4.3 Dynamic disorder

In our daily lives, we frequently encounter obstacles such as roadblocks, toll booths, accidents, or speed limits that disrupt vehicular flow dynamics during commutes. Similar situations arise in pedestrian movement, where factors like narrow doorways, fluctuations in crowd density, and bottlenecks cause temporary slowdowns and congestion. Analogous phenomena occur in the microscopic world, where RNA polymerase pausing and backtracking during gene transcription—due to the binding of regulatory proteins to DNA—create temporary disruptions that affect transcription rates. The binding of regulatory proteins to

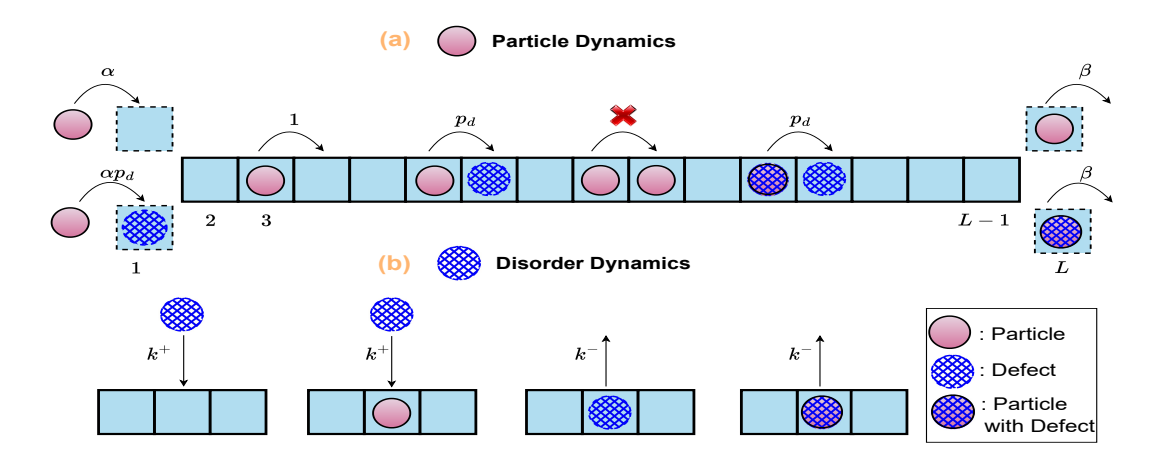


Figure 1.8: Schematic representation of dynamic disorder dynamics on a TASEP with OBC.

DNA or RNA introduces dynamic hindrances, influencing transcription rates and gene expression patterns [86, 98, 40, 25]. These disruptions or obstructions can be classified into two categories: static and dynamic. Static defects refer to fixed slow sites in a transport system where particles encounter reduced hopping rates at specific locations. In contrast, dynamic defects fluctuate over time and are not permanently positioned. For example, certain microtubule-associated proteins (MAPs) bind to microtubules at specific sites, creating permanent obstacles for molecular motor proteins like kinesins and dyneins, thereby impacting cargo transport efficiency along microtubules. During translation, mRNA regions can dynamically fold and unfold, affecting ribosome movement through codons, or mRNA-binding proteins may transiently associate with the transcript, temporarily blocking ribosome progression. Similarly, in traffic systems, roads may periodically switch between high and low flow states due to traffic signals, lane closures, or weather conditions, exemplifying dynamic defects.

In this context, numerous variations of the Totally Asymmetric Simple Exclusion Process (TASEP) have been explored over the years to investigate the influence of dynamic defects on the stationary properties of the system [78, 132, 41, 70, 58, 140, 116, 133, 117]. A schematic representation of this model is illustrated in FIG.1.8. Across these studies, a consistent observation is that the presence of defects imposes restrictions, leading to a reduction in the maximal possible current within the system.

1.4.4 Finite resources

It is evident that the availability of resources in physical or biological processes is often limited. This observation is particularly significant in the context of living cells, where protein

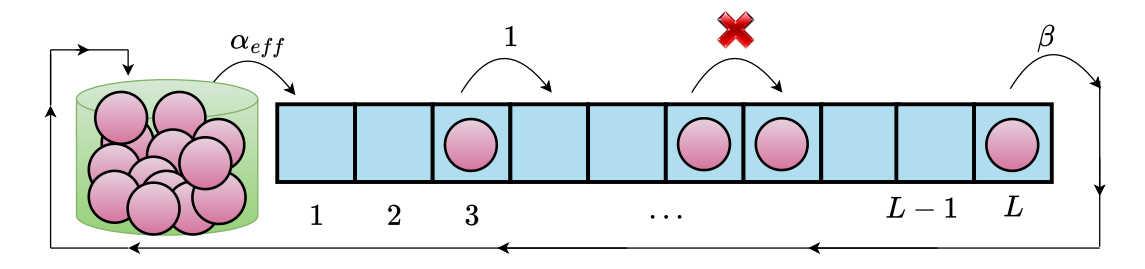


Figure 1.9: Schematic representation of a particle coming from a finite reservoir on a TASEP with OBC.

synthesis—a complex and vital process—occurs in two stages: transcription and translation [26]. During translation, ribosomes move along the mRNA strand, synthesizing proteins based on the encoded genetic information. However, the number of ribosomes within a cell is finite, akin to the limited number of motor proteins that facilitate directed transport along microtubules, enabling individual motor proteins to traverse the microtubule track multiple times [18, 79]. Despite this, much of the stochastic modeling using the TASEP assumes infinite resources.

To address this limitation, it is necessary to develop TASEP models that account for finite resources. In this regard, Adams et al. [1] introduced the first constrained TASEP model, where the total number of particles in the system was limited, serving as a critical control parameter. Physically, the availability of resources influences the entry rates in such systems. In this model, particles enter the first site of the lattice from a finite-capacity reservoir at a rate proportional to the reservoir's capacity and exit from the last site, rejoining the reservoir while maintaining a constant total number of particles in the system at all times. A schematic representation of this model is provided in FIG.1.9. A key feature of incorporating finite resources is that the delocalized shock observed in the standard single-lane TASEP, which lies along a straight line in the $\alpha - \beta$ parameter space, expands into a localized region. This modification has a non-trivial impact on the stationary properties of the one-dimensional TASEP, prompting researchers to propose further extensions of TASEP with finite particle supplies [33, 32, 22, 57, 56, 54, 66, 137, 138]. In the following chapter, we will summarize the findings of selected primary studies at the appropriate points.

1.4.5 Bidirectional transport

On many streets, it is common to observe situations where a single lane accommodates two opposing flows of vehicles. Several studies have explored this bidirectional transport on a single lane, as referenced in [81, 84]. Similar bidirectional transport phenomena occur at the

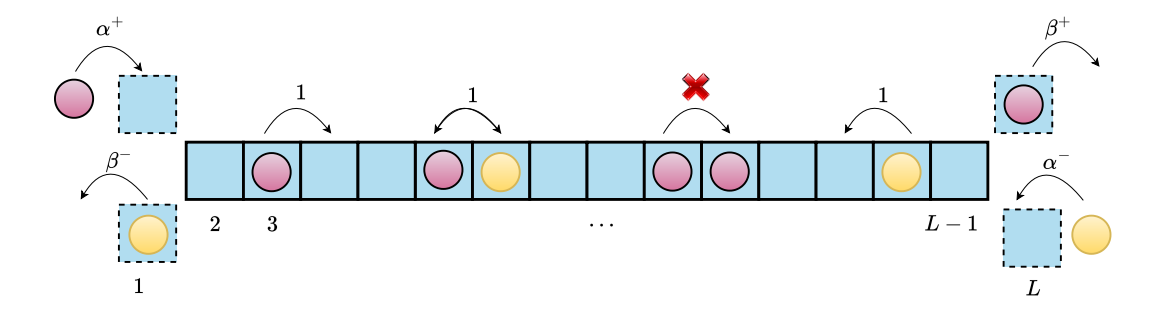


Figure 1.10: Schematic representation of two species of particles exhibiting bi-directional transport dynamics on a TASEP with OBC.

microscopic level within cells, where molecular motors such as kinesin and dynein move in opposite directions along microtubules [60, 59]. These distinct motors may share a single microtubule, necessitating proper coordination during their collective movement for the cell to function effectively. Such scenarios have inspired researchers to model the bidirectional transport of multiple particle species moving in opposite directions on a one-dimensional lattice within the framework of TASEP. A schematic representation of this model is shown in FIG.1.10. The introduction of bidirectional transport has revealed spontaneous symmetry-breaking phenomena, beginning with the work of Evans et al. on the "bridge model" [44, 43], where a symmetry break in the stationary-state density of two particle species was observed despite symmetrical dynamical conditions for both types of particles.

Subsequently, to incorporate various distinct features associated with different species exhibiting bidirectional transport on single or multiple lanes, several extensions of the standard bidirectional-TASEP model have been explored. These extensions include dynamics such as non-conserving processes, limited resource availability, stochastic directional switching mechanisms, and a new class of bridge models fed by junctions, among others [94, 107, 111, 139]. Additionally, the understanding of symmetry breaking has been extended to non-Markovian bidirectional transport processes [69]. Nevertheless, the occurrence of symmetry-breaking phenomena remains a topic of ongoing discussion [31, 126].

1.5 Aims & Objectives

This thesis aims to closely examine transport phenomena in various naturally occurring dynamic stochastic processes, focusing on directions that have not been comprehensively explored in the past. By utilizing the fundamental TASEP model, we seek to understand their long-term behavior by capturing their steady-state characteristics. To address unresolved

questions during the analysis of TASEP-based models with diverse dynamical features, we primarily employ theoretical techniques such as mean-field theory, alongside numerical tools like Monte Carlo simulations and Gillespie algorithms.

It is fair to say that much of contemporary research is interdisciplinary, and our work is no exception. It emerges from the integration of ideas and knowledge across multiple disciplines, including Mathematics, Physics, Biology, and Statistical Mechanics. Below, we outline the primary goals and objectives of this thesis.

- 1. Dynamic disorder is a common feature in many biological and physical transport processes, and we investigate its influence on particle dynamics in a standard TASEP under resource-limited conditions. In this system, particles and defects compete for access under constrained availability, resulting in modified entry rates. Additionally, we establish a theoretical framework to analyze dynamic disorder in an open TASEP model with non-conserving dynamics driven by Langmuir Kinetics. This effort is motivated by the reliance on numerical methods to study the system's stationary properties, highlighting the necessity for analytical approaches to gain a more comprehensive understanding of its intricate dynamics.
- 2. Inspired by the drop-off behavior of ribosomes during translation, we propose to explore the dynamics of local resetting on a one-dimensional lattice under resource-constrained conditions. Since existing models in the literature fail to fully capture the microscopic mechanisms governing such processes, our goal is to establish a theoretical framework and analyze how the resetting rate affects the stationary properties of the system, such as phase diagrams, density profiles, and phase transitions. Following this, we will explore the bi-directional flow of two distinct particle species moving in opposite directions and exhibiting local resetting. The primary focus will be on understanding how local resetting influences symmetry-breaking phenomena arising from bidirectional particle movement. Given the scarcity of research on TASEP models with local resetting, this study aims to provide deeper insights into the stochastic transport dynamics in such systems.
- 3. Additionally, we aim to investigate how local resetting dynamics interact with defects in a dynamically disordered TASEP. While disorder generally reduces particle flux, local resetting alters the system's maximal current, presenting a significant challenge in characterizing the stationary-state behavior of such systems. This study is motivated by the limited understanding of models incorporating dynamic disorder. To our

- knowledge, no prior research has examined these dynamics, which have the potential to model various biological transport processes.
- 4. The challenge of efficiently separating colloidal particles of different sizes in densely packed narrow channels, a process essential for applications such as filtering unwanted particles from blood or isolating various types of blood cells. Given the irregular structures of these channels, we investigate this problem through a geometrically adapted single-channel TASEP model, where each lattice site is linked to a pocket-like structure capable of holding a fixed number of particles. The focus is on analyzing the steady-state properties of this model under both finite and infinite particle reservoir conditions.

1.6 Outline of the thesis

Having outlined the objectives we aim to accomplish through various generalizations of TASEP-based models—previously unexplored and designed to approximately, though not precisely, mimic real-world transport scenarios—we now present a structured framework for the thesis. The entire work is organized into eight chapters, consisting of six core chapters (Chapters 2-7) that form the main contributions to the thesis, complemented by an introductory chapter (Chapter 1) and a concluding chapter (Chapter 8). This framework organizes our goals and objectives into the following chapters:

Chapter 1: Introduction

This chapter provides an overview of the research topic and its context within the broader field. It begins with a review of relevant literature, summarizing key theories and concepts while identifying gaps in current knowledge. The motivation for the study is discussed, along with its significance and potential contributions to the field. The chapter also outlines the research problems addressed and explains why they are important to investigate. A brief overview of the methodology is included, describing the approaches used and their relevance to the research objectives. Finally, the chapter concludes with a summary of the thesis structure, explaining how each chapter contributes to achieving the overall goals of the study.

Chapter 2: Role of site-wise dynamic defects in a resource-constrained exclusion process

In this chapter, we investigate an exclusion process with site-wise dynamic disorder in a

resource-constrained environment. Dynamic defects, which hinder particle flux, stochastically appear and disappear across the lattice with a constrained binding rate and a constant unbinding rate, respectively. The impact of resource constraints on the system's stationary properties is analyzed through the filling factor. Analytical results derived from naive mean-field theory are validated with Monte Carlo simulations and found well aligned for faster defects, regardless of the affected hopping rate, and for slower defects with a large affected hopping rate. For slower defects with a small affected hopping rate, correlations emerge, necessitating an enhanced mean-field approach that provides more accurate approximations than the naive mean-field method. These correlations diminish as the affected hopping rate increases. Our theoretical framework consolidates the parameters governing defect kinetics—affected hopping rate, defect binding (unbinding) rate, and defect density—into a single parameter termed the obstruction factor. The implications of the obstruction factor are thoroughly explored by examining its limiting cases. The phase boundaries obtained through different mean-field approaches are distinctly influenced by their respective obstruction factors.

Chapter 3: Site-wise dynamic defects in a non-conserving exclusion process

This chapter explores an open, dynamically disordered, totally asymmetric simple exclusion process with bulk particle attachment and detachment. Using a mean-field approach, we derive analytical expressions for particle and defect densities, validated by Monte Carlo simulations. We analyze the system's steady-state properties, including phase transitions, boundary layers, and phase diagrams. Defect dynamics are simplified by combining two parameters into an obstruction factor, which determines an effective binding constant. The obstruction factor's influence on the phase diagram is examined across various binding constants and detachment rates. A critical obstruction factor value is identified, where slight changes cause significant qualitative shifts in phase diagram structure. Additionally, critical detachment rates are determined, marking quantitative transitions in stationary phases as functions of the obstruction factor. The system exhibits three to seven stationary phases, depending on the obstruction factor, binding constant, and detachment rate. Finally, the obstruction factor's impact on shock dynamics is investigated, revealing no finite-size effects.

Chapter 4: Totally asymmetric simple exclusion process with local resetting in a resourceconstrained environment

In this chapter, motivated by mRNA translation processes where stochastic degradation of mRNA-ribosome machinery is modeled through resetting dynamics, we study an open to-

tally asymmetric simple exclusion process with local resetting at the entry site in a resource-constrained environment. The influence of resource constraints on the system's stationary properties is analyzed using the filling factor. Mean-field approximations are employed to derive stationary state features, such as density profiles and phase diagrams, and the role of the resetting rate is investigated. The effects of the resetting rate and finite-size dynamics on shock behavior are also examined.

Chapter 5: Local Resetting in a Bidirectional Transport System

In this chapter, we explore a totally asymmetric simple exclusion process with open boundaries in a bidirectional configuration, where two oppositely charged particle species move in opposite directions and locally reset to their respective entry sites. This model is inspired by the two-sided motion of ribosomes during the initiation of mRNA translation, coupled with their decay. Steady-state properties, such as density profiles and phase diagrams, are theoretically analyzed using a mean-field framework. The inclusion of resetting introduces non-trivial effects, leading to the emergence of two novel asymmetric phases in the phase diagram. The system exhibits a variety of symmetric and asymmetric phase combinations depending on the resetting rates, revealing rich behavior and spontaneous symmetry-breaking phenomena even at low resetting rates. The impact of the resetting rate on the domain wall is also examined, showing that one stationary phase with a localized domain wall disappears at higher resetting rates. Additionally, the interaction between the two species at the boundaries is studied, highlighting the effects of resetting dynamics on boundary densities.

Chapter 6: Local resetting in a dynamically disordered exclusion process

In this chapter, to model the recycling process and the obstructions encountered by mRNA polymerase during gene transcription, we study an open, dynamically disordered, totally asymmetric simple exclusion process where particles reset locally to the entry site across the lattice. Stationary-state properties, such as density profiles, current, and phase boundaries, are derived using mean-field approximations. The phase diagram features five stationary phases: three pure phases and two coexisting phases, both of which exhibit localized domain walls. The influence of the resetting rate and obstruction factor on the system's stationary properties, including phase diagrams, is thoroughly analyzed. With increasing resetting rate or obstruction factor, the quadruple and triple points in the phase diagram shift antidiagonally, expanding the region dominated by the maximal-current phase. Additionally, potential phase transitions and domain wall behavior under varying resetting rates and obstruction factors are investigated. The finite-size effect on the system's stationary-state

1.6 Outline of the thesis

27

characteristics is also examined.

Chapter 7: Far from equilibrium transport on TASEP with pockets

In this chapter, we study a geometric adaptation of a TASEP with open boundary conditions, where each site in a one-dimensional channel is connected to a lateral space (pocket). The capacity q of each pocket determines the maximum number of particles it can hold. For the case q = 1, where both the lattice and pocket adhere to the hard-core exclusion principle, we employ continuum mean-field approximations. For pockets with multiple capacities (q > 1), which violate the hard-core exclusion principle, we combine a probability mass function with mean-field theory. The model is analyzed for both finite and infinite reservoirs. Explicit expressions for particle density are derived, and the phase diagram in the $\alpha - \beta$ parameter space is examined as a function of q and attachment-detachment rates. Notably, the phase diagram's topology remains consistent near q = 1. The competition between the lattice and pocket for finite resources, along with unequal Langmuir kinetics, leads to a back-and-forth transition phenomenon. Additionally, we explore the limiting case $q \to \infty$.

Chapter 8: Conclusion and Future work

This chapter presents a summary of the findings discussed in the preceding chapters of the thesis. Additionally, it highlights potential extensions of the proposed problems that could be explored in future research.



Role of site-wise dynamic defects in a resource-constrained exclusion process

Preamble

The first chapter introduced the Totally Asymmetric Simple Exclusion Process (TASEP), a paradigmatic lattice gas model demonstrating non-equilibrium phenomena in a discrete one-dimensional lattice. Building upon this foundation, the present chapter explores a dynamically disordered variant of TASEP in a resource-constrained environment. In this model, both particles and dynamic defects enter the lattice from a reservoir with finite capacity, reflecting more realistic conditions often encountered in natural and engineered systems. The subsequent sections will elucidate the motivation behind this extension, detail the proposed model, outline the methodological approach, and present the steady-state outcomes of this modified system. This investigation aims to bridge the gap between idealized TASEP models and the resource limitations inherent in many real-world transport processes.

2.1 Background

Even though many of the physical systems in nature like pedestrian traffic or filament length kinetics compete for resources in a pool of limited availability [18, 29], still a great number of TASEP models and their extensions are based on the fact that the system is connected to an infinite reservoir [37]. To consider the effect of the finite availability of resources, recently, the studies have been extended by coupling a limited reservoir (or pool) to the open TASEP [1, 22, 32, 33, 54, 141]. Such a constraint can be understood in the context of protein synthesis as having a finite number of ribosomes (which model particles in TASEP) in a cell, or in the context of traffic (with cars as particles) as the 'parking garage problem' [56]. In contrast to the open TASEP connected to an infinite reservoir, the particles remain conserved in the system with a finite pool. To meet the demand and supply of limited resources and the incorporation of dynamics invoked due to particle conservation in the system, the system exhibits a novel feature such as the formation of a localized domain wall [66, 137, 138].

While understanding these properties is of fundamental theoretical interest, the TASEP and its generalizations have also acquired fame as models for practical problems where some obstacle or defect often impedes traffic. Be it a traffic situation at a macroscopic level, where a faulty vehicle or a traffic light (defect) on a busy road can cause congestion, or at a microscopic level, where the progress of RNA polymerase (molecular motor) during gene transcription is slowed down by DNA-bound structures (obstacles) [2]. The messenger-RNA (mRNA), which is composed of a sequence of codons, is synthesized during the transcription of the DNA template and is further decoded by transfer-RNA(tRNA) in the ribosome during translation to produce an amino acid chain. The codon specificity and concentration of freely diffusing tRNA governs the rate of translation at each codon site [129]. Most of the time, the protein formed out of the chains of amino acids or the cluster of tRNA acts as a hindrance to the movement of the motor protein [122].

The path blocking of RNA polymerase during gene transcription introduces inhomogeneity to the system. It has been thoroughly investigated in the context of a more intricate TASEP model, where the defects are static, i.e., their locations are either randomly dis-

tributed spatially or at some specific sites [41, 58, 70, 78, 132]. The study of TASEP with the static disorder has been well explored in the literature. In contrast, the case of random dynamic defects is yet to be explored. Motivated by the random occurrence and disappearance of dynamic DNA proteins that obstruct the movement of molecular motors along micro-tubules, we propose the study of a single-channel TASEP with the dynamic disorder, where the particles and defects hop in and out of the lattice from a finite reservoir. Recently, a study was conducted on a dynamically disordered single-channel TASEP (dd-TASEP) with a fixed entry rate (corresponding to an infinite reservoir), and the defect causes complete obstruction to the particle movement [140].

In the suggested model, a dynamically disordered TASEP is coupled to two distinct finite pools of resources, one of which consists of particles and the other of which is made up of defects. In the present model, the entry dynamics have been modified in context to the model presented in ref. [140]. To better understand the system, we will investigate the model with the mean-field approach. The obtained results will be used to analyze the effect of the dynamic disorder defect on the phase diagram of TASEP with a limited availability pool. The chapter is organized in the following manner: The dynamic rules associated with the model are defined in section 2.2. The master equations for various transitions in the model are derived in the section2.3. In section 2.4, the continuum naive mean-field approximation is utilized to solve master equations and procure density profiles. The phase diagrams and effects of various parameters are discussed in detail in subsection 2.4.1. The discrepancies between naive mean-field and simulations are discussed in section 2.5. The enhanced mean-field framework is carried out in section 2.6. Finally, the study's outcomes are summarized in section 2.7.

2.2 Model description

The proposed model consists of a single-channel TASEP with dynamic disorder, with both ends connected to a finite reservoir of particles (R_1) . The sites of the one-dimensional lattice are labeled as j = 1, 2, ..., L, where j = 1 (L) represents the entry (exit), and the

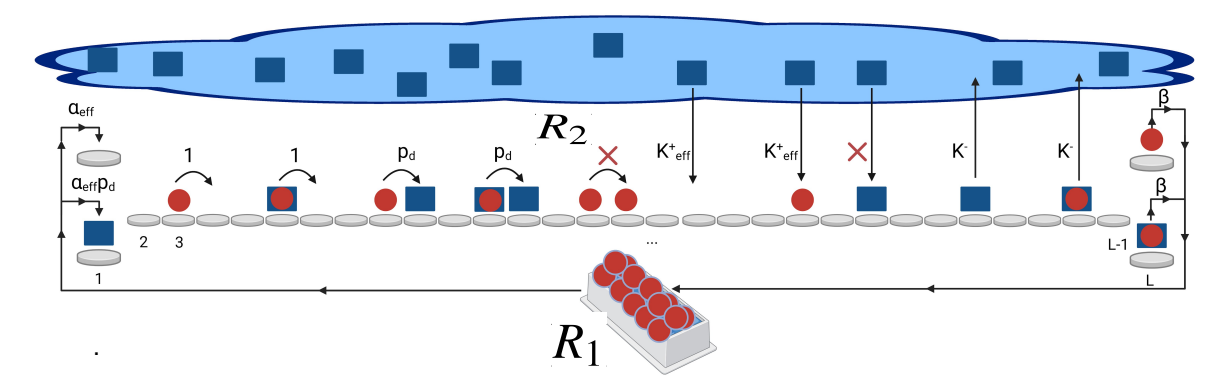


Figure 2.1: A schematic diagram of the proposed model, where the particles (in red) enter the first site of the lattice (j=1) from a finite reservoir (R_1) with the rate $\alpha_{\rm eff}$ or $\alpha_{\rm eff}p_d$, depending upon the defect occupancy at the first site. The particles hop horizontally on the lattice with rate 1 or p_d depending upon the defect occupancy at the arrival site. Particles exit the lattice from its last site (j=L) with the rate β . The defects or obstacles (in blue) binds and unbinds vertically on the lattice site from another finite reservoir (R_2) with rate $k_{\rm eff}^+$ and k^- , respectively.

remaining sites $(2 \le j \le L - 1)$ are referred to as the bulk of the lattice. The particle can only get inside the lattice from R_1 through the entry site, hops uni-directionally (left to right) on the lattice, and rejoin it back through the exit site, representing the non-equilibrium process on the lattice. To incorporate the site-wise dynamic disorder throughout the lattice, we consider another species of particles called *defects* (or *obstacles*), which slow down the particle movement on the lattice. The defect dynamics on the lattice are as follows: regardless of the particle occupancy on the lattice sites, the defects can stochastically bind (or unbind) to (or from) any lattice site with rate k_{eff}^+ (or k^-) from another finite reservoir of defects (R_2) . Both particles, as well as defects, individually follow the hard-core exclusion principle. It means that each site can hold at most one particle, or one defect, or both.

The particle dynamics and associated rates that are influenced by the presence of the defects at the different lattice sites (Entry, Exit and Bulk), as shown in FIG. 2.1, are defined as follows:

1. Entry: For a particle-free entry site, a particle from R_1 enters the lattice with a rate $\alpha_{\rm eff} p_d$ ($p_d < 1$) if the defect is present at the arrival site or with a rate $\alpha_{\rm eff}$ otherwise. In case, the entry site is occupied by a particle, then this particle hops to its adjacent particle-free site with a unit rate if the defect is unavailable at the arrival site or with a

rate p_d otherwise.

- 2. *Exit*: Irrespective of the defect's presence at the last site, if the particle is present at the last site, it exits the lattice with a rate β to rejoin the R_1 .
- 3. Bulk: A particle present at any bulk site hops to its adjacent particle-free site with a unit rate if the defect is unavailable at the arrival site or with a rate p_d otherwise.

We have also considered the binding (or unbinding) of defects at the boundary sites in the proposed model. Notably, our model for the infinite reservoir of particles and defects will not boil down to the model introduced in ref.[140]. In addition to considering finite reservoirs for particles and defects, we have also considered the entry rate affected by the presence of the defect at the first site. Moreover, the involvement of the binding (or unbinding) process of defects at the boundary sites in the proposed model has a significant effect on the stationary state properties of the system.

Furthermore, the finite resources in the R_1 affect the entry rate of particles, and as a result, the effective entrance rate α_{eff} is defined such that it depends on the number of particles (N_{R_1}) in the R_1 . Similarly, the effective binding rate k_{eff}^+ depends on the number of defects (N_{R_2}) in the R_2 . The effective entry and binding rates follow the relationship given by:

$$\alpha_{\text{eff}} = \alpha g(N_{R_1}), \text{ and } k_{\text{eff}}^+ = k^+ g(N_{R_2})$$
 (2.1)

where α and k^+ are innate rates. The choice of g controls the system dynamics, and the inflow rate of particles (or defects) is proportional to the number of particles (or defects) in the R_1 (or R_2) [1]. Therefore, g, defined as $g(N_{R_i}) = \frac{N_{R_i}}{N_{t_i}}$, is a monotonically increasing function, where $i \in \{1,2\}$ and $N_{t_1}(N_{t_2})$ refers to the total number of particles (defects) in the system. To explore the effect of N_{t_i} on system dynamics, we define the filling factor [57],

$$\mu_i = \frac{N_{t_i}}{L}.\tag{2.2}$$

The limiting case, $\mu_i \to \infty$ corresponds to the case of an infinite reservoir where both the entry rate and the binding rate become constant and independent of the number of particles

(or defects) in the reservoir, i.e., $\alpha_{\rm eff}=\alpha$ and $k_{\rm eff}^+=k^+$.

2.3 Theoretical analysis

To provide analytical support to the process involved in the proposed model, we define random variables σ_j and v_j for the particle and defect occupation number, respectively, at the j^{th} lattice site. Both σ_j and v_j are binary since both particles and defects on the lattice fulfill the exclusion criterion individually. The $\sigma_j = 0$ ($v_j = 0$) denotes that the site j is particle (defect) free, and similarly $\sigma_j = 1$ ($v_j = 1$) denotes that the site j is particle (defect) occupied. The master equation for the evolution of the average particle occupation number in the bulk of the lattice ($2 \le j \le L - 1$) is given by:

$$\frac{d\langle \sigma_j \rangle}{dt} = J_{j-1,j} - J_{j,j+1}, \tag{2.3}$$

where,

$$J_{i-1,j} = \langle \sigma_{i-1}(1 - v_i)(1 - \sigma_i) \rangle + p_d \langle \sigma_{i-1}v_i(1 - \sigma_i) \rangle$$
 (2.4)

is the particle current from site j to site j+1 and $\langle \cdots \rangle$ denote the statistical average. Therefore, the master equation for transitions at the left-lattice boundary is given by:

$$\frac{d\langle \sigma_1 \rangle}{dt} = J_{entry} - J_{1,2},\tag{2.5}$$

where, J_{entry} is the particle current at the entry site (j = 1) and $J_{1,2}$ is the particle current that emerges as the particle hops from site j = 1 to j = 2 and are respectively given as:

$$J_{entry} = \alpha_{\text{eff}} \langle (1 - \sigma_1)(1 - v_1) \rangle + \alpha_{\text{eff}} p_d \langle (1 - \sigma_1) v_1 \rangle, \tag{2.6}$$

In the above equation, note that the second term on the right is due to the consideration of defect binding at the left boundary which was not considered in ref. [140]. At the right-lattice boundary, the evolution of the average particle occupation number is determined according to:

$$\frac{d\langle \sigma_L \rangle}{dt} = J_{L-1,L} - J_{exit}, \qquad (2.7)$$

where, $J_{L-1,L}$ represents the particle current due to the hopping of the particle from site j = L - 1 to site j = L and J_{exit} is the particle current when the particle leaves the lattice from the exit site (j = L), and they are respectively expressed as:

$$J_{exit} = \beta \langle \sigma_L \rangle. \tag{2.8}$$

Moreover, the master equation for the evolution of the average defect occupation number in the lattice is given by:

$$\frac{d\langle \mathbf{v}_j \rangle}{dt} = k_{\text{eff}}^+ \langle (1 - \mathbf{v}_j) \rangle - k^- \langle \mathbf{v}_j \rangle, \quad 1 \le j \le L.$$
 (2.9)

To understand the stationary state dynamics of the system, the eq. (2.3) is required to be solved utilizing the boundary conditions given by eq. (2.5) and eq. (2.7). It is evident that the equations involve one and two-point correlators, making them difficult to solve in their current form. In the next sections, we try to approximate the correlators with the naive and other enhanced mean-field approaches to obtain the steady-state solution to the master equations.

2.4 Naive mean-field framework

We employ the naive mean-field approximation that neglects all the possible correlations present in the obtained set of master equations, i.e., $\langle \sigma_j \sigma_{j+1} \rangle = \langle \sigma_j \rangle \langle \sigma_{j+1} \rangle$ and $\langle \sigma_j v_{j+1} \rangle = \langle \sigma_j \rangle \langle v_{j+1} \rangle$. We define the average particle density and defect density at site j as $\rho_j = \langle \sigma_j \rangle$ and $\rho_{d,j} = \langle v_j \rangle$, respectively, and the expression of the particle current reduces to:

$$J_{j-1,j} = \rho_{j-1}(1 - \rho_{d,j})(1 - \rho_j) + p_d \rho_{j-1} \rho_{d,j}(1 - \rho_j), \tag{2.10}$$

$$J_{entry} = \alpha_{eff}(1 - \rho_1)(1 - \rho_{d,1}) + \alpha_{eff}\rho_d(1 - \rho_1)\rho_{d,1}, \tag{2.11}$$

$$J_{exit} = \beta \rho_L. \tag{2.12}$$

Now, in order to derive the continuum limit of the model, we coarse-grain the lattice by introducing a quasi-continuous variable $x = \varepsilon j \in [0,1]$, with the lattice constant as $\varepsilon = \frac{1}{L}$ and re-scaled time $t' = \frac{t}{L}$. In the eq. (2.3), the Taylor series expansion of $\rho(x \pm \varepsilon)$ and retaining the terms up to the first order. Further, we drop the subscript j due to the spatial homogeneity on the lattice reforms eq. (2.3) and eq. (2.9) into,

$$-\left(\frac{\varepsilon}{2}\right)(1-\rho_d+p_d\rho_d)\frac{\partial^2\rho}{\partial x^2}+\frac{\partial\rho}{\partial t'}+\frac{\partial J}{\partial x}=0, \qquad (2.13)$$

and

$$\frac{d\rho_d}{dt'} = k_{\text{eff}}^+(1 - \rho_d) - k^-\rho_d, \quad 1 \le j \le L, \tag{2.14}$$

respectively, where

$$J_N = (1 - \rho_d + p_d \rho_d) \rho (1 - \rho), \tag{2.15}$$

denotes the steady-state current in the bulk of the lattice obtained through the naive meanfield approach. Clearly, the parameters p_d and ρ_d are responsible for the hindrance caused to the particle movement on the lattice. The ρ_d directly obstructs the particle flux on the lattice, whereas the p_d obstructs it inversely. Thus, we define:

$$z = \rho_d (1 - p_d), \tag{2.16}$$

as the obstruction factor that triggers the particles' hindrance and helps reduce the parameter space. The eq. (2.15) referring to the particle current in the bulk of the lattice concludes that the effective hopping rate of the particle is 1-z which turns out to be similar to that of a static defect disorder in the case of localised single dynamic defect [133]. The obstruction factor always remains constrained to a range of 0 and 1. For $\rho_d \to 0$ or $p_d \to 1$, the obstruction due to defects becomes negligible as $z \to 0$ and defects do not hinder the particle movement on the lattice. As a result, the steady-state current on the lattice is reduced to that of the conventional TASEP. However, as $\rho_d \to 1$ and $p_d \to 0$, the maximum obstruction is observed in the particle movement; hence, the steady-state current completely vanishes all over the lattice.

The derivation of boundary densities are computed as follows; the average particle occupation number at steady state for site j = 1 evolves according to:

$$\left(\alpha_{\text{eff}}\langle(1-\sigma_{1})(1-v_{1})\rangle + \alpha_{\text{eff}}p_{d}\langle(1-\sigma_{1})v_{1}\rangle\right) - \left(\langle\sigma_{1}(1-v_{2})(1-\sigma_{2})\rangle + p_{d}\langle\sigma_{1}v_{2}(1-\sigma_{2})\rangle\right) = 0,$$
(2.17)

Deploying naive mean-field approximations and utilizing the average particle density ρ_j and average defect density $\rho_{d,j}$, we obtain continuity equation for site j=1 at steady state as,

$$\left(\alpha_{\text{eff}}(1-\rho_{1})(1-\rho_{d}) + \alpha_{\text{eff}}p_{d}(1-\rho_{1})\rho_{d}\right) - \left(\rho_{1}(1-\rho_{1})(1-\rho_{d}) + p_{d}\rho_{1}(1-\rho_{1})\rho_{d}\right) \approx 0.$$
(2.18)

The above equation can also be expressed as:

$$\alpha_{\text{eff}}(1-z)(1-\rho_1) - J_N(\rho_1) = 0 \tag{2.19}$$

where, J_N denotes the steady state current in the lattice obtained through naive mean-field approximations. Similarly, the continuity equation for site j = L at steady state is given by:

$$J_N(\rho_L) - \beta \rho_L = 0 \tag{2.20}$$

respectively.

Stationary-state solution of the first order differential equation (2.13) in the thermodynamic limit ($\varepsilon \to 0$) while utilizing one boundary condition at a time implies that the system can be found in one of the following phases: entry-dominated low-density phase (or LD phase), exit-dominated high-density phase (or HD phase), and bulk-dominated maximal current phase (or MC phase). Apart from these phases, an LD-HD coexistence phase also occurs, representing a delocalized shock S* moving throughout the lattice. This shock is boundary-induced and appears on a line only [82, 80, 140].

Table 2.1: Expressions for the existence conditions of the density phases in the lattice with infinite resources through naive mean-field theory.

Density Phase	Phase region	Particle Density
		(ρ)
LD	$ \alpha_{\rm eff} < \min\left(\frac{\beta}{1-z}, \frac{1}{2}\right) $	$lpha_{ m eff}$
HD	$\frac{\beta}{1-z} < \min\left(\alpha_{\mathrm{eff}}, \frac{1}{2}\right)$	$1-\frac{\beta}{1-z}$
MC	$\min\left(\alpha_{\rm eff},\frac{\beta}{1-z}\right) \geq \frac{1}{2}$	$\frac{1}{2}$
S*	$ \alpha_{\text{eff}} = \frac{\beta}{1-z}, \alpha_{\text{eff}} < \frac{1}{2} $	-

At stationary state, the boundary conditions in eq. (2.5) and eq. (2.7) are useful to approximate the boundary densities as $\rho_{LD} \approx \rho_1$ and $\rho_{HD} \approx \rho_L$, where ρ_{LD} (ρ_{HD}) represents the left (right) boundary density, respectively:

$$\rho_{LD} = \alpha_{\text{eff}}, \tag{2.21}$$

and

$$\rho_{HD} = 1 - \frac{\beta}{1 - z}.\tag{2.22}$$

The MC phase is specified by the condition that $\frac{\partial J_N}{\partial \rho} = 0$, which leads to the equation that has only one real root: $\rho = \frac{1}{2}$. The particle density in an entry-dominated phase only depends on the effective entry rate $\alpha_{\rm eff}$. An exit-dominated phase depends on the parameters β and z whereas the maximal-current phase remains independent of any parameter. The Table. 2.1 lists the phase boundaries computed using the extremal current principle as well as the boundary densities obtained in eq. (2.21) and eq. (2.22) [80, 109]. The stationary state

solution to the defect density can be computed from eq. (2.14) as:

$$\rho_d = \frac{k_{\text{eff}}^+}{k_{\text{eff}}^+ + k^-}. (2.23)$$

Table 2.2: Bounds on μ for the existence of the LD phase.

Choice of α , β & z	Constraint on μ
$\alpha \ge \max\left(\frac{\beta}{1-z}, \frac{1}{2}\right)$	$\mu < \min\left(\frac{\alpha\beta}{\alpha(1-z)-\beta}, \frac{\alpha}{2\alpha-1}\right)$
$\frac{\beta}{1-z} \le \alpha < \frac{1}{2}$	$rac{lpha}{2lpha-1}<\mu<rac{lphaeta}{lpha(1-z)-eta}$
$\frac{1}{2} \le \alpha < \frac{\beta}{1-z}$	$\frac{lphaeta}{lpha(1-z)-eta}<\mu<rac{lpha}{2lpha-1}$
$ \alpha < \min\left(\frac{\beta}{1-z}, \frac{1}{2}\right) $	$\mu > \max\left(\frac{\alpha\beta}{\alpha(1-z)-\beta}, \frac{\alpha}{2\alpha-1}\right)$

2.4.1 Defect-particle interplay in the presence of finite resources

The assumption of finite resources in the R_1 only affects the entry rate of particles, whereas the exit rate of particles is assumed to be independent of N_{R_1} . Similarly, the unbinding of defects is independent of the N_{R_2} . It is believed that the free particles (or defects) in the R_1 (or R_2) are homogeneously distributed and not correlated within the reservoir. To determine the modified rates for the entry ($\alpha_{\rm eff}$ or $\alpha_{\rm eff}p_d$) and the defect binding ($k_{\rm eff}^+$), we use the conservation of number of particles in the system, which in its continuum form states that $N_{t_i} = N_{R_i} + L \int_0^1 \rho$ (or ρ_d) dx. We utilize it to retrieve a relationship involving the reservoir

density and filling factor for R_1 and R_2 given by:

$$\mu_1 = \rho_{R_1} + \rho, \tag{2.24}$$

and

$$\mu_2 = \rho_{R_2} + \rho_d, \tag{2.25}$$

respectively, where ρ_{R_i} is the density of the reservoir R_i which is defined as $\rho_{R_i} = \frac{N_{R_i}}{L}$. The defect density in eq. (2.23) is plugged into eq. (2.25) to obtain the defect-reservoir density (ρ_{R_2}) from the below given equation,

$$k^{+}\rho_{R_{2}}^{2} + \left(\mu_{2}(k^{-} - k^{+}) + k^{+}\right)\rho_{R_{2}} - k^{-}\mu_{2}^{2} = 0.$$
 (2.26)

One obtained solution of the above equation can easily be neglected on physical grounds. The other one is used to obtain the defect density in the case of the finite reservoir as a function of k^+ , k^- and μ_2 :

$$\rho_d = \frac{-k^+ - \mu_2(k^- - k^+) + \sqrt{\left(k^+ + \mu_2(k^- - k^+)\right)^2 + 4k^+ k^- \mu_2^2}}{-k^+ + \mu_2(k^- + k^+) + \sqrt{\left(k^+ + \mu_2(k^- - k^+)\right)^2 + 4k^+ k^- \mu_2^2}}.$$
 (2.27)

Since the maximum number of defects and particles that the lattice can accommodate is L, the standard open-TASEP with dynamic defects (corresponding to infinite particles and defects) is approached when $N_{t_i} \gg L$. Both the finite reservoirs play an important role when the total number of particles (or defects) in the system is of the order of $N_{t_i} \sim L$ or smaller. Furthermore, the phase boundaries corresponding to distinct density phases are obtained by computing ρ_d from eq. (2.27) as well as ρ_{R_1} from eq. (2.24).

2.4.2 Theoretical calculations for phase existence and phase boundaries

This section aims to obtain the possible density phases possessed by the lattice in the presence of dynamic defects, where both particles and defects enter the lattice from a reservoir containing a finite number of resources. The following parameters completely determine the phase plane of the given system: α_{eff} , β , and z, according to the rules given in Table. 2.1. We will obtain the existence condition for the different density phases and the corresponding phase boundaries for different choices of μ_1 and μ_2 . For the sake of simplicity, we considered the case $\mu_2 = \mu_1 = \mu$, whereas no qualitative changes are observed for the other case $\mu_1 \neq \mu_2$.

Low-Density (LD) phase:

We assume the lattice is in an entry-dominated phase and utilize its particle density from Table. 2.1 into eq. (2.24) to obtain the particle-reservoir density in this phase as:

$$\rho_{R_1} = \frac{\mu^2}{\mu + \alpha}.\tag{2.28}$$

The conditions for the existence of the LD phase in the lattice are given as:

$$\alpha < \min\left(\frac{\beta(\mu+\alpha)}{\mu(1-z)}, \frac{\mu+\alpha}{2\mu}\right).$$
(2.29)

In addition, the constraints on μ (for a fixed choice of α and β) for the existence of this phase are provided in Table. 2.2.

High-Density (HD) Phase:

In this case, the lattice is assumed to be in an exit-dominated phase, and similarly, we obtain the expression for the reservoir density in this phase as:

$$\rho_{R_1} = \mu - 1 + \frac{\beta}{1 - z}.\tag{2.30}$$

The conditions for the existence of the HD phase in the lattice are given as follows:

$$\beta \mu < \alpha \Big(\beta + (1 - z)(\mu - 1) \Big), \tag{2.31}$$

and

$$2\beta < 1 - z. \tag{2.32}$$

Although the above inequalities intersect and give rise to a common region comprising the HD phase for $\mu > 0.5$ only but for α , β satisfying $\beta - \alpha(1-z) < 0$, a more precise bound on μ for the existence of this phase can be obtained as:

$$\mu > \frac{\alpha(\beta - (1-z))}{\beta - \alpha(1-z)}.\tag{2.33}$$

Shock (S) Phase:

The conservation of particle number in the lattice leads to a localized shock denoted by S. Furthermore, the shock can be thoroughly characterized by obtaining its location and height in the lattice. The expression for shock position can be obtained using particle number conservation and given as,

$$s = \frac{(\mu - \alpha)\left(\alpha(1 - z) - \beta\right)}{\alpha\left(2\beta - 1 + z\right)}.$$
(2.34)

whereas the height of the shock is given as,

$$\Delta = 1 - \frac{2\beta}{1 - z}.\tag{2.35}$$

Clearly, the shock height only depends on the parameter β . In contrast, its position is a function of all three parameters α , β , μ , and the obstruction factor z. The S phase exists for 0 < s < 1, and it is not just confined to a line but a region. The conditions for the existence of the S phase in lattice using the fact that the transition from LD to S phase occurs when

s=1 and the transition from HD to S phase occurs when s=0 [57] is given as:

$$\alpha\beta < \mu(\alpha(1-z)-\beta) < \alpha(1-z-\beta),$$
 (2.36)

For a fixed α , β and z the eq. (2.36) suggests that there always exists a range of μ for which the S phase arises.

Maximal-Current (MC) Phase:

The expression for the reservoir density in the MC phase is provided as:

$$\rho_{R_1} = \mu - \frac{1}{2}.\tag{2.37}$$

The existence of the MC phase in the lattice occurs in the region:

$$\alpha \left(2\mu - 1\right) > \mu,\tag{2.38}$$

and

$$2\beta > 1 - z. \tag{2.39}$$

In the region α < 0.5, the MC phase ceases to exist for any choice of μ whereas, for α > 0.5, the bound obtained on μ for the existence of this phase is:

$$\mu > \frac{\alpha}{2\alpha - 1}.\tag{2.40}$$

2.4.3 Phase plane analysis for faster defect dynamics

Now, we explore the stationary properties of the system and analyze the effects of the filling factor and obstruction factor on $\alpha - \beta$ parameter space. The filling factor μ denotes the average number of particles available for each lattice site, and therefore μ will significantly affect the phase plane. The phase planes in FIG. 2.2 are constructed for faster defect

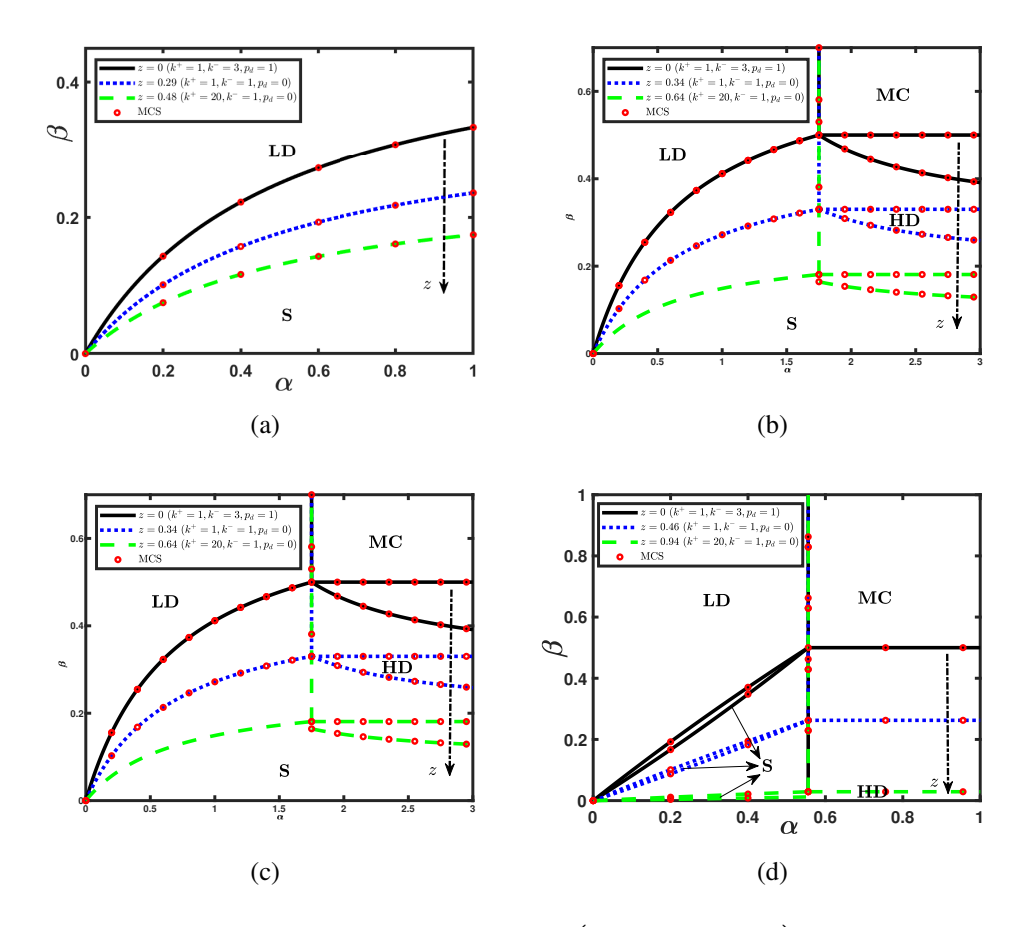


Figure 2.2: The effect of the obstruction factor $\left(z = \rho_d(1 - p_d)\right)$ on the phase diagrams obtained through naive mean-field approach for the following choices of the filling factor: (a) $\mu = 0.5$, (b) $\mu = 0.7$, (c) $\mu = 1$, and (d) $\mu = 5$.

dynamics only, i.e. $(k^+,k^-\gtrsim 1)$, and it clearly illustrates that for smaller values of μ , the phase plane consists of two distinct phases, the LD and S phase. The LD phase dominates the phase plane, and an S phase only appears for the smaller values of β . This can be explained as follows: the system's scarcity of particles leads to a reduced effective entry rate. As a result, the phase plane majorly exhibits an LD phase. But for smaller values of β , the exit of the particle is hindered, causing a boundary layer that enters the lattice in the form of a stationary shock. It is also evident that as the value of μ increases from 0 to 0.5, the effective entry rate increases and causes the boundary layer to enter the bulk of the lattice. This, in turn, leads to an expansion in the S phase and a shrinkage in the LD phase. As the value of μ increased beyond 0.5, the MC and HD phases began to appear in the phase plane.

The critical value of $\mu=0.5$ can easily be obtained from eq. (2.33) and eq. (2.40). The further increase in the value of μ observes no significant topological changes in the phase plane except for the shift in the phase boundaries, which is due to the expansion of HD and MC phases and the shrinkage of LD and S phases. For a system with an infinite number of particles or $\mu \to \infty$, the phase plane does not converge to the open dynamically disordered TASEP with infinite resources studied in ref.[140]. This is due to the modification of particle-defect dynamics at the boundary in our model.

Now, we will discuss the effect of the obstruction factor on the stationary properties of the system. Similar to the filling factor, the change in the obstruction factor also introduces a shift in the phase boundaries. For a fixed choice of μ , the phase boundaries shift vertically upwards (downwards) as z decreases (increases), as shown in FIG.2.2. To better understand the repercussions caused to the stationary properties due to obstruction, we now analyze the limiting cases $z \to 0$ and $z \to 1$. As z decreases, the particle faces less obstruction, and the phase boundaries shift vertically upward with shrinkage in the LD and MC phases and an expansion of the S and HD phases. The FIG. 2.2 clearly shows that in the limit $z \to 0$, the obstruction on the lattice completely fades away, resulting in the phase plane converging to that of a standard-TASEP with finite resources [54]. Notably, for the same reason discussed above, the model introduced in ref.[140] doesn't converge to the standard open-TASEP with infinite resources for $p_d \to 1$ corresponding to the case $z \to 0$.

On the other hand as z increases, the particle faces more obstruction, and the phase boundary shifts vertically downward, resulting in the expansion of the LD and MC phases with shrinkage in the S and HD phases. In the limit $z \to 1$, the obstruction factor reaches its maximum value, bringing a zero steady-state current to the system. Moreover, for the limiting case, $z \to 1$, the coordinates of the quadruple point $(\frac{\mu}{2\mu-1}, \frac{1-z}{2})$ approaches α -axis, leading to the complete vanish of the S as well as the HD phase. As a result, the phase plane will only consist of either the LD phase or both the LD and MC phases depending on the choice of μ , which is also evident from FIG. 2.2.

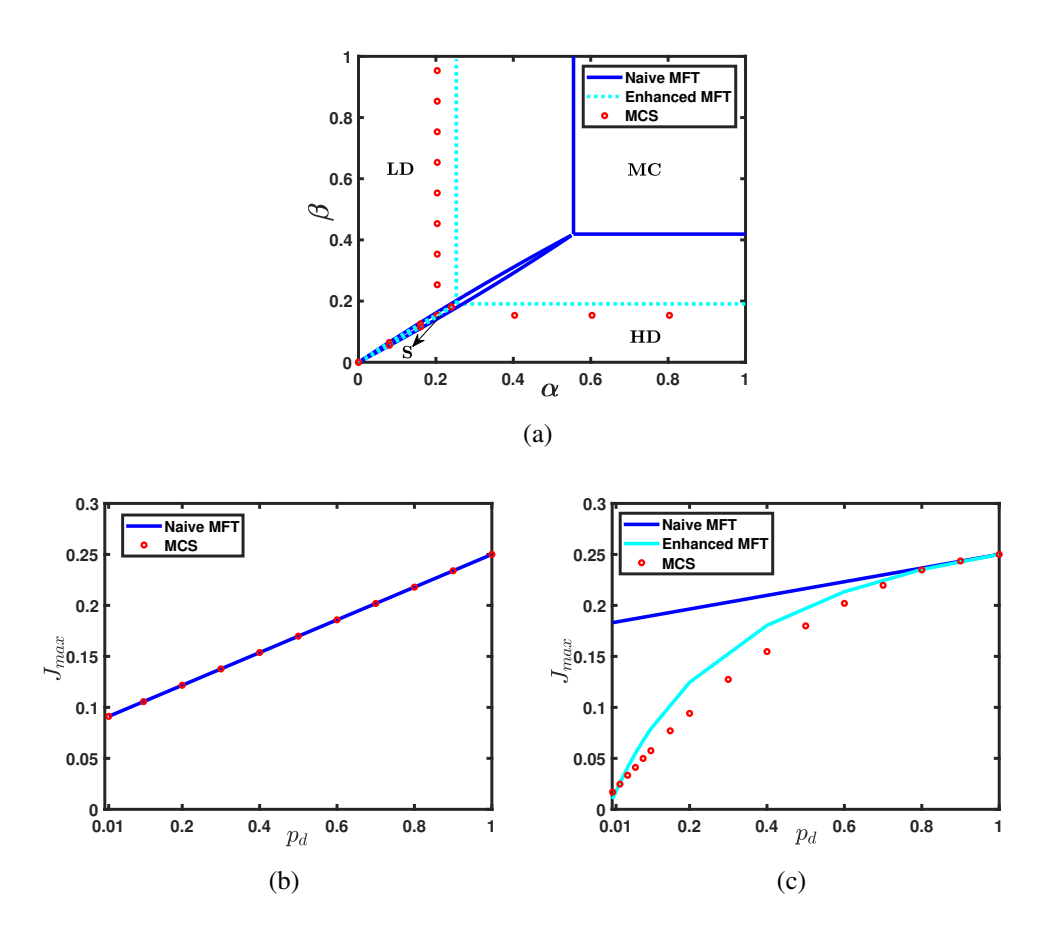


Figure 2.3: a) The phase diagram obtained for $\mu = 5$ shows the breakdown of the naive mean-field for slow defects with $p_d = 0$, here the binding and unbinding rates are chosen as $k^+ = 0.02$, and $k^- = 0.1$, respectively. Maximum current J_{max} as a function of the affected hopping rate p_d for the following binding/un-binding rates (b) $k^+ = 5$, $k^- = 1$, (c) $k^+ = 0.005$, $k^- = 0.01$.

2.5 Failure of naive mean-field theory

Till now, we have only considered fast defects $(k^+, k^- \gg 1)$ and observed that the theoretical results obtained through the naive mean-field approach yield a good match with the simulations. Motivated by the work in ref.[140], we investigate the proposed theory for slow defects $(k_{\rm eff}^+, k^- \ll 1)$. The FIG. 2.3 (a) clearly shows that the naive-mean field prediction breaks down while constructing a phase plane for smaller defects with $p_d = 0$. To explore further, we compute the maximal current J_{max} as a function of p_d for both fast as well as slow defects, where $J_{max} = J(\rho = \frac{1}{2})$. The FIG. 2.3 (b) clearly shows that the maximal current obtained through the naive mean-field agrees very well with the simulation data for faster

defect dynamics. For slower defect dynamics, we observe a deviation in the maximal current from simulations for smaller affected hopping rates, but it matches reasonably well for the larger values of p_d . To explore the failure of naive mean-field theory for slower defects with smaller affected hopping rates, we compute the correlations between particle-particle and particle-defect residing on the consecutive neighboring lattice sites. The two-point classical correlation function between particle-particle as well as particle-defect on neighbouring sites j and j+1, where $(1 \le j < L)$, is defined by,

$$C(\sigma_{i}, \sigma_{i+1}) = \langle \sigma_{i} \sigma_{i+1} \rangle - \langle \sigma_{i} \rangle \langle \sigma_{i+1} \rangle, \tag{2.41}$$

and

$$C(\sigma_j, \nu_{j+1}) = \langle \sigma_j \nu_{j+1} \rangle - \langle \sigma_j \rangle \langle \nu_{j+1} \rangle, \tag{2.42}$$

respectively, where the two-point correlator $\langle \sigma_j \sigma_{j+1} \rangle$ and one-point correlator $\langle \sigma_j \rangle$ are defined as $P(\sigma_j = 1, \sigma_{j+1} = 1)$ and ρ , respectively.

The FIG. 2.4 illustrates the particle-defect and particle-particle correlations obtained through simulations for faster and slower defect dynamics for different choices of p_d . It is also evident from FIG. 2.4 (a) that for faster defects, there are no particle-defect correlations present in the system. As a result, the naive mean-field theory works very well, whereas, for the slower defects, we observe some particle-defect correlations for smaller values of p_d . Moreover, in FIG. 2.4 (b), we also observe some strong particle-particle correlations in the system for the case of slow defects with smaller values of p_d , which reduce with the increase in the values of p_d . This can be explained as follows: the slow defects that cause complete hindrance ($p_d = 0$) to particle movement spend more time on the lattice before unbinding, leading to the formation of particle clusters, which in turn results in particle-particle correlations.

Furthermore, a particle-defect correlation is observed because a defect causes particles to pile up in front of the defect. So far, it seems that the slow binding/un-binding rates are solely responsible for these correlations, but with the increase in p_d , we observe a decrease in these correlations. For this reason, the maximal current predicted by the naive mean-field

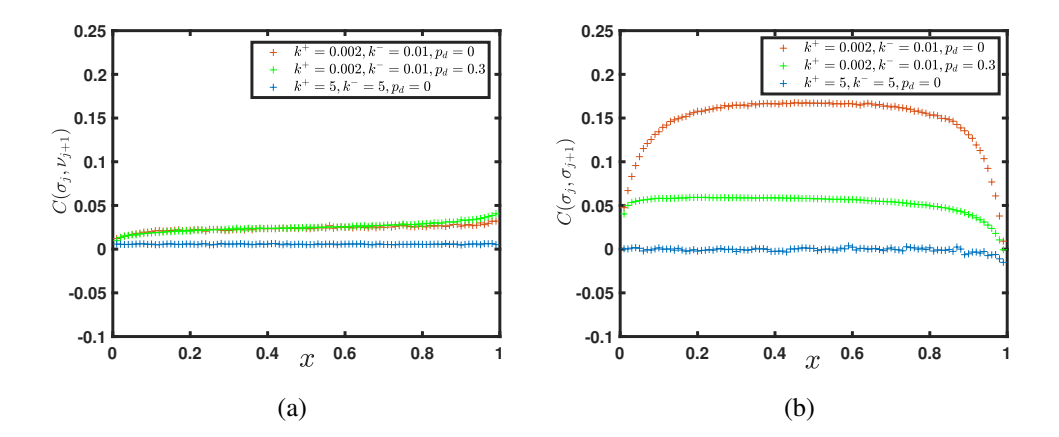


Figure 2.4: Correlations between (a) particle-defect residing on neighboring sites and (b) particle-particle residing on neighboring sites obtained through simulations.

matches well with the simulations for larger values of p_d . Hence, it can be concluded that the affected hopping rate and slow defects are responsible for inducing the correlations into the system. The generalized mean-field approaches, which consider some types of correlations, can be used to investigate system dynamics. In the next section, we will adopt an enhanced mean-field theory that has been proved effective in dealing with slow defects with smaller values of p_d in an infinite system [140].

2.6 Enhanced mean-field framework

Due to the dynamic nature of the defect, some correlations are observed for the case of slower defects and thus justify the failure of the naive mean-field. Therefore, we adopt an enhanced mean-field approach which minimizes the particle-particle correlation in the system that arise due to slower defects in company with small affected hopping rate [140]. Now, to take into account the correlations between the random variables v_{i+1} and σ_i , the expression of current in the the bulk of the lattice can be factorised as:

$$J_{j-1,j} = \langle \sigma_{j-1}(1 - v_j)(1 - \sigma_j) \rangle + p_d \langle \sigma_{j-1}v_j(1 - \sigma_j) \rangle,$$

$$\approx \langle \left((1 - v_j) + p_d v_j \right) \sigma_{j-1} \rangle \langle (1 - \sigma_j) \rangle.$$
(2.43)

Table 2.3: Expressions for the existence conditions of the density phases in the lattice with infinite resources through enhanced mean-field theory.

Density Phase	Phase region	Particle Density
		(ρ)
LD	$ \alpha_{\text{eff}} < \min\left(\frac{\beta}{1-z}, \frac{1-z_E}{2(1-z)}\right) $	$\frac{\alpha_{\rm eff}(1-z)}{1-z_E}$
HD	$\frac{\beta}{1-z} < \min\left(\alpha_{\text{eff}}, \frac{1-z_E}{2(1-z)}\right)$	$1 - \frac{\beta}{1 - z_E}$
MC	$\min\left(lpha_{ ext{eff}}, rac{eta}{1-z} ight) \geq rac{1-z_E}{2(1-z)}$	1/2
S*	$ \alpha_{\text{eff}} = \frac{\beta}{1-z}, \alpha_{\text{eff}} < \frac{1-z_E}{2(1-z)} $	-

For faster defects, the sites behave effectively as having a static, effective hopping rate 1-z, similarly to what has been conjectured for localised, single dynamic defects [133]. Therefore, in enhanced mean-field approximation, the effective hopping rate is approximated utilizing the concept of mean-free time. In this case, the effective hopping rate of a particle $(\langle (1-v_i)+p_dv_i\rangle)$ is inversely proportional to τ_f , where τ_f refers to the mean-free time spent by a particle before hopping onto the next site. Hence, the term $\langle (1-v_j)+p_dv_j\rangle:=\tau_f^{-1}$. Further, the following two processes are considered in order to approximate the waiting time of a particle. If a particle encounters a no-defect site (with probability $1 - \rho_d$), it hops with a unit rate. In the event a particle encounters a defect (with probability ρ_d), it hops with the rate p_d while the defect is still present at the arrival site, or it waits for the defect to unbind with the rate k^- , and then hops with a unit rate. As we are dealing with the case of slow defects, therefore, in the limit of small $k_{\rm eff}^+,\,k^-,\,p_d\ll 1$, the time taken by a particle to hop after defect unbinding is 1, which is quite negligible in comparison to the unbinding time $\frac{1}{k^{-}}$. Hence, the approximate value for a particle's waiting time in the presence of slow defects can be obtained as $\tau_f \approx (1 - \rho_d) + \left(\frac{1}{k^- + p_d}\right) \rho_d$. Notably, this approximation fails for defects with $k_{\rm eff}^+ \sim 1$ because the possibility of rebinding of defects prior to particle hop cannot be ignored. Following the same sequence of steps adopted in section 2.4, we obtain the expression for the steady-state current through an enhanced mean-field theory given by,

$$J_E = \left(1 - \frac{\rho_d \left(1 - (k^- + p_d)\right)}{k^- + p_d + \rho_d \left(1 - (k^- + p_d)\right)}\right) \rho(1 - \rho), \tag{2.44}$$

Similar to the naive mean-field theory, the modified obstruction factor for the enhanced mean-field approach can be defined as $z_E := \frac{\rho_d \left(1 - (k^- + p_d)\right)}{k^- + p_d + \rho_d \left(1 - (k^- + p_d)\right)}$. It is a unified parameter that will collectively discuss the effect of ρ_d , p_d , and k^- on system dynamics. The modified obstruction factor remains bounded between 0 and 1, provided $k^- + p_d < 1$. The values of ρ_d and p_d for which the limiting cases $z_E \to 0$ and $z_E \to 1$ occur are similar to the ones obtained for z.

Analogously, one can derive the boundary densities for slow defects through the enhanced mean-field framework, and the system exhibits the same stationary phases: LD phase, HD phase, MC phase, and an LD-HD coexistence phase. For enhanced mean-field theory, we utilize the bulk current obtained in eq. (2.44) along with the boundary conditions in eq. (2.6) and eq. (2.8) to compute the stationary state densities at the left boundary boundary and right boundary as $\rho_{LD} = \frac{\alpha_{\rm eff}(1-z)}{1-z_E}$ and $\rho_{HD} = 1 - \frac{\beta}{1-z_E}$, respectively. Likewise, the condition $\frac{\partial J_E}{\partial \rho} = 0$ suggests that the maximal-current is attained at $\rho = \frac{1}{2}$. Contrary to the naive mean-field framework, the particle density in an entry-dominated phase depends on z as well as z_E along with the effective entry rate $\alpha_{\rm eff}$. The exit-dominated phase depends on the parameters β and z_E whereas the maximal-current phase remains independent of any parameter. The phase boundaries for enhanced mean-field theory that are computed using the extremal current principle, as well as the boundary densities, are listed in Table. 2.3.

2.6.1 Theoretical calculations of phase existence and phase boundaries for $k^+, k^-, p_d \ll 1$ in the presence of finite resources

Now, we employ enhanced mean-field theory to obtain the possible density phases possessed by the lattice in the presence of slow defect dynamics. Since the system happens to be in a finite environment of particles and defects, the filling factor μ plays an important role in determining the stationary phases and expression of phase boundaries. We will also utilize the conditions obtained in Table. 2.3 for the existence of the stationary phases. For the sake of simplicity, we again consider $\mu_2 = \mu_1 = \mu$, whereas the other case, $\mu_1 \neq \mu_2$ can be discussed following the same analogy.

Low-Density (LD) Phase:

We assume the lattice is in a low-density phase and obtain the particle-reservoir density from eq. (2.24) and Table. 2.3 as:

$$\rho_{R_1} = \frac{\mu^2 (1 - z_E)}{\mu (1 - z_E) + \alpha (1 - z)}.$$
(2.45)

The lattice is found in an entry-dominated phase for:

$$\alpha < \min\left(\frac{\beta\left(\mu(1-z_{E}) + \alpha(1-z)\right)}{\mu(1-z_{E})(1-z)}, \frac{\mu(1-z_{E}) + \alpha(1-z)}{2\mu(1-z)}\right). \tag{2.46}$$

For a fixed choice of α and β , the constraints on μ for the existence of this phase are provided in Table. 2.4.

High-Density (HD) Phase:

The particle-reservoir density in an exit-dominated phase is given as:

$$\rho_{R_1} = \mu - 1 + \frac{\beta}{1 - z_F}. (2.47)$$

The conditions for the existence of the HD phase in the lattice are:

$$\beta \mu < \alpha (1-z) \Big(\beta + (1-z_E)(\mu - 1) \Big),$$
 (2.48)

and

$$2\beta < 1 - z_E. \tag{2.49}$$

For $\mu > 0.5$ only, the above inequalities intersect to give rise to the region comprising the HD phase.

Table 2.4: Bounds on μ for the existence of LD phase through enhanced mean-field theory.

Choice of α , β , $z \& z_E$	Constraint on μ
$\alpha \ge \max\left(\frac{\beta}{1-z}, \frac{1-z_E}{2(1-z)}\right)$	$\mu < \min\left(\frac{\alpha\beta(1-z)}{(1-z_E)(\alpha(1-z)-\beta)}, \frac{\alpha(1-z)}{2\alpha(1-z)-1+z_E}\right)$
$\frac{\beta}{1-z} \le \alpha < \frac{1-z_E}{2(1-z)}$	$\frac{\alpha(1-z)}{2\alpha(1-z)-1+z_E} < \mu < \frac{\alpha\beta(1-z)}{(1-z_E)(\alpha(1-z)-\beta)}$
$\frac{1-z_E}{2(1-z)} \le \alpha < \frac{\beta}{1-z}$	$rac{lphaeta(1-z)}{(1-z_E)(lpha(1-z)-eta)}<\mu<rac{lpha(1-z)}{2lpha(1-z)-1+z_E}$
$\alpha < \min\left(\frac{\beta}{1-z}, \frac{1-z_E}{2(1-z)}\right)$	$\mu > \max\left(\frac{\alpha\beta(1-z)}{(1-z_E)(\alpha(1-z)-\beta)}, \frac{\alpha(1-z)}{2\alpha(1-z)-1+z_E}\right)$

Shock (S) Phase:

To completely characterize the shock, we obtain the shock position using the particle conservation number that is given by:

$$s_1 = \frac{\mu(1-z_E)\Big(\alpha(1-z)-\beta\Big) - \alpha(1-z)(1-z_E-\beta)}{\alpha(1-z)(2\beta-1+z_E)}.$$
 (2.50)

whereas the height of the shock is given as,

$$\Delta_1 = 1 - \frac{2\beta}{1 - z_F}. (2.51)$$

Contrary to the previous case, the shock height also depends on the modified obstruction z_E along with the parameter β . On the other hand s_1 is a function of parameters α , β , μ , z and z_E . The conditions for the existence of an S phase in the lattice are computed as:

$$\beta \mu (1 - z_E) + \alpha \beta (1 - z) < \alpha \mu (1 - z_E) < \frac{\beta \mu}{1 - z} - \alpha \beta + \alpha (1 - z_E),$$
 (2.52)

The above expression suggests that for a feasible choice of α , β , z and z_E , a μ exists for which the S phase always exists.

Maximal-Current (MC) Phase:

The expression for the particle-reservoir density for the maximal current phase is provided as:

$$\rho_{R_1} = \mu - \frac{1}{2}.\tag{2.53}$$

The region possessing the MC phase in the lattice is given by:

$$\alpha \left(2\mu - 1\right) > \frac{(1 - z_E)\mu}{1 - z},$$
 (2.54)

and

$$2\beta > 1 - z_E. \tag{2.55}$$

The eq. (2.54) clearly shows that the MC phase ceases to exist for any choice of μ in the region $\alpha < \frac{1-z_E}{2(1-z)}$ whereas for $\alpha > \frac{1-z_E}{2(1-z)}$, we obtain the bound on μ for the existence of this phase as:

$$\mu > \frac{\alpha(1-z)}{2\alpha(1-z) - 1 + z_E}.$$
 (2.56)

Utilizing the above analysis based on enhanced mean-field theory, we again plotted the phase boundaries for the same set of parameters for which the naive mean-field breaks down, see FIG. 2.3 (a). Clearly, the results predicted by the enhanced mean-field theory are much more consistent with the Monte Carlo simulations than the naive mean-field theory. Moreover, one can also infer from FIG. 2.3 (c) that the values of J_{max} obtained through enhanced mean-field approximation produce a good match with the simulations not only for the larger values of p_d but also for the smaller ones.

2.6.2 Phase plane analysis for slower defect dynamics with $p_d \ll 1$

This section aims to clarify how a slower defect affects the system's steady state behavior differently compared to a faster defect. This can be achieved by examining the effects of z_E and μ on the system's stationary properties. Similar to the case of fast defects, the smaller values of μ produce only two phases, namely, the LD and the S phase, see FIG. 2.5 (a). Likewise, as μ increases to 0.5, no new phase appears in the phase plane except for the shrinkage in the LD phase and the expansion of the S phase. Two more phases, HD and MC, join the phase diagram as soon as μ surpasses the critical value of 0.5. Hence, the effect of μ brings no different topological changes to the phase plane compared to the faster defects. For the same reason, the phase plane does not converge to the open dynamically disordered TASEP with infinite resources in the limit $\mu \to \infty$.

Now, we explore the effect of the modified obstruction factor z_E on the system dynamics for slower defects. In FIG. 2.5, we observe that for a fixed choice of μ , the phase boundaries also intend to shift with respect to z_E . In contrast to the case of fast defects, the shift can occur either vertically or anti-diagonally towards the origin. For a fixed choice of $\mu \leq 0.5$, the phase boundaries either shift vertically upwards (downwards) as z_E decreases (increases);

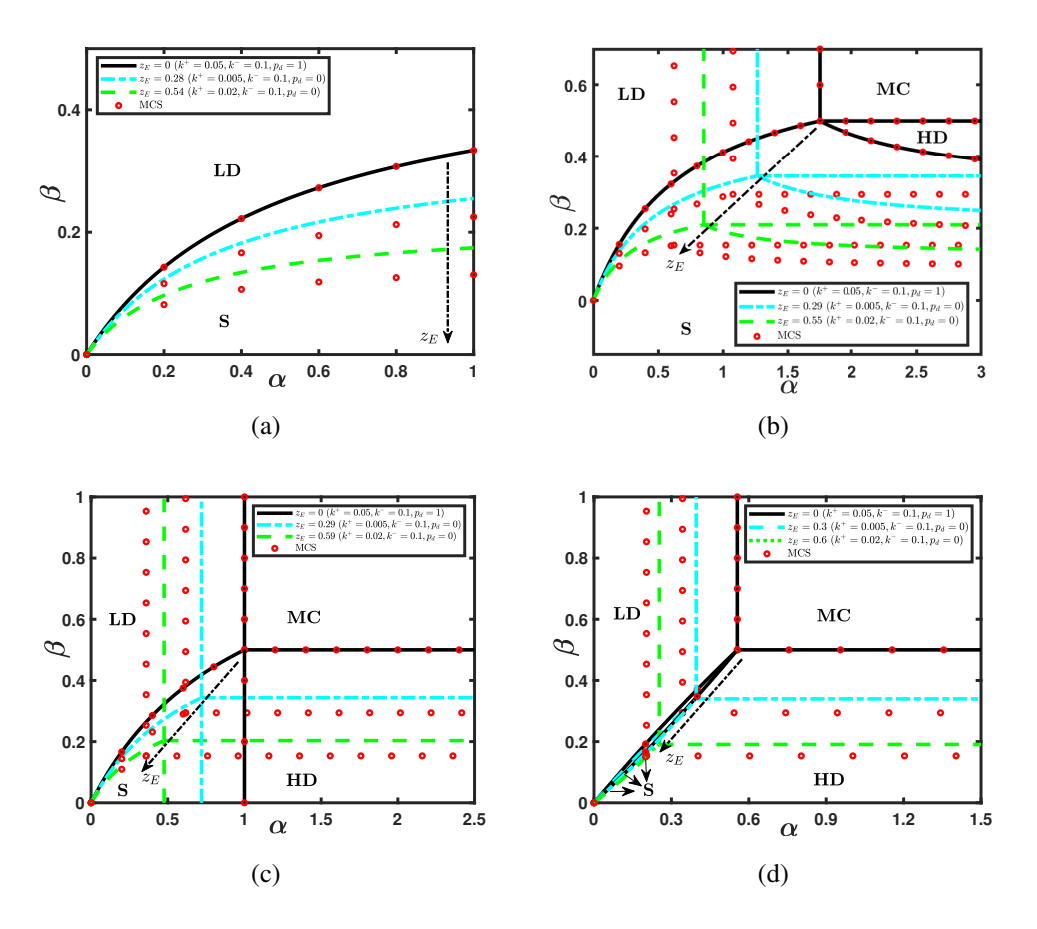


Figure 2.5: The effect of the modified obstruction factor on the phase diagrams obtained through enhanced mean-field approach the following choices of the filling factor (μ): (a) $\mu = 0.5$, (b) $\mu = 0.7$, (c) $\mu = 1$, and (d) $\mu = 5$.

this is in accordance with the effect of z in case of faster defects. For $\mu > 0.5$, the shift in the quadruple point $(\frac{(1-z_E)\mu}{(1-z)(2\mu-1)}, \frac{1-z_E}{2})$ occurs anti-diagonally with respect to z_E . Moreover, the limiting case $z_E \to 0$ nullifies the hindrance caused to particles due to the defect, and the phase plane converges to the standard-TASEP with finite resources [54]. Similarly, as z_E increases, the limiting case $z_E \to 1$ maximizes the obstruction and vanishes the steady state current on the lattice. In this limit, the phase plane only consists of the LD phase for $\mu \le 0.5$, whereas only an MC phase is observed for $\mu > 0.5$, which corresponds to a continuous transition of the quadruple point towards the origin.

So far, we have dealt with two different versions of mean-field approaches to study the stationary state properties of the system. The general expression for the steady-state current

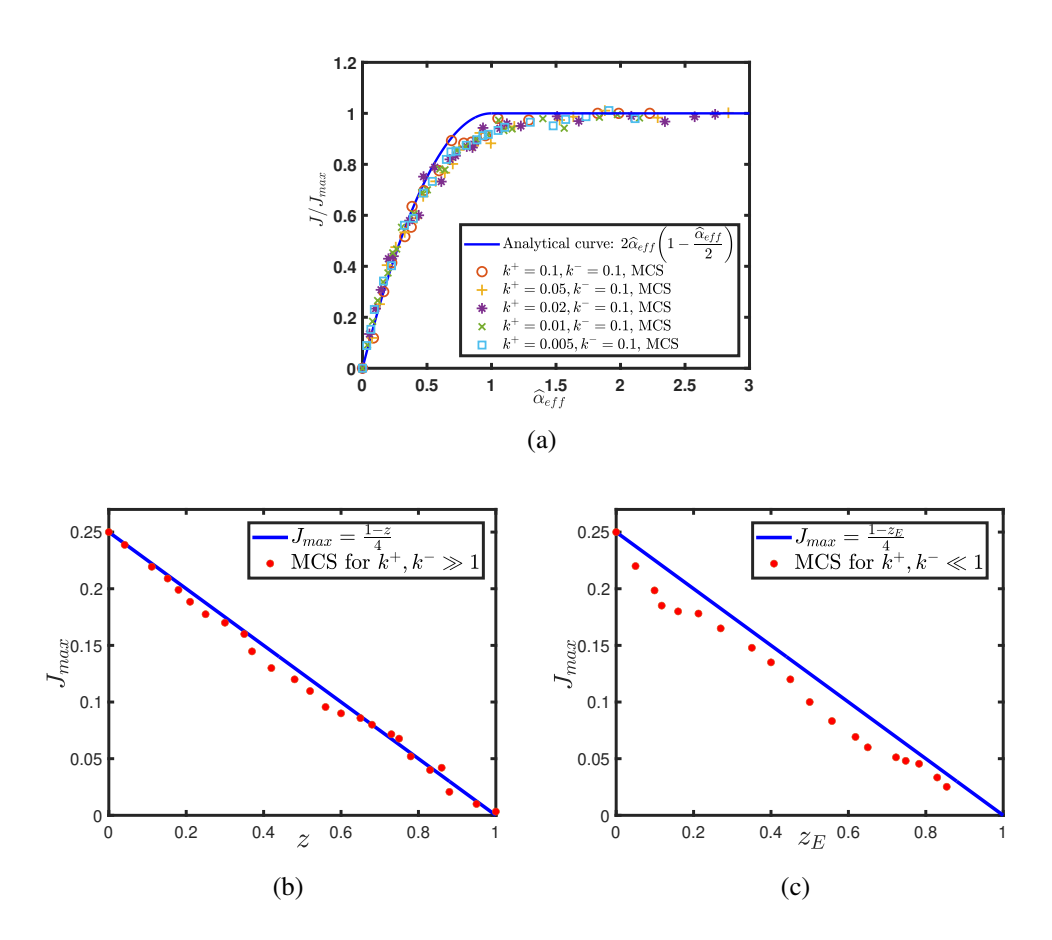


Figure 2.6: (a) Re-normalized current J/J_{max} as a function of $\widehat{\alpha}_{eff}$ for $\beta=1, \mu=1$. Maximum current J_{max} as a function of (b) z and (c) z_E for $L=1000, \mu=1$.

in the lattice is given by:

$$J = c\rho(1-\rho), \tag{2.57}$$

where,

$$c = \begin{cases} 1 - z; & \text{Naive MFT,} \\ 1 - z_E; & \text{Enhanced MFT.} \end{cases}$$
 (2.58)

Under the assumption ($\alpha_{\text{eff}} < \frac{\beta}{c}$), the expression for the current in the LD and MC phase is given by,

$$J = \begin{cases} \alpha_{\text{eff}}(1-z)(1 - \frac{\alpha_{\text{eff}}(1-z)}{c}); & \alpha_{\text{eff}} < \frac{c}{2(1-z)}, \\ \frac{c}{4}; & \alpha_{\text{eff}} \ge \frac{c}{2(1-z)}. \end{cases}$$
 (2.59)

2.7 Conclusion 57

Further, it can also be expressed in the form of a re-normalized current, i.e., $\frac{J}{J_{max}} = \frac{4J}{c}$ as a function of the parameter $\widehat{\alpha}_{\text{eff}} := \frac{2\alpha_{\text{eff}}(1-z)}{c}$ which is given by,

$$\frac{4J}{c} = \begin{cases}
2\widehat{\alpha}_{\text{eff}} (1 - \frac{\widehat{\alpha}_{\text{eff}}}{2}); & \widehat{\alpha}_{\text{eff}} < 1, \\
1; & \widehat{\alpha}_{\text{eff}} \ge 1.
\end{cases}$$
(2.60)

The FIG. 2.6 (a) illustrates that the curve of simulation-based re-normalized current as a function of $\hat{\alpha}_{eff}$, for different parameters β, k^+, k^- merge onto a single curve which agrees very well with the analytical expression obtained in eq. (2.60). It is thus concluded that the extremal current principle correctly identifies the phase transition in the proposed model.

The FIG. 2.6(b) clearly illustrates the effect of the obstruction factor z and z_E on the maximal current J_{max} , for different choices of k^+, k^- (or defect density on the lattice). It is observed that with an increase in the strength of the obstruction leads to the decrease in the value of the J_{max} . As expected, the decrease in the obstruction increases the value of the maximal current in the system's steady state. Moreover, in the limit $z \to 0$ (or $z_E \to 0$), the J_{max} for all different defect densities reaches its maximum value, i.e., 0.25, which is the same as the maximum current in a homogeneous TASEP.

2.7 Conclusion

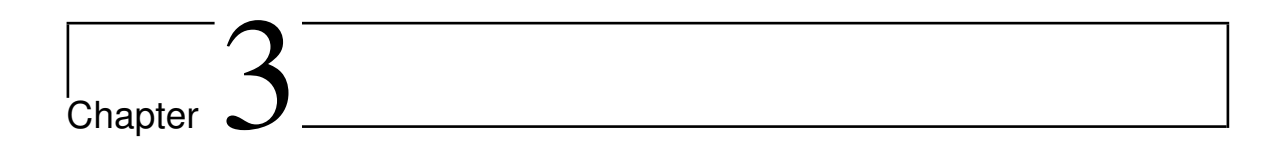
In this chapter, we attempted to thoroughly study the properties of a single-channel TASEP with dynamic disorder in a finite environment. The interplay of particle and dynamic defects is analyzed in the conserved system, where a defect can bind (or unbind) to (or from) a site irrespective of the presence of a particle. Initially, we employed the naive mean-field approximations to solve the master equations in the continuum limit and obtain steady-state results such as phase diagrams, current, and particle and defect density. The extremal current principle and particle number conservation is utilized to obtain the phases in the stationary state. We also defined a new parameter called the obstruction factor that quantifies the hindrance caused to the particle flux on the lattice. More importantly, it unifies the roles of

parameters p_d and ρ_d and helps collectively study their effect on the stationary properties of the system.

Initially, we obtained the explicit expression of boundary densities and phase boundaries for the case of infinite resources. We utilized them to obtain the steady-state results for the case of finite resources. Later, we scrutinized the stationary properties of the system with respect to μ as well as z. It is observed that the theoretical findings agree very well with Monte Carlo simulations for faster defect dynamics irrespective of p_d . In the case p_d is large, the naive mean-field works well irrespective of fast or slow defect rates. Further, the naive mean-field breaks down as soon as we introduce the slower defects with smaller affected hopping rates. This aspect of the failure of the naive mean-field has not been explored before [140].

To overcome this failure, we compute the particle-particle and particle-defect correlations for both faster and slower defects with varying affected hopping rates. It is found that the smaller affected hopping rate, along with the slow defects, is responsible for the failure of the naive mean-field. To encounter the situation, an enhanced mean-field approach of increasing complexity is employed to obtain steady-state results. The obstruction factor causes either vertical or anti-diagonal shifts depending upon the faster or slower defects in the system, whereas the number of phases remains dependent on the filling factor. The consequence of the obstruction factor on the maximal current has also been observed. The results obtained analytically agree well with the Monte Carlo simulations. For details regarding the numerical tools used, please refer to Section. 1.3.2.

The proposed model is inspired by the biological processes such as gene transcription where the proteins bounded on DNA act as a bottleneck when RNA polymerase synthesizes messenger RNA from a DNA template. Besides transcription, our model serves a more realistic approach to study vehicular traffic, where speed-breakers, faulty vehicles, or traffic lights meet the purpose of a defect. In contrast to the ref. [140], the proposed model with infinite resources reduces to the standard open-TASEP, in the limit $p_d \to 1$ (or $z \to 0$). The approach developed in our work can be generalized to study complex networks with the dynamic disorder.



Site-wise dynamic defects in a non-conserving exclusion process

Preamble

Building upon our previous investigation, this chapter explores an extended TASEP model with unrestricted resource capacity and non-conserving dynamics in the presence of dynamic disorder. This adaptation aims to simulate various physical and biological phenomena, such as the attachment and detachment of enzyme RNA polymerase during its movement along DNA. In this model, both particles and dynamic defects can attach to or detach from the lattice bulk, providing a more realistic representation of systems where entities can enter or exit at any point along the transport pathway.

3.1 Background

TASEP has undergone several generalizations that imitate different facets of transportation ranging from micro to macro. One such non-conserving model that integrates an equilibrium process, i.e., Langmuir Kinetics (LK), with the non-equilibrium process TASEP is known as TASEP-LK. The LK dynamics represent the adsorption/desorption of particles on a lattice and their rates are re-scaled while preserving the inverse proportionality to the system size in order to study the conflict between the TASEP and the LK dynamics. This model is inspired by the diffusive and directed motion along the microtubule that is alternated by the processive molecular motors [3] and encompasses several intricate aspects, including the presence of a delocalized domain wall resulting in a phase of coexistence between low and high densities [102, 45, 103].

The existence of a disorder that slows or momentarily obstructs particle movement is one of the important aspects that are visible in almost all transport systems. For instance, a vehicle on the road may be stopped or slowed down by other vehicles or periodically switching traffic lights or during gene transcription; the molecular traffic is often "roadblocked" by histones that form the core of nucleosomes or by microtubule-binding proteins, etc. [41, 70]. These obstacles (or defects) can either be static or dynamic, leading to position-dependent hopping rates (site-wise disorder) and, thus, have a significant influence on the system dynamics. The defects have been extensively studied in the context of TASEP. Earlier, TASEP with static obstacles has been studied extensively. These defects permanently reside at a location called a specific site, and these sites were assigned hopping rates that were distinct from the others. Examples include the investigation of the role of single local inhomogeneity or quenched site-wise inhomogeneity, a random distribution of spatially varying hopping rates [66, 2, 129, 78, 132]. Dynamic defects, on the other hand, are more pertinent to research due to their ability to replicate the dynamics of several natural and realistic transport systems. Stochastic dynamic defects, alternatively known as dynamic defects, can emerge or disappear randomly at specific sites, altering the hopping rate compared to unaffected sites. This variation may impede particle movement, but particles move at their regular hopping rate in unobstructed regions. Previously, studies have explored uncontrolled disordered 3.1 Background 61

systems involving a single dynamic defect that binds or unbinds at a fixed location within a TASEP model with periodic boundary conditions [133] and has also been studied for open boundary conditions [117]. Several other modifications, such as interaction dynamics [68], non-conserving dynamics [100], reservoir crowding [101], etc., were incorporated into an open TASEP model where a single dynamic defect binds/unbinds at a fixed site. Another generalization of a single dynamic defect has been proposed in a closed lattice [116] where the defect diffuses as well as binds/unbinds throughout the lattice (no fixed site).

The scenario where multiple dynamic defects appear/disappear on the lattice, also termed a site-wise disorder, has been explored less. Although it seems more realistic and is capable of mimicking natural phenomena such as the traffic jams due to the binding/unbinding of microtubule-associated proteins [25] from microtubules which are observed in several in vivo [119] and in vitro, [104] experiments. In literature, the study of site-wise disorder has been investigated under the framework of exclusion process [9, 140]. Some versions of TASEP incorporating dynamic disorder (ddTASEP) have been investigated in a resource-constrained environment [16] whereas in [99], the model has additional feedback (the particle-defect interaction) where defects are removed by particles. Further, recently an effort has been made to numerically study a generalization of an open ddTASEP model that incorporates the Langmuir kinetics for particles [51]. However, it lacks three crucial aspects: (i) the role of defects in the particle dynamics is not incorporated at the boundary sites which ultimately govern the stationary properties of the system such as boundaryinduced phase transitions; (ii) lack of uniform proportionality in the affected attachment rate and affected hopping rate of particles due to defects and (iii) the steady-state numerical solution for density is insufficient to characterize the influence of all the parameters. Therefore, in light of the above-mentioned shortcomings, we propose to analyze the role of the non-conserving dynamics of the totally asymmetric simple exclusion process with the dynamic disorder. In contrast to the previously studied model [140, 51], we have inculcated the concept of an affected hopping rate at the entry site also, which significantly impacts the system's stationary state properties, particularly when compared to the reference [51],

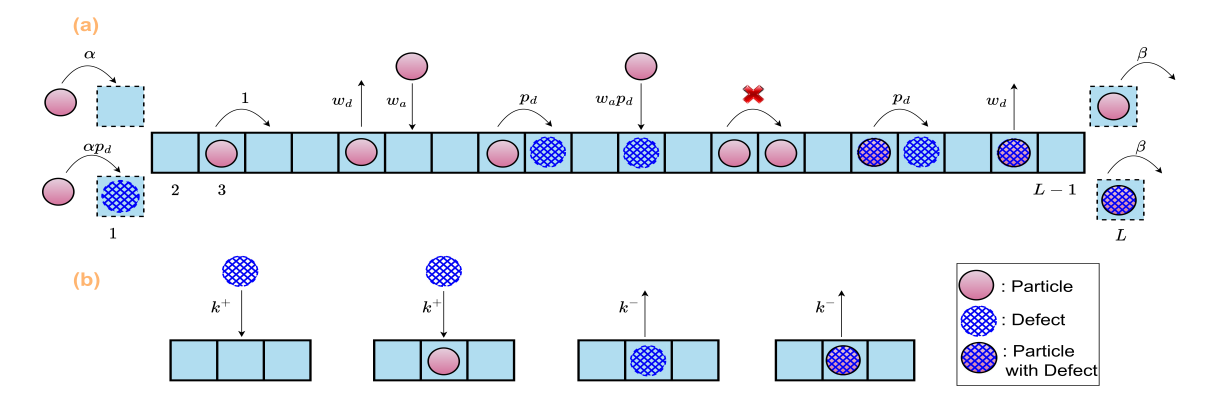


Figure 3.1: A diagrammatic representation of a non-conserving TASEP model depicting the dynamics of particles (highlighted in pink) and defects or obstacles (illustrated in a blue mesh). (a) Depicts different particle dynamics, including entry, exit, hopping, and attachment/detachment, along with the corresponding rates at which these events occur in the presence and absence of defects. (b) Illustrates the dynamics of defects on the lattice, including defect binding/unbinding and their corresponding rates.

the obstruction due to the defects in the proposed model affects the particle hopping and attachment rates in uniform proportion. To explore the dynamics of the model, we approach the system theoretically via mean-field approximation, and we mainly intend to address the following points: (i) What impact do site-wise dynamic defects have on the stationary properties of the standard TASEP-LK system, including particle flux, density profiles, and stationary phases? (ii) What factors affect the system's stationary properties? (iii) Does the system remain symmetric with respect to particle-hole in the presence of dynamic defects? (iv) Does the domain wall remain localized in the presence of defects? If yes, what is the impact of defects on the domain wall?

3.2 Model overview

In actual transportation scenarios, obstacles frequently impede movement. On highways, these obstacles might be intersections or traffic signals, while in the microscopic domain, molecular traffic is often obstructed by proteins that are bound or temporary alterations to the 'lanes' through which traffic flows. Motivated by these stochastic disorders, we propose a model representing an open, dynamically disordered TASEP with LK dynamics. It is

3.2 Model overview 63

represented through a one-dimensional discrete lattice comprising L sites, each labeled from j=1 to L. Here, particles enter through the initial site (j=1), traverse both horizontally and vertically within the bulk $(2 \le j \le L-1)$, and exit via the final site (j=L). Particles moving horizontally only exhibit a unidirectional horizontal movement (left to right). Moreover, the adsorption/ desorption of particles also pertains to the lattice, where particles can also join or leave the lattice by a vertical movement from all sites other than the first and last sites. The lattice also includes a different type of entity known as defects (or obstacles), which introduce dynamic disorder and impede the movement of particles throughout the lattice. In contrast to particle movement, the defects only exhibit vertical movement and can randomly bind/unbind on every lattice site. Individually, both particles and defects adhere to the hard-core exclusion principle. Therefore, each site can only accommodate a single particle, defect, or a combination of the two. As depicted in FIG. 3.1, the events showcasing possible particles and defects dynamics on the lattice, along with their corresponding occurrence probabilities, are illustrated as follows:

- Particle dynamics: The dynamics of particles are significantly influenced by defect occupancy; hence, these dynamics at various lattice locations are characterized as follows:
 - (a) At entry: If the first site has no particle, a particle can enter the lattice through this site with a rate α if it has no defect or with a rate αp_d ($p_d < 1$) otherwise. In case the first site is particle-occupied and its immediate right neighbor is particle-vacant, the particle can move to this neighboring site at a unit rate if the arrival site has no defect or with a rate of p_d otherwise.
 - (b) At bulk: If a particle occupies a bulk site, it first attempts detachment at a rate of w_d . If detachment fails and its immediate right neighbor is particle-vacant, the particle moves to the neighboring site with a unit rate if no defect is present at the arrival site or with a rate of p_d otherwise. At a bulk site without a particle, a particle can attach at a rate of w_a if no defect is present at the arrival site or at a rate of $w_a p_d$ otherwise.

- (c) At exit: A particle present at the last lattice site can leave the lattice with a rate β .
- 2. **Defect dynamics**: A defect can randomly bind (unbind) at a site without (with) a defect with a rate k^+ (k^-). Note that the particle's presence on the arrival site has no effect on the dynamics of defects, but the converse is not true.

An event such as hopping of the particle, attachment/detachment of the particle, or binding/unbinding of the defect is selected depending on the probability proportional to their corresponding rates.

Notably, the proposed model is distinctive from the ref. [140] in the sense that the attachment and detachment of particles are considered to make it more realistic. Moreover, this study not only addresses the dynamics of defects (binding/unbinding) at the boundary sites but also examines its impact on particle dynamics through modified rates at the boundaries, a consideration which was absent in the references [140, 51]. In the later part, we will explicitly discuss that these considerations will produce a non-trivial effect on the stationary-state characteristics of the model. In the subsequent section, we will offer mathematical underpinning by formulating master equations that depict the temporal evolution of the average particle and defect density, elucidating the process involved, and obtaining the stationary-state solution by solving them in the thermodynamic limit.

3.3 Master equations

Individually, both particles and defects obey the hard-core exclusion principle; therefore, we introduce two binary random variables σ_j and v_j each denoting the occupancy of the particle and defect on the lattice, respectively. The random variable σ_j (or v_j) = 0/1 signifies the absence/presence of particle (or defect) at j^{th} lattice site. Now, these variables are employed to formulate the master equation showcasing the evolution of the average occupation number for each entity, starting with the particles. The particle density in the bulk of the lattice

evolves as follows:

$$\frac{d\langle \sigma_j \rangle}{dt} = J_{j-1,j} + w_a \langle (1 - v_j)(1 - \sigma_j) \rangle + w_a p_d \langle v_j(1 - \sigma_j) \rangle - J_{j,j+1} - w_d \langle \sigma_j \rangle, \quad (3.1)$$

where,

$$J_{i-1,j} = \langle \sigma_{i-1}(1 - v_i)(1 - \sigma_i) \rangle + p_d \langle \sigma_{i-1}v_i(1 - \sigma_i) \rangle$$
(3.2)

 $\langle \cdots \rangle$ denotes the statistical average and $J_{j-1,j}$ is the particle-flux from $j-1^{\text{th}}$ site to j^{th} site. The equation governing the evolution of particle density at both the left-lattice and right-lattice boundaries is formulated as:

$$\frac{d\langle \sigma_1 \rangle}{dt} = \alpha \langle (1 - \sigma_1)(1 - v_1) \rangle + \alpha p_d \langle (1 - \sigma_1)v_1 \rangle - J_{1,2}, \text{ and},$$
 (3.3)

$$\frac{d\langle \sigma_L \rangle}{dt} = J_{L-1,L} - \beta \langle \sigma_L \rangle, \tag{3.4}$$

respectively. Lastly, the master equation dictating the evolution of the average defect density within the lattice is provided as follows:

$$\frac{d\langle \mathbf{v}_j \rangle}{dt} = k^+ \langle 1 - \mathbf{v}_j \rangle - k^- \langle \mathbf{v}_j \rangle, \quad 1 \le j \le L. \tag{3.5}$$

In order to comprehend the stationary-state dynamics of the system, the aforementioned equations require a solution. However, solving them in their current state poses a challenge due to the presence of one-, two-, and three-point correlators. Therefore, in the subsequent section, mean-field approximations are applied to these equations in an attempt to elucidate stationary-state attributes such as density profile, potential stationary phases, phase transitions, and current.

3.4 Continuum mean-field approximations

By employing mean-field approximations, all potential particle-particle and particle-defect correlations are disregarded within the aforementioned system of master equations, namely $\langle \sigma_j \sigma_{j+1} \rangle = \langle \sigma_j \rangle \langle \sigma_{j+1} \rangle$ and $\langle \sigma_j v_{j+1} \rangle = \langle \sigma_j \rangle \langle v_{j+1} \rangle$. Additionally, we introduce the notations $\rho_j = \langle \sigma_j \rangle$ and $\rho_{d,j} = \langle v_j \rangle$ to represent the average particle density and defect density, respectively, at site j. This simplification results in reducing Eq. (3.1) to:

$$\frac{d\rho_j}{dt} = J_{j-1,j} + w_a \left((1 - \rho_{d,j})(1 - \rho_j) + p_d \rho_{d,j}(1 - \rho_j) \right) - J_{j,j+1} - w_d \rho_j, \tag{3.6}$$

where,

$$J_{j-1,j} = \rho_{j-1}(1 - \rho_j)(1 - \rho_{d,j} + p_d \rho_{d,j}). \tag{3.7}$$

The evolution equations for average particle density at the left and right boundaries are reformulated as:

$$\frac{d\rho_1}{dt} = \alpha(1 - \rho_1)(1 - \rho_{d,1} + p_d\rho_{d,1}) - J_{1,2}, \text{ and,}$$
(3.8)

$$\frac{d\rho_L}{dt} = J_{L-1,L} - \beta \rho_L,\tag{3.9}$$

respectively. Furthermore, the evolution of average defect density within the lattice follows the subsequent equation:

$$\frac{d\rho_{d,j}}{dt} = k^{+}(1 - \rho_{d,j}) - k^{-}\rho_{d,j}, \quad 1 \le j \le L.$$
(3.10)

To obtain the continuum version of the model, we coarse-grain the lattice by introducing $x = \varepsilon j \in [0,1]$ as the quasi-continuous space variable and $\varepsilon = \frac{1}{L}$ as the lattice constant. Then, the terms up to the first order of ε are retained in the Taylor series expansion of $\rho_{j\pm 1} \approx \rho(x\pm \varepsilon)$ in Eq. (3.6) to get the reformulation of Eq. (3.6) and Eq. (3.10) as:

$$\frac{\partial \rho}{\partial t'} + \frac{\partial J}{\partial x} = \Omega_a (1 - \rho_d + p_d \rho_d) (1 - \rho) - \Omega_d \rho, \tag{3.11a}$$

$$\frac{\partial \rho_d}{\partial t} = k^+ (1 - \rho_d) - k^- \rho_d \tag{3.11b}$$

respectively. Here, $t' = \frac{t}{L}$ is the re-scaled time variable, and $\Omega_a = w_a L$, $\Omega_d = w_d L$ are the modified Langmuir kinetic rates. Furthermore, the subscript j is also omitted, considering

the spatial homogeneity of the lattice.

It is essential to utilize a modified detachment rate that is constant for $L \to \infty$ (in large systems) because the discrepancy between bulk and boundary dynamics becomes apparent only if particles remain on the lattice for a sufficient duration before detachment. A similar rationale justifies the adjusted attachment rate. The average particle current within the lattice bulk, considering a finite ε , is expressed as $J = (1 - \rho_d + p_d \rho_d) \left(-\frac{\varepsilon}{2} \frac{\partial \rho}{\partial x} + \rho (1 - \rho) \right)$ whereas in the thermodynamic limit $(\varepsilon \to 0^+)$, it becomes $J = (1 - \rho_d + p_d \rho_d) \rho (1 - \rho)$. The right-hand side of the Eq. (3.11a) can also be expressed as $\Omega_d(K^*+1)\left(\frac{K^*}{K^*+1}-\rho\right)$. This suggests that the density governed by the Langmuir isotherm (ρ_l) defined as $\frac{K^*}{K^*+1}$ will exhibit either an attracting or a repelling behavior with respect to the nonlinear relationship between current and density because this net source term is positive or negative, depending on whether the density ρ is below or above ρ_l where $K^* = K(1 - \rho_d + p_d\rho_d)$ and $K = \frac{\Omega_d}{\Omega_d}$ is the binding constant. This will prove to be a crucial concept while discussing density profiles in subsequent sections. If the density at the left end dips below the Langmuir isotherm and the current-density relation's slope is positive, $\frac{\partial J}{\partial \rho} > 0$, then the particles will accumulate into the bulk of the lattice through Langmuir kinetics. Consequently, the density increases towards ρ_l as one progresses away from the left boundary. Conversely, with a negative slope $(\frac{\partial J}{\partial \rho} < 0)$, indicating densities greater than 1/2, the density profiles diverge from the Langmuir isotherm as one moves away from the left boundary [103].

The hindrance to particle movement within the lattice is directly proportional to the number of defects present on the lattice, or equivalently ρ_d , and inversely proportional to the affected hopping rate p_d . Consequently, we have introduced an obstruction factor that rationalizes the role of defects in impeding particle movement and reduces the model's parameter space. This simplification will facilitate the focused study of defects on the stationary-state characteristics of the system in subsequent sections. It is defined as:

$$z = \rho_d (1 - p_d), \tag{3.12}$$

Utilizing the Eq. (3.12), the expression for the stationary-state current in the bulk of the

lattice reduces to:

$$J = (1 - z)\rho(1 - \rho), \tag{3.13}$$

The above-obtained expression for the particle current indicates that the proposed model can be perceived as a generalization of the standard TASEP model or a model with static localized defects, where the effective hopping rate of particles is 1-z [133]. Note that the obstruction factor, being a function of ρ_d and p_d , remains confined within the range of 0 and 1, as both parameters are bounded in the same range. The obstruction on the lattice diminishes to zero either when there are no defects on the lattice ($\rho_d = 0$) or when the affected hopping rate due to defects attains the standard unit hopping rate ($p_d = 1$). For this case, the expression for the current in Eq. (3.13) shows that the model reduces to that of a standard open TASEP with LK dynamics [103]. Conversely, the particle faces maximum hindrance when all lattice sites are entirely occupied by defects, i.e., $\rho_d = 1$, and simultaneously, the defects prevent particle hopping in their presence, indicated by $p_d = 0$. For this case, the particle current vanishes from the lattice and can be easily validated from Eq. (3.13).

In the next section, we will obtain a stationary state analytical solution to the derived continuum equations for the particle as well as defect density and compare it to simulation results.

3.5 Analytical solution at stationary state

Theoretical defect density at the stationary state can be readily computed from Eq. (3.11b) as:

$$\rho_d = \frac{k^+}{k^+ + k^-}. (3.14)$$

At stationary state, the nonlinear differential Eq. (3.11a) in the limit $\varepsilon \to 0$, reduces to a first order differential equation,

$$\frac{\partial J}{\partial x} = \Omega_d(K^* + 1) \left(\frac{K^*}{K^* + 1} - \rho \right), \tag{3.15}$$

Next, we will elucidate in detail how one can analytically solve the continuum equation, Eq. (3.11a), in the steady state. This discussion will lead to a categorization of the potential solutions based on the entry rate (α) , exit rate (β) , the effective binding constant $(K^* = K(1-z))$, and the detachment rate (Ω_d) .

One can easily verify that the Eq. (3.11a) of the system remains invariant under the following transformations: $\rho(x) \leftrightarrow 1 - \rho(1-x)$, $w_a(1-z) \leftrightarrow w_d$. This implies that $K^* \leftrightarrow 1/K^*$ and hence this symmetry with respect to K^* allows us to restrict our choices to values with $K^* \geq 1$. Then, the two scenarios that need to be distinguished are $K^* = 1$ and $K^* > 1$. The scenario where $K^* = 1$ is somewhat hypothetical and requires careful manipulation of the binding constant and obstruction factor, but it is technically more straightforward to analyze. Therefore, we will address this case first. Additionally, we will compare these results with the outcomes obtained from Monte Carlo simulations.

3.5.1 Analysis for $K^* = 1$

Theoretical computation of the average particle density becomes mathematically simplified when $K^* = 1$, as Eq. (3.15) factorizes to:

$$(2\rho - 1)\left((1 - z)\frac{\partial \rho}{\partial x} - \Omega_d\right) = 0.$$
 (3.16)

Upon solving Eq. (3.16), we retrieve two different solutions: a constant density $\rho_{MC}(x) = \frac{1}{2}$ associated with a maximal-current (MC) phase, and a linear profile $\rho(x) = \frac{\Omega_d}{1-z}x + C$. These solutions are similar to the case of TASEP-LK without dynamic defects [103] except for the normalization of the coefficient of x in the linear solution. To ascertain the value of the integration constant C in the linear density profile, we first determine the estimate to boundary densities ρ_1 and ρ_L utilizing Eqs. (3.8) and (3.9) as:

$$\rho_1 = \alpha \text{ and } \rho_L = 1 - \beta^*, \tag{3.17}$$

where $\beta^* = \frac{\beta}{1-z}$. Now, the linear density profile yields two solutions: an entry-dominated one, corresponding to the low-density (LD) phase, achieved by matching the linear solution with the left boundary; and another exit-dominated, corresponding to the high-density (HD) phase, obtained by matching the linear solution with the right boundary. These solutions are as follows:

$$\rho_{\alpha}(x) = \frac{\Omega_d}{1 - z} x + \alpha,$$

$$\rho_{\beta}(x) = \frac{\Omega_d}{1 - z} (x - 1) + 1 - \beta^*.$$
(3.18)

Since we have the density solution for the standard stationary phases, we can derive a general density profile $\rho(x)$ by combining three possible solutions: ρ_{α} , ρ_{β} , and ρ_{MC} . Firstly, the position separating the low-density profile $\rho_{\alpha}(x)$ from the density profile $\rho_{MC}(x)$ is computed as $x_{\alpha} = \frac{(1-2\alpha)(1-z)}{2\Omega_d}$. Additionally, we compute the position $x_{\beta} = \frac{2\beta+2\Omega_d+z-1}{2\Omega_d}$ that separates the high-density profile $\rho_{\beta}(x)$ from the density profile $\rho_{MC}(x)$. Various scenarios arise depending on the relative ordering of x_{α} and x_{β} , and the corresponding density profiles for these situations are provided as follows:

1. If $x_{\alpha} \leq x_{\beta}$, the continuous and piecewise linear density profile exhibiting the coexistence of three phases is given by:

$$\rho(x) = \begin{cases} \frac{\Omega_d}{1-z} x + \alpha; & 0 \le x \le x_{\alpha}, \\ \frac{1}{2}; & x_{\alpha} \le x \le x_{\beta}, \\ \frac{\Omega_d}{1-z} (x-1) + 1 - \beta^*; & x_{\beta} \le x \le 1. \end{cases}$$
(3.19)

2. If $x_{\alpha} > x_{\beta}$, a jump discontinuity between the densities $\rho_{\alpha}(x)$ and $\rho_{\beta}(x)$, arises at a point x_w in the form of a shock. The density profile exhibiting the co-existence of two phases is given by:

$$\rho(x) = \begin{cases} \frac{\Omega_d}{1 - z} x + \alpha; & 0 \le x \le x_w, \\ \frac{\Omega_d}{1 - z} (x - 1) + 1 - \beta^*; & x_w \le x \le 1. \end{cases}$$
(3.20)

where the position of the shock $x_w = \frac{\beta - \alpha(1-z) + \Omega_d}{2\Omega_d}$ is obtained by utilizing the current-continuity principle at the discontinuity x_w . For $x_w \in (0,1)$, the shock is to be visible in the bulk of the lattice. Moreover, for $x_w \leq 0$ ($x_w \geq 1$), the shock or the LD-HD co-existence phase exits from the left (right) end of the lattice leading to the LD (HD) phase whose density profile is given by $\rho_{\beta}(x)$ ($\rho_{\alpha}(x)$). The height of the shock Δ is given by,

$$\Delta = \rho_{\beta}(x_w) - \rho_{\alpha}(x_w) = 1 - (\alpha + \beta) - \frac{\Omega_d}{1 - z}.$$
(3.21)

In the limit $z \to 0$, all the above-obtained results match that of an open TASEP with LK [103] whereas in the limit $\Omega_d \to 0^+$, the LK dynamics begin to vanish from the lattice and the stationary state density profiles converge to that of an open TASEP with site-wise dynamic defects [16].

3.5.1.1 Existence of stationary phases

We briefly review the stationary properties of the homogeneous open TASEP, extensively studied through mean-field analysis. It was observed that the system could exist in one of three phases depending on the entry and exit rates: entry-dominated low density (LD), exit-dominated high density (HD), and bulk-dominated maximal current (MC). The transition from both LD and HD phases to the MC phase occurs as a second-order transition concerning density. However, the phase transition from LD to HD is first-order. In this regard, when the entry rate equals the exit rate, an LD-HD coexistence phase (Shock (S) phase) emerges, characterized by a delocalized shock traversing the lattice. Upon the incorporation of Langmuir Kinetics, the shock becomes anchored (localized shock) and extends beyond a line, encompassing a region. Furthermore, we observe various combinations of the primary phases LD, MC, and HD [45, 103].

In our proposed model, the lattice can possess a maximum of 21 different combinations of key phases LD, HD, and MC. However, not all of them may exist for any parameter value. Now we discuss in detail the existence of the probable stationary phases and theoretically derive their existential conditions.

(a) **LD phase:** In a lattice within an entry-dominated phase, the density profile is delineated by $\rho_{\alpha}(x)$ with a boundary layer on the right end. The phase boundaries containing the LD phase in the $\alpha - \beta$ parameter space are specified as:

$$\alpha < \min\left(\beta - \Omega_d, \frac{1-z}{2} - \Omega_d\right). \tag{3.22}$$

(b) **HD phase:** In a lattice characterized by an exit-dominated phase, the density profile is given by $\rho_{\beta}(x)$, with a boundary layer present at the left end. The phase boundaries encompassing the HD phase within the $\alpha - \beta$ parameter space are outlined as follows:

$$\beta < \min\left(\alpha(1-z) - \Omega_d, \frac{1-z}{2} - \Omega_d\right). \tag{3.23}$$

(c) **MC phase:** Following the expression of the current, the gradient of the current vanishes, and the maximal current is attained for $\rho = 1/2$. Hence, in this phase, the density profile in the bulk of the lattice is given by $\rho_{MC}(x) = 1/2$, along with the presence of boundary layers at both ends. This phase exists when α and β^* satisfies:

$$\alpha > \frac{1}{2} \text{ and } \beta^* > \frac{1}{2}.$$
 (3.24)

(d) **S phase:** In the shock phase, the density profile consists of a curve that is discontinuous at a point x_w , combining low and high-density profiles. The density to the left of x_w is represented by $\rho_{\alpha}(x)$, and to the right of x_w , it is denoted by $\rho_{\beta}(x)$. The conditions for the presence of this phase in the lattice are as follows:

$$\beta + \alpha(1-z) < 1-z-\Omega_d$$
 and $|\beta - \alpha(1-z)| < \Omega_d$. (3.25)

(e) **LD-MC phase:** There exists a two-phase co-existence region (or LD-MC phase) wherein the density at the left of x_{α} is expressed by $\rho_{\alpha}(x)$ and at the right of x_{α} is given by 1/2 with a boundary layer on the right end. The conditions for the existence

of this phase in the lattice are given as:

$$\frac{1}{2} - \frac{\Omega_d}{1 - z} < \alpha < \frac{1}{2} \text{ and } \beta^* > 1/2.$$
 (3.26)

(f) **MC-HD phase:** The density profile for the two-phase coexisting region (or MC-HD phase) is given by a continuous combination of two curves. To the left of x_{β} , the density is 1/2, while to the right of x_{β} , it is represented by $\rho_{\beta}(x)$ with a boundary layer on the left end. The conditions for the presence of this phase in the lattice are outlined as follows:

$$\alpha > \frac{1}{2} \text{ and } \frac{1-z}{2} - \Omega_d < \beta < \frac{1-z}{2}.$$
 (3.27)

(g) **LD-MC-HD** phase: Similarly, a three-phase coexistence region (or LD-MC-HD phase) may occur. As mentioned earlier, it exists when $x_{\alpha} \leq x_{\beta}$, and the condition for its presence in the lattice is given by:

$$\beta + \alpha(1-z) > 1 - z - \Omega_d, \quad \alpha < \frac{1}{2} \quad \text{and} \quad \beta^* < \frac{1}{2}.$$
 (3.28)

Now, we provide the argument to discard the prospect of the existence of the remaining fourteen phases. The existence of the three phases MC-LD, HD-LD, HD-MC can be discarded based on the argument that it is impossible to concatenate the density profiles for the above-discussed phases either continuously or discontinuously for $\Omega_d > 0$ while keeping $\rho_{\alpha}(x) < 1/2$, $\rho_{\beta}(x) > 1/2$. The rest eleven co-existing three phases involve the combination with any of the above three discarded phases and hence can be discarded following a similar argument. For example, the LD-MC-LD ceases to exist because it is a combination of the LD phase with the MC-LD phase, and the latter has already ceased to exist. Therefore, up to seven distinct stationary phases may be observed in the phase diagram when $K^* = 1$.

3.5.2 $K^* \neq 1$

Considering the particle-hole symmetry, we restrict our focus to the case $K^* > 1$. In contrast to the previous case i.e., $K^* = 1$, the continuum equation governing the particle density in Eq. (3.15) cannot be simplified, rendering the analysis considerably more intricate. For additional analysis, we transform Eq. (3.15) into the format of a re-scaled density σ , for which the solution is already established [103]:

$$\sigma(x) = \frac{K^* + 1}{K^* - 1} (2\rho - 1) - 1. \tag{3.29}$$

Clearly, the density $\rho(x) \in [0,1]$ implies that the re-scaled density $\sigma(x) \in \left[\frac{-2K^*}{K^*-1}, \frac{2}{K^*-1}\right]$ and here the condition $\sigma(x) = 0$ represents the Langmuir isotherm $\rho_l = \frac{K^*}{K^*+1}$ which is similar to that in [103]. The continuum equation (3.15) simplifies to:

$$\left(\frac{\sigma+1}{\sigma}\right)\frac{\partial\sigma}{\partial x} = \frac{(K^*+1)^2\Omega_d}{(K^*-1)(1-z)}.$$
(3.30)

Integrating the aforementioned equation results in:

$$|\sigma(x)|\exp(\sigma(x)) = Y(x), \tag{3.31}$$

where Y(x) is given by:

$$Y(x) = |\sigma(x_0)| \exp\left(\frac{(K^* + 1)^2 \Omega_d}{(K^* - 1)(1 - z)}(x - x_0) + \sigma(x_0)\right), \tag{3.32}$$

and x_0 is a reference point that takes on the value of 0 or 1, as the values of $\sigma(x_0)$ are known at the boundaries, thus providing:

$$Y_{\alpha}(x) = |\sigma(0)| \exp\left(\frac{(K^* + 1)^2 \Omega_d}{(K^* - 1)(1 - z)} x + \sigma(0)\right),$$

$$Y_{\beta}(x) = |\sigma(1)| \exp\left(\frac{(K^* + 1)^2 \Omega_d}{(K^* - 1)(1 - z)} (x - 1) + \sigma(1)\right).$$
(3.33)

Equation (3.31) possesses an explicit solution expressed in terms of the Lambert-W function, and can be formulated as:

$$\sigma(x) = W(Y(x)); \quad \sigma(x) \ge 0$$

$$\sigma(x) = W(-Y(x)); \quad \sigma(x) < 0$$
(3.34)

The Lambert-W function encompasses two real-valued branches: $W_0(x)$ and $W_{-1}(x)$. Depending on the domain and range of these branches, the solution to Eq. (3.34) is derived as:

$$\sigma(x) = \begin{cases} W_{-1}(-Y(x)); & \sigma < -1, \\ W_{0}(-Y(x)); & -1 \le \sigma < 0, \\ W_{0}(Y(x)); & \sigma \ge 0. \end{cases}$$
(3.35)

The entry-dominated solution (σ_{α}) and exit-dominated solution (σ_{β}) can be obtained to align with the left and right boundary densities, respectively. These solutions can then be converted back to yield the solutions ρ_{α} and ρ_{β} in terms of the Lambert-W function, as follows:

$$\rho_{\alpha}(x) = \frac{1}{2} \left(\frac{K^* + 1}{K^* - 1} \left(W_{-1}(-Y_{\alpha}(x)) + 1 \right) + 1 \right),$$

$$\rho_{\beta}(x) = \frac{1}{2} \left(\frac{K^* + 1}{K^* - 1} \left(\sigma_{\beta}(x) + 1 \right) + 1 \right).$$
(3.36)

where, $\sigma_{\beta}(x)$ is given as:

$$\sigma_{\beta}(x) = \begin{cases} W_0(Y_{\beta}(x)); & 0 \le \beta^* \le 1 - \rho_l, \\ 0; & \beta^* = 1 - \rho_l, \\ W_0(-Y_{\beta}(x)); & 1 - \rho_l \le \beta^* \le \frac{1}{2}. \end{cases}$$
(3.37)

Note that similar to the TASEP, the density solution ρ_{α} , associated with the low-density regime, remains stable for $\alpha < 1/2$, while the solution corresponding to the high-density regime, ρ_{β} , is stable for $\beta^* \leq 1/2$.

Similar to the scenario with $K^=1$, we now derive a comprehensive solution for the density profile by considering various feasible combinations of the solutions ρ_{α} and ρ_{β} . In the parameter range where $\alpha, \beta^* \leq \frac{1}{2}$, different solutions emerge depending on whether $1-\beta^*$ surpasses, falls short of, or equals ρ_l . These solutions converge towards the Langmuir isotherm within the bulk while satisfying both boundary conditions [103]. When $\beta^* = 1 - \rho_l$, a flat profile of ρ_{β} is obtained, aligning with the Langmuir isotherm value ρ_l . Within this range, a domain wall emerges, characterized by a density expressed through a combination of $\rho_{\alpha}(x)$ and $\rho_{\beta}(x)$, given by:

$$\rho(x) = \begin{cases} \rho_{\alpha}(x); & x \le x_w, \\ \rho_{\beta}(x); & x > x_w. \end{cases}$$
(3.38)

where x_w is the position of the domain wall that can be determined utilizing the condition $\rho_{\alpha}(x_w) = 1 - \rho_{\beta}(x_w)$. The height of the domain wall Δ is given by $\rho_{\beta}(x_w) - \rho_{\alpha}(x_w)$. If $0 < x_w < 1$, a region consisting of a shock (S) phase is formed. If $x_w > 1$ then the lattice is in the low-density regime whose bulk is characterized by the density profile $\rho_{\alpha}(x)$ with a boundary layer on the right end. If $x_w < 0$ then the lattice in a high-density regime whose density profile is characterized by $\rho_{\beta}(x)$ with a boundary layer on the left end. In the leftregion phases ($\alpha < 1/2, \beta^* < 1/2$), the phase boundaries extend for $\beta^* > 1/2$, remaining independent of the exit rate β and aligned parallel to the β -axis. When $\alpha = 1/2$, the system transitions into the High-Density (HD) phase, where the bulk profile fails to match the entry rate, resulting in a boundary layer at the left end. Further increases in α primarily affect this boundary layer at the left end. However, an increase in β^* beyond 1/2 introduces a boundary layer at the right end. Consequently, the HD phase for $\beta^* \geq 1/2$ stands distinct from the HD phase for $\beta^* < 1/2$. In the bulk, the density profile remains unaffected by the entrance and exit rates, α and β , at the left and right boundaries. It is characterized by the extremal solution $W_0(-Y_{\beta=1/2})$ and is termed the "High-Density Meissner (HD_M)" phase. The term "Meissner" (M phase) in this context draws an analogy to the Meissner effect observed in superconducting materials, where bulk properties dominate the system's behavior rather than boundary conditions. Hence, we deduce that a maximum of four possible stationary phases can occur in the phase diagram for $K^* > 1$ that are LD, HD, S, and HD_M phase.

Obtaining a generalized analytical stationary-state solution for Eq. (3.11a) poses a significant challenge due to the presence of complex features, including dynamic disorder and non-conserving particle dynamics within our system. Therefore, numerical techniques serve as a viable alternative for solving it, and this approach has been widely adopted in the literature to approximate solutions for such intricate systems. Retaining the time derivative within the system, we obtain density solutions at a steady state in the limit as t tends to ∞ , where t denotes the number of time steps. Employing the forward-in-time and central-in-space (FTCS) scheme, we derive the finite-difference equation as:

$$\rho_{j}^{i+1} = \rho_{j}^{i} + \Delta t' \left(\left(1 - \rho_{d,j}^{i} (1 - p_{d}) \right) \left(\frac{\varepsilon}{2} \left(\frac{\rho_{j+1}^{i} - 2\rho_{j}^{i} + \rho_{j-1}^{i}}{\Delta x^{2}} \right) + \left(\frac{\rho_{j+1}^{i} - \rho_{j-1}^{i}}{2\Delta x} \right) (2\rho_{j}^{i} - 1) + \Omega_{a} (1 - \rho_{j}) \right) - \Omega_{d} \rho_{j} \right).$$
(3.39)

$$\rho_{d,j}^{i+1} = \rho_{d,j}^{i} + \Delta t' \left(k^{+} (1 - \rho_{d,j}^{i}) - k^{-} \rho_{d,j}^{i} \right). \tag{3.40}$$

The symbols ρ_j^i and $\rho_{d,j}^i$ represent the numerical approximation of particle density and defect density at the point (x_j,t_i) . Here, the spatial variable $\Delta x = 1/L$ and the temporal variable $\Delta t'$ adhere to the stability criterion of the finite-difference scheme mentioned above, $\Delta t'/\Delta x^2 \leq 1$. Similarly, Eq. (3.3) and Eq. (3.4) are employed to derive the finite-difference equations at the left and right boundaries as:

$$\rho_1^{i+1} = \rho_1^i + \triangle t' \left(\left(1 - \rho_{d,1}^i (1 - p_d) \right) \left(\alpha (1 - \rho_1^i) - \rho_1^i (1 - \rho_2^i) \right) \right), \tag{3.41}$$

and

$$\rho_L^{i+1} = \rho_L^i + \triangle t' \left(\left(1 - \rho_{d,L}^i (1 - p_d) \right) \left(\rho_{L-1}^i (1 - \rho_L^i) - \beta \rho_L^i \right) \right). \tag{3.42}$$

respectively.

3.6 Results & Discussion

In previous sections, the analysis has been conducted with respect to the parameter K^* , which was introduced to simplify and solve Eq. (3.11a), which involves two parameters that are obstruction factor z and the binding constant K. Both z and K are of great relevance as defect dynamics are controlled by z, and it quantify the hindrance caused by the defects to the particle movement, whereas K is responsible for particle dynamics and signifies the ratio of particle attachment with respect to particle detachment. Therefore, we now again introduce them to investigate the effect of each of these parameters individually and compare the results with the existing literature. We begin with the analytical construction of the phase diagrams within the $\alpha - \beta$ plane utilizing the theoretical results obtained in the last two sections in order to study the effect of z, K, and Ω_d on the system's stationary characteristics. We conduct numerical Monte Carlo simulations employing the Gillespie algorithm with a random sequential update rule to verify our theoretical conclusions; please refer to Sec. 1.3.2.1 for details regarding simulations. Note that the binding constant K fundamentally reshapes the phase diagram's topology by modulating the symmetry and connectivity of the Langmuir Kinetics (LK) energy landscape. This arises from its logarithmic coupling in the effective Hamiltonian

$$H = -k_B T \sum_{i=2}^{L-1} \sigma_i \ln K,$$

which assigns an energy cost proportional to $\ln K$ for each occupied site. Crucially, at K=1, the energy terms vanish ($\ln 1=0$), erasing the directional bias in the LK transition graph and inducing particle-hole symmetry [103]. This symmetry collapse triggers a *topological transition* in the $\alpha - \beta$ phase diagram:

- For $K \neq 1$, the Hamiltonian's directional preference ($\ln K \neq 0$) creates distinct phase boundaries between high-density (HD), low-density (LD), and Meissner (M) phases.
- At K = 1, these boundaries merge into a singular manifold where bulk-driven M-phase behavior dominates, akin to symmetry-protected topological phases in condensed matter.

The transition at K = 1 acts as a topological bifurcation point, with K controlling the "twisting" of phase boundaries. For example, K > 1 expands the M-phase domain by enhancing bulk adsorption, while K < 1 favors boundary-dominated HD/LD phases. This framework positions K as a tunable parameter governing both local energy landscapes and global phase connectivity, with direct implications for the stability and spatial extent of the Meissner regime. Hence, it is expected that K will significantly affect the topology of the phase diagram in the $\alpha - \beta$ plane. To investigate the individual impact of each of these parameters on the system's stationary properties, we initially fix the parameter K and vary the rest. It must be noted that as we discuss the role of K and z individually, unlike the ref. [103], the transformations: $\rho(x) \leftrightarrow 1 - \rho(1-x)$, $w_a \leftrightarrow w_d$ no longer implies $K \leftrightarrow 1/K$. Therefore, the analysis is done for every choice of K, namely, K = 1, K > 1, and K < 1, where we further study the impact of z and Ω_d on the steady-state features in each of these cases. Furthermore, the phase diagrams are developed in each scenario specifically for faster defect dynamics $(k^+, k^- \gtrsim 1)$, as the naive mean-field approximation aligns closely with the Monte Carlo results within this parameter range [140]. We initially constructed the phase diagrams using the analytical expressions of the phase separation lines. Subsequently, to verify the proximity of these lines, we conduct Monte Carlo simulations at points near these lines, with detailed information provided in 1.3.2.1. Note that the phase boundaries determined through simulation depend on the magnitude of the defect binding/unbinding rates. The lower rates result in deviations from mean-field predictions due to system correlations, while faster defect dynamics align more closely with theoretically obtained results. In our model, we have considered these rates to be equal to or strictly greater than 1. Moreover, the phase boundaries determined through simulations are calculated with an estimated error of less than 2%, and the same is being taken care of by the size of the markers representing the Monte Carlo simulations.

3.6.1 System behavior for K = 1

In this context, the mathematical analysis is streamlined due to the equivalence of the attachment and detachment rates, denoted by $\Omega_a = \Omega_d \equiv \Omega$. Subsequently, we delve into an

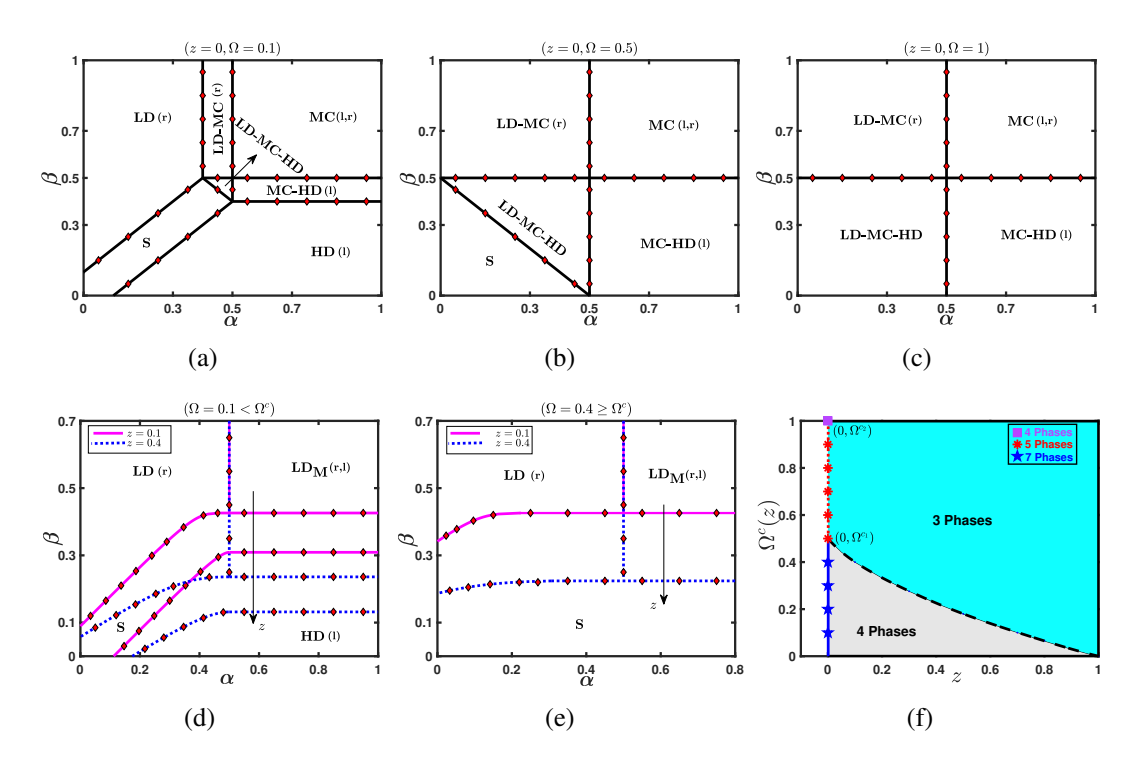


Figure 3.2: (a)-(e) demonstrates how the phase diagram is influenced by z and Ω when K=1. Solid and dashed lines represent theoretical predictions derived from mean-field theory, while Monte Carlo simulation results are depicted with diamonds. The presence of boundary layers at the left or right end of the system is highlighted by "(l)" and "(r)" respectively. In (f), the plot illustrates Ω^c as a function of z, with different symbols (stars, circles, and squares) distinguishing the two critical values Ω^{c_1} and Ω^{c_2} obtained for z=0.

examination of the phase diagram's structure within the $\alpha - \beta$ parameter space, exploring its variations across different values of z and Ω . For K=1, K^* is a monotonically decreasing function of z and it assumes values $K^* \leq 1$ for $z \in [0,1)$. To assess the influence of the obstruction factor, we generate the phase diagrams for various choices of Ω . Additionally, the effect of z is examined for a fixed Ω by varying z. The upper and lower panels of FIG. 3.2 depict the phase diagrams corresponding to z=0 and $z\neq 0$, respectively.

For different values of Ω , we retrieve exactly the same phase diagrams obtained in ref. [103] in the limit $z \to 0$. We reproduce them here for the sake of comparison and analyzing the effect of z. For $\Omega < \Omega^{c_1} = 0.5$, a comparatively richer phase diagram exhibiting seven stationary phases is observed, as shown in FIG. 3.2 (a). An increase in Ω till the critical value Ω^{c_1} doesn't produce any topological changes in the phase diagram except the shifting

of the phase boundaries. The boundary between the LD and LD-MC phases shifts leftward, while the boundary between the HD and MC-HD phases shifts downward. This leads to an enlargement of the LD-MC, HD-MC, and LD-MC-HD phases and a reduction of the LD, HD, and S phases, while the MC phase remains unaffected. Once Ω reaches the critical value Ω^{c_1} , the LD and HD phases completely disappear from the phase diagram, and it now consists of five stationary phases only, see FIG. 3.2 (b). Further increasing $\Omega > \Omega^{c_1}$ only affects the region $\alpha, \beta < 0.5$, where the S phase shrinks and the LD-MC-HD expands whereas the LD-MC and MC-HD phases remain intact. Ultimately, at $\Omega = \Omega^{c_2} = 1$, the S phase vanishes entirely, rendering the phase diagram greatly simplified, with only four phases remaining, as depicted in FIG. 3.2 (c).

Now, we investigate the effect of the obstruction factor on the phase diagram for different choices of attachment-detachment rates. As soon as some obstruction is introduced in the lattice, the topology of the phase diagram changes drastically and becomes much simpler, consisting of four phases, see FIG. 3.2 (d) in comparison to the phase diagram obtained for zero obstruction factor, see FIG. 3.2 (a). For $\Omega < \Omega^c(z)$, the phase diagram consists of LD, S and HD phases along with the emergence of a LD_M phase; see FIG. 3.2 (d) corresponding to $\Omega = 0.1$. Further, increasing the obstruction factor on the lattice while fixing Ω results in an expansion of the LD and LD_M phases, whereas the region consisting of the S and HD phases shrinks. This can be explained as follows: an escalation in the obstruction factor intensifies the impedance to particle movement throughout the lattice, consequently enlarging the domain encompassing both the LD phase and the LD_M phases. Likewise, augmenting Ω enlarges the area encompassing the LD and S phases while the HD phase diminishes. In instances where $\Omega \geq \Omega^{c}(z)$, we note the total absence of the HD phase, resulting in a phase diagram comprising only three phases: LD, LD_M, and S phases, as depicted in FIG. 3.2 (e). In this case, the effect of increasing z remains the same. The FIG. 3.2 (f) shows the graph of the Ω^c , which is a monotonically decreasing function of z. The graph demonstrates that for z > 0, there is only one critical value of Ω , beyond which the number of stationary phases appearing in the phase diagram decreases from four to three. Nevertheless, when z = 0, two critical values exist: $\Omega^{c_1} = 0.5$ and $\Omega^{c_2} = 1$. For $\Omega \ge \Omega^{c_1}$, the

number of stationary phases decreases from seven to five, while for $\Omega \ge \Omega^{c_2}$, it decreases from five to four.

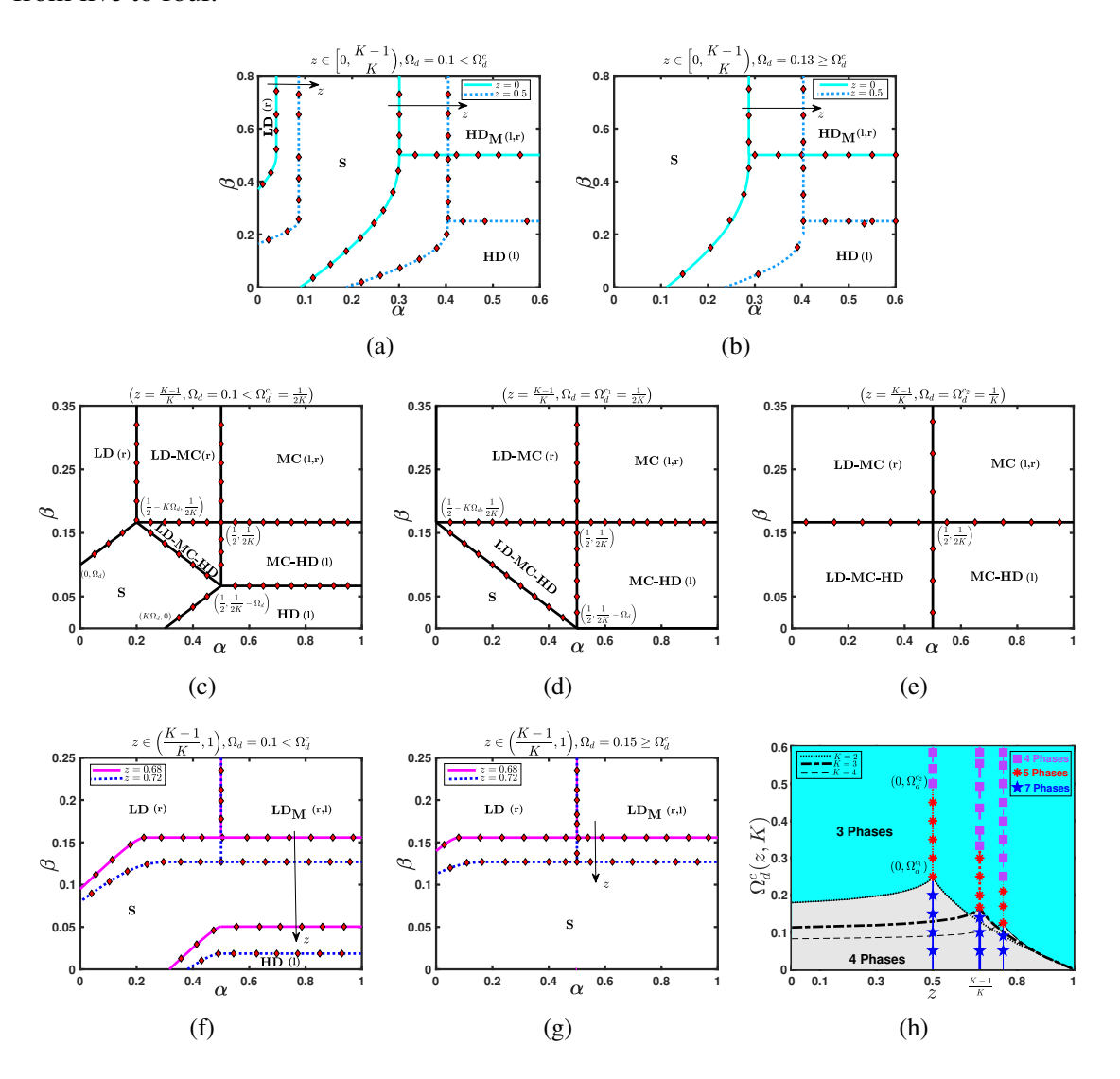


Figure 3.3: (a)-(g) shows the effect of z and Ω_d on the phase diagram for K=3. Solid and dashed lines denote the theoretical outcomes through mean-field theory, whereas diamonds denote the Monte Carlo simulation results. In (h), the plot shows Ω_d^c as a function of z and K. Here, the symbol star, circle, and square distinguish the two critical values Ω^{c_1} and Ω^{c_2} obtained corresponding to $z=\frac{K-1}{K}$.

The phase diagram's structure differs significantly when considering equal attachment-detachment rates and a non-zero obstruction factor compared to the results obtained in ref. [103] (refer to the top and bottom panels of FIG. 3.2). Clearly, the presence of defects in the proposed model for the equal attachment-detachment rate of particles has made the phase

diagram much simpler, which can possess at most four stationary phases depending upon the choice of Ω and z.

3.6.2 System behavior for K > 1

In general, one would anticipate $K \neq 1$ because the case K = 1 requires a specific adjustment between the attachment and detachment rates. Therefore, without loss of generality, we first discuss the case K > 1 and try to understand the effect of z and Ω_d on the stationary state features of the system. Analogous to the previous case, we first examine the influence of the obstruction factor by delineating the phase diagram for various selections of Ω_d . In contrast to the prior scenario, in this case, the parameter K^* varies depending on both K and z. We have three different cases corresponding to the range of z according to which K^* is either > 1 or = 1 or < 1. The panels at the top, middle, and bottom of FIG. 3.3 depict the phase diagrams corresponding to z values within the ranges $\left[0, \frac{K-1}{K}\right)$, $z = \frac{K-1}{K}$, and $\left(\frac{K-1}{K}, 1\right)$, respectively.

In the limit $z \to 0$, the phase diagram for $\Omega_d < \Omega_d^c(z,K)$ consists of four stationary phases: LD, S, HD, and HD_M, see FIG. 3.3 (a). It validates the findings of the ref. [24] corresponding to K=3 and $\Omega_d=0.1$. As soon as some obstruction is introduced in the lattice, i.e., for $z \in \left(0, \frac{K-1}{K}\right)$, the phase boundary between the LD and the S phase as well as the one between the HD_M and the S phase shifts towards the right resulting in shrinkage in the region consisting of HD_M and HD phase whereas an expansion of the region consisting of LD and the S phase. Unlike the scenario with K=1, the inclusion of the obstruction doesn't induce significant topological alterations in the phase diagram, except for expansions and contractions in the regions encompassing stationary phases. When $\Omega_d \geq \Omega_d^c(z,K)$, the boundary separating the LD and S phases shifts leftward, leading to the total absence of the LD phase. Consequently, the phase diagram comprises only three stationary phases, as depicted in FIG. 3.3 (b). The impact of varying z in $(0, \frac{K-1}{K})$ remains the same for this choice of Ω_d .

Once the obstruction factor reaches $\frac{K-1}{K}$, as illustrated in FIG. 3.3 (c), FIG. 3.3 (d), and FIG. 3.3 (e), the phase diagram undergoes notable topological changes. The phase diagram becomes more intricate and diverse for values of z smaller than $\frac{K-1}{K}$. It showcases seven

stationary phases when $\Omega_d < \Omega_d^{c_1}(K) = \frac{1}{2K}$, as depicted in FIG. 3.3 (c). The average density profiles for these seven stationary phases have been obtained in FIG. 3.4. As Ω_d increases till the critical value $\Omega_d^{c_1}(K)$, the phase boundary separating LD and LD-MC phases shifts to the left, whereas the phase boundary between the HD and MC-HD phases shifts downward, leading to an enlargement of LD-MC, HD-MC, and LD-MC-HD phases, and a contraction of LD, HD, and S phases, while the MC phase remains unaffected. For $\Omega_d = \Omega_d^{c_1}(K)$, the LD and HD phases completely disappear from the phase diagram, and now it consists of only five stationary phases; see FIG. 3.3 (d). As Ω_d increases in the range $(\Omega_d^{c_1}(K), \Omega_d^{c_2}(K) = \frac{1}{K})$, the phase diagram is only affected in the region α , $\frac{\beta}{1-z} < 0.5$, where the S phase shrinks and the LD-MC-HD expands, whereas the phases LD-MC, MC-HD, and MC remain intact. Finally, when Ω equals $\Omega_d^{c_2}(K)$, the S phase vanishes entirely, rendering a simpler phase diagram exhibiting just four phases; refer to FIG. 3.3 (e).

Now, we discuss the case $z>\frac{K-1}{K}$. The phase diagram again becomes topologically simpler, as shown in FIG. 3.3 (f) and FIG. 3.3 (g). For $\Omega_d<\Omega_d^c(z,K)$, the phase diagram showcases four stationary phases: HD, S, LD, and LD_M, as shown in FIG 3.3 (f) corresponding to $\Omega=0.1$. For a further increase in z in the range $\left(\frac{K-1}{K},1\right)$, the phase boundary separating the S phase from LD as well as the LD_M phase shifts downwards, this leads to an enlargement of the LD and LD_M phases, while the S and HD phases diminish. For $\Omega_d \geq \Omega_d^c(z,K)$, the phase boundary between the HD and S phase shifts downwards, causing the complete disappearance of the HD phase, and the phase diagram exhibits only three stationary phases; see FIG. 3.3 (g). The influence of varying z in $\left(\frac{K-1}{K},1\right)$ remains the same for this choice of Ω_d .

In comparison to the case K=1, FIG. 3.3 (h) shows the critical values of Ω_d^c which is a function of z as well as K. For a fixed K, $\Omega_d^c(z,k)$ is a non-monotonic function that monotonically increases for $z<\frac{K-1}{K}$, whereas it monotonically decreases for $z>\frac{K-1}{K}$ and attains its maximum value at $z=\frac{K-1}{K}$. Meanwhile, for a fixed value of z, it is a monotonically decreasing function of K. Clearly, for $z\neq\frac{K-1}{K}$, there exists only one critical value of Ω_d , beyond which the number of stationary phases changes from four to three. However, when $z=\frac{K-1}{K}$, two critical values emerge: $\Omega_d^{c_1}=\frac{1}{2K}$ and $\Omega_d^{c_2}=\frac{1}{K}$. In this scenario, if Ω

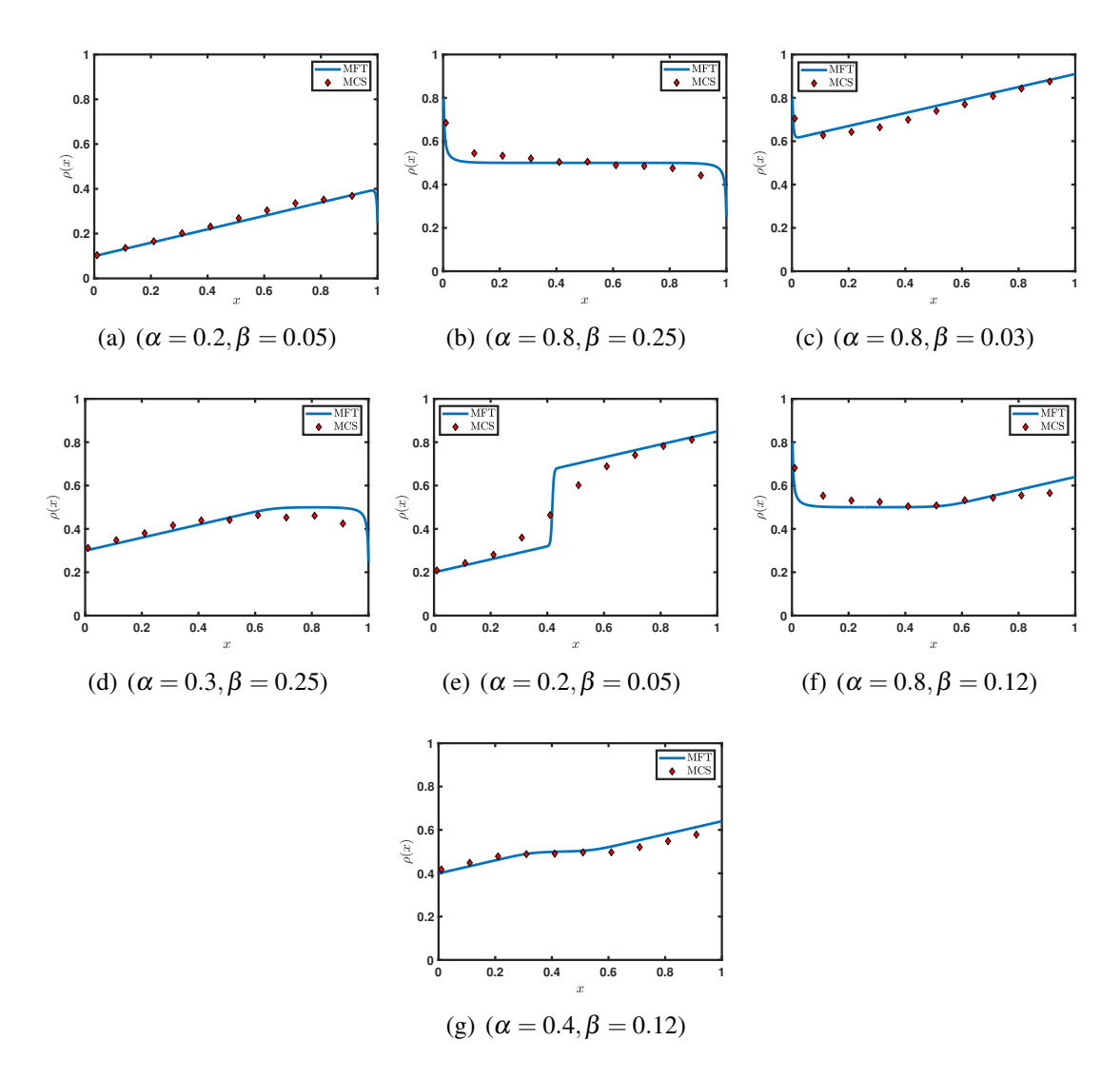


Figure 3.4: Average density profiles: (a) LD, (b) MC, (c) HD, (d) LD-MC, (e) LD-HD, (f) MC-HD, and (g) LD-MC-HD phases. Mean-field solutions (solid curves) contrasted with Monte Carlo simulations (markers). Parameters: K = 3, $\Omega_d = 0.1$, $z = \frac{K-1}{K}$. Sub-captions detail (α, β) configurations.

exceeds $\Omega_d^{c_1}$, the count of stationary phases decreases from seven to five. Likewise, when Ω surpasses $\Omega_d^{c_2}$, the number of stationary phases decreases from five to four. It must be noted that $z^c = \frac{K-1}{K}$ is the general critical value of the obstruction factor for which the phase diagram's structure becomes intricate, featuring a maximum of seven stationary phases.

For an attachment rate larger than the detachment rate, the topology of the proposed model's phase diagrams remains the same compared to the ref. [103] for $z < z_c$ except for

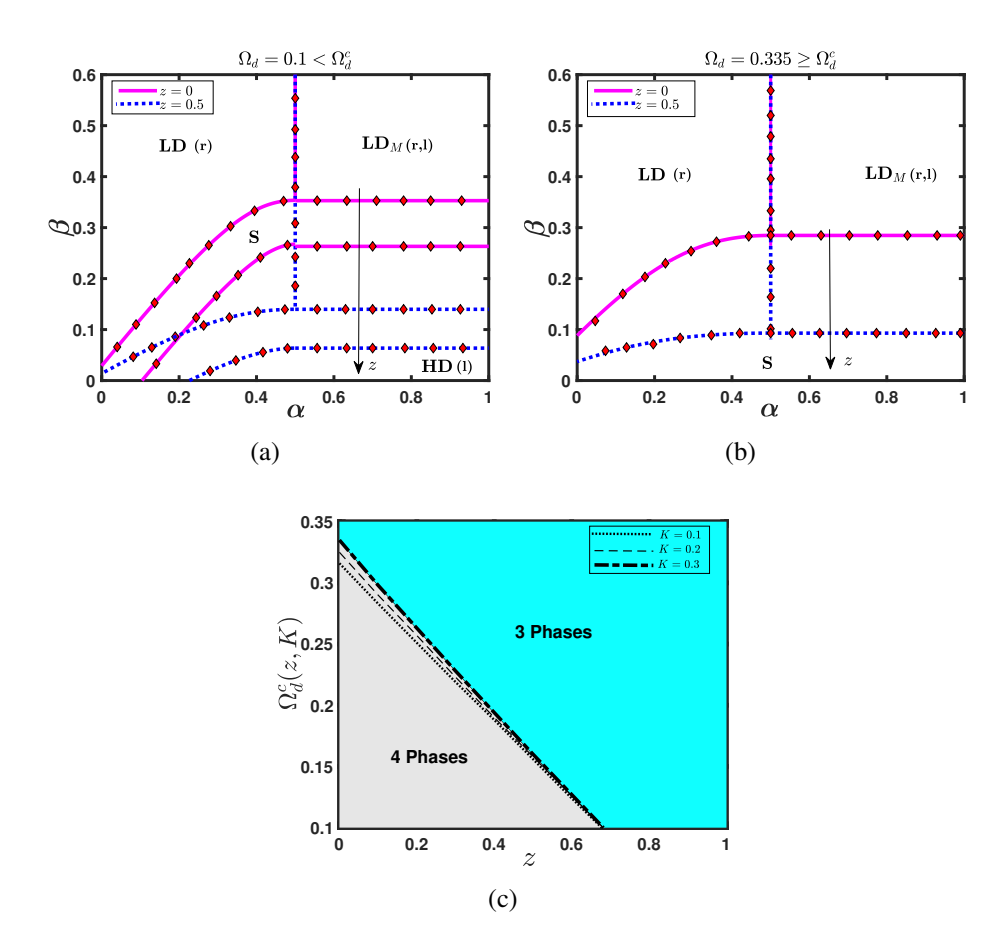


Figure 3.5: (a)-(b) shows the effect of z and Ω_d on the phase diagram for K=0.3. Solid and dashed lines denote the theoretical outcomes through mean-field theory, whereas diamonds denote the Monte Carlo simulation results. In (c), the graph depicts Ω_d^c varying with z and K.

expansion or shrinkage of some phase regions (see top panel of FIG.3.3). But for $z \ge z_c$, the topology changes significantly in comparison to the ref. [103] (see middle and bottom panels of FIG.3.3). Depending on the effective binding constant K^* , the phase diagram of the proposed model can exhibit several stationary phases, including LD-MC-HD, LD-MC, MC-HD, MC, and LD_M.

3.6.3 System behavior for K < 1

Due to the defects considered in the proposed model, the particle-hole symmetry is violated with respect to K, as discussed at the beginning of this section. Therefore, the case K < 1

needs to be discussed separately. Similar to the previous case, we first establish the phase diagram for various Ω_d choices and analyze the influence of the obstruction factor. The parameter K^* is a function of both K and z in this case as well, and $K^* < 1$ for any possible combination of z and K < 1.

As z approaches zero, the phase diagram exhibits four stationary phases: high density (HD), shock (S), low density (LD), and LD_M, for $\Omega_d = 0.1 < \Omega_d^c(z)$, as depicted in FIG 3.5 (a). It validates the findings of the ref. [24] corresponding to K = 0.3 and $\Omega_d = 0.1$. When some obstruction is introduced to the lattice, the phase boundary that separates the S phase from the LD as well as LD_M phases shifts downward, expanding the LD and LD_M phases while contracting the S and HD phases, as shown in FIG. 3.5 (a). However, when $\Omega_d = 0.335 \ge \Omega_d^c(z)$, the high-density (HD) phase is entirely absent, resulting in a phase diagram with only three stationary phases, as illustrated in FIG. 3.5(b). The influence of z within the (0,1) range remains consistent for this particular value of Ω_d .

The FIG. 3.5 (c) shows the graph of the Ω_d^c which is a linear as well as monotonically decreasing function of z and K. The graph demonstrates that for $z \in [0,1)$ there exists only one critical value of Ω_d , beyond which the number of stationary phases appearing in the phase diagram reduces from four to three.

For an attachment rate smaller than the detachment rate, the obstruction factor does not change much topology of the phase diagram in comparison to the ref. [103] except for the shrinkage and expansion of the phase region. Now, we briefly revisit the link mentioned in Section 3.2 between the proposed model and the investigation presented in Ref. [51] to showcase several distinctions in their stationary state results. Firstly, the impact of parameters ρ_d and p_d , responsible for obstructions caused by defects, on the stationary state characteristics of the system, encapsulated through a single parameter z. Secondly, in the scenario of equal attachment-detachment rates and non-zero obstruction, the proposed model exhibits a maximum of four stationary phases in its phase diagrams, while in [51] the phase diagram consists of seven stationary phases. For this case, the phase diagram also includes a low-density Meissner (HD_M) phase, which was not observed in the [51]. Moreover, the topology of these phase diagrams differs significantly from our observations in [51]. In

the case of disparate attachment-detachment rates and non-zero obstruction, the phase diagram within our proposed study can feature up to seven stationary phases in the phase diagram, while in [51], the system can exhibit a maximum of four stationary phases. The configurations of these phase diagrams exhibit variations compared to the findings in [51], contingent upon the selection of attachment-detachment rates and the obstruction factor. This discrepancy can be elucidated by considering the significance of boundary densities in an open system, as they strongly influence the stationary properties and phase diagrams. The inclusion of the effects of defects binding/unbinding at the boundaries, which is absent in ref. [51], is a probable reason for this distinction. Lastly, unlike the model proposed in [51], our system's stationary-state results are obtained analytically, providing a comprehensive characterization of the influence of all parameters.

3.7 Shock analysis & Finite-size effect

One distinctive aspect of the proposed model is the emergence of the localized shock (S) phase, where the shock position remains constant over time. Typically, a qualitative examination of shock dynamics can be straightforwardly conducted using the continuity (or hydrodynamic) equation, which is expressed as:

$$\frac{\partial \rho}{\partial t'} + \frac{\partial J}{\partial x} = \omega_d L(K^* - (1 + K^*)\rho). \tag{3.43}$$

In this context, the flow-density relation, denoted by $J=(1-z)\rho(1-\rho)$, is well-established, allowing for the analysis of the equation above. However, the description provided by the first-order differential equation (3.43) becomes invalid as soon as a discontinuity arises between the densities ρ_{α} and ρ_{β} and at the intersection points of the characteristic lines corresponding to (3.43). The propagation speed of this discontinuity, given by $v=\beta^*-\alpha$, is set by mass current balance — a quantity inherently tied to the obstruction factor through its direct influence on particle flow. To establish the formation of a shock, the discontinuity must reach a position where the mass current through it is zero, thus ensuring the shock remains stationary, indicating that v must be zero.

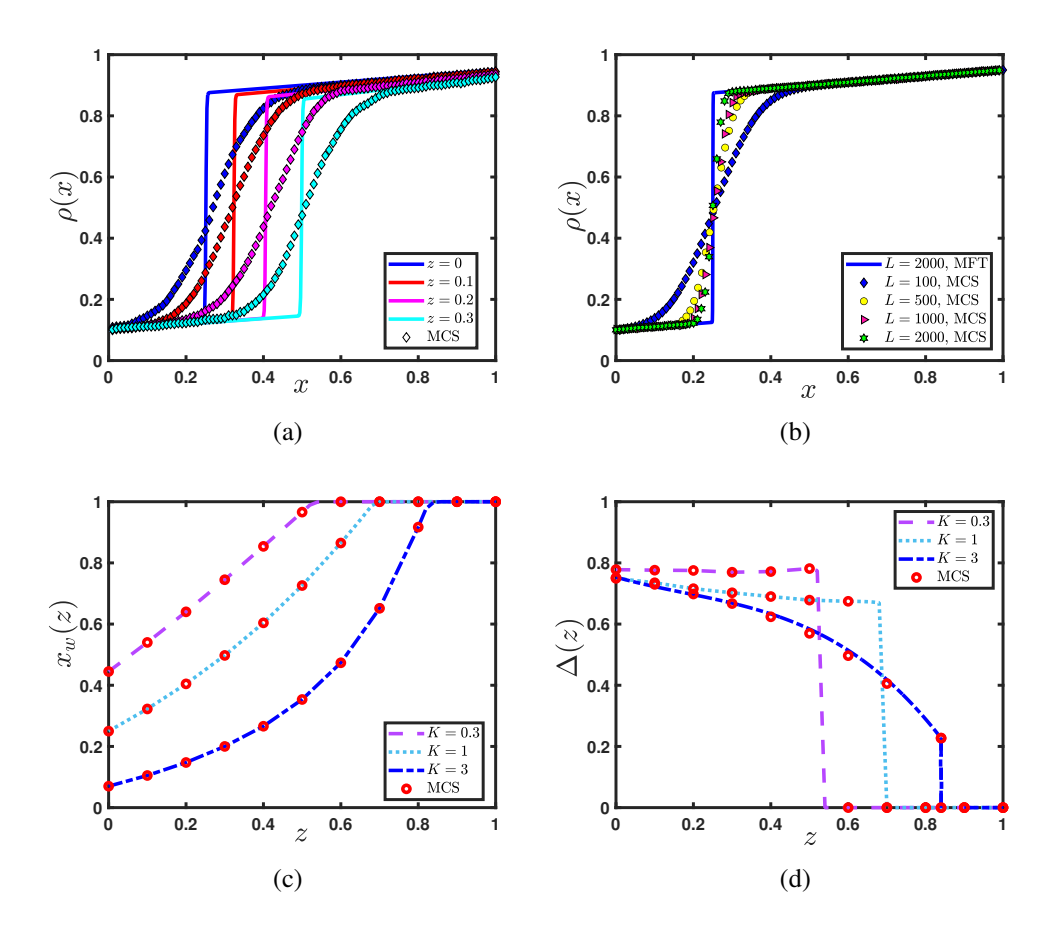


Figure 3.6: (a) Examining shock profiles under varying z for $\alpha = 0.1$, $\beta = 0.05$, $\Omega_d = 0.1$, and K = 1. (b) Finite-size effects on shock profiles at z = 0. Investigating (c) shock displacement and (d) shock amplitude across z.

Progressing further involves analyzing how the obstruction factor influences the shock profiles. A comprehensive shock profile spanning the entire system can be derived by aligning the boundary densities ρ_{α} and ρ_{β} at the location of the shock, which needs to be identified. For K=1, the precise formulae for the shock position (x_w) and its height (Δ) are provided as follows:

$$x_w = \frac{\beta - \alpha(1 - z) + \Omega_d}{2\Omega_d}, \& \Delta = 1 - (\alpha + \beta) - \frac{\Omega_d}{1 - z}.$$
 (3.44)

Evidently, the shock's position is consistently influenced by z, increasing as z increases, while its height shows the opposite trend, decreasing as z increases. Although obtaining explicit expressions for x_w and Δ for $K^* \neq 1$ remains challenging, their corresponding Monte

Carlo results are depicted in FIG. 3.6 (c) and 3.6 (d), with fitted curves confirming their dependency on z. In FIG. 3.6 (a), for fixed values of α , β , and K, it's evident that the shock profile shifts from the left to the right boundaries with increasing obstruction on the lattice. This shift occurs because as z increases, particles encounter more obstructions from defects, decreasing particle density. Consequently, the HD phase's elimination and the LD phase's expansion are observed. These findings are consistent with the phase diagrams discussed in the preceding section.

Finite-size effects for finite L have been accounted for by incorporating second-order terms in the mean-field description. Discrepancies between the second-order mean field and the Monte Carlo results arise from shock fluctuations, which are inaccurately captured by mean-field theory and require separate treatment. Nonetheless, it's noteworthy that the shock is indeed localized, and its width grows sub-extensively, indicating sharpness as $L \to \infty$, as shown in FIG 3.6 (b).

3.8 Conclusion

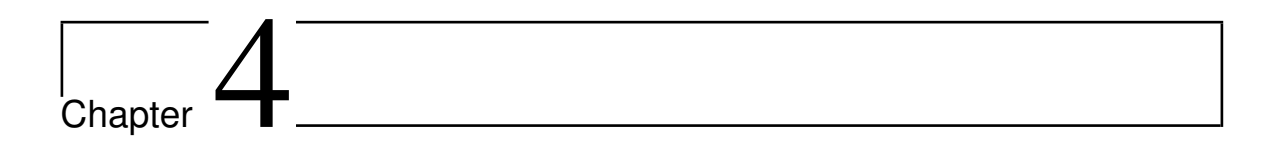
We've extensively examined stochastic transportation within a one-dimensional system, incorporating dynamic disorder in a totally asymmetric simple exclusion process alongside Langmuir kinetics dynamics. The dynamic defects represent disorder that stochastically binds/unbinds throughout the lattice and hinders particle movement. The particle movement has been subject to these dynamic defects and hops with an affected hopping rate p_d . The model is inspired by the imbalance in the transcription of genes due to obstruction, but the model is generic and can be utilized to imitate any other non-equilibrium stochastic transport phenomena where dynamic defects are present.

To explore how dynamic defects influence the stationary-state characteristics of the system, we derive master equations in the thermodynamic limit under the framework of the continuum mean-field approximation. Moreover, we introduce a parameter termed the obstruction factor (z), which amalgamates the impact of defect density on the lattice (ρ_d) and the affected hopping rate (p_d) on the system's stationary properties. In addition, we de-

3.8 Conclusion 91

fine an effective binding constant that incorporates the effect of obstruction on the binding constant. The system dynamics are controlled by the entry rate (α) and exit rate (β) , and the other three important controlling parameters are z, binding constant (K), and total detachment rate Ω_d . The explicit expression of analytical solutions for the density profile and phase boundaries are obtained for K = 1/(1-z) whereas, for the rest of the values of K, the stationary state solution has been implicitly expressed in the form of Lambert W function.

The theoretical solution has enabled us to delineate and extensively analyze the topology of the phase diagram. Since the proposed model doesn't obey the particle-hole symmetry, the analysis is performed for three distinct choices of binding constant, K = 1, > 1 and < 1. In each case, the z and Ω_d effects have been studied on the phase diagram. At the critical value of the obstruction factor (z^c) , the topology of the phase diagram changes significantly. At $z = z^c$, the phase diagram displays a richer structure consisting of either seven or five, or four stationary phases depending upon the value of Ω_d . Whereas for $z \neq z^c$, the phase diagram consists of either four or three stationary phases depending on Ω_d . In this case, with an increase in the magnitude of the obstruction factor, the LD or LD_M phases expand, whereas the S phase and the HD phase shrink. Furthermore, the impact of Ω_d on the phase diagrams is explored, revealing that an escalation in Ω_d diminishes the number of phases within the system. For $z \neq z^c$, there exists a unique critical value Ω_d^c about which the number of stationary phases changes from three to four. While for $z = z^c$, there exist two critical values of $\Omega_d^{c_1}$ and $\Omega_d^{c_2}$ such that about $\Omega_d^{c_1}$, the number of phases changes from seven to five whereas about $\Omega_d^{c_2}$, the number of phases changes from five to four. The variation in the number of stationary phases with respect to the obstruction parameter z can be understood as follows: with the increase in the obstruction factor, the dynamic defects increasingly hinder the particle flux in the bulk, effectively making the bulk dynamics more rate-limiting. Despite the bulk becoming rate-limiting, the boundary dynamics (α and β) still play a significant role in determining stationary phases. Consequently, the interplay between bulk obstructions and boundary conditions influences the number of distinct stationary phases that the system can possess. This behavior highlights the critical role of the obstruction parameter in dictating the system's overall phase structure. Further, we examine the impact of the obstruction factor on the height (and position) of the de-localized shock, which is a monotonically decreasing (increasing) function of z. Finally, we conclude that the proposed theoretical work aimed to simulate dynamic aspects of potential defective cellular and vehicular transport processes and to provide light on stationary qualities. The proposed study can be utilized to understand the role of the disorder in the form of defects on the stationary properties of the stochastic transport systems. Examples of such systems include the biological process of gene transcription, where DNA binding proteins and the low concentration of tRNA act as a disorder [41], transport processes along the microtubule where processive molecular motors switch between directed and diffusive motion [3] etc. The study can be expanded to include additional realistic aspects relevant to various physical and biological systems.



Totally asymmetric simple exclusion process with local resetting in a resource-constrained environment

Preamble

Building upon the dynamically disordered TASEP with Langmuir Kinetics explored in Chapter 3, where particle and defect numbers were non-conserved, we now introduce a novel phenomenon: local resetting. This mechanism emulates real-world dynamical systems that experience interruptions and subsequent resumptions from specific points in their phase space. Interestingly, under certain conditions, this local resetting dynamics shares similarities with Langmuir Kinetics. The present chapter focuses on a resource-constrained environment, where the number of particles in the system is regulated by a key parameter, which we will elaborate on in subsequent sections. This approach allows us to investigate how limited resources and local resetting interact within the TASEP framework, providing insights into more realistic transport scenarios encountered in nature and engineered systems.

4.1 Background

In order to model the observables in various real-life dynamical systems that are interrupted and resumed from a certain point in the phase space, the diffusion process in the conventional TASEP is accompanied by a non-equilibrium process called stochastic resetting. For example, resetting the Brownian particle to its initial position with some fixed rate [47]. This simple act of resetting leads to many non-trivial findings, such as non-trivial stationary state, non-monotonic mean first passage time, etc. In recent times, the concept of stochastic resetting dynamics has been applied to address several microbiological issues such as the interplay of degradation of random mRNA and ribosome loading of mRNA in the translation process [136]. It has many further applications, ranging from the search and optimization algorithms [93], predator-prey system model [131], chemical reactions [113], and biopolymerization [114] etc. Stochastic resetting occurs in two ways either global or local. Much of the literature has already been vigorously explored under the global aspect - where resetting is either applied to a single degree of freedom or it is simultaneously applied to multiple degrees of freedom [49, 48, 74, 10]. Local resetting where particles can reset their position independently of one another is more challenging than the global resetting considered, where the whole system is simultaneously reset to some reference state. The local resetting was first introduced and investigated in a symmetric simple exclusion process with periodic boundary conditions [92, 106]. The analysis was then extended to the TASEP with periodic boundary conditions, showing that the intermediate resetting regime arises for the resetting rate of the order inverse lattice length [92, 106]. A similar situation is observed in the TASEP-LK model, where the attachment-detachment rates of particles are re-scaled in the order of the inverse lattice length to observe the competition between boundary and bulk dynamics. This highlights a crucial connection between the resetting process and the LK dynamics, demonstrating how the resetting process is a unique instance of the LK process in which only the detachment process is present (from the bulk of the system) [92, 106].

Many TASEP models and their extensions are based on the assumption that the system is connected to an infinite reservoir [37], despite the fact that many physical systems in nature, such as ribosomes in a cell for protein synthesis, vehicles in the context of traffic, pedes-

trian traffic or filament length kinetics, all these compete for resources in a pool of limited availability [18, 29, 56]. In order to take into account the impact of restricted availability of resources, studies have lately been expanded by linking a finite reservoir (or pool) to the open TASEP [1, 57, 33, 32, 22, 54]. In contrast to the open TASEP connected to an infinite reservoir, the particles remain conserved in the system with a finite pool and the system exhibits a novel feature such as the transition line separating the low-density and high-density phases is expanded to a region where a localized domain wall is formed [66, 137, 138].

While much of the literature has focused on TASEP models with stochastic resetting, either in open boundary conditions or with periodic boundary conditions, most real-life systems, as discussed above, only compete in a finite pool of resources. Our interest here is to review work along this line of investigation by considering a TASEP with local resetting at the injection node under the availability of limited resources. The stationary state features will be studied theoretically using mean-field approximations and validated using Monte Carlo simulations. Our focus is to explore the consequences of the interplay between local resetting and the filling factor in the presence of finite resources and understand the stationary state behavior of the TASEP–LR in the thermodynamic limit.

In a manner similar to the original TASEP model, which serves as a model for simulating the movement of mRNA and ribosomes during protein synthesis [88], or the TASEP–LK model, which includes both attachment and detachment processes, thought to be a fundamental illustration of molecular motor dynamics on microtubules for intracellular transport processes [103]. As a result, our LR-inclusive model might be used as a mechanism for ribosome rescue and recycling or to address premature translation termination brought on by ribosome detachment prior to reaching the stop codon (drop-off phenomenon) [21, 50]. The resetting node represents the mRNA site where ribosomes bind to start the translation.

4.2 Model description

We consider a one-dimensional discrete lattice with L sites in which particles diffuse on the lattice as well as locally reset following the Markovian stochastic rules, (see FIG. 4.1).

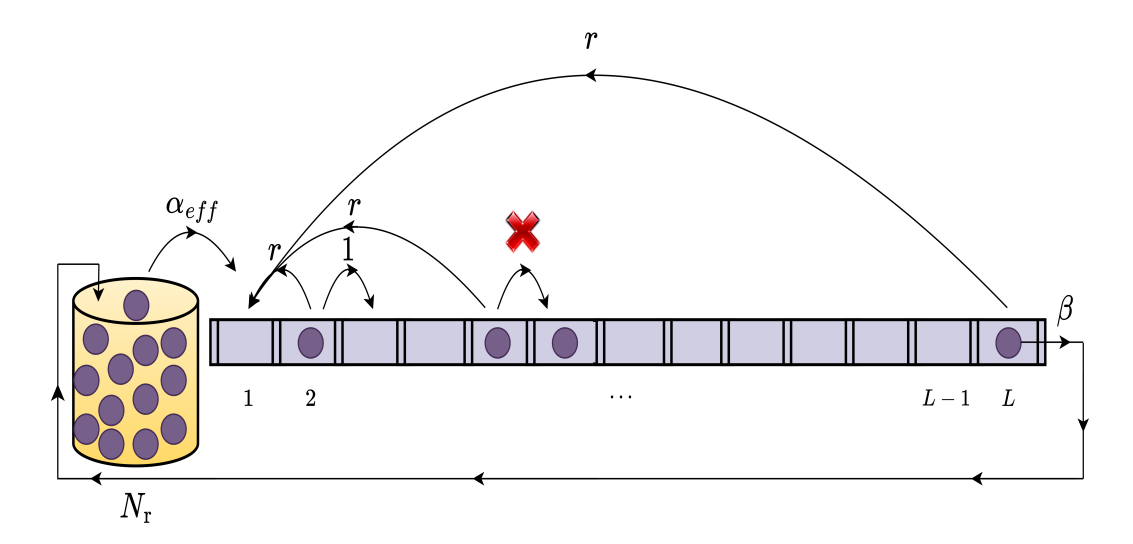


Figure 4.1: Schematic diagram of the TASEP with local resetting at the entry site. The rate of each process is represented by a matching symbol, and it is believed that lattice sites are arranged from left to right. If the arrival site is unoccupied, the hopping process has a unit rate; otherwise, it is prohibited (zero rate).

The lattice sites are labeled as i = 1, 2, ..., L, where i = 1(L) represents the entry(exit), and the remaining sites (i = 2, ..., L - 1) are referred to as the bulk of the lattice. The open boundaries of the lattice are connected to a finite reservoir of particles from which the particles enter the lattice through the first site and rejoin the reservoir back through its last site. The particles on the lattice hop uni-directionally from left to right and the resetting phenomena of particles occur at the entry site only. Each lattice site adheres to the hardcore exclusion principle and follows the restriction that only one particle can occupy a lattice site. The proposed model can also be viewed as a periodic TASEP model having a special site that violates the exclusion principle.

The following describes the particle dynamics and the corresponding rates that take place at the entry, bulk, and exit lattice sites: If the entry site is occupied, then the particle hops to the site on the right with a unit rate, provided it is vacant. For an unoccupied entry site, a particle from the reservoir enters the first site with a rate $\alpha_{\rm eff}$. For an occupied bulk and exit site, the particle initially tries to reset itself with a rate r from this lattice site to the entry site, provided the entry site is vacant. Otherwise, the bulk particle will attempt to hop to its adjacent empty site on the right with a unit rate or if the particle is at the last site, then

it returns to the reservoir with a rate β .

The proposed model is motivated by the dynamical aspects of the so-called drop-off phenomenon, which is the premature cessation of the translation process as a result of stalled ribosomes along with their rescue and recycling [88, 21, 50]. But from the theoretical point of view, our study is general and it may serve as a basis for more detailed investigations along the lines [21, 30]. The model described in FIG. 4.1 can non-trivially be linked to the TASEP-LK model for some entry rate α_{eff} , exit rate β , attachment rate $w_A = 0$ and detachment rate $w_D = r(1 - \rho_1)$. Furthermore, in the proposed model, the reservoir can additionally be considered a unique lattice site connected to both ends of the lattice. Furthermore, the relation $\alpha_{\rm eff} = \alpha g(N_{\rm r})$ is used to establish the effective entry rate, or $\alpha_{\rm eff}$, which is based on the number of particles in the reservoir (N_r) . The system dynamics and the inflow rate of particles that is proportional to the number of particles in the reservoir are determined by the choice of g [1]. As a result, g can be thought of as a monotonically growing function, defined as $g(N_{\rm r}) = \frac{N_{\rm r}}{N_{tot}}$ where N_{tot} denotes the total number of particles in the system (lattice and reservoir combined). In order to investigate the impact of the total population of the particles relative to the size L of the lattice on the system dynamics, we utilize the notion of filling factor, which is defined as $\mu = \frac{N_{tot}}{L}$ [57]. It describes the average number of particles available for each lattice site and it lies in the range $[0,\infty)$. The limiting situation, $\mu \to \infty$, corresponds to the case of an infinite reservoir where the entry rate becomes a constant, i.e., $\alpha_{\rm eff} = \alpha$.

4.3 Theoretical analysis under mean-field approximation

Let τ_i be the binary random variable that specifies the occupational number for the i^{th} lattice site since the lattice meets the exclusion requirement. The random variable τ_i takes the value 0 or 1 depending on whether the site is occupied or unoccupied. The following master equation describes the evolution of the average site occupancy number in the bulk of the lattice $(2 \le i \le L - 1)$:

$$\frac{d\langle \tau_i \rangle}{dt} = \langle \tau_{i-1}(1 - \tau_i) \rangle - \langle \tau_i(1 - \tau_{i+1}) \rangle - r\langle (1 - \tau_1)\tau_i \rangle. \tag{4.1}$$

theory. Table 4.1: Expressions for the existence conditions of the density phases in the lattice with finite resources through mean-field

MC-HD	LD-HD	MC	HD	LD	Density Phase
$oldsymbol{lpha}_{ ext{eff}} < rac{eta(1-eta)}{-rac{1}{R}\left(1-2eta-\ln(2-2eta) ight)},$	$lpha_{ m eff} > rac{eta(1-eta)}{1-rac{1}{(R-2)}W_0igg((R-2)eta\exp(R-2eta)igg)},$	$lpha_{ m eff} > -W_0igg(-\expigg(-(1+rac{R}{2})igg)igg)igg(1+rac{1}{2}W_0igg(-\expigg(-(1+rac{R}{2})igg)igg)igg)igg),$	$m{lpha_{ m eff}} > rac{m{eta(1-eta)}}{-rac{1}{(R+2)}W_{-1}igg((-R-2)(1-m{eta})\exp(2m{eta}-2)igg)},$	$lpha_{ m eff} < -W_0igg(-\expigg(-(1+rac{R}{2})igg)igg)igg(1+rac{1}{2}W_0igg(-\expigg(-(1+rac{R}{2})igg)igg)igg)igg),$	
$oldsymbol{lpha}_{ ext{eff}} > rac{eta(1-eta)}{rac{1}{R}\left(2eta-1-\ln(2eta) ight)}.$	$lpha_{ m eff} < rac{eta(1-eta)}{-rac{1}{(R+2)}W_{-1}igg((-R-2)(1-eta)\exp(2eta-2)igg)}.$	$oldsymbol{lpha}_{ ext{eff}} < rac{eta(1-eta)}{rac{1}{R}\left(2eta-1-\ln(2eta) ight)}.$	$m{lpha_{ m eff}} > rac{eta(1-eta)}{-rac{1}{R}\left(1-2eta-\ln(2-2eta) ight)}.$	$oldsymbol{lpha_{ ext{eff}}} < rac{eta(1-eta)}{1-rac{1}{(R-2)}W_0igg((R-2)eta\exp(R-2eta)igg)}.$	Phase Region

The first two terms in the above equation represent the gain and loss current due to particle hopping whereas the third term also represents a loss term due to the resetting process of the particle in the bulk. The average site occupancy number changes at the lattice boundaries in accordance with the following equations:

$$\frac{d\langle \tau_1 \rangle}{dt} = \alpha_{\text{eff}} \langle (1 - \tau_1) \rangle - \langle \tau_1 (1 - \tau_2) \rangle + r \langle (1 - \tau_1) \sum_{i=2}^{L} \tau_i \rangle, \tag{4.2}$$

$$\frac{d\langle \tau_L \rangle}{dt} = \langle \tau_{L-1}(1 - \tau_L) \rangle - \beta \langle \tau_L \rangle - r \langle (1 - \tau_1) \tau_L \rangle, \tag{4.3}$$

Due to the existence of one- and two-point correlators, the aforementioned system of equations cannot be directly solved. Therefore, we utilize the mean-field approximation, which ignores any potential correlations inherent in the aforementioned set of equations, i.e. $\langle \tau_i \tau_j \rangle = \langle \tau_i \rangle \langle \tau_j \rangle$.

Now, to understand the behavior in the bulk of the system in its continuum limit (or thermodynamic limit), we coarse grain the lattice by introducing a quasi-continuous position variable $x = \frac{i}{L} \in [0, 1]$, the lattice constant as $\varepsilon = \frac{1}{L}$ and a re-scaled time $t' = \frac{t}{L}$.

Replacing the binary discrete variable τ_i with a continuous local average density at i^{th} site as $\rho_i = \langle \tau_i \rangle \in [0,1]$ and retaining the terms up to the first order of ε in the Taylor series expansion of $\rho(x \pm \varepsilon)$ and substituting it in the density evolution Eq. (4.1) for the bulk. Further, we drop the subscript i due to the spatial homogeneity on the lattice to reform Eq. (4.1) into,

$$\frac{\partial \rho}{\partial t'} + \frac{\partial J}{\partial x} = -\lambda \rho, \tag{4.4}$$

where $\lambda = R(1-\rho_1)$, R = rL is the modified resetting rate and $J = \left(-\frac{\varepsilon}{2}\frac{\partial\rho}{\partial x} + \rho(1-\rho)\right)$ denotes the average particle current in the bulk of the lattice for a finite ε whereas in the thermodynamic limit ($\varepsilon \to 0^+$), it becomes $J = \rho(1-\rho)$. The following can explain the necessity of introducing a modified resetting rate: the struggle between bulk and boundary dynamics in large systems will only be evident if particles get enough time to spend on the lattice before resetting themselves to the first site, therefore, a macroscopic resetting rate R is

introduced, which remains constant for $L \to \infty$. The macroscopic resetting rate R is a crucial variable whose behavior in the thermodynamic limit $L \to \infty$ establishes the importance of the resetting process in comparison to conventional TASEP.

On similar grounds, the master equation for boundary conditions is reformed into,

$$\frac{d\rho_1}{dt} = \alpha_{\text{eff}}(1 - \rho_1) + r(1 - \rho_1) \sum_{i=2}^{L} \rho_i - \rho_1(1 - \rho_2), \tag{4.5}$$

$$\frac{d\rho_L}{dt} = \rho_{L-1}(1 - \rho_L) - \beta \rho_L - r(1 - \rho_1)\rho_L, \tag{4.6}$$

In the following, we shall drop the time index to focus on the stationary state of the differential eq. (4.4) and obtain:

$$\frac{\partial J}{\partial x} = -\lambda \rho. \tag{4.7}$$

Integration of the above equation w.r.t *x* yields:

$$\rho(x)\exp\left(-2\rho(x)\right) = \rho(x_0)\exp\left(-2\rho(x_0) - \lambda(x - x_0)\right),\tag{4.8}$$

where x_0 is some reference point that can assume the value 0 or 1 corresponding to the left and right boundary sites, respectively. The equation (4.8) has an explicit solution for particle density in terms of the Lambert-W function [34] given by:

$$\rho(x) = -\frac{1}{2}W\left(-2\rho(x_0)\exp\left(-2\rho(x_0) - \lambda(x - x_0)\right)\right). \tag{4.9}$$

The function W(x) is a multi-valued function that has two real branches $W_0(x)$ and $W_{-1}(x)$. The branch $W_0(x)$ is defined for $x \ge -1/e$ whereas $W_{-1}(x)$ is defined for $-1/e \le x \le 0$ and both the branches meet at x = -1/e. The branch $W_0(x)$ ($W_{-1}(x)$) is bound within the interval $[-1,\infty]$ ($[-\infty,-1]$) and corresponds to the $\rho(x) \le 1/2$ ($\rho(x) \ge 1/2$).

At stationary state, the density solution in an entry-dominated low-density phase is obtained by matching the boundary condition on the left end i.e. $\rho(x=0) = \rho_1$ and is written

as:

$$\rho_{LD}(x) = -\frac{1}{2}W_0 \left(-2\rho_1 \exp(-2\rho_1 - \lambda x)\right), \tag{4.10}$$

whereas the boundary condition on the right end i.e. $\rho(x=1) = 1 - \beta$ is utilized to obtain the density solution in an exit-dominated high-density phase and is given by:

$$\rho_{HD}(x) = -\frac{1}{2}W_{-1}\left(-2(1-\beta)\exp\left(-2(1-\beta) + \lambda(1-x)\right)\right). \tag{4.11}$$

Note that the density solution in the LD (HD) phase given by Eq. (4.10) (Eq. (4.11)) clearly satisfies the left (right) boundary condition as well as matches in the bulk. However, due to the presence of boundary layers, these expressions do not satisfy the right (left) boundary, respectively. The stationary state density solution in the maximal current phase is specified by the condition: $\rho(x=0) = \frac{1}{2}$ and is obtained as:

$$\rho_{MC}(x) = -\frac{1}{2}W_0 \left(-\exp(-1 - \lambda x)\right). \tag{4.12}$$

Till now, we have discussed the density profiles in one of the three following phases, namely, low-density (LD), high-density (HD), and maximal-current (MC) phases. Further, there may be the possibility of having the bulk density as the combination of the above-mentioned phases which can be obtained utilizing the current continuity principle and depending on how the combination of the above-obtained solutions is matched [103]. Taking into account the nature of phases, there are a total of twelve possible combinations of co-existing phases. However, the current-continuity principle restricts to only two possible co-existing phases: an LD-HD phase and an MC-HD phase both representing a localized shock in the lattice. Now, we analyze the aforementioned phases theoretically to obtain the density profiles and the existence conditions.

The density profile exhibiting the co-existence of the LD and HD phase is given by:

$$\rho_{LD-HD}(x) = \begin{cases} \rho_{LD}(x); & 0 \le x \le x_w, \\ \rho_{HD}(x); & x_w \le x \le 1. \end{cases}$$
(4.13)

whereas the density profile representing the co-existence of the MC and HD phase is given by:

$$\rho_{MC-HD}(x) = \begin{cases} \rho_{MC}(x); & 0 \le x \le x_w, \\ \rho_{HD}(x); & x_w \le x \le 1. \end{cases}$$
(4.14)

Here, the x_w corresponds to the position of the shock in the co-existence phases LD-HD phase and MC-HD phase. It can be obtained utilizing the fact that in both cases the density jumps from $\rho(x_w) < 1/2$ to $1 - \rho(x_w) > 1/2$ maintaining the current continuity. Hence, the domain-wall position x_w along with the density $\rho(x_w)$ can be obtained from conditions $\lim_{x \to x_w^-} \rho(x) = \rho(x_w)$ and $\lim_{x \to x_w^+} \rho(x) = 1 - \rho(x_w)$, which together can be reformed into the relation given as,

$$W_0 \left(-2\rho_1 \exp(-2\rho_1 - \lambda x_w) \right) - W_{-1} \left(-2(1-\beta) \exp\left(-2(1-\beta) + \lambda(1-x_w) \right) \right) = 2, \quad (4.15)$$

where the numerical value of ρ_1 clearly depends on the choice of the co-existing phase. The expression for the height of the shock is given as:

$$\Delta = \rho_{HD}(x_w) - \rho_{LD}(x_w). \tag{4.16}$$

The following set of equations is utilized to determine ρ_1 in each stationary phase:

$$\rho(0)\exp\left(-2\rho(0)\right) = \rho(1)\exp\left(-2\rho(1) - 1\right),\tag{4.17}$$

and

$$\alpha_{\text{eff}}(1-\rho_1) = \rho(1)(1-\rho(1)).$$
 (4.18)

The Eq. (4.17) is a direct implication from Eq. (4.8) whereas Eq.(4.18) follows from the current-continuity principle. The Table. 4.1 lists the phase boundaries computed using the extremal current principle as well as the boundary densities [80, 109]. The upcoming section

will explore the steady-state features like density profiles and phase diagrams of the lattice.

4.4 Existence of stationary phases & phase boundaries under the competition of finite resources

The assumption of finite resources in the reservoir only affects the entry rate of particles, whereas the exit rate of particles is independent of $N_{\rm r}$. It is assumed that the free particles in the reservoir are homogeneously distributed and not correlated within the reservoir. To determine the modified entry rate ($\alpha_{\rm eff}$), the conservation of the number of particles in the system is utilized, which in its continuum form states that $N_{tot} = N_{\rm r} + L \int_0^1 \rho(x) \ dx$. Since the dynamics pertaining to the reservoir significantly affect the system, we define $\rho_{\rm r} = \frac{N_{\rm r}}{L}$ to be the density of the reservoir and utilize particle number conservation to retrieve the following relationship:

$$\mu = \rho_{\rm r} + \int_0^1 \rho, \tag{4.19}$$

Considering the fact that the lattice can accommodate a maximum of L particles, the standard open-TASEP with local resetting (corresponding to infinite particles) is approached when $N_{tot} \gg L$. The interplay of the finite reservoir and resetting comes into play when the total number of particles in the system is of the order of $N_{tot} \sim L$ or smaller [54]. So far, we have deduced that there are five possible stationary phases that can exist in the phase diagram. Now, we utilize Eq. (4.19) with the results obtained in the previous section to derive the condition for the existence of the above-discussed stationary state phases in the presence of finite resources. Clearly, the explicit form of existence conditions is difficult to obtain for all the phases but the following implicit relation is ensured for the existence of a stationary phase:

$$\rho_{\rm r} = \mu - \int_0^1 \rho(x) dx \tag{4.20}$$

where $\rho(x)$ denotes the density profile to the corresponding stationary phase. In the next section, we will utilize the numerical methods to solve Eq. (4.4) along with Eqs. (4.5) and (4.6).

4.5 Simulations

In the previous section, we obtained the density profile and condition for the existence of phases in the implicit form using the Lambert-W function. In this section, firstly, we would like to provide a numerical scheme that can be used to solve the system of coarse-grained differential Eqs. (4.4), (4.5) and (4.6). Moreover, this scheme can also be utilized for the extended or generalized version of the proposed model. The differential equations (or continuum master equations) for which the numerical scheme is adopted are derived using the mean-field approximations; hence, we also utilize the Monte Carlo simulations to validate these approximations and compute the steady-state density profiles and the average current.

4.5.1 Direct simulation

We have obtained a generalized analytical formulation of the density profile at the stationary state (Eq. (4.9)). Now, we provide an alternative method to obtain the numerical solution to the second-order continuum mean-field equation (Eq. (4.4)). An important aspect of providing the numerical scheme is that the computation of the stationary state reservoir density ρ_R utilizing the system of Eq. (4.20) and Eq. (4.2) make the problem complex as the Eq.(4.2) itself is dependent on the local densities of all other sites. The time derivative is retained in the system and the density solutions at a steady state are procured in the limit $t \to \infty$. In this numerical solution, the geometric domain is discretized into grid points of the form $(i\Delta x, n\Delta t')$, where $\Delta x = 1/L$ and $\Delta t'$ are the grid spacing corresponding to the spatial and temporal variables, respectively. Assuming ρ_i^n as the numerical approximation of the particle density at each grid point, we utilize the forward-in-time and central-in-space (FTCS) scheme to obtain the finite-difference equation corresponding to differential eq. (4.4) as:

$$\rho_{i}^{n+1} = \rho_{i}^{n} + \triangle t' \left(\frac{\varepsilon}{2} \left(\frac{\rho_{i+1}^{n} - 2\rho_{i}^{n} + \rho_{i-1}^{n}}{\triangle x^{2}} \right) + \left(\frac{\rho_{i+1}^{n} - \rho_{i-1}^{n}}{2\triangle x} \right) (2\rho_{i}^{n} - 1) - R(1 - \rho_{1})\rho_{i}^{n} \right). \tag{4.21}$$

Analogously, Eq. (4.2) and Eq. (4.3) are utilized to obtain the finite-difference equations at the left and right boundary, respectively as:

$$\rho_{1}^{n+1} = \rho_{1}^{n} + L \triangle t' \left(\alpha (1 - \rho_{1}^{n}) \rho_{1}^{n} (1 - \rho_{2}^{n}) + r (1 - \rho_{1}^{n}) \sum_{i=2}^{L} \rho_{i}^{n} - \rho_{1}^{n} (1 - \rho_{2}^{n}) \right), \quad (4.22)$$

and

$$\rho_{L}^{n+1} = \rho_{L}^{n} + L \triangle t' \left(\rho_{L-1}^{n} (1 - \rho_{L}^{n}) - \beta \rho_{L}^{n} \right). \tag{4.23}$$

The above system of explicit finite difference scheme will be stable against small amplitude perturbations for $\triangle t'/\triangle x^2 \le 1$.

4.5.2 Monte Carlo simulations

As the implicit density profile computed in section 4.3, 4.4, and the density obtained via direct simulation utilizes mean field approximation. To validate them, we perform Monte Carlo simulations using a Gillespie algorithm with a random sequential update rule [55]. Each step of the algorithm consists of choosing an event in accordance with the dynamical rules as defined in Sec. 4.2. An event (a particle attempts to hop or resets to the first site) is selected with a probability proportional to the rates. Accordingly, the time increments are chosen from exponentially distributed random numbers. The lattice length is taken to be L = 500 and the simulations are run for 10^8 time steps. To facilitate the onset of a steady state, we ignore the first 5% of time steps and the average particle density is calculated for an interval of 10L. The results wherever obtained from Monte Carlo simulations are denoted by markers.

4.6 Results & discussion

In the following section, we investigate the influence of the filling factor & the resetting rate on the phase diagrams which will further be utilized to scrutinize their impact on the stationary properties of the system.

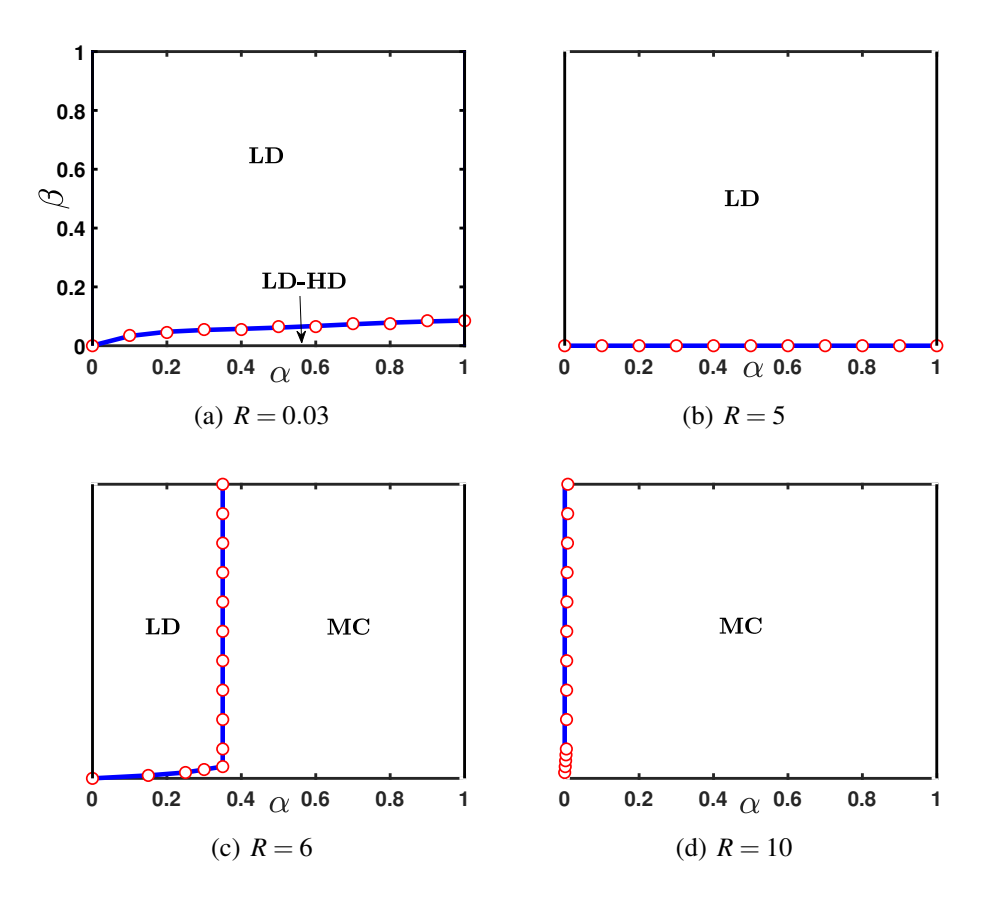


Figure 4.2: Stationary state phase diagrams for $\mu=0.1$ and different values of R. The markers are results from Monte Carlo simulations (MCS) and the solid lines are results from a continuum mean-field (CMF) approximation. The transition from LD to the LD-HD phase is discontinuous, resulting in a first-order transition. The transition from LD to the MC phase displays a continuous transition and hence is a second-order phase transition.

4.6.1 Phase diagram: Role of Filling factor & Resetting rate

We derive the phase diagrams in the α - $\beta \in [0,1] \times [0,1]$ parameter space using the results discussed in the previous sections to study the role of the total number of particles and the macroscopic resetting rate on the stationary properties of the system. The resetting dynamics in the bulk and the boundary-induced non-equilibrium dynamics mutually interact and, eventually, produce collective effects if the particles stay long enough on the lattice before resetting to the first site. Hence, it is expected that R plays a crucial role in the topology of the phase diagram. On the other hand, the filling factor μ represents the average number of particles available for each lattice site, and due to the global constraint on the

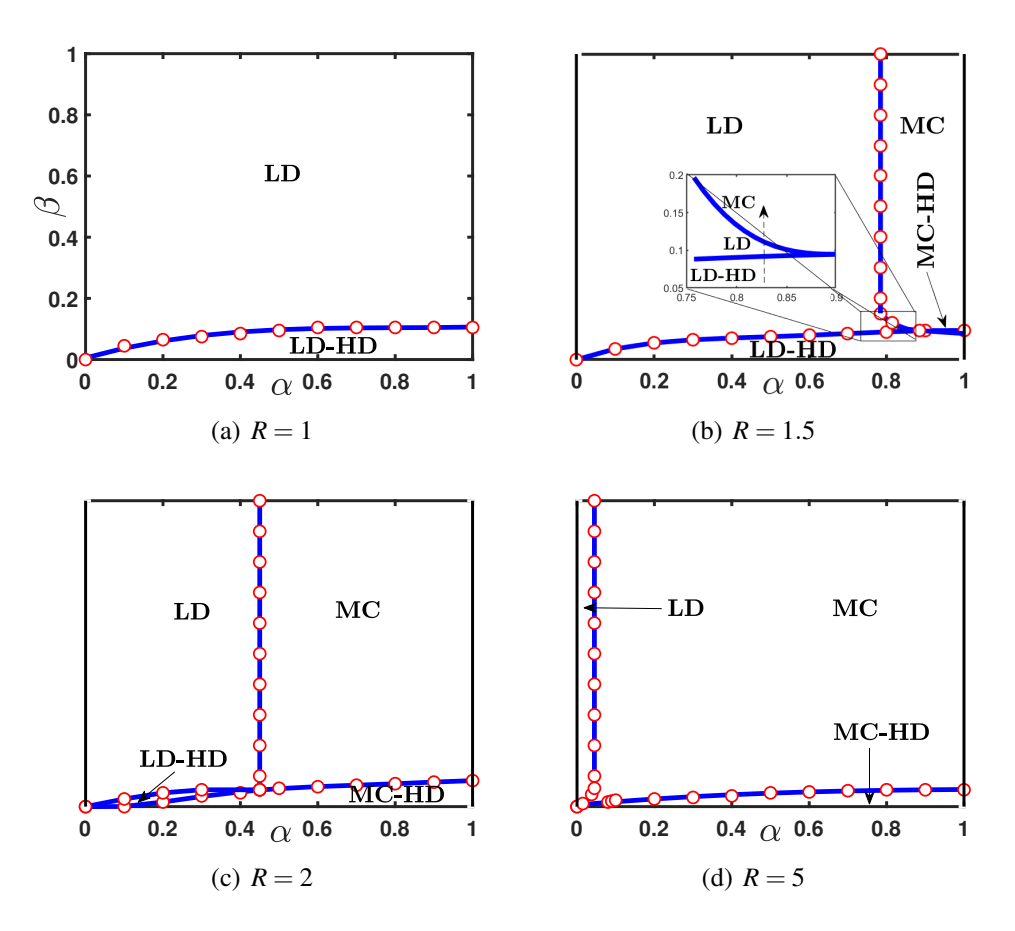


Figure 4.3: Stationary state phase diagrams for $\mu=0.3$ and different values of R. The markers are results from Monte Carlo simulations (MCS) and the solid lines are results from a continuum mean-field (CMF) approximation. The transition from MC to the MC-HD phase is discontinuous, whereas in (c), the transition from LD-HD to the MC-HD phase displays a continuous transition.

number of particles imposed by μ , it is expected that μ will also significantly affect the composition of the phase diagram. As a result, we chose to construct the phase diagrams for different values of μ and R. The phase diagrams are constructed corresponding to those values of R, which shows a reasonable amount of change in the topology of the phase diagrams.

For a smaller value of μ i.e. $\mu = 0.1$, the FIG. 4.2 (a) illustrates the phase diagram for a smaller value of R consisting of two distinct phases, the LD and LD-HD phases. The LD phase dominates the phase plane, and an LD-HD phase only appears for the smaller values of β . This can be explained as follows: the system's scarcity of particles leads to

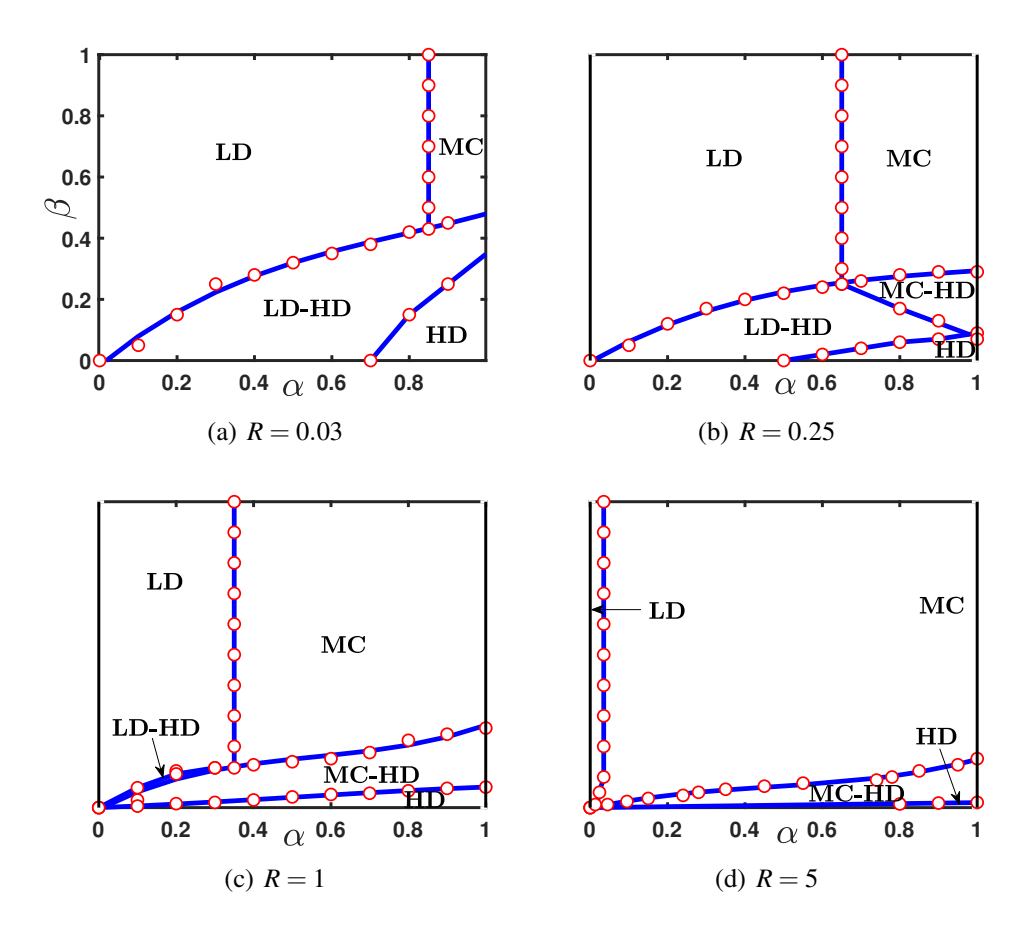


Figure 4.4: Stationary state phase diagrams for $\mu=1$ and different values of R. The markers are results from Monte Carlo simulations (MCS) and the solid lines are results from a continuum mean-field (CMF) approximation. The transition from LD-HD as well as the MC-HD phase to the HD phase is discontinuous.

a reduced effective entry rate. As a result, the phase plane majorly exhibits an LD phase. But for smaller values of β , the exit of the particle is hindered, causing a boundary layer that enters the lattice in the form of a stationary shock. It is also evident that as the value of R increases in the range (0,5), it causes the boundary layer to exit the bulk of the lattice. This, in turn, leads to a shrinkage in the LD-HD phase and an expansion in the LD phase. For R = 5, the LD-HD phase completely vanishes and the LD phase covers the whole space in the phase diagram. For R > 5, the resetting phenomena cause the MC phase to begin appearing in the phase diagram. These findings are in contrast with the conventional TASEP (without resetting) in the presence of finite resources. The further increase in the value of R observes no significant topological changes in the phase plane except for the shift in the

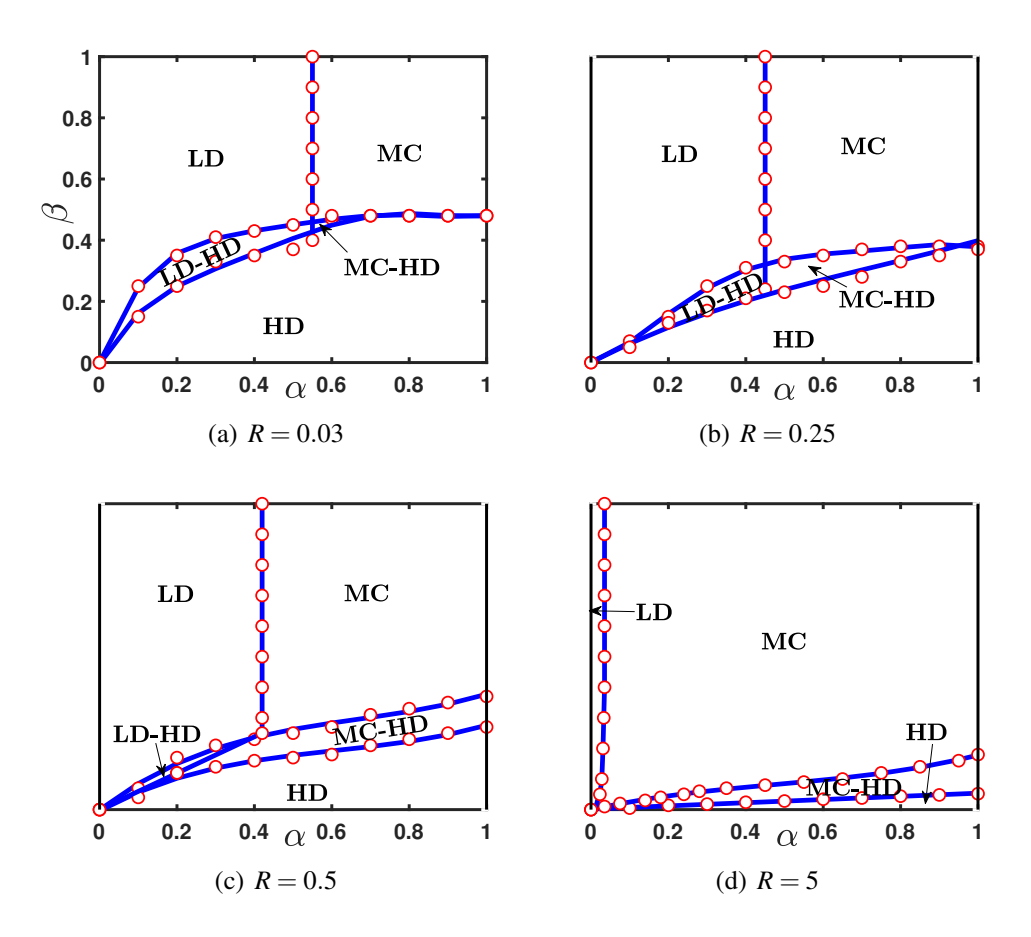


Figure 4.5: Stationary state phase diagrams for $\mu = 10$ and different value of R. The markers are results from Monte Carlo simulations (MCS) and the solid lines are results from continuum mean-field (CMF) approximation.

phase boundary due to the expansion of the MC phase and the shrinkage of the LD phase. For larger values of *R*, the phase plane is majorly dominated by the MC phase.

For a relatively larger value of μ i.e., $\mu = 0.3$, the phase diagram for $R \in [0,1]$ behaves similarly corresponding to the smaller value of μ as shown in FIG. 4.3 (a). As R increases from 1, two more phases, namely MC and MC-HD also join the phase diagram for larger values of α , see FIG. 4.3 (b). Contrary to the case $R \in [0,1]$, the LD phase shrinks for R > 1, whereas the MC phase and MC-HD phase expand, see FIG. 4.3 (c). As R increases, the MC phase continues to expand, whereas the rest of the three phases (the LD phase, LD-HD phase, and MC-HD phase) shrink, and finally, for R = 5, the LD-HD phase completely vanishes from the phase diagram leaving behind four stationary phases: LD, MC, and MC-

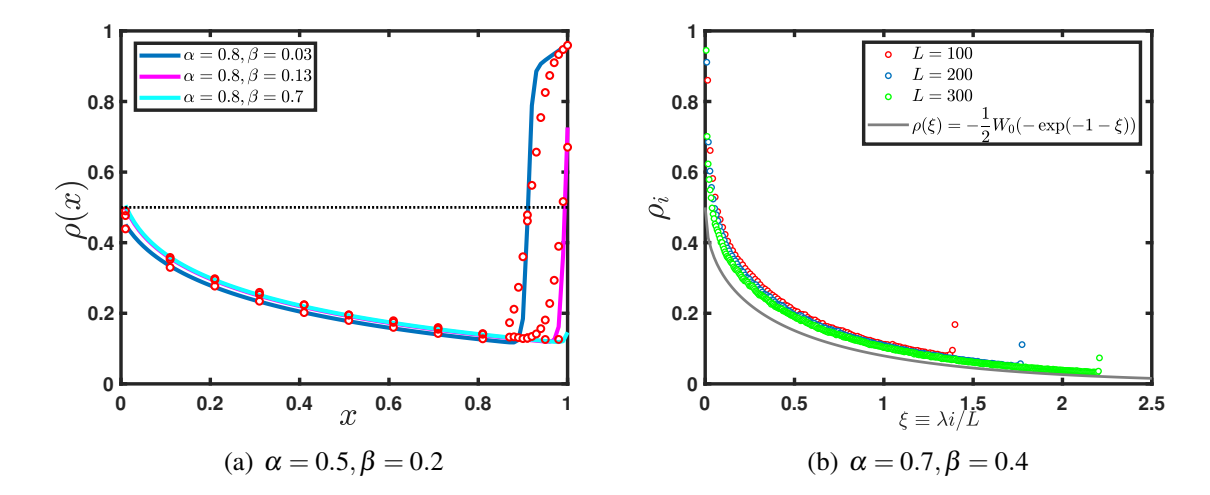


Figure 4.6: (a) Transition of the stationary state density profile from the LD-HD phase to the LD phase and thereafter to the MC phase for $\mu=0.3$, R=1.5. The black dotted line is marked to show $\rho=0.5$. (b) Stationary density profile as a function of the scaled position variable $\xi\equiv\lambda i/L$, in the large resetting regime: r=R/L=0.1 and $\mu=1$. The solid lines denote the mean-field continuum profile and the markers denote Monte Carlo results.

HD phases. The further increase in the value of R causes further expansion of the MC phase, whereas both the LD phase and the MC-HD phase continue to shrink. Moreover, in contrast to the phase diagram of TASEP-LR corresponding to infinite resources [105], we also observe a transition in the stationary phase from the LD-HD phase to the LD phase and further to the MC phase in the phase diagram corresponding to $\mu = 0.3$ and R = 1.5, see FIG. 4.6 (a).

When the total number of particles in the system is the same as the number of lattice sites is considered i.e., $\mu=1$, the phase diagram for a smaller value of R becomes much richer as compared to the case $\mu<1$. Here, the MC phase appears for much smaller values of R in contrast to the case $\mu<1$. Moreover, a new stationary phase, namely, the HD phase also appears in the phase diagram for a very smaller value of R which was not observed earlier ($\mu<1$) for any value of R, see FIG. 4.4 (a). Increasing the value of R to 0.25 leads to the formation of an additional phase, MC-HD phase and as a result, the phase diagram exhibits all possible five stationary phases as shown in FIG. 4.4 (b). The subsequent rise in the value of R up to 1 causes contraction in the LD phase, LD-HD phase, and HD phase, whereas the MC phase and the MC-HD phase expand, see FIG. 4.4 (c). For larger values of R, the LD-

HD phase vanishes completely and the MC phase continues to expand whereas now MC-HD phase also contracts along with the LD and HD phases, see FIG. 4.4 (d). Finally, we discuss the impact of the resetting rate for the larger value of μ . For the sake of simplicity, we assumed $\mu = 10$ and observed that now even for a very small R, the phase diagram consists of all possible five stationary phases, see FIG. 4.5 (a). The effect of increasing R remains the same as discussed for previous cases, see FIG. 4.5 (b), 4.5 (c), and 4.5 (d).

As a result, after carefully examining the phase diagrams for different values of μ and R, we discuss the stationary state features in both the small and large resetting scenarios. In the small resetting regime, the resetting rate r vanishes faster than 1/L, which makes it simple to verify that the stationary state phase diagram trivially reduces to that of a conventional TASEP with finite resources. In the latter case (large resetting regime), the resetting dominates over the injection, extraction as well as hopping process, and the phase diagram is majorly occupied by the MC phase. To validate this, the FIG. 4.6 (b) illustrates a density profile in the large resetting regime corresponding to a specific parameter choice. It exhibits both finite-difference and Monte Carlo results of a stationary density profile for increasingly large and finite size L which is characterized by $\rho_1 \to 1$ and $\rho_L \to 0$. The numerical inspection suggests that the bulk density profile for $L \to \infty$ is similar to the MC phase. To support this statement, the analytically obtained stationary density profile for the MC phase in Eq. (4.12) is written as a function of a scaled position variable $\xi = \lambda i/L$. FIG. 4.6(b) clearly demonstrates that the analytically derived density profile for the MC phase closely agrees with the results from Monte Carlo simulations.

4.6.2 Influence of R and μ on stationary state density & current

In this section, we will scrutinize the impact of the resetting rate and filling factor on the stationary state density profiles and the current in the system. Initially, for a fixed choice of μ , we examine the significance of the resetting rate on the density, followed by an analysis of the exit, entry, and bulk current in the system, as shown in FIG 4.7 (a). The top and the bottom panels in FIG. 4.7 (a) illustrates the density profile and the current across the lattice, respectively, for a fixed μ and varying R. With an increase in R, the left end density of the

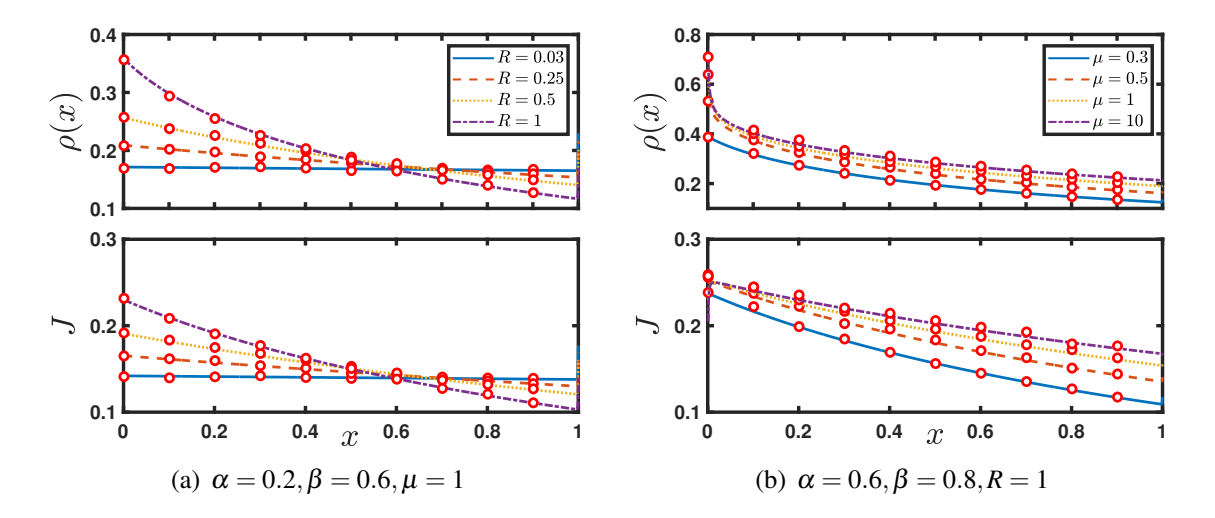


Figure 4.7: Stationary state density and current displaying (a) the effect of R, (b) the effect of μ . The markers represent outcomes obtained through Monte Carlo simulations (MCS), while the solid lines depict results derived from the continuum mean-field (CMF) approximation.

lattice increases while the right end density decreases. This can also be explained as follows: when the reset rate is high, the particles at the bulk or the exit site detach easily and attach to the first site leading to an increase in the density at the entry. The bulk density profile exhibits a non-monotonic behavior with respect to R. The density in the left part of the lattice increases, while the density in the right part decreases. From the bottom panel, it is evident that an increase in the resetting rate results in a decrease in the exit current, whereas the entry current increases. Conversely, the bulk current increases in the left segment of the lattice and decreases in the right segment with an increase in the resetting rate. The resetting rate induces similar effect on both the stationary state density and current due to a relationship between them.

Subsequently, we explore the effect of the filling factor for a fixed choice of the resetting rate on the density as well as current, as illustrated in FIG 4.7 (b). The effect of μ is shown on the density profile and the lattice current, respectively, in the top and bottom panels of FIG. 4.7 (b). Unlike the previous case, it is evident from the top panel that as μ increases, the density increases uniformly throughout the lattice. This can be argued as: with the increase in the filling factor, there is an increase in the average number of particles available for each

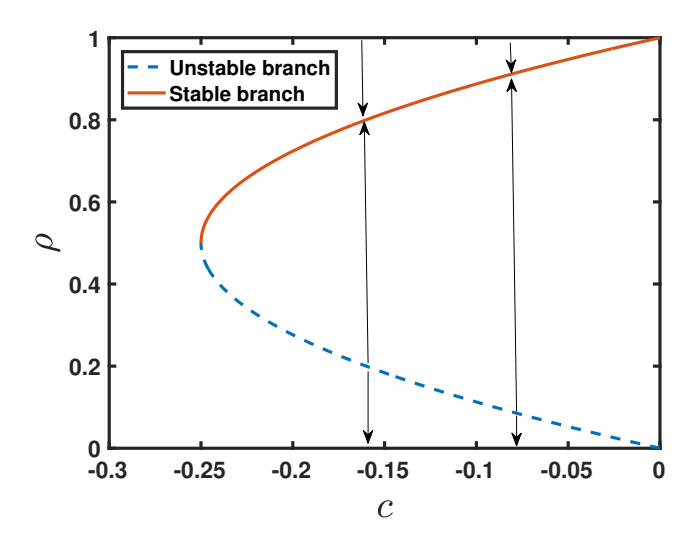


Figure 4.8: Fixed-point diagram.

site resulting in a uniform increase in the density of the lattice. It is also evident from the top panel of FIG. 4.7 (b) that the increase in the average densities is reasonable when μ increases from 0 to 1. For further increase in the μ , the sufficient particles enter the lattice resulting in the saturation of the density profile. Finally, it converges to the one corresponding to the resetting model for infinite resources as $\mu \to \infty$ [105]. The bottom panel reveals that all entry, bulk, and exit currents increase relative to the filling factor which is in accordance with the correlation between the current in the system and its densities.

4.6.3 Comparison of the proposed model with TASEP-LK with detachment only

Due to the local resetting of particles from all the bulk sites to the entry site, the proposed model can be thought of as a special TASEP–LK model with detachment–only [21]. Note that this relationship is not an exact one but holds only at the mean-field approximation. Now, we will swiftly discuss this connection. For low values of the detachment rate, the phase diagram in the ref. [21] also contains the same set of five stationary phases as we observed in the proposed model: LD, HD, MC, LD-HD, and MC-HD. As the detachment rate increases, there is a loss of particles from the bulk of the lattice leading to the expansion

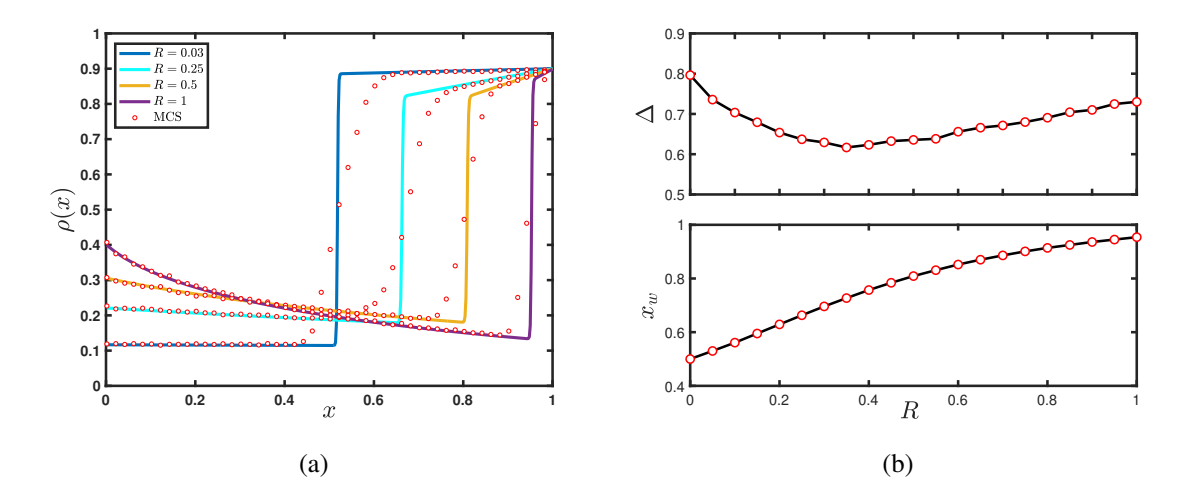


Figure 4.9: Effect of R on the (a) LD-HD shock profile and (b) its height and position for $\mu = 1$ and $\alpha = 0.2, \beta = 0.1$. The markers represent outcomes obtained through Monte Carlo simulations (MCS), while the solid lines depict results derived from the continuum mean-field (CMF) approximation.

of the LD and MC phase and the HD phase shrinks whereas the LD-HD phase and the MC-HD phase expand initially. As the detachment rate is increased to a certain threshold value, the phase diagram in ref.[21] stops exhibiting the HD phase whereas the LD-HD phase and MC-HD phase begin to contract beyond this value while the LD and the MC continue to expand. Lastly, for large values of the detachment rate, the phase diagram becomes equally occupied by both LD and MC phases about the transition line at $\alpha = 1/2$.

In contrast, the FIG. 4.5 of the proposed model for larger values of μ illustrates that the region containing LD-HD phase shrinks from the beginning itself along with the HD phase whereas only the MC-HD phase expands together with the growth of the MC phase as the resetting rate increases. It appears that the HD phase occurs for even high values of the resetting rate, in contrast to the scenario in ref. [21], albeit existing in a relatively tiny region. Additionally, for large values of the resetting rate, the particles free themselves from the bulk of the lattice to re-enter the lattice and making the effective entry rate larger. Therefore, only the MC phase dominates the phase diagram in the resetting model, however, the rest of the phases shrink.

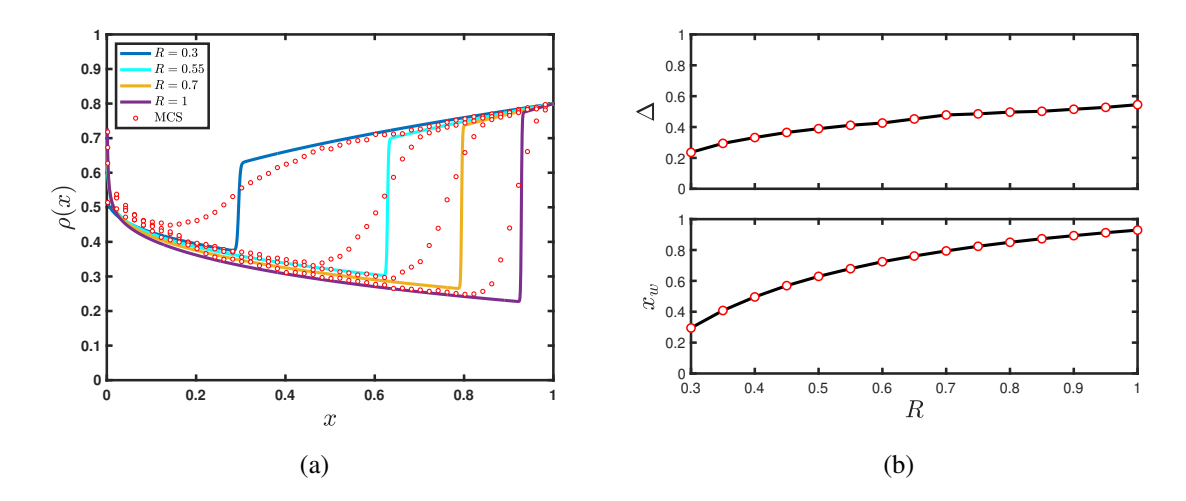


Figure 4.10: Effect of R on the (a) MC-HD shock profile and (b) its height and position for $\mu = 1$ and $\alpha = 0.9, \beta = 0.2$. The markers represent outcomes obtained through Monte Carlo simulations (MCS), while the solid lines depict results derived from the continuum mean-field (CMF) approximation.

4.6.4 Shock dynamics & Finite-size effect

Now, we discuss the features of the localized shock that appear either in the LD-HD phase or MC-HD phase where the position of the shock doesn't vary stochastically with respect to time. The stationary density profiles for the LD-HD (MC-HD) shock exhibit a low-density (maximal-current) profile on the left and a high-density profile on the right, separated by a domain wall or shock. Both these shocks are categorized as upward shocks since the density profile on the left end of the domain wall connects to a high density on the right end. Note that our system cannot possess any downward shock, which can be justified by utilizing fixed point theory [95]. Assuming the non-conserving terms to be zero, the integration of the Eq. 4.4 gives:

$$\frac{\varepsilon}{2} \frac{\partial \rho}{\partial x} - \rho (1 - \rho) = c, \tag{4.24}$$

where c is the integration constant. The FIG. 4.8 illustrates the two-dimensional fixed-point diagram in the $c - \rho$ plane that is obtained from the fixed points of the Eq. (4.24). It shows that no point on the upper (unstable) branch of this curve can be connected to a point in the lower (unstable) branch utilizing a vertical line.

The implicit expression for the stationary state density profile, the position and the height

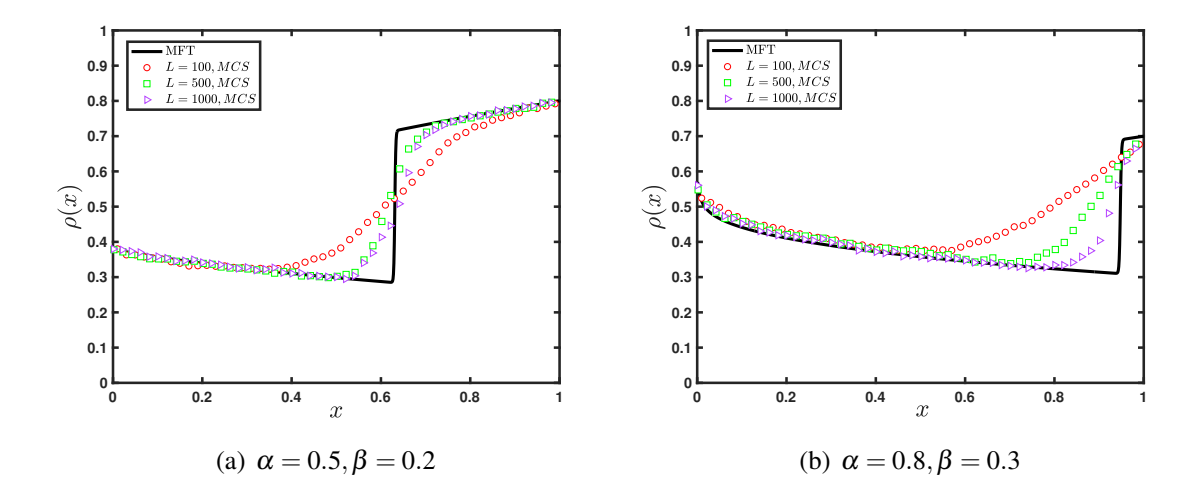


Figure 4.11: Finite size effect on (a) the LD-HD density profile as well as (b) the MC-HD density profile for $\mu=1$ and R=0.25. The markers represent outcomes obtained through Monte Carlo simulations (MCS), while the solid lines depict results derived from the continuum mean-field (CMF) approximation.

of the domain wall has been obtained in Sec. 4.3. Now, we study the impact of the resetting rate on the shock profiles starting with the LD-HD profile. The FIG. 4.9(a) shows that both the height and the position of the LD-HD shock profile change with respect to the resetting rate. The top panel of FIG. 4.9(b) shows the non-monotonic behavior of the height of the LD-HD shock with respect to the resetting rate. The shock height initially decreases up to some critical value of the resetting rate and increases afterward. However, the position of the LD-HD shock monotonically increases with the resetting rate (see bottom panel of FIG. 4.9(b)). Initially, the position of the domain wall increases linearly with R and saturates to 1 as the shock exits from the right end of the lattice. This finding can be validated by the phase diagram, where the transition of the LD-HD phase to the LD phase occurs with an increase in the resetting rate. The effect on the shock in the MC-HD phase with respect to the resetting rate is illustrated in FIG. 4.10(a). Clearly, both the height and the position of the shock change with respect to R. In the MC-HD phase, the position as well as the height of the shock show a monotonic increasing behavior with R before saturating, see FIG. 4.10(b).

Lastly, we examine the finite-size effect on the shock profiles. We have plotted the density profiles for a point in the LD-HD region as well as the MC-HD region with $\mu=1$

4.7 Conclusion

and for different values of L (see FIG. 4.11). As expected, the shock profile becomes sharper with increasing lattice size L, confirming the presence of finite-size effects in our system. However, these effects do not alter the stationary-state behavior reflected in the density profile.

4.7 Conclusion

Motivated by the biological process of mRNA translation where the resetting dynamics models the observed stochastic decay of mRNA-ribosome machinery, involve lanes whose dynamics depend on competition for a pool of limited particles. Hence, we made an effort to extensively investigate the characteristics of a single-channel TASEP with stochastic local resetting in a resource-constrained environment. In order to study the stationary state of a TASEP-LR where local resetting occurs at the entry node, we used the mean-field approximation to solve the master equations in the continuum limit and determine the explicit expression of the density profiles in terms of a Lambert-W function. The existence region of the stationary phases is obtained numerically using finite difference schemes. All these steady-state characteristics such as phase diagrams, and particle density accord very well with the Monte Carlo simulations in the thermodynamic limit.

The total number of particles remains constant in the system and is characterized by the filling factor. Another important factor is the macroscopic resetting rate, whose behavior in the thermodynamic limit $L \to \infty$ establishes the significance of the resetting process. While the filling factor intends to investigate the influence of the total number of particles on the system dynamics. We scrutinized the stationary properties of the system for different choices of the filling factor while scaling the resetting rate simultaneously. The phase diagram has the possibility of the following five stationary phases: the LD phase, the MC phase, the HD phase, the LD-HD phase, and the MC-HD phase depending upon the choice of the filling factor and resetting rate. In the large resetting regime, the phase diagram becomes completely dominated by the MC phase irrespective of the choice of the filling factor. In contrast to the standard TASEP with finite resources, the proposed model for smaller values

of the filling factor possesses an MC phase whereas the LD-HD phase vanishes completely in the intermediate as well as large resetting regime. However, as soon as the resetting rate vanishes, the phase diagram of the proposed model behaves likewise to the standard TASEP with finite resources. In contrast to the resetting model corresponding to infinite resources [105], we observe two new phase transitions which arguably induce a change in the topology of the phase diagram. The first phase transition has been observed for a smaller value of the filling factor and an intermediate choice of the resetting rate. It occurs in the following manner: LD-HD \rightarrow LD \rightarrow MC phase whereas the second phase transition is observed when the system has a number of particles equivalent to the lattice size with an intermediate resetting rate, it takes place as follows: HD \rightarrow LD-HD \rightarrow MC-HD \rightarrow MC phase. We also established a relationship with the TASEP–LK detachment-only model, where the stationary properties of both models have been compared at the mean-field level. Lastly, we investigated the role of the resetting rate on the shock dynamics and examined the finite size effect on their stationary state properties.

Now, we conclude the proposed theoretical work with its potential applications in the microscopic realm of biological systems where the conventional TASEP describes the ribosome dynamics. While the model is generic in nature, it holds versatile potential for applications in situations involving the attachment or detachment of particles. For instance, it has the capability to simulate the dynamic facets of phenomena such as the drop-off phenomenon. This refers to the premature halt of the translation process caused by stalled ribosomes, encompassing their subsequent rescue and recycling processes [103, 21, 50]. The work can be extended to incorporate more realistic features related to diverse physical and biological systems.



Local Resetting in a Bidirectional Transport System

Preamble

The model studied in the previous chapter investigates the local particle resetting in a single-species TASEP, we now extend our focus to a more complex and biologically relevant scenario. Intracellular transport often involves bidirectional movement, exemplified by kinesin and dynein motors traversing cytoskeletal filaments in opposite directions. Motivated by the significance of bidirectional particle transport, this chapter presents a generalized TASEP model incorporating stochastic local resetting for two distinct particle species. These particles are programmed to hop stochastically in opposite directions along a lattice. Our primary objective is to elucidate the intricate interplay between the local resetting phenomenon and bidirectional transport. To achieve this, we employ mean field theory to derive stationary phase diagrams and density profiles. This approach allows us to uncover the emergent behaviors that arise from the combination of bidirectional movement and local resetting, providing insight into more realistic intracellular transport scenarios.

5.1 Background

To simulate the behaviors observed in numerous real-life dynamical systems, which often experience interruptions and resume from specific points in phase space. This non-equilibrium phenomenon is known as stochastic resetting [47], in general, it takes place on a global or local scale. In global resetting, the entire system is reset simultaneously to a reference state, and its literature is well explored [49, 48, 74, 10]. In contrast, the challenges in the realm of local resetting are more formidable, where particles have the autonomy to reset their positions independently. The process of resetting finds numerous applications, and its incorporation with TASEP yields numerous non-trivial discoveries [93, 113, 114]. The dynamics of local resetting were initially integrated into a closed symmetric exclusion process [92, 106], and subsequently, the analysis was expanded to the closed TASEP model where an intermediate resetting regime appears as the resetting rate scales as the inverse of the system size. This emphasizes the idea that the resetting process can be conceptualized as a particular instance of the LK dynamics, where the particles attach with a zero rate and detach with some effective rate equivalent to the resetting rate [92, 106]. Lately, research has also explored the TASEP model with local resetting under resource constraints [17].

Many non-equilibrium transport processes, such as axonal transport in neurons, involve the motion of motor proteins along the microtubules in opposing directions, leading to bidirectional transport. Bidirectional flow is evident not only in natural systems but also in man-made systems. For instance, it can be observed in vehicular or pedestrian flow on a single-lane road where two-way traffic is permitted [28, 81]. Motivated by such scenarios, the TASEP has been extended from a single-species model to a multispecies analog [37, 4, 134, 7, 8, 23, 6]. In this configuration, two distinct species move in opposite directions along the lattice to encompass bidirectional transport. Each species engages with each other within the bulk of the lattice, exchanging positions when they come into contact. These models exhibit a symmetry-breaking phenomenon and phase separation [43, 77, 44, 108, 31, 111, 126]. The emergence of a symmetry-breaking phenomenon was first observed in the "bridge model" under analogous dynamical conditions [42]. Other studies on bidirectional transport support inconsistent outcomes regarding the presence of

5.2 Model definition 121

asymmetric low-density phases in a region between mean-field approaches and simulations in the thermodynamic limit [31, 5]. Nevertheless, the system with bidirectional transport showcases novel phenomena, yet our understanding of the mechanisms responsible for these phenomena is limited[43, 77, 44, 108, 31, 111, 126, 5].

In the present chapter, we consider a TASEP with two types of oppositely charged particles moving in the opposite direction, where local resetting of both particles occurs at the injection node. The effect of local resetting on bidirectional transport has not been investigated yet. The theoretical findings due to the interplay of non-equilibrium dynamics arising from bidirectional motion and particle resetting on the lattice are captured under the mean-field approach. It is interesting to scrutinize the qualitative and quantitative impact of the local resetting phenomenon on the stationary properties of the system, such as density profiles, phase diagrams, boundary densities, and symmetry breaking. The chapter is organized as follows: The model and the dynamical rules are defined in Section 5.6.2. In Section 5.6.3, theoretical analysis is outlined within the mean-field framework, followed by the examination and derivation of existence conditions for the stationary phases in Section 5.6.4. All the theoretical results validated by the Monte Carlo simulations are thoroughly discussed in Section 5.6 and we conclude with the closing remarks in Section 5.7.

5.2 Model definition

The model consists of a 1D discrete lattice of length L, accommodating two oppositely charged species of particles represented by "+" and "-" symbols. Each site in the lattice is labeled as $i=1,2,\ldots,L$. Site i=1 (and i=L) indicates the left (right) boundary of the lattice, while the remaining sites ($i=2,\ldots,L-1$) are termed the lattice bulk. Each species diffuses in opposite directions as well as being locally reset to its corresponding entry site following the stochastic rules, as shown in FIG. 5.1. Without loss of generality, the + (-) particles hop uni-directionally on the lattice from left (right) to right (left). The particles adhere to the hard-core exclusion principle, ensuring that a single site cannot be occupied by more than one particle. The + species of particles enter the lattice from the left end, while

the – species of particles are introduced from the right end. Both species of particles follow the uniformity in the dynamics and the corresponding rates, except for their direction. A + (-) particle enters the lattice through the first (last) site with entry rate α , whereas it exits from the last (first) site with rate β . Each species of particle hops in the bulk of the lattice at a unit rate. When two different species of particles encounter each other on the lattice, they swap their positions with a rate q. The resetting phenomenon occurs at all lattice sites. A positive or negative particle located at the bulk or their respective exit sites can reset itself to its corresponding entry site at a rate r, given that the arrival site is unoccupied.

The proposed study is inspired by the fact that many of the important biological transport processes are modeled as the movement of particles along an ordered chain of sites, such as mRNA translation, feature different mechanisms, such as the initiation process and the drop-off phenomena [21, 30]. However, from a theoretical standpoint, our investigation is comprehensive and may lay the groundwork for more in-depth research.

5.3 Theoretical analysis under mean-field framework

In this section, we will provide mathematical support to the process involved in the proposed model by analyzing and solving the master equations for the temporal evolution of the average particle density for each species at a stationary state. The occupancy of each species of particle at the i^{th} lattice site is represented by the binary random variables τ_i^+ and τ_i^- , respectively. These variables are assigned values 0 or 1, depending on either positive, negative or none species of particles occupying the i^{th} site; nevertheless, they simultaneously cannot assume 1, in accordance with the hard-core exclusion principle. The average occupancy density of each species on lattice sites i = 2, ..., L-1 (bulk) evolves according to the following kinetic master equations:

$$\frac{d\langle \tau_i^+ \rangle}{dt} = J_{i-1,i}^+ - J_{i,i+1}^+ - r\langle (1 - \tau_1^+ - \tau_1^-) \tau_i^+ \rangle, \qquad (5.1)$$

$$\frac{d\langle \tau_i^- \rangle}{dt} = J_{i+1,i}^- - J_{i,i-1}^- - r\langle (1 - \tau_L^+ - \tau_L^-) \tau_i^- \rangle. \qquad (5.2)$$

$$\frac{d\langle \tau_i^- \rangle}{dt} = J_{i+1,i}^- - J_{i,i-1}^- - r\langle (1 - \tau_L^+ - \tau_L^-) \tau_i^- \rangle. \tag{5.2}$$

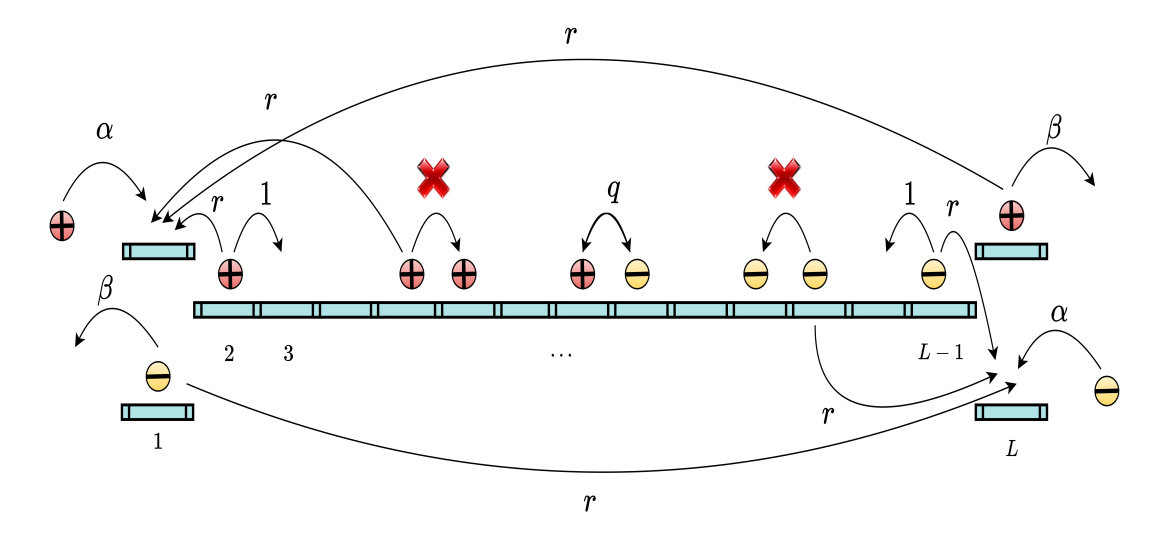


Figure 5.1: Schematic diagram illustrating the bidirectional transport with local resetting along a one-dimensional channel. The channel accommodates two oppositely directed species of particles: plus particles (in red) and minus particles (in yellow) move from left to right and vice versa, respectively. Allowed transitions are shown by arrows, and their corresponding rates are represented by a matching symbol. Entrance rates of both species of particles are equal to α if there is no particle at their corresponding entry site. Exit rates for both species are β . Each species undergoes hopping with a unit rate when the arrival site is unoccupied, or they swap positions at a rate of q when they encounter each other on adjacent sites.

where $\langle \cdots \rangle$ denotes the time average. The initial and second components in Eq. (5.1) (Eq. (5.2)) signify the current gain and loss resulting from the motion of the + (-) particle, while the third component signifies a loss attributed to the resetting current of the + (-) particle. The expressions for the current terms $J_{i,i+1}^+$ and $J_{i+1,i}^-$ are given as:

$$J_{i,i+1}^{+} = \langle \tau_i^{+} (1 - \tau_{i+1}^{+} - \tau_{i+1}^{-}) \rangle + q \langle \tau_i^{+} \tau_{i+1}^{-} \rangle, \tag{5.3}$$

$$J_{i+1,i}^{-} = \langle \tau_{i+1}^{-} (1 - \tau_i^{+} - \tau_i^{-}) \rangle + q \langle \tau_{i+1}^{+} \tau_i^{-} \rangle.$$
 (5.4)

In the equations above, the first component signifies the movement of one species of particle to an adjacent unoccupied site in a preferred direction, while the second component indicates their exchange when they come across each other. For q = 1, the two bulk current Eqs. (5.3) and (5.4) decouple, and here we examine this case.

At boundaries, the average site occupancy number for + and - particles evolves based

on subsequent equations:

$$\frac{d\langle \tau_1^+ \rangle}{dt} = J_{\text{entry}}^+ - J_{1,2}^+ + r\langle (1 - \tau_1^+ - \tau_1^-) \sum_{i=2}^L \tau_i^+ \rangle, \tag{5.5}$$

$$\frac{d\langle \tau_L^+ \rangle}{dt} = J_{L-1,L}^+ - J_{\text{exit}}^+ - r\langle (1 - \tau_1^+ - \tau_1^-) \tau_L^+ \rangle, \tag{5.6}$$

$$\frac{d\langle \tau_1^- \rangle}{dt} = J_{2,1}^- - J_{\text{exit}}^- - r\langle (1 - \tau_L^+ - \tau_L^-) \tau_1^- \rangle, \tag{5.7}$$

$$\frac{d\langle \tau_L^- \rangle}{dt} = J_{\text{entry}}^- - J_{L,L-1}^- + r\langle (1 - \tau_L^+ - \tau_L^-) \sum_{i=2}^L \tau_i^- \rangle.$$
 (5.8)

(5.9)

where,

$$J_{\text{entry}}^{+} = \alpha \langle (1 - \tau_1^{+} - \tau_1^{-}) \rangle, J_{\text{exit}}^{+} = \beta \langle \tau_L^{+} \rangle, \tag{5.10}$$

$$J_{\text{entry}}^{-} = \alpha \langle (1 - \tau_L^{+} - \tau_L^{-}) \rangle, J_{\text{exit}}^{-} = \beta \langle \tau_1^{-} \rangle.$$
 (5.11)

To solve the above system of equations in the presence of one- and two-point correlators, we resort to the simplest approach, referred to as the mean-field approximation. It neglects all spatial correlations among particles and factorizes the relevant correlation function as the product of their averages:

$$\langle \tau_i^+ \tau_j^+ \rangle = \langle \tau_i^+ \rangle \langle \tau_j^+ \rangle, \quad \langle \tau_i^- \tau_j^- \rangle = \langle \tau_i^- \rangle \langle \tau_j^- \rangle.$$
 (5.12)

To determine the model's continuum limit, we approximate the difference equations using a continuum approach by establishing a quasi-continuous position variable $x=\frac{i}{L}\in[0,1]$, the lattice constant $\varepsilon=\frac{1}{L}$, and a re-scaled time $t'=\frac{t}{L}$. Further, the binary discrete variables τ_i^+ and τ_i^- are replaced with a continuous local average density at i^{th} site, that is, $\rho_i^\pm=\langle\tau_i^\pm\rangle\in[0,1]$. Now, retain the terms up to the first order of ε in the Taylor series expansion of $\rho^\pm(x\pm\varepsilon)$ and substitute it in the density evolution Eq. (5.1) and Eq. (5.2) for the bulk. Moreover, taking into account the lattice's structural homogeneity, the subscript i is dropped,

and the equations are turned into,

$$\frac{\partial}{\partial t'} \begin{pmatrix} \rho^+ \\ \rho^- \end{pmatrix} + \frac{\partial}{\partial x} \begin{pmatrix} J^+ \\ J^- \end{pmatrix} = \begin{pmatrix} -\lambda_1 \rho^+ \\ -\lambda_L \rho^- \end{pmatrix}, \tag{5.13}$$

where $J^{\pm}=\rho^{\pm}(1-\rho^{\pm})$ denotes the average particle current corresponding to each species in the bulk of the lattice, $\lambda_k=R\left(1-\rho_k^+-\rho_k^-\right)$, where k=1,L. We define R=rL as the macroscopic resetting rate that remains constant as $L\to\infty$. As our interest lies in large system sizes, the interplay between bulk and boundary dynamics becomes evident only if particles spend sufficient time interacting before getting reset. The behavior of the macroscopic resetting rate R in the thermodynamic limit $L\to\infty$ is a crucial factor in understanding why stochastic resetting is important compared to the dynamics of conventional TASEP.

On similar grounds, the expression for boundary currents is reformed into,

$$J_{\text{entry}}^{+} = \alpha (1 - \rho_{1}^{+} - \rho_{1}^{-}), J_{\text{exit}}^{+} = \beta \rho_{L}^{+}, \tag{5.14}$$

$$J_{\text{entry}}^{-} = \alpha (1 - \rho_L^{+} - \tau_L^{-}), J_{\text{exit}}^{-} = \beta \rho_1^{-}.$$
 (5.15)

Clearly, the expression of J^{\pm} shows that the currents of the two species are uncoupled in the bulk, whereas the boundary currents corresponding to distinct species are coupled via Eq. (5.15). This can be explained intuitively in the following manner: there is an effective interaction between these two species of particles at the boundaries where they obstruct each other's entry, whereas away from the boundaries, a positive particle does not distinguish between a hole and a negative particle, or vice versa. Therefore, based on the current continuity in the bulk and the boundaries of the lattice, the effective entry rates for both species can be calculated as follows:

$$\alpha^{+} = \frac{J^{+}}{\frac{J^{+}}{\alpha} + \frac{J^{-}}{\beta}}, \quad \alpha^{-} = \frac{J^{-}}{\frac{J^{-}}{\alpha} + \frac{J^{+}}{\beta}}.$$
 (5.16)

Now, we employ Eqs. (5.13), (5.14), (5.15), along with (5.16) to ascertain the steady-state characteristics of each species. We use their respective densities and currents to deduce

their effective entry rates (α^{\pm}) from the expressions obtained above. These explicitly obtained expressions for the effective rates will help to quantify the stationary properties of the system, such as phase diagrams, density profiles, particle currents, and possible phase transitions. Furthermore, considering the aforementioned effective entry rates, one can conceptualize the proposed model as two distinct TASEP models with local resetting, interconnected solely at the boundaries, with each model accommodating only one species of particle. The stationary state density solution corresponding to each species can be obtained by dropping the time index in differential eq. (5.13) and solving the following obtained equation:

$$\frac{\partial J^{\pm}}{\partial x} = -\lambda_k \rho^{\pm}. \tag{5.17}$$

The k is assigned values 1 and L corresponding to + and - species of particles, respectively. Integrating the above equation with respect to x from some reference point x_0 results in:

$$\rho^{\pm}(x) \exp\left(-2\rho^{\pm}(x)\right) = \rho^{\pm}(x_0) \exp\left(-2\rho^{\pm}(x_0) - \lambda_k(x - x_0)\right). \tag{5.18}$$

The (5.18) can further be reformed to write an explicit expression of density for each species in terms of the Lambert-W function, as [34]:

$$\rho^{\pm}(x) = -\frac{1}{2}W\left(-2\rho^{\pm}(x_0)\exp\left(-2\rho^{\pm}(x_0) - \lambda_k(x - x_0)\right)\right). \tag{5.19}$$

Now, we briefly examine the various real branches of the multi-valued Lambert-W function W(x) and their respective ranges before deriving the stationary-state solution for each species in the three fundamental phases: low density, high density, and maximal current phase. It possesses two real branches, denoted as $W_0(x)$ and $W_{-1}(x)$. The branch $W_0(x)$ exists within the range $[-1,\infty]$ for $x \ge -1/e$, while $W_{-1}(x)$ exists within the range $[-\infty,-1]$ for $-1/e \le x \le 0$, and both branches converge at x = -1/e.

Given the open boundary conditions in the system, the stationary state solutions for the + species of particles in entry-dominated low-density (LD) and maximal-current (MC) phases can be obtained by assuming the conditions $\rho^+(x_0 = 0) = \rho_1$ and $\rho^+(x_0 = 0) = \rho_2$

5.4 Direct simulation 127

1/2, respectively. While the respective exit-dominated high-density (HD) solution can be obtained by utilizing the condition $\rho^+(x_0=1)=1-\beta$. In the case of low, high, and maximal-current density solutions for – species of particles, the boundary conditions will interchange as – particles enter the lattice from the right end and exit from the left end. To determine ρ_1 and ρ_L in the density profiles' expressions for the positively and negatively charged particle species in the entry-dominated phase, we employ (5.18) and the current-continuity principle at the entry node and near the extraction node, resulting in the following set of equations:

$$\rho^{\pm}(0) \exp\left(-2\rho^{\pm}(0)\right) = \rho^{\pm}(1) \exp\left(-2\rho^{\pm}(1) - \lambda_{k}\right), \tag{5.20}$$

and

$$\alpha^{\pm}(1-\rho_k^{\pm}) = \rho^{\pm}(x_k) \left(1-\rho^{\pm}(x_k)\right), \tag{5.21}$$

where $x_k = 0(1)$ for k = 1 (*L*).

It is crucial to observe that, as the expressions are derived by meeting only one boundary condition, boundary layers emerge on the opposite end of the density solution in the LD (low-density) or HD (high-density) phase for each species. Moreover, the current continuity on the lattice guarantees the presence of exactly two additional stationary phases, manifested as localized domain walls, namely LD-HD and MC-HD phases, for each species. The regions of existence for the phases mentioned above and the density expressions corresponding to each species are provided in Table 5.1. The following section will delve into the $\alpha - \beta$ parameter space to scrutinize the effect of the resetting phenomenon on the steady-state characteristics of the system.

5.4 Direct simulation

This section provides an alternative approach to obtaining the stationary state density solution corresponding to each species with the help of Eq. (5.19)). The primary advantage of utilizing this scheme is its reduced complexity in contrast to the computation of con-

Table 5.1: Expressions for both species' existence conditions, stationary state phases, and densities using a mean-field technique.

MC-HD	LD-HD	MC	HD	LD	Phase
$egin{aligned} lpha^\pm &< rac{eta(1-eta)}{-rac{1}{R}\left(1-2eta-\ln(2-2eta) ight)}, \ lpha^\pm &> rac{eta(1-eta)}{R\left(2eta-1-\ln(2eta) ight)}. \end{aligned}$	$egin{align*} oldsymbol{lpha}^{\pm} > & \dfrac{eta(1-eta)}{1-(R-2)}W_0igg((R-2)eta \exp(R-2eta)igg)}, \ oldsymbol{lpha}^{\pm} < & \dfrac{eta(1-eta)}{-rac{eta(1-eta)}{(R+2)}W_{-1}igg((-R-2)(1-eta)\exp(2eta-2)igg)}. \end{aligned}$	$lpha^{\pm}>-W_0igg(-\expig(-(1+rac{R}{2})igg)igg)igg(1+rac{1}{2}W_0igg(-\expig(-(1+rac{R}{2})igg)igg)igg),$ $lpha^{\pm}<rac{eta(1-eta)}{rac{R}{2}igg(2eta-1-\ln(2eta)igg)}.$	$egin{aligned} lpha^\pm > & rac{eta(1-eta)}{-rac{1}{(R+2)}W_{-1}igg((-R-2)(1-eta)\exp(2eta-2)igg)}, \ lpha^\pm > & rac{eta(1-eta)}{-rac{1}{R}igg(1-2eta-\ln(2-2eta)igg)} \end{aligned}$	$lpha^\pm < -W_0igg(-\expig(-(1+rac{R}{2})igg)igg)igg(1+rac{1}{2}W_0igg(-\expig(-(1+rac{R}{2})igg)igg)igg),$ $lpha^\pm < rac{eta(1-eta)}{1-rac{1}{(R-2)}W_0igg((R-2eta)igge}.$	Phase region
$ \rho_{\text{HC}}^{+}(x) \; ; \; x_{w} \leq x \leq 1, \rho_{\text{HD}}^{+}(x) \; ; \; x_{w} \leq x \leq 1. $	$ \rho_{\text{LD}}^{+}(x) \; ; \; 0 \le x \le x_{w}, \rho_{\text{HD}}^{+}(x) \; ; \; x_{w} \le x \le 1. $	$-\frac{1}{2}W_0\left(-\exp(-1-\lambda_1x)\right)$	$-\frac{1}{2}W_{-1}\left(-2(1-\beta)\exp\left(-2(1-\beta)+\lambda_{1}(1-x)\right)\right)$	$-\frac{\mathrm{i}}{2}W_0\left(-2\rho_1^+\exp(-2\rho_1^+-\lambda_1x)\right)$	$ ho^+$
$ \rho_{MC}^{-}(x) : x_{w} \leq x \leq 1, $ $ \rho_{HD}^{-}(x) : x_{w} \leq x \leq 1. $	$ \rho_{\text{HD}}^{-}(x) ; 0 \le x \le x_w, \rho_{\text{HD}}^{-}(x) ; x_w \le x \le 1. $	$-\frac{1}{2}W_0\left(-\exp\left(-1-\lambda_L(x-1)\right)\right)$	$-\frac{1}{2}W_{-1}\left(-2(1-\beta)\exp\left(-2(1-\beta)-\lambda_{L}x\right)\right)$	$-rac{1}{2}W_0igg(-2 ho_L^-\expigg(-2 ho_L^\lambda_L(x-1)igg)igg)$	ρ-

5.4 Direct simulation 129

ditions for the existence of asymmetric phases discussed in Section 5.5.2. Secondly, this scheme can be readily extended if the model is generalized to incorporate additional dynamics where analytical approaches may not be applicable. The estimate of the (\pm) species of particle density is represented numerically by the notation $\rho_{i,n}^{\pm}$ at i^{th} lattice site, n^{th} time step and in the limit $n \to \infty$, the stationary-state solution is assured. The finite-difference equation for the continuum density evolution Eq. (5.13) in the bulk utilizing the forward-intime and central-in-space (FTCS) scheme is given by:

$$\rho_{i,n+1}^{+} = \rho_{i,n}^{+} + \Delta t' \left(\frac{\varepsilon}{2} \left(\frac{\rho_{i+1,n}^{+} - 2\rho_{i,n}^{+} + \rho_{i-1,n}^{+}}{\Delta x^{2}} \right) + \left(\frac{\rho_{i+1,n}^{+} - \rho_{i-1,n}^{+}}{2\Delta x} \right) (2\rho_{i,n-1}^{+}) - R(1 - \rho_{1}^{+} - \rho_{1}^{-})\rho_{i,n}^{+} \right), \quad (5.22)$$

where the spatial ($\triangle x = 1/L$) and temporal ($\triangle t'$) grid spacing variables adhere to the condition $\triangle t'/\triangle x^2 \le 1$ to ensure the stability of the scheme against small perturbations. As postulated in the model, explicit determination of boundary conditions in the continuum limit is unattainable because interactions between species and particle resetting from the bulk exclusively occur at the boundaries. At boundaries, we employ Eq. (5.5) and Eq. (5.6) to derive finite-difference scheme provided by:

$$\rho_{1,n+1}^{+} = \rho_{1,n}^{+} + L \triangle t' \left((1 - \rho_{1,n}^{+} - \rho_{1,n}^{-}) \left(\alpha + r \sum_{i=2}^{L} \rho_{i,n}^{+} \right) - \rho_{1,n}^{+} (1 - \rho_{2,n}^{+}) \right), \quad (5.23)$$

and

$$\rho_{L,n+1}^{+} = \rho_{L,n}^{+} + L \triangle t' \left(\rho_{L-1,n}^{+} (1 - \rho_{L,n}^{+}) - \rho_{L,n}^{+} \left(\beta + r(1 - \rho_{1,n}^{+} - \rho_{1,n}^{-}) \right) \right).$$
 (5.24)

Similarly, comparable finite-difference equations for the negative particles may also be constructed by simply switching the boundary conditions.

5.5 Stationary phases for bidirectional model

To examine the impact of local resetting of each species on their bidirectional transport, we first explore the viable stationary phases that may persist in the phase diagram plotted in an $\alpha - \beta$ parameter space. For clarification, if X and Y represent the respective stationary phases exhibited by the + and - particles, then the stationary phase in the phase diagram is indicated by X/Y. As explained in Section 5.6.3, the lattice density in the proposed model for each species can exhibit five distinct stationary phases: LD, HD, MC, LD-HD, or MC-HD. Previous studies on bidirectional transport have revealed that despite considering identical dynamics and equal dynamic rates for both species, except for their movement direction, the stationary properties of both species may or may not display similar characteristics [43, 44]. Hence, based on the observed stationary properties, we categorize the analysis into two cases: symmetric and asymmetric phases.

5.5.1 Symmetric phases

Within symmetric phases, both species display analogous stationary state characteristics, including densities ($\rho^+ = \rho^-$) and particle currents ($J^+ = J^-$). To derive the existence condition for such phases, the system can be conceptualized as two independent single-species TASEP models connected solely at the boundaries. In this setup, each species enters the respective lattice from opposite ends with an effective entry rate α^+ (or α^-) and exits the lattice with a rate β . Now, by employing the expressions of the effective entry rates in Eq. (5.16), an effort is made to establish conditions that result in identical dynamics and stationary properties for each species. These conditions are given as:

$$\alpha^{+} = \alpha^{-} = \frac{\alpha\beta}{\alpha + \beta} \tag{5.25}$$

The results from the previous section indicate that the single-specie TASEP model with local resetting can manifest one of five stationary phases: LD, HD, MC, LD-HD, or MC-HD. Hence, in the bidirectional transport setting, the resetting dynamics can manifest only five

symmetric phases: LD/LD, HD/HD, MC/MC, (LD-HD)/(LD-HD), and (MC-HD)/(MC-HD). Now, we utilize the above-obtained expression of effective entry rates and the existence condition of each stationary phase outlined in Table 5.1 to conclude that only two symmetric phases are viable, namely LD-LD and MC-MC. The presence of the HD/HD phase can be dismissed on the grounds that the overall particle density on the lattice cannot surpass unity. For the (LD-HD)/(LD-HD) and (MC-HD)/(MC-HD) phases, the conditions outlined in Table 5.1 do not yield a feasible region in the $\alpha - \beta$ parameter space for any given preference of the resetting mechanism. The existence of other phases can be discarded based on similar mathematical arguments.

5.5.2 Asymmetric phases

While both species demonstrate analogous dynamics on the one-dimensional lattice, their interaction at the boundaries may still impact the symmetry of the system. As a result, certain asymmetric phases arise in the system, wherein the stationary properties, including densities and currents of each species, tend to differ, resulting in:

$$J^+ \neq J^-, \ \rho^+ \neq \rho^-.$$
 (5.26)

Considering the fact that a single-species TASEP model with local resetting can exhibit a maximum of up to five stationary phases: LD, HD, MC, LD-HD, or MC-HD. The potential number of asymmetric phases that may exist in a bidirectional system with local resetting amounts to $5^2 = 25$. The asymmetric phases, including MC/HD, HD/MC, (LD-HD)/MC, MC/(LD-HD), (MC-HD)/MC, MC/(LD-HD), (LD-HD)/HD, HD/(MC-HD), (MC-HD)/HD, and HD/HD, are eliminated from consideration due to the constraint that the total particle density on the lattice cannot exceed unity. Following similar mathematical arguments, one can eliminate the existence of the (LD-HD/MC-HD) or (MC-HD/LD-HD) phases. Although we established the implicit form of the density profile expression and the prerequisites for the occurrence of stationary phases using the Lambert-W function and effective entry rates outlined in Table 5.1, explicit determination of the feasibility conditions

for asymmetric phases is challenging due to the inequality of effective entry rates for both species ($\alpha^+ \neq \alpha^-$). Therefore, we employ a numerical approach detailed in Section 5.4 to solve the bulk density evolution equation (Eq. (5.13)) along with the boundary equations (Eqs. (5.5)-(5.8)). Furthermore, this technique may also be used with the broader or specialized form of the suggested model, where an analytical approach may not be possible. Since the theoretical expressions found in the previous section are subject to several approximations that neglect all correlations, we perform Monte Carlo simulations for 10^9 time steps using the random sequential update rule on the lattice of length L = 1000. At each time step, a random lattice site is chosen and an event (entry, hopping, resetting, or exit) is performed at the respective site with a probability proportional to the rates in accordance with the dynamical rules as defined in Sec. 5.6.2. The configurations obtained in the first 5% time steps are ignored in order to ensure that the stationary state is achieved, and the mean density of particles is computed for an interval of 10L.

5.6 Results and discussion

Inspired by symmetry-breaking behaviors found in a bidirectional TASEP model, in this section, we aim to investigate the role of the resetting phenomenon in the stationary properties of transport in a bidirectional system. The interaction between the non-equilibrium dynamics arising from open boundaries and the resetting phenomena in the bulk is expected to generate intricate collective effects. As a result, it is anticipated that R plays an important role in both qualitative and quantitative aspects of the phase diagram's topology, particularly concerning symmetry breaking and the emergence of new stationary phases. To explore the impact of resetting phenomena on the bidirectional transport system, we generate stationary state phase diagrams in the α - $\beta \in [0,1] \times [0,1]$ parameter space. These diagrams are constructed for various resetting rates and will be utilized to provide insights into their influence on the system's stationary properties. We follow a systematic procedure to delineate the boundaries between these stationary phases. We begin by fixing the value of α and then vary β up to two decimal places within the interval [0,1], thereby identifying critical

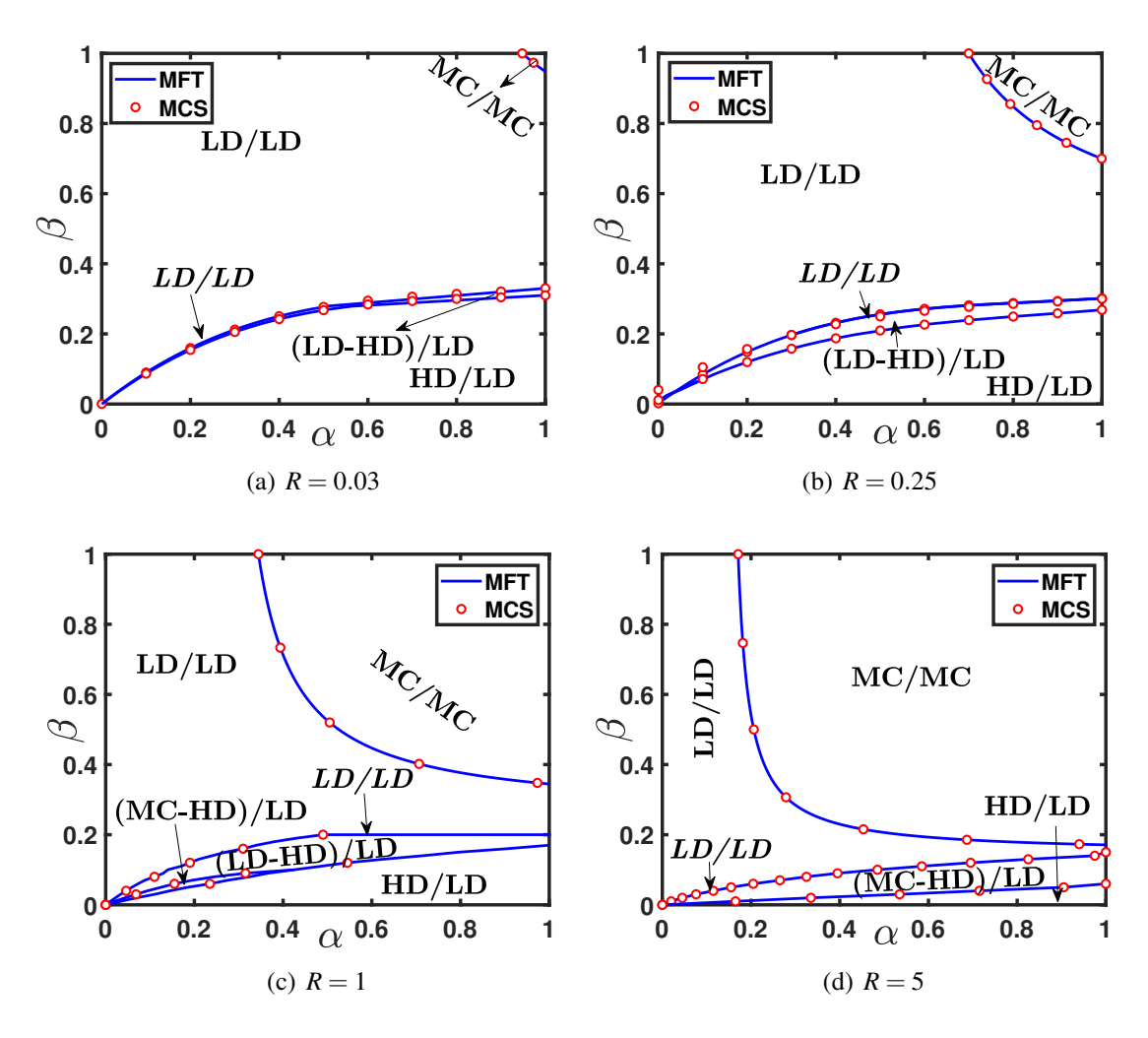


Figure 5.2: The stationary state phase diagrams for (a) R = 0.03, (b) R = 0.25, (c) R = 1 and (d) R = 5 with q = 1. The asymmetric LD/LD phase has been written in italic fonts to distinguish it from the symmetric LD/LD phase.

points of β where phase transitions occur. Similarly, we fix β and vary α up to two decimal places to pinpoint critical values of α corresponding to phase transitions. Subsequently, we connect these critical values of β and α for each observed phase, forming phase boundary lines. These lines represent the phase boundaries for the respective phases. This process is repeated for all phases to generate the complete phase diagram. Hence, the phase boundaries are computed within an estimated error of less than 2%, and the same is being taken care of by the size of the markers representing the Monte Carlo simulations.

5.6.1 Role of resetting rate on phase diagrams

It is clear from the bulk equation (5.17) and the boundary equations (5.5)-(5.8) that the stationary state results obtained for R = 0 will be identical to the bidirectional TASEP model without resetting [44, 43]. Its phase diagram includes two symmetric phases, namely LD/LD and MC/MC phases, along with two asymmetric phases: LD/LD and HD/LD phases. With the introduction of resetting dynamics into the system, i.e., for a small resetting rate (R = 0.03), the system exhibits the symmetry-breaking phenomenon, marked by the appearance of a new asymmetric phase denoted as (LD-HD)/LD. This phase is observed in the region between the LD/LD and HD/LD phases in the phase diagram (refer to FIG. 5.2 (a)). Now, the phase diagram consists of three asymmetric phases: LD/LD, (LD-HD)/LD, and HD/LD phases, along with the two symmetric phases: LD/LD and MC/MC phases; see FIG. 5.2 (a). It is important to note that, even with minimal resetting dynamics and symmetric dynamic rates for both + and - species of particles, the system exhibits three distinct asymmetric phases. Furthermore, the asymmetric LD/LD phase is restricted to a curve that delineates a boundary between the LD/LD and (LD-HD)/LD phase regions. As the value of R increases up to 0.25, the phase diagram undergoes minimal changes, with the expansion of the MC/MC phase and a newly emerged (LD-HD)/LD phase. However, the region encompassing the LD/LD and HD/LD phases experiences a reduction; refer to FIG. 5.2 (b).

With a further increase in R, a novel asymmetric phase (MC-HD)/LD emerges, as shown in the phase diagram constructed for R=1, see FIG. 5.2 (c). The phase diagram for R=1 encompasses a total of six potential stationary phases, including four asymmetric phases (LD/LD, (LD-HD)/LD, HD/LD, and (MC-HD)/LD phases) and two symmetric phases (LD/LD, MC/MC), as shown in FIG. 5.2 (c). The symmetry-breaking phenomena continue to prevail with the increase in the resetting rate. Moreover, when R is increased beyond one, the topology of the phase diagram does not change except for the shrinkage in (LD-HD)/LD, HD/LD, and LD/LD phases, whereas the MC/MC and (MC-HD)/LD expand. Lastly, FIG. 5.2 (d) depicts the phase diagram for R=5, where the number of asymmetric phases reduces to three since (LD-HD)/LD vanishes from the phase diagram due to its con-

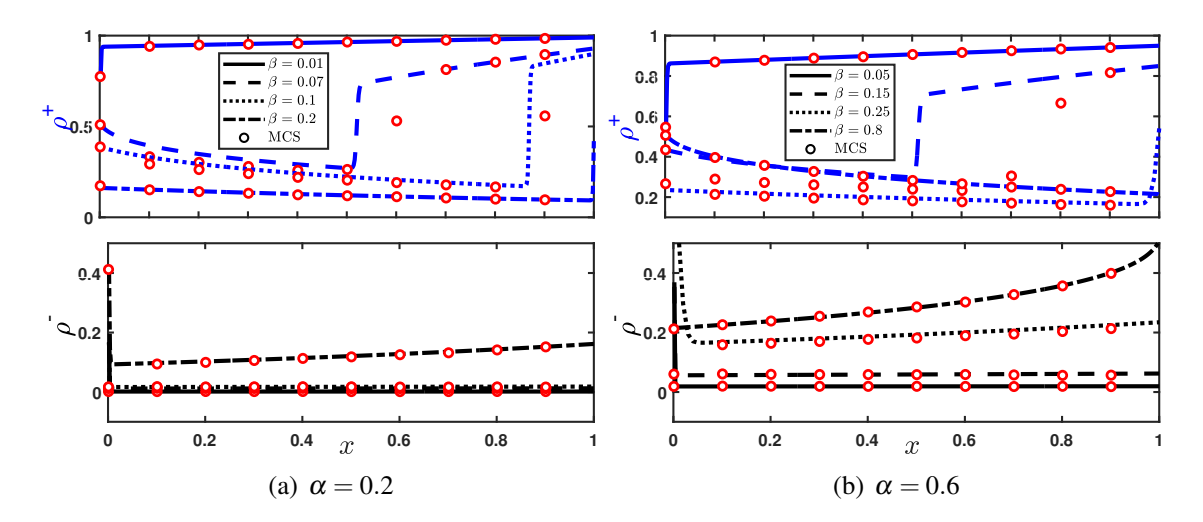


Figure 5.3: The stationary state phase transition in ρ^+ and ρ^- for a fixed α while varying β , where R = 1.

tinued shrinkage, whereas the number of symmetric phases remains conserved. It is worth noting that the asymmetric phase (LD-HD)/LD, which appeared for a small resetting rate, intriguingly ceases to exist when the resetting rate is increased significantly. This can be explained as follows: at low resetting rates, the influence on the effective entrance and exit rates is minimal. However, as the rate *R* increases, entry/exit rates experience substantial alterations, eventually reaching a threshold value where the dynamics of the bulk become rate-limiting. Consequently, this gives rise to the (MC-HD)/LD phase.

Having scrutinized the phase diagrams for various R values, we now delve into the examination of stationary state properties in the limiting cases of different resetting regimes, particularly the small $(R \to 0)$ and substantial reset framework $(R \to \infty)$. The resetting phenomena progressively disappear in the insignificant resetting framework, resulting in a stationary state phase diagram that reduces to that of a traditional bidirectional TASEP model without resetting [44, 43]. Resetting takes precedence over other particle dynamics in the later case, resulting in a phase diagram predominantly characterized by the symmetric MC/MC phase. This influence of R mirrors the behavior observed in the single-directional open TASEP with local resetting. Additionally, the phase diagrams' count of stationary state phases displays a non-monotonic variation concerning the resetting rate, transitioning from $4 \to 5 \to 6 \to 5$ as R increases.

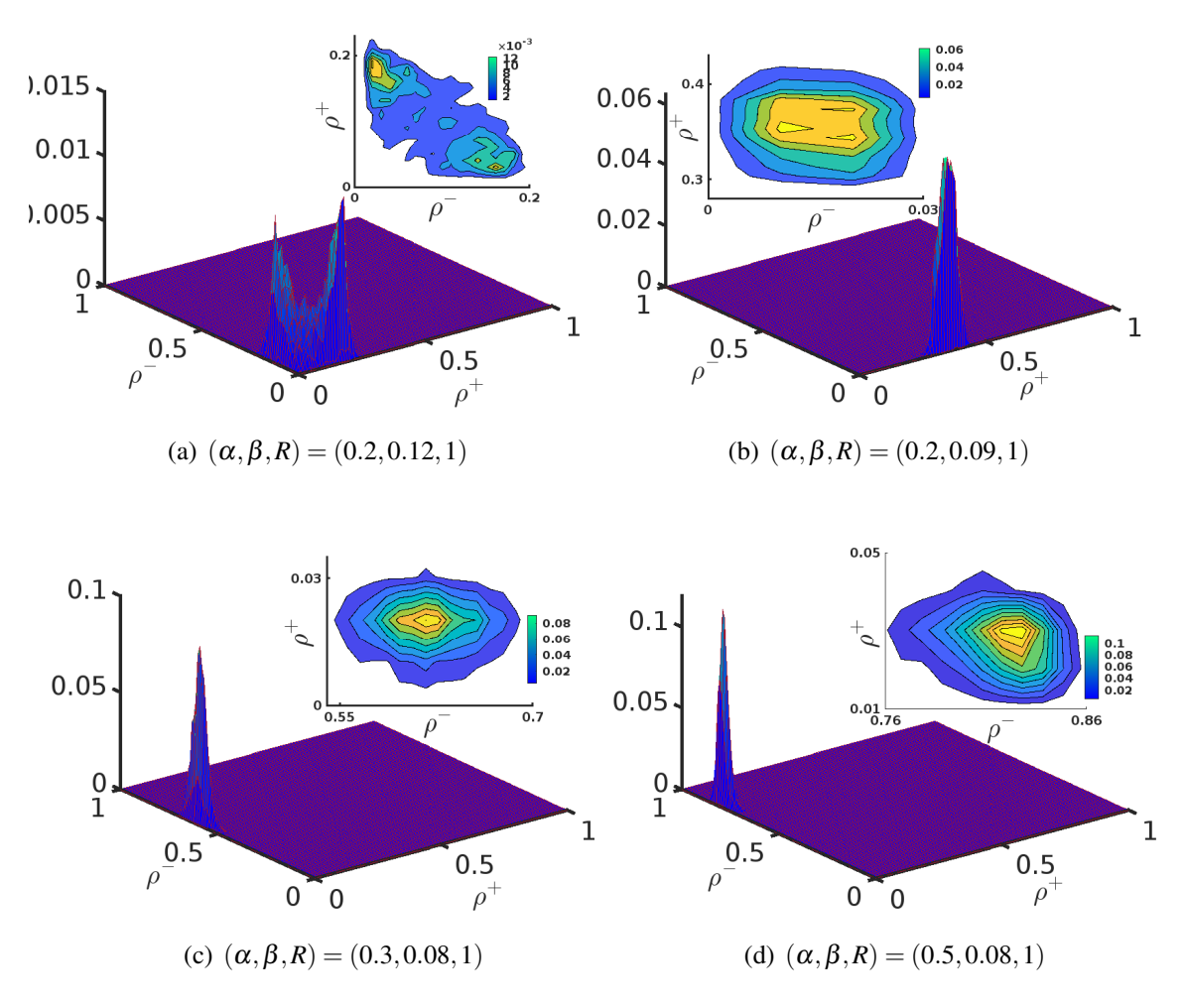


Figure 5.4: Particle density histogram for the asymmetric phases: (a) *LD/LD*, (b) (LD-HD)/LD, (c) (MC-HD)/LD (d) HD/LD with the parameters defined in the captions of the figures, respectively.

Now, we delve into the density profiles and phase transitions, with particular emphasis on the recently emerged phases, i.e., the (LD-HD)/LD and (MC-HD)/LD phases. For a small choice of an entry rate for both particle species, as the exit rate for both species increases, the + particles originating from high density undergo two distinct shocks and subsequently adopt a low-density profile. Meanwhile, the – particles persist in a low-density profile as the exit rate rises (see FIG. 5.3 (a)). Hence, it demonstrates a phase transition from the HD/LD phase to the LD/LD phase, passing through the (MC-HD)/LD and (LD-HD)/LD phases. Conversely, with a comparatively higher selection of the entry rate, FIG. 5.3 (b) showcases

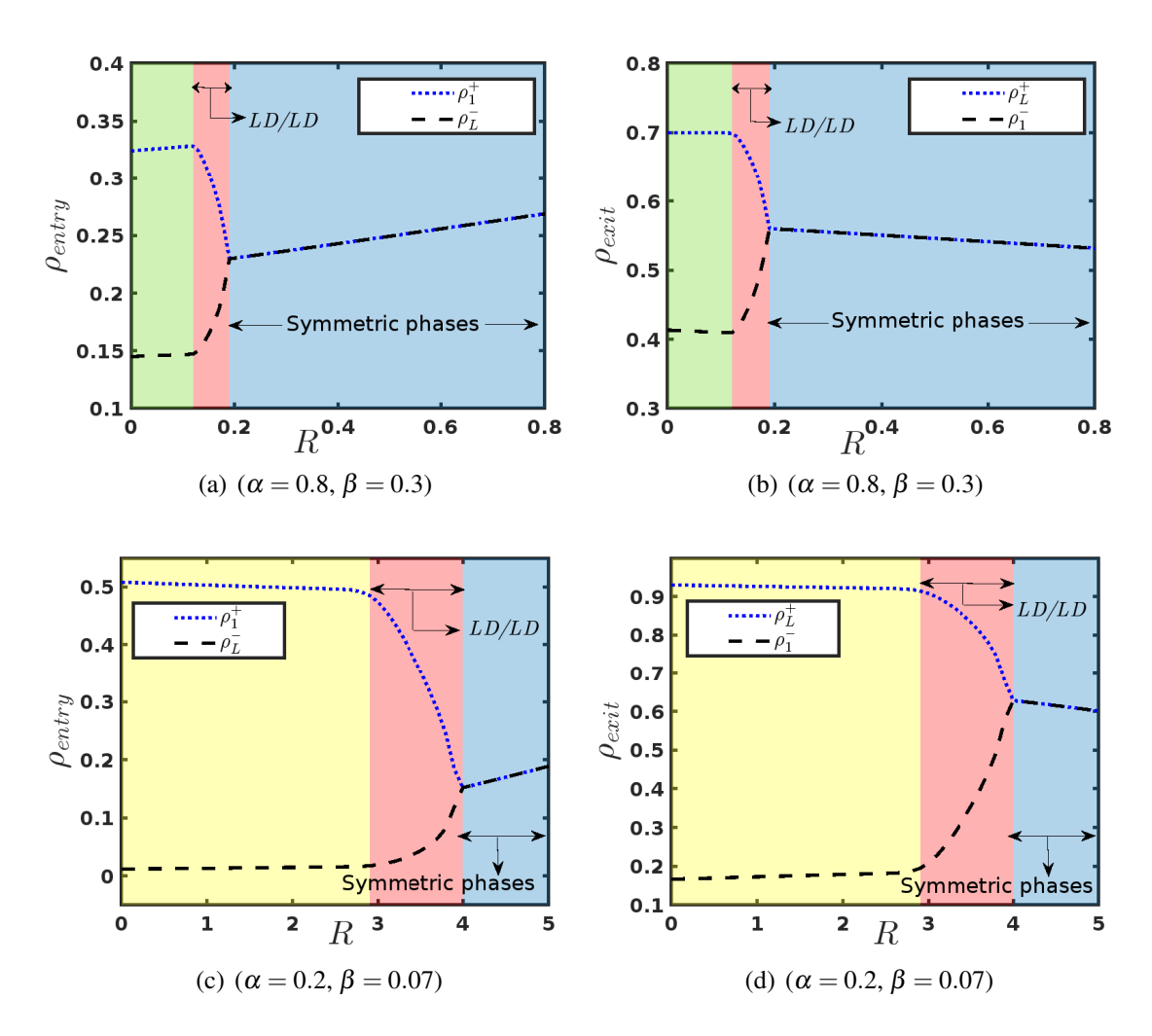


Figure 5.5: Impact of the resetting phenomena on the stationary state entry and exit densities for a fixed choice of entry and exit rate for both species.

the phase transition from the HD/LD phase to the MC/MC phase through the (LD-HD)/LD phase. In this scenario, the + particles undergo a transition from a high-density profile to a low-density profile through an LD-HD shock only, subsequently reaching a maximal current phase as β increases.

5.6.2 Spontaneous symmetry-breaking phenomena (SSB)

A distinctive feature of a bidirectional system is the emergence of spontaneous symmetrybreaking in the density profiles of both + and - particle species while maintaining the

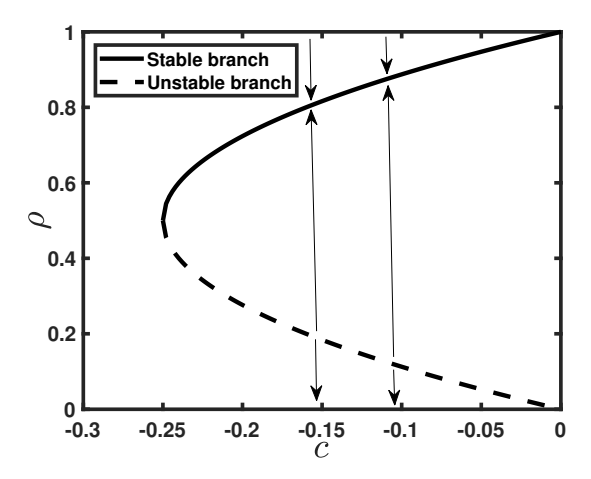


Figure 5.6: In the fixed-point diagram of the boundary-layer differential equation, the solid and dashed lines represent the two fixed-point branches. The vertical arrows signify that the upper and lower fixed-point branches are stable and unstable, respectively. These arrows indicate the direction of the boundary-layer solution flow as x increases. The coordinates (-0.25, 0.5) correspond to the bifurcation point. The flow toward or away from this particular point is depicted by vertical downward arrows on the y-axis.

same values for all the parameters. Symmetry-breaking phenomena have been reported theoretically, and the phase boundaries agree well with the Monte Carlo simulations; see FIG. 5.2. To thoroughly explore this phenomenon, we create particle density histograms via Monte Carlo simulations by continuously tracking the instantaneous densities of each species of particle, i.e., ρ^+ and ρ^- . In the simulations, with a system size of L=1000, we discard the initial 10^9 time steps and subsequently collect data for 9×10^9 time steps. The double spike in the density histogram distribution with two off-diagonal maxima shows the occurrence of an asymmetrical phase. FIG. 5.4 displays typical density histogram plots for the LD/LD, (LD-HD)/LD, (MC-HD)/LD, and HD/LD phases.

Clearly, the histograms in FIG. 5.4 show different values in the different regions depending upon the asymmetric phase. All of them represent $\rho^+ \neq \rho^-$ and validate the presence of symmetry breaking. The peaks are also demonstrated by the means of the contour plots drawn in the insets of the figure. The color code represents the increase in the intensity of the particles.

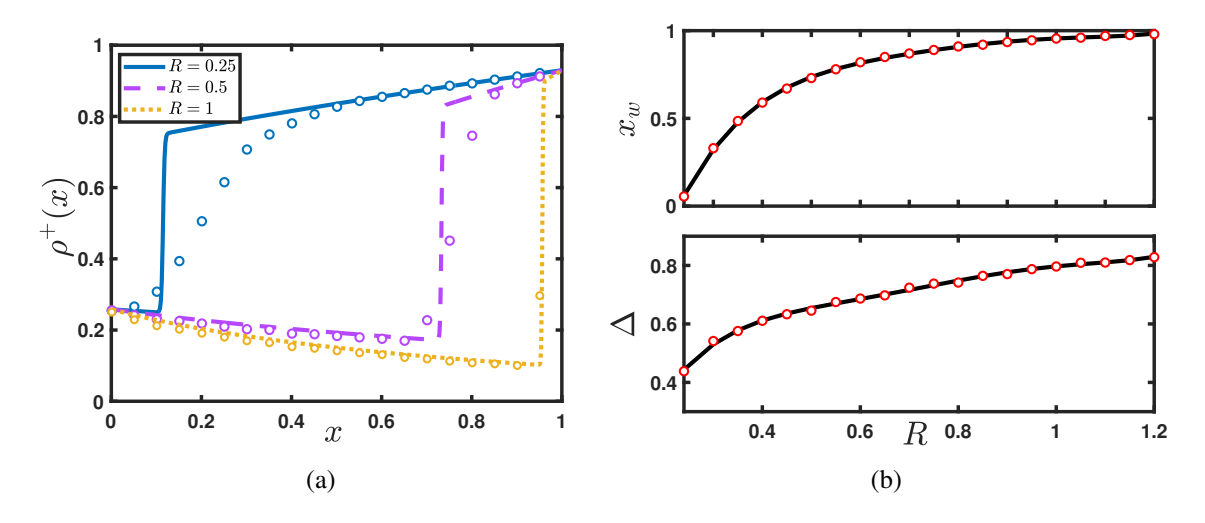


Figure 5.7: The influence of the resetting dynamics is depicted on (a) the (LD-HD)/LD phase and (b) the domain wall's position and height for $\alpha=0.1$ and $\beta=0.07$. The solid lines represent mean-field results, whereas the markers ("circles") represent the Monte Carlo results.

5.6.3 Influence of *R* on Entry & Exit

Recall the single-species TASEP models with local resetting, where, for a high resetting rate, the particles on lattice sites $i=2,\ldots,L$ reset rapidly to the first site. As a result, the system observes an increased (decreased) density at the entry (exit) site. Given that both species interact at the boundaries in the bidirectional system, in this section, we will examine how the resetting rate influences the boundary densities of both species, for fixed entry and exit rates. Clearly, for $\alpha=0.8$ and $\beta=0.3$, the system observes a phase transition from the HD/LD phase to the (LD-HD)/LD phase for the smaller values of R. Here, the density at the boundary sites for both species does not change much and almost remains constant; see the leftmost region (in green) in FIG. 5.5 (a) and (b). With a further increase in R, the system undergoes a phase transition from the (LD-HD)/LD phase to the asymmetric LD/LD phase. In the course of this transition, both boundary densities of + particles decrease, while they increase for - particles. This continues until the boundary densities of both species match. Upon appreciating the values of R, the asymmetric LD/LD phase transits to the symmetric LD/LD phase and subsequently progresses to the symmetric MC/MC phase. For further increase in R, the system continues to prevail in the symmetric phases. In such phases, the

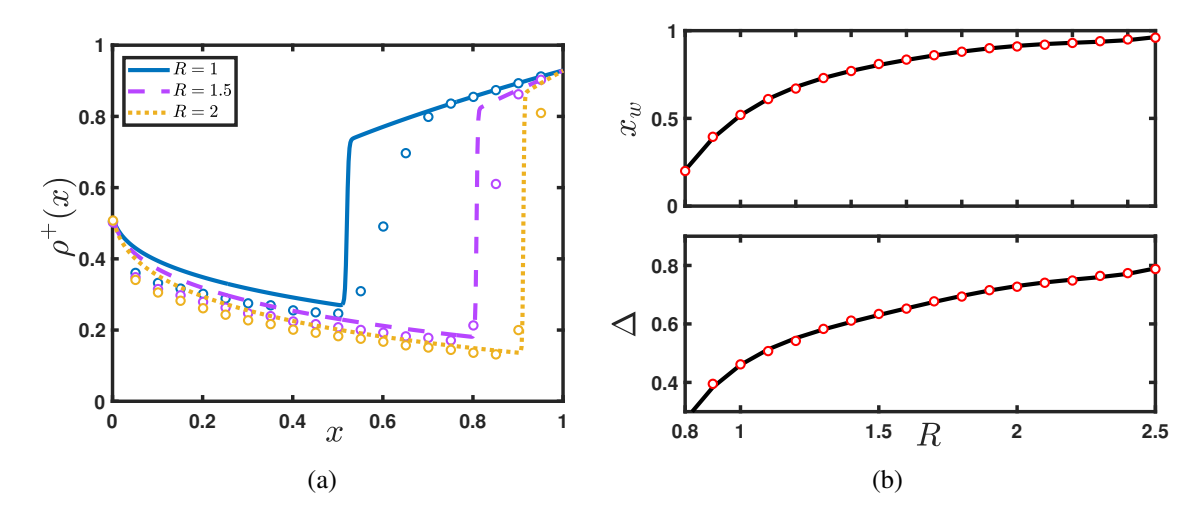


Figure 5.8: The influence of the resetting dynamics is depicted on (a) the (MC-HD)/LD phase and (b) the domain wall's position and height and position for $\alpha = 0.2$, $\beta = 0.07$. The solid lines represent mean-field results, whereas the markers ("circles") represent the Monte Carlo results.

density at the entry site for both species of particles continues to increase as the resetting rate increases, while the exit site density decreases.

To check the robustness of the above-obtained results, we investigate the impact of the resetting rate on small values of entry and exit rates for both species. It is apparent from FIG. 5.5 (c) and (d) that qualitatively, we observe the same impact of *R* on the boundary densities of both species as discussed in the previous case. Except in this case, the asymmetric shock phase is of the MC-HD type, achieved from an HD/LD phase, and the asymmetric phases transit to symmetric phases for larger values of the resetting rate. After examining both scenarios, we conclude that the asymmetric *LD/LD* phase serves as a bridge between the asymmetric and symmetric phases. This phenomenon can be elucidated as follows: In the absence of resetting, the interaction between both the species at the entry and exit points leads to the persistence of asymmetric phases in the phase diagram of a bidirectional TASEP model. Our proposed study also observes these asymmetric phases for negligible or intermediate resetting regimes. However, in large resetting regimes, both species have minimal interaction time at the boundaries, leading the system to achieve symmetry in the form of symmetric phases. Additionally, the substantial values of the resetting rate play a crucial

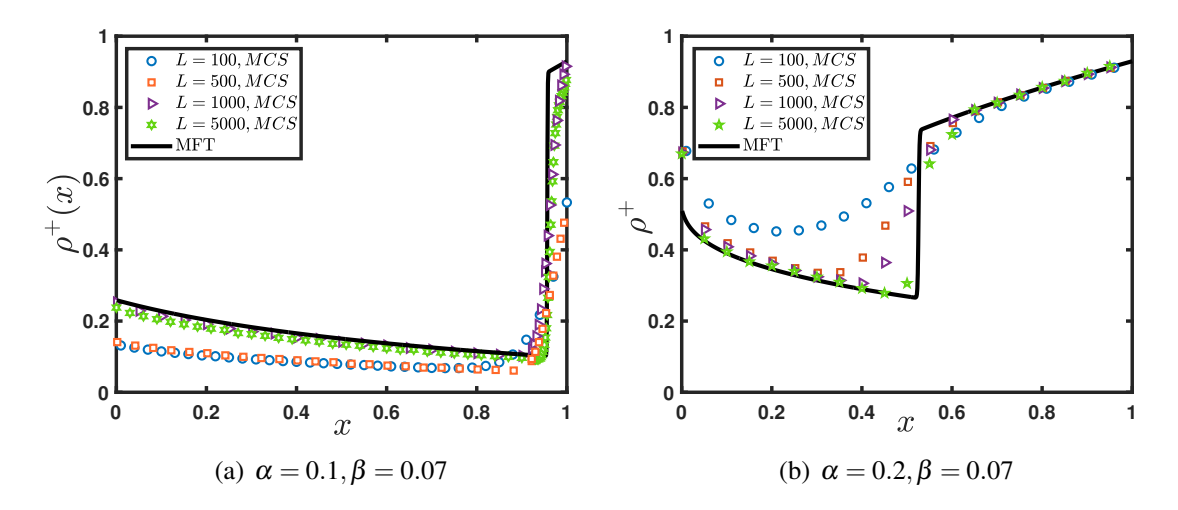


Figure 5.9: Finite size effect on (a) the LD-HD density profile as well as (b) the MC-HD density profile for R = 1. The solid lines represent mean-field results, whereas the markers ("circles") represent the Monte Carlo results.

role in determining the asymmetry dynamics within the system.

5.6.4 Shock dynamics

The steady-state characteristics of the proposed model reveal intriguing phenomena in phase diagrams, particularly the emergence of two asymmetric phases containing an uprising shock, namely (LD-HD)/LD and (MC-HD)/LD phases. It must be noted that the lattice in the proposed model cannot manifest a declining shock. This assertion is substantiated by a fixed-point diagram created from the fixed points of the equation derived from the integration of Eq. 5.13. This can be reasoned as follows: in FIG. 5.6, a high-density point on the unstable part of the curve cannot be connected to a low-density point on the unstable part of the curve using a vertical line, as indicated by the directions of the arrows in the boundary-layer solution flow [95]. This prompts an investigation into the influence of the resetting rate on the characteristics of the shock profile. Initially, we delve into the dynamics of the shock by scrutinizing its location and comprehending the transitions into other phases with an increase in the resetting rate. One can determine the implicit expression for the shock position (x_w) on the lattice by applying current continuity at x_w , where both the left- and right-hand-side currents of the lattice at x_w are equal. This leads to the condi-

tions $\lim_{x\to x_w^-} \rho^{\pm}(x) = \rho^{\pm}(x_w)$ and $\lim_{x\to x_w^+} \rho^{\pm}(x) = 1 - \rho^{\pm}(x_w)$, which can be rephrased as follows:

$$W_{0}\left(-2\rho_{k}^{\pm}\exp(-2\rho_{k}^{\pm}-\lambda_{k}x_{w})\right)-W_{-1}\left(-2(1-\beta)\exp\left(-2(1-\beta)+\lambda_{k}(1-x_{w})\right)\right)=2, \quad (5.27)$$

where the value of ρ_k^{\pm} needs to be computed numerically based on the conditions for either the low-density or maximal current phase, depending on which shock phase is under consideration. Similarly, the height of the domain wall in the LD-HD or MC-HD phases can be determined using the following equation:

$$\Delta^{\pm} = \rho_{\text{HD}}^{\pm}(x_w) - \rho_{\text{MC/LD}}^{\pm}(x_w). \tag{5.28}$$

Now that we have derived the expressions for both the position and height of the localized domain wall, we can use them to examine the impact of resetting dynamics on these localized structures. Commencing with the LD-HD profile, with an increase in resetting rate, the low-high density shock shifts to the right, whereas the height of the shock increases, as shown in FIG. 5.7 (a). To further explore, we plotted the graphs representing the change in position and height of the LD-HD shock with respect to the pace of the resetting process, respectively; see FIG. 5.7 (b). These plots utilize the best-fit polynomial as the numerical tool for the discrete simulation data. For $\alpha = 0.1$ and $\beta = 0.07$, the system possesses an HD phase for R = 0, therefore, the position of the LD-HD shock remains at the left end of the lattice. With a further increase in R, the shock's location continuously shifts to the right, ultimately exiting the lattice from the right end, where its value saturates at 1; refer to top panel FIG. 5.7 (b). This observation aligns with the phase diagrams presented in FIG. 5.2, where an increase in the resetting rate indicates the shift from the LD-HD phase to the LD phase. Additionally, the height of the LD-HD domain wall also increases monotonically with the resetting rate, as shown in the bottom panel of FIG. 5.7 (b). Next, we explore the influence of the resetting rate on the shock profile, i.e., the MC-HD phase. In FIG. 5.8 (a), 5.7 Conclusion 143

the density profiles of the MC-HD phase are presented for several choices of the resetting rates. Likewise, the position of the MC-HD domain wall shifts to the right, whereas its height exhibits a monotonically increasing trend with respect to R before reaching saturation, as illustrated in FIG. 5.8 (b). Therefore, we deduce that both shocks exhibit similar behavior in relation to R.

To analyze the impact of the lattice size on the shock profiles, density profiles have been procured by fixing R and varying L for a specific point within both the LD-HD and MC-HD regions (refer to FIG. 5.9). It is evident that the vertical sharpness of the shock profile increases with larger lattice sizes, indicating that while the system properties are influenced by finite-size effects, the stationary-state density profile remains unchanged.

5.7 Conclusion

Motivated by the bidirectional movement of ribosomes along mRNA molecules during translation initiation and similar scenarios in vehicular traffic, we examined the bidirectional transport of two species of particles diffusing in opposite directions on a one-dimensional discrete lattice, incorporating local resetting to their respective entry sites, utilizing a single-channel TASEP. In this model, the impact of resetting dynamics can be interpreted as a stochastic degradation in the average ribosome density along the mRNA's length. We considered the case where two different types of species swap their positions with rate q=1 when encountering each other. Within the mean-field framework, the study explores the influence of system dynamics, including entry, exit, and, notably, the resetting rate, on essential stationary state characteristics. These characteristics encompass density profiles, phase diagrams, phase regions, phase transitions, and boundary densities, presented in an implicit form utilizing the Lambert-W function. Additionally, a numerical scheme for conducting a direct integration of the master equation is provided, which is easily extendable for future generalizations. Since all the results utilize mean-field approximations, stochastic simulations are performed to validate these findings.

Firstly, the effect of R is investigated on the phase diagrams. For a negligible resetting

rate $(R \to 0)$, the phase diagram indicates that our model reduces to the conventional bidirectional TASEP without resetting, which guarantees the applicability of our approach. As soon as a small resetting rate is introduced into the system, a non-trivial effect in the form of a new asymmetric phase ((LD-HD)/LD) emerges in the phase diagram. For $R \sim 1$, the phase diagram unveils another new asymmetric phase ((MC-HD)/LD), introducing greater complexity to the phase diagram with a maximum of six stationary phases. For further increase in R, the asymmetric (LD-HD)/LD phase is eliminated from the phase diagram, representing a nonmonotonic trend in the number of perceived phases in the phase diagram with respect to R. In a large resetting regime ($R \to \infty$), majorly only the symmetric phase MC/MC prevails in the phase diagram. Moreover, the phase transitions are illustrated by plotting density profiles and verifying them through Monte Carlo simulations.

Regardless of providing both species with identical dynamics, the proposed model exhibits a breakdown in symmetry, even for very small magnitudes of the resetting rate. Additionally, we shed light on the phenomenon of symmetry breaking by generating particle density histograms based on Monte Carlo simulation results. The presence of peaks in the histogram along the anti-diagonal of the density plane for both species substantiates the existence of asymmetric phases. Given the significance of entry and exit dynamics in a system with resetting dynamics, the influence of the resetting rate is examined on the boundary densities of both species. Our findings indicate that initially, a non-monotonic trend in boundary densities is observed with respect to *R*. However, when the resetting rate is high, the entry site density of both species increases uniformly while decreasing uniformly at the exit site with respect to *R*. Lastly, the effect of finite system size on the stationary properties is also examined.

Inspired by diverse stochastic transport processes, including the movement of ribosomes during translation initiation and the premature termination of the translation process (or drop-off phenomenon), followed by subsequent rescue and recycling processes [103, 21, 50]. Our endeavor was to grasp the aforementioned features within the context of bidirectional transport coupled with local resetting, aiming for a qualitative understanding of the underlying physics through steady-state characteristics. Moreover, the model is

5.7 Conclusion 145

inherently generic and possesses the potential for generalization to encompass additional realistic features associated with various physical and biological systems.
realistic reactives associated with various physical and offological systems.



Local resetting in a dynamically disordered exclusion process

Preamble

Various physical and microscopic processes exhibit both dynamic disorder and resetting phenomena. For instance, in protein synthesis, ribosomes traverse mRNA strands, encountering dynamic defects like rare codons while also experiencing drop-off and reinitiation. Similarly, pedestrian dynamics involve temporary obstacles and individuals stepping aside before rejoining, while traffic flow includes dynamic defects such as lane closures alongside vehicle exits and re-entries.

To elucidate the collective interplay between dynamic disorder and resetting phenomena, this chapter integrates these dynamics into a TASEP model. Our theoretical analysis employs mean-field approximation, enabling a comprehensive description of the system's stationary properties. This approach allows us to investigate how the combination of dynamic disorder and resetting impacts particle transport, providing insights into a wide range of real-world processes.

6.1 Background

Inspired by several other observations in numerous real-life dynamical systems, where processes are intermittently interrupted and resumed from certain points, the diffusion process in the conventional TASEP is accompanied by a non-equilibrium process called stochastic resetting. Although the concept initially surfaced in "restart" algorithms within computer science, it represents an intriguing mechanism that is relevant across a spectrum of disciplines, including physics, chemistry, biology, ecology, engineering, and economics [136, 93, 131, 113, 114]. Stochastic resetting manifests in two distinct manners: global and local. Much of the existing literature extensively delves into the global aspect, where resetting is either applied to individual degrees of freedom or simultaneously to multiple degrees of freedom [49, 48, 74, 10]. Local resetting, where particles can independently reset their positions, presents greater complexity than global resetting, where the entire system is simultaneously reset to a reference state. The concept of local resetting was initially introduced and explored in a symmetric simple exclusion process with periodic boundary conditions [92, 106]. Subsequently, this analysis was extended to the TASEP with periodic boundary conditions, revealing the emergence of an intermediate resetting regime when the resetting rate is of the order of the inverse lattice length [92, 106]. A similar scenario unfolds in the TASEP-LK model, where the attachment-detachment rates of particles are rescaled to the order of the inverse lattice length to observe the interplay between boundary and bulk dynamics. This underscores a vital connection between the resetting process and the LK dynamics, illustrating how the resetting process represents a unique instance of the LK process wherein only the detachment process is active from the system's bulk [92, 106].

The movement in the majority of the above-mentioned transport processes is often obstructed by entities called defects or obstacles. For example, on a macroscopic scale, a faulty vehicle or a malfunctioning traffic light can cause congestion, while on a microscopic scale, DNA-bound structures impede RNA polymerase during gene transcription [2]. The TASEP has also been extended to model the practical issues where obstacles or defects frequently disrupt traffic flow, and its extensions have gained prominence. Defects come in two forms: static or dynamic. Static defects bind to locations that are either randomly dispersed or fixed,

a topic extensively explored within the TASEP framework [78, 132, 41, 70, 58]. However, the exploration of random dynamic defects remains largely uncharted. Recently, attention has turned to models related to dynamically disordered TASEP (dd-TASEP), where defects bind and unbind sporadically across lattice sites [140, 101, 16].

Inspired by realistic traffic scenarios, such as gene transcription, where both resetting and dynamic disorders are present and play a crucial role, we study a one-dimensional TASEP incorporating site-wise dynamical defects and local resetting phenomena to mimic realistic traffic scenarios.

In this study, we examine particle motion on a lattice with dynamic defects, incorporating local resetting of particles from all sites to the entry site. A primary aim is to assess whether the basic approximate mean-field theory can effectively depict the steady-state properties of a system characterized by dynamic disorder along with local resetting. Subsequently, our focus shifts to analyzing the quantitative or qualitative influence of resetting rates and defects on stationary state characteristics, such as density profiles, current and phase transitions. We aim to elucidate the topological shifts in the phase diagram resulting from variations in hindrance to particle movement and resetting rates. These theoretical insights are validated through extensive Monte Carlo simulations. The chapter is structured as follows: Section 6.2 concisely describes the model along with the dynamic rules of particles and defects. In Section 6.3, we tackle the system's master equations in both boundary and bulk regions of the lattice, employing mean-field approximations in the thermodynamic limit. Section 6.4 analytically explores the steady-state characteristics of the system, encompassing potential stationary phases, density profiles, and current. We conduct an in-depth analysis of the model regarding key parameters such as resetting rate and defect dynamics concerning phase diagrams and transitions in Section 6.6. Finally, we summarize the significant stationary-state findings in the model in Section 6.7.

6.2 Model dynamics

Motivated by the intricacies of diverse stochastic transport processes, including the recycling of mRNA polymerase during gene transcription and challenges in their movement

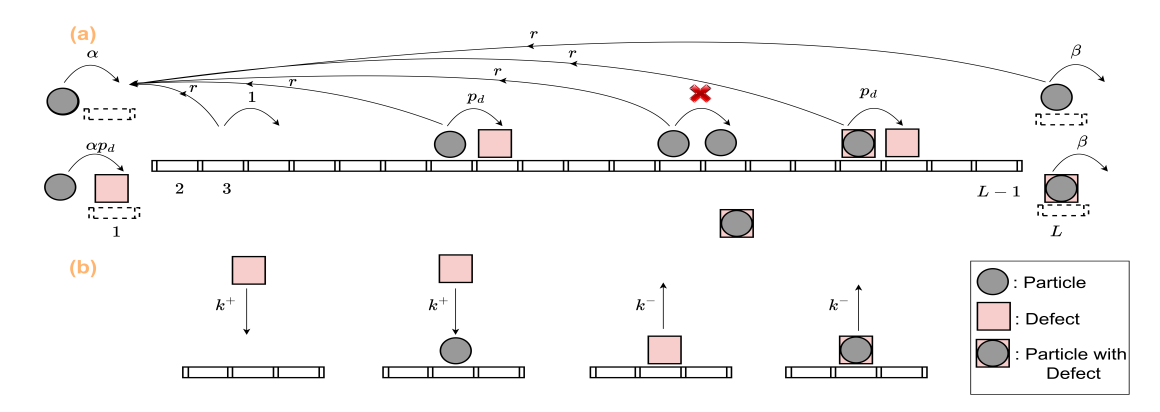


Figure 6.1: Schematic picture of the TASEP model with dynamics defects and local resetting.

posed by structures around which DNA is tightly packed, we present an open TASEP model that incorporates the dynamics of local resetting and dynamic disorder. This model involves a one-dimensional discrete lattice with L lattice sites, and each lattice site is represented by the notation $i=1,2,\ldots,L$, with i=1 and L corresponding to the first and last lattice sites, respectively, while the remaining sites are referred to as the bulk of the lattice. Further, every site can accommodate two types of entities: a particle and a *defect*. Both entities individually adhere to the hard-core exclusion principle, ensuring that a vacant lattice site can host at most one particle or defect, and both entities can also occupy the same site simultaneously. The particles represent the non-equilibrium dynamics on the TASEP, whereas the disorder that impedes particle hopping on the lattice is incorporated through an equilibrium process of binding/unbinding of entities called defects. Additionally, we introduce binary random variables τ_i and σ_i to denote the occupancy status of the particle and defect, respectively, at the ith lattice site. As illustrated in FIG. 6.1, we employ these variables to outline the potential dynamics of particles and defects at each infinitesimal time step, along with their associated occurrence probabilities, as follows:

1. Particle dynamics:

(a) At Entry: The particles access the lattice through the first site with a rate α or αp_d depending upon the defect occupancy at the arrival site, where $0 \le p_d < 1$ is the affected hopping rate that accounts for the obstruction caused by defects

in particle movement.

$$\tau_1 = 0, \sigma_2 = 0 \xrightarrow{\alpha} \tau_1 = 1, \tag{6.1}$$

$$\tau_1 = 0, \sigma_2 = 1 \xrightarrow{\alpha p_d} \tau_1 = 1, \tag{6.2}$$

(b) In Bulk: The particles in the bulk of the lattice hop unidirectionally from left to right with a rate 1 or p_d depending on the presence of a defect at the arrival site.

$$\tau_i = 1, \tau_{i+1} = 0, \sigma_{i+1} = 0 \xrightarrow{1} \tau_i = 0, \tau_{i+1} = 1,$$
 (6.3)

$$\tau_i = 1, \tau_{i+1} = 0, \sigma_{i+1} = 1 \xrightarrow{pd} \tau_i = 0, \tau_{i+1} = 1,$$
 (6.4)

(c) At Exit: The particle present at the last site either departs from the lattice with a rate β or resets to the first site with a rate r.

$$\tau_L = 1 \xrightarrow{\beta} \tau_L = 0, \tag{6.5}$$

$$\tau_L = 1, \tau_1 = 0 \xrightarrow{r} \tau_L = 0, \tau_1 = 1,$$
(6.6)

2. Defect dynamics: The defects randomly bind or unbind vertically at any lattice site with a rate k^+ and k^- , respectively.

$$\sigma_i = 0 \underset{k^-}{\overset{k^+}{\rightleftharpoons}} \sigma_i = 1. \tag{6.7}$$

Note that defects' binding/unbinding probabilities do not differ depending on the presence/absence of particles, underscoring that their dynamics take precedence over other processes. Further, since we are dealing with an open system, the boundary rates significantly influence the stationary properties. Therefore, unlike in the reference [140], we have not only considered the binding and unbinding of defects at the boundary sites but also taken into account their effects on particle dynamics at the boundaries.

6.3 Mathematical framework employing mean-field approximation

In this section, we will formulate a mathematical structure utilizing mean-field approximations to establish a framework for the processes mentioned earlier. This framework will contribute to comprehending the stationary state behavior of the model. Now, we employ the dynamic rules outlined previously to describe the stochastic evolution of the particle and defect densities on the lattice in terms of their respective time averages, $\langle \tau_i \rangle$ and $\langle \sigma_i \rangle$, as follows:

- 1. Particle evolution master equations.
 - (a) At the bulk of the lattice:

$$\frac{d\langle \tau_i \rangle}{dt} = J_{i-1,i} - J_{i,i+1} - r\langle (1 - \tau_1)\tau_i \rangle; \quad 1 < i < L, \tag{6.8}$$

where $J_{i-1,i} = \langle \tau_{i-1}(1-\sigma_i)(1-\tau_i) \rangle + p_d \langle \tau_{i-1}\sigma_i(1-\tau_i) \rangle$ represents the particle current from the $(i-1)^{\text{th}}$ lattice site to the i^{th} site due to hopping. The last term contributes to the particle current arising from the resetting process.

(b) At the left boundary of the lattice:

$$\frac{d\langle \tau_1 \rangle}{dt} = \alpha \langle (1 - \tau_1)(1 - \sigma_1) \rangle + \alpha p_d \langle (1 - \tau_1)\sigma_1 \rangle + r \langle (1 - \tau_1) \sum_{i=2}^{L} \tau_i \rangle - J_{1,2}. \quad (6.9)$$

(c) At the right boundary of the lattice:

$$\frac{d\langle \tau_L \rangle}{dt} = J_{L-1,L} - \beta \langle \tau_L \rangle - r \langle (1 - \tau_1) \tau_L \rangle. \tag{6.10}$$

2. Defect evolution master equations.

$$\frac{d\langle \sigma_i \rangle}{dt} = k^+ \langle 1 - \sigma_i \rangle - k^- \langle \sigma_i \rangle; \quad 1 \le i \le L.$$
 (6.11)

The presence of one-, two-, or three-variables in the correlator functions of the above-obtained system of equations makes them challenging to solve in their current form. Hence, we adopt a naive mean-field approximation, where the correlator function is simplified as a product of individual spatial variables, disregarding all possible correlations in the system, i.e., $\langle \tau_i \tau_{i+1} \rangle = \langle \tau_i \rangle \langle \tau_{i+1} \rangle$ and $\langle \tau_i \sigma_{i+1} \rangle = \langle \tau_i \rangle \langle \sigma_{i+1} \rangle$. Further, the notations $\rho_i = \langle \tau_i \rangle$ and $\rho_{d,i} = \langle \sigma_i \rangle$ are utilized to denote the average particle and defect density at the i^{th} lattice site, respectively. The expression of the particle current from $(i-1)^{\text{th}}$ site to i^{th} site is reformed as:

$$J_{i-1,i} = (1 - \rho_{d,i} + p_d \rho_{d,i}) \rho_{i-1} (1 - \rho_i)$$
(6.12)

As our focus is on solving the mean-field equations in the thermodynamic limit, i.e., $L \to \infty$, we derive the continuum limit of the model by coarse-graining the lattice, introducing the lattice constant $\varepsilon = \frac{1}{L}$, spatial variable $x = \varepsilon i \in [0,1]$, re-scaled time $t' = \varepsilon t$ and reduced resetting rate $R = r/\varepsilon$. Additionally, retaining the terms up to the first order in the Taylor series expansion of $\rho(x \pm \varepsilon)$ in Eq. (6.9) reforms the particle and defect density evolution Eqs. (6.9) and (6.11) into:

$$\frac{\partial \rho}{\partial t'} + \frac{\partial J}{\partial x} = -\lambda \rho, \tag{6.13a}$$

$$\frac{\partial \rho_d}{\partial t'} = k^+ (1 - \rho_d) - k^- \rho_d, \tag{6.13b}$$

here, $J = (1 - \rho_d + p_d \rho_d) \rho (1 - \rho)$ denotes the particle current in the bulk of the lattice, $\lambda = R(1 - \rho_1)$ and the subscript i is dropped to account for spatial homogeneity in the continuum limit.

Before delving into the stationary-state solution of the system, it's essential to high-light two critical considerations made during the aforementioned transformation. Firstly, the resetting rate is rescaled to a macroscopic rate in proportion to the inverse of the lattice length. This scaling enables the examination of the interaction between boundary and bulk dynamics in extensive systems. Secondly, the impact of obstruction caused by defects is predominantly encapsulated by two parameters, p_d and ρ_d , which can be amalgamated

through the introduction of a novel parameter termed the obstruction factor, defined as:

$$z = \rho_d (1 - p_d), \tag{6.14}$$

Utilizing this, the expression for the bulk current in the lattice is simplified to:

$$J = (1 - z)\rho(1 - \rho). \tag{6.15}$$

For $0 \le \rho_d \le 1$ and $0 \le p_d < 1$, the obstruction factor z remains within the range (0,1). It is apparent from Eq. (6.14) that the obstruction factor becomes zero when $\rho_d = 0$ or $p_d = 1$, and the current expression in bulk reduces to that of the standard TASEP model with local resetting [105]. Conversely, when $\rho_d = 1$ and $p_d = 0$, the obstruction factor reaches its maximum value, resulting in maximum obstruction by the defects to particle movement, causing the particle current in the bulk of the lattice to reduce to zero. These findings are also intuitively validated: obstruction vanishes from the lattice when there are no defects present or when the affected hopping rate returns to the usual hopping rate. Conversely, particles are completely obstructed if each defect causes maximum obstruction and all lattice sites contain defects.

6.4 Theoretical Analysis

To investigate how the resetting rate and obstruction factor influence the stationary state properties of the system, including density profiles, particle current, phase transitions, and phase diagrams, we solve the mean-field equations derived in the preceding section under the thermodynamic limit.

By setting the time derivative to zero in Eq. (6.13b), the stationary-state solution to the defect density on the lattice can be obtained as:

$$\rho_d = \frac{k^+}{k^+ + k^-}. (6.16)$$

At the stationary state, Eq. (6.13a), which governs the particle density on the lattice, simplifies to:

$$\frac{\partial J}{\partial x} = -\lambda \rho. \tag{6.17}$$

where $J = (1-z)\rho(1-\rho)$ represents the particle flux in the bulk of the lattice. Moreover, to derive the solution for the profile $\rho(x)$, the aforementioned equation is integrated from a reference point x_0 to x, resulting in:

$$\rho(x)\exp\left(-2\rho(x)\right) = \rho(x_0)\exp\left(-2\rho(x_0) - \frac{\lambda}{1-z}(x-x_0)\right),\tag{6.18}$$

Since the considered system is open, the boundary rates govern the potential phase transitions. In this scenario, it is convenient to initiate the analysis by considering reference points at $x_0 = 0$ and 1, representing the left and right boundaries, respectively. Further, Eq.(6.9) and Eq.(6.10) are utilized to obtain the stationary-state boundary densities, ρ_1 and ρ_L . Now, the general solutions for various phases corresponding to different boundary conditions are derived in terms of the Lambert-W function.

1. **Low-density (LD) phase**: The bulk solution obtained in Eq. (6.18) is matched with the stationary-state left boundary density, i.e., $\rho(x_0 = 0) = \rho_1$, to obtain the implicit expression of the stationary-state particle density in an entry-dominated phase in terms of the suitable real-valued branch of the Lambert-W function as:

$$\rho_{\rm LD}(x) = -\frac{1}{2}W_0 \left(-2\rho_1 \exp(-2\rho_1 - \frac{\lambda}{1-z}x) \right), \tag{6.19}$$

Evidently, solving for ρ_1 directly from Eq. (6.9) is impractical due to the dependence of other sites' density on the first site. To determine ρ_1 , $\rho(0)$, and $\rho(1)$, we rely on two additional equations. The first equation stems from the requirement that the theoretical density solution $\rho(x)$ must concurrently match both boundaries:

$$\rho(0) \exp\left(-2\rho(0)\right) = \rho(1) \exp\left(-2\rho(1) + \frac{\lambda}{1-z}\right), \tag{6.20}$$

The second equation is derived by equating the stationary state currents near the boundaries:

$$\alpha(1 - \rho_1) = \rho(1)(1 - \rho(1)). \tag{6.21}$$

2. **High-density (HD) phase**: Similarly, the implicit density profile of the stationary state exit-dominated phase is derived by aligning the bulk solution from Eq. (6.18) with the stationary-state right boundary density, i.e., $\rho(x_0 = 1) = \rho_L = 1 - \frac{\beta}{1-z}$ as:

$$\rho_{\text{HD}}(x) = -\frac{1}{2}W_{-1}\left(-2\left(1 - \frac{\beta}{1 - z}\right)\exp\left(-2\left(1 - \frac{\beta}{1 - z}\right) + \frac{\lambda}{1 - z}(1 - x)\right)\right). \tag{6.22}$$

Note that, in general, $\rho_{LD}(x=1) \neq \rho_L$, and $\rho_{HD}(x=0) \neq \rho_1$ due to the presence of boundary layers.

3. **Maximal-current (MC) phase**: For the maximal-current phase, the condition $\rho(x_0 = 0) = \rho_1 = \frac{1}{2}$ is utilized to obtain the stationary state density profile as:

$$\rho_{MC}(x) = -\frac{1}{2}W_0 \left(-\exp(-1 - \frac{\lambda}{1 - z}x) \right). \tag{6.23}$$

Further, depending on how these three standard stationary phases $\rho_{LD}(x)$, $\rho_{HD}(x)$ and $\rho_{MC}(x)$ are matched, the system may exhibit several different combinations of coexisting phases.

4. **Low-high density (LD-HD) phase**: We begin by exploring the combination of low-and high-density phases, where the current-continuity principle suggests that the system can no longer exhibit a continuous density profile from the combination of these phases [80, 109]. Hence, it leads to a shock or domain wall in the average density profile, which is given by:

$$\rho_{\text{LD-HD}}(x) = \begin{cases} \rho_{\text{LD}}(x); & 0 \le x \le x_w, \\ \rho_{\text{HD}}(x); & x_w \le x \le 1, \end{cases}$$
(6.24)

6.5 Numerical solution 157

where the discontinuity occurs at the position x_w . To ascertain the location of the shock in the coexistence phases (LD-HD phase and MC-HD phase), we leverage the observation that in both cases, the density at the shock position x_w , i.e., $\rho_{\text{LD-HD}}(x_w)$ undergoes a jump from a density less than 1/2 to a density greater than 1/2. The shock density at this position and its neighborhood can be related through the following conditions:

$$\rho_{\text{LD-HD}}(x_w) = \lim_{x \to x_w^-} \rho_{\text{LD-HD}}(x) = \rho_{\text{LD}}(x_w),$$
(6.25)

$$\rho_{\text{LD-HD}}(x_w) = \lim_{x \to x_w^-} \rho_{\text{LD-HD}}(x) = \rho_{\text{LD}}(x_w),$$

$$1 - \rho_{\text{LD-HD}}(x_w) = \lim_{x \to x_w^+} \rho_{\text{LD-HD}}(x) = \rho_{\text{HD}}(x_w).$$
(6.25)

Further, the expression for the height of the shock is given as:

$$\Delta = \rho_{\rm HD}(x_w) - \rho_{\rm LD}(x_w). \tag{6.27}$$

5. Maximal current-high density (MC-HD) phase: Similarly, the system exhibits another stationary phase, MC-HD, that has a discontinuous density profile given by:

$$\rho_{\text{MC-HD}}(x) = \begin{cases} \rho_{\text{MC}}(x); & 0 \le x \le x_w, \\ \rho_{\text{HD}}(x); & x_w \le x \le 1. \end{cases}$$
(6.28)

Similar to the LD-HD phase, one can derive the conditions to determine the position and height of the shock in the MC-HD phase. With the understanding of stationary state densities and current on the lattice, we derive the analytical expression of the phase boundaries separating these phases in the next section.

6.5 Numerical solution

This section presents an alternative method for obtaining the stationary state density solution for particles on the lattice, utilizing Eq. (6.13a). The main advantage of employing this approach lies in its reduced complexity. Additionally, this method can be easily expanded to accommodate additional dynamics in cases where analytical approaches may not be feasible.

The particle and defect density estimation at the i^{th} lattice site is denoted numerically as ρ_i^n and $\rho_{d,i}^n$, respectively, at the n^{th} time step, with the assurance of reaching the stationary-state solution as n tends towards infinity. The finite-difference equation for the continuum density evolution in bulk, utilizing the forward-in-time and central-in-space (FTCS) schemes, is expressed as follows in Eq. (6.13a):

$$\rho_{i}^{n+1} = \rho_{i}^{n} + \Delta t' \left(\left(1 - \rho_{d,i}^{n} (1 - p_{d}) \right) \left(\frac{\varepsilon}{2} \left(\frac{\rho_{i+1,n} - 2\rho_{i}^{n} + \rho_{i-1}^{n}}{\Delta x^{2}} \right) + \left(\frac{\rho_{i+1,n} - \rho_{i-1}^{n}}{2\Delta x} \right) (2\rho_{i,n-1}) - R(1 - \rho_{1})\rho_{i}^{n} \right). \quad (6.29)$$

In this scheme, the spatial ($\triangle x = 1/L$) and temporal ($\triangle t'$) grid spacing variables are chosen such that they satisfy the condition $\triangle t'/\triangle x^2 \le 1$, ensuring stability against small perturbations. As posited in the model, explicitly determining boundary conditions in the continuum limit is unfeasible due to particle resetting occurring exclusively at lattice boundaries. For boundary treatments, we utilize Eq. (6.9) and Eq. (6.10) to derive the finite-difference scheme presented as:

$$\rho_1^{n+1} = \rho_1^n + L \triangle t' \left(1 - \rho_{d,1}^n (1 - p_d) \right) \left((1 - \rho_1^n) \left(\alpha + r \sum_{i=2}^L \rho_i^n \right) - \rho_1^n (1 - \rho_2^n) \right), \quad (6.30)$$

and

$$\rho_{L}^{n} = \rho_{L}^{n} + L \triangle t' \left(1 - \rho_{d,L}^{n} (1 - p_{d}) \right) \left(\rho_{L-1}^{n} (1 - \rho_{L}^{n}) - \rho_{L}^{n} \left(\beta + r(1 - \rho_{1}^{n}) \right) \right).$$
(6.31)

Similarly, one can obtain an FTCS scheme to numerically determine the defect density from

Eq. (6.13b) as:

$$\rho_{d,i}^{n+1} = \rho_{d,i}^{n} + \left(k^{+}(1 - \rho_{d,i}^{n}) - k^{-}\rho_{d,i}^{n}\right). \tag{6.32}$$

6.6 Results and discussion: Stationary-state characteristics

To clearly understand the impact of the crucial parameters, such as the obstruction factor and resetting rate, on the steady-state characteristics of the model, we begin with the construction of the stationary phase diagrams. We leverage the current-continuity principle and the results derived in the preceding section for various stationary phases to calculate ρ_1 and $\rho(1)$ in Eq. (6.21), enabling us to establish these phase boundaries.

As previously discussed, the coexisting phases represent a discontinuous blend of two phases, with the latter segment of the density profile for both coexisting phases corresponding to the HD phase. Therefore, we have $\rho(1) = 1 - \beta^*$, where $\beta^* = \frac{\beta}{1-z}$. The boundary separating the LD-HD coexistence phase from the HD (LD) phase is identified by setting the shock position $x_w = 0$ (1) in Equations (6.25) and (6.26). A similar approach can be employed to determine the boundary between the MC-HD coexistence phase and both the MC and HD phases.

To determine the phase boundary between the LD and the MC phase, we utilize the conditions for which ρ_1 and $\rho(0)$ simultaneously satisfy $\rho(0) = \rho_1 = \frac{1}{2}$. Further, $\rho(1)$ can be computed from the Eq. (6.20). One can obtain the analytical expressions of the phase boundaries by simply substituting these ρ_1 , and $\rho(1)$ in Eq. (6.21).

We have outlined the phase boundaries in Table 6.1, delineating the regions where each stationary phase may exist within the $\alpha - \beta$ parameter space or the phase diagram. While analytical expressions for the density profile and phase boundaries at the stationary state have been derived, an alternative numerical method is also presented in Appendix 6.5 for determining the solution to the second-order continuum mean-field equations, Eq. (6.13a) and Eq. (6.13b). An important aspect of providing the numerical scheme is the computation of the stationary state density at the left boundary of the lattice, which is dependent on the

Table 6.1: Formulations outlining the conditions for the presence of stationary phases within a lattice via mean-field theory. Here, $Y = \frac{R}{1-z}$.

local densities of all other sites. In the subsequent section, we will employ these conditions to formulate the phase diagrams while varying R and z, aiming to comprehend their influence on the regions housing different stationary phases within the phase diagram.

6.6.1 Phase diagrams: Role of obstruction factor & resetting rate

Now, employing these transition lines, we form the phase diagram in the $\alpha - \beta$ parameter space corresponding to different choices of z and R, as depicted in FIG. 6.2. The phase boundaries depicted in each phase diagram are also validated via extensive Monte Carlo simulations, with comprehensive details provided in Section. 1.3.2.1. Initially, phase diagrams are generated for various resetting rates while maintaining the obstruction factor at zero. Subsequently, in each of these phase diagrams, we increase the magnitude of the obstruction factor to explore its influence on the phase diagrams. For generality, the values of z and R are chosen randomly to encompass the potential range and extreme cases.

Before delving into the detailed analysis of the phase diagram by varying both parameters simultaneously, we revisit their individual effects on the phase diagrams. The phase diagram of conventional open dynamically disordered TASEP (ddTASEP) without resetting consists of four standard stationary phases: LD, MC, HD, and a delocalized LD-HD coexisting phase [140, 15]. For z=0, the phase diagram of ddTASEP converges to that of the standard open TASEP. However, as the magnitude of z increases, the triple point shifts vertically downwards, reducing the HD phase and enhancing the region containing the LD and the MC phase. For z=1, the $\alpha-\beta$ plane gets equally divided between the LD and the MC phase while the HD phase completely disappears. On the other hand, the phase diagram of the standard open TASEP with local resetting (TASEP-LR) consists of two localized coexisting phases: the LD-HD and the MC-HD phase, in addition to the LD, MC, and HD phases [105]. Increasing the resetting rate expands the region containing the MC phase in the phase diagram while it reduces the region of the rest of the phases. Now, we scrutinize in detail into how the introduction of both these parameters affects the phase diagram of the proposed model.

For a very small resetting rate, i.e., for R = 0.03, FIG. 6.2 (a) shows that the phase

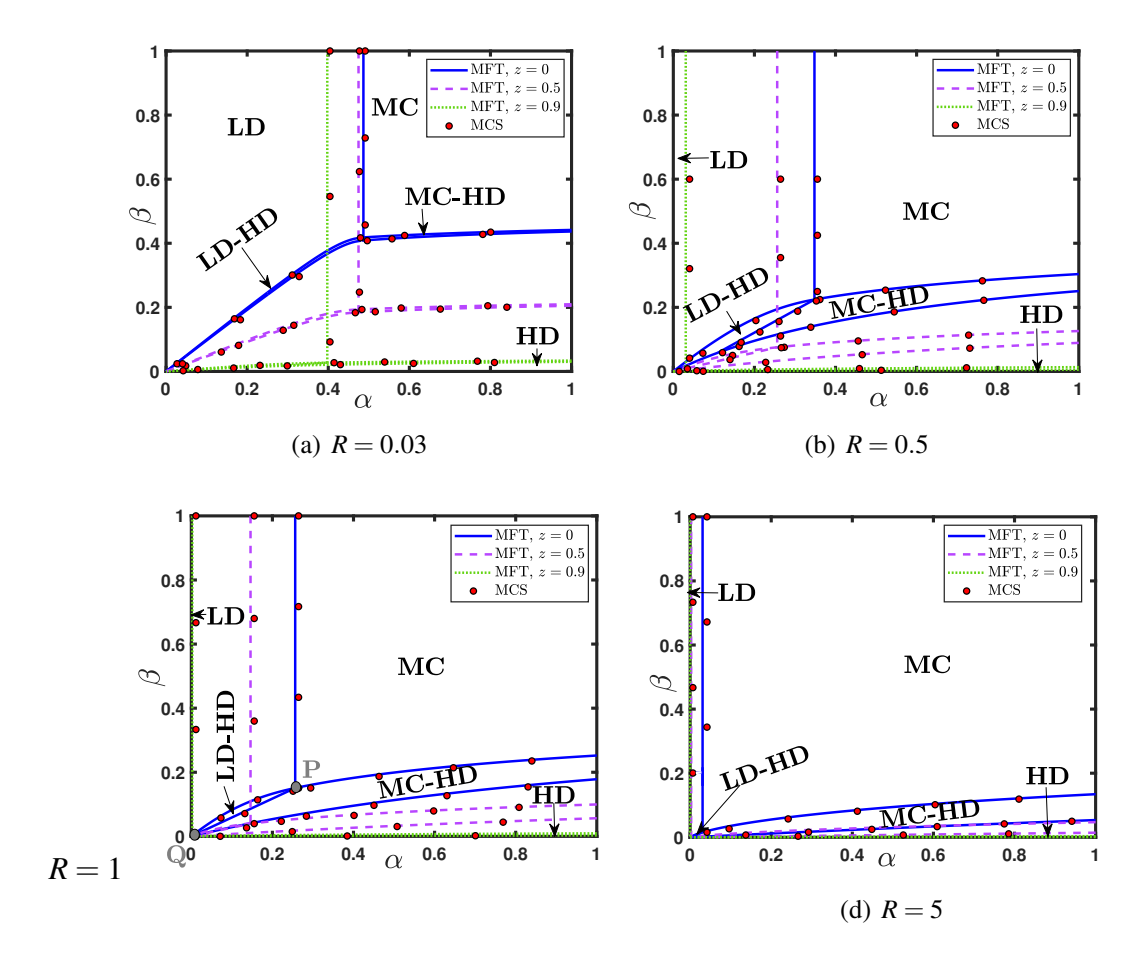


Figure 6.2: Role of the obstruction factor on the stationary state phase diagrams for different choices of the resetting rate.

diagram exhibits the existence of all five possible stationary phases irrespective of the choice of the obstruction factor as well as quadruple point $P(\alpha_1,\beta_1) = \left(\frac{2\beta_1(1-\beta_1)}{1-z},1+0.5W_{-1}\left(Y_1\right)\right)$ and a triple point $Q(\alpha_2,\beta_2) = \left(\frac{2\beta_2(1-\beta_2)}{1-z},-0.5W_0\left(Y_1\right)\right)$, where $Y_1 = -e^{-\left(1+\frac{R}{2(1-z)}\right)}$. The transition curves separating the LD and MC phases from each other and the co-existing phases meet at point P, whereas the curves delineating the HD and the co-existing phases meet at point Q. However, the co-existing phases, the LD-HD and the MC-HD phases lie in a tiny region between two curves, and as $R \to 0$, the LD-HD phase becomes confined to a line, whereas the MC-HD phase vanishes from the phase diagram. Consequently, in this limit, the phase diagram for each choice of the obstruction factor seems to converge to that of an open, dynamically disordered TASEP. For zero obstruction, we recover the phase

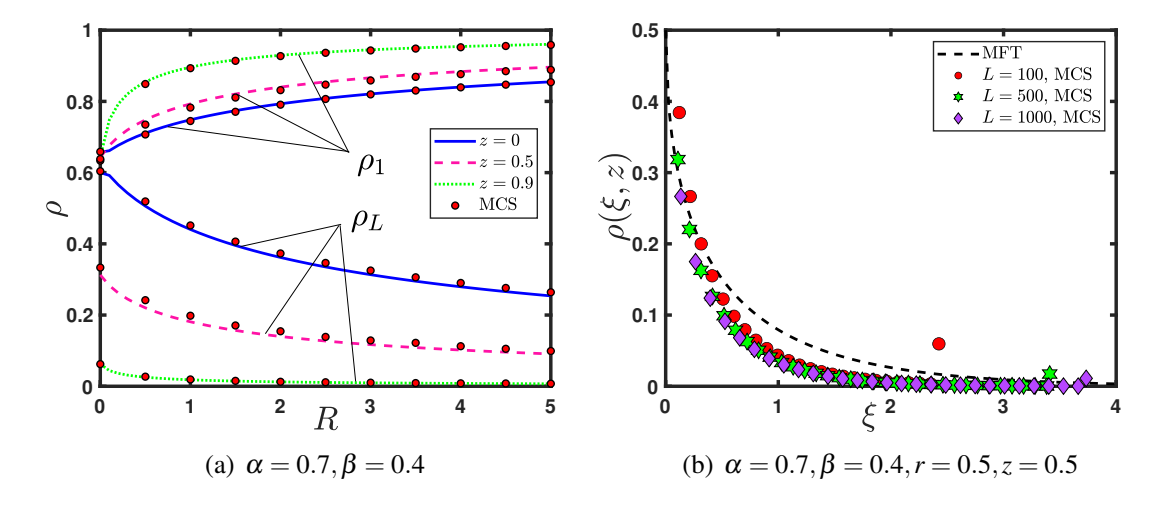


Figure 6.3: (a) Effect of R and z on stationary-state density at entry site and exit site. (b) The MC phase density profile as a function of the re-scaled variable $\xi = \lambda i/L$, where the dotted curve represents the analytical expression of $\rho(\xi,z) = -1/2W_0(-\exp(-1-\xi/(1-z)))$ obtained through the mean-field approach.

diagram corresponding to the conventional open TASEP with small local resetting [105].

Increasing the obstruction to the particle movement to 50% shifts the quadruple point P and the triple point Q anti-diagonally in the phase diagram; see FIG. 6.2 (a). As a result, the MC phase expands, whereas the rest of the phases shrink. For a 90% obstruction on the lattice, the area encompassing the LD and MC phases is significantly predominant in the phase diagram due to a further anti-diagonal shift in the points P and Q. Meanwhile, the area representing the HD phase alongside the co-existing phases exists for a very small range of β . In case of complete obstruction, i.e., z = 1, the system only contains the LD and the MC phase.

Parallel to the case of a low resetting rate, as *R* increases to 0.5, the phase diagram for each choice of the obstruction factor still comprises all five possible stationary phases, as shown in FIG. 6.2 (b). In the absence of the obstruction, the phase diagram for this choice of resetting rate also exactly resembles that of the TASEP-LR model corresponding to the intermediate resetting regime. Increasing the obstruction factor causes a similar impact on the systems phase diagrams even with this choice of resetting rate. Finally, to confirm this trend, we have also constructed the phase diagrams and examined the impact of the

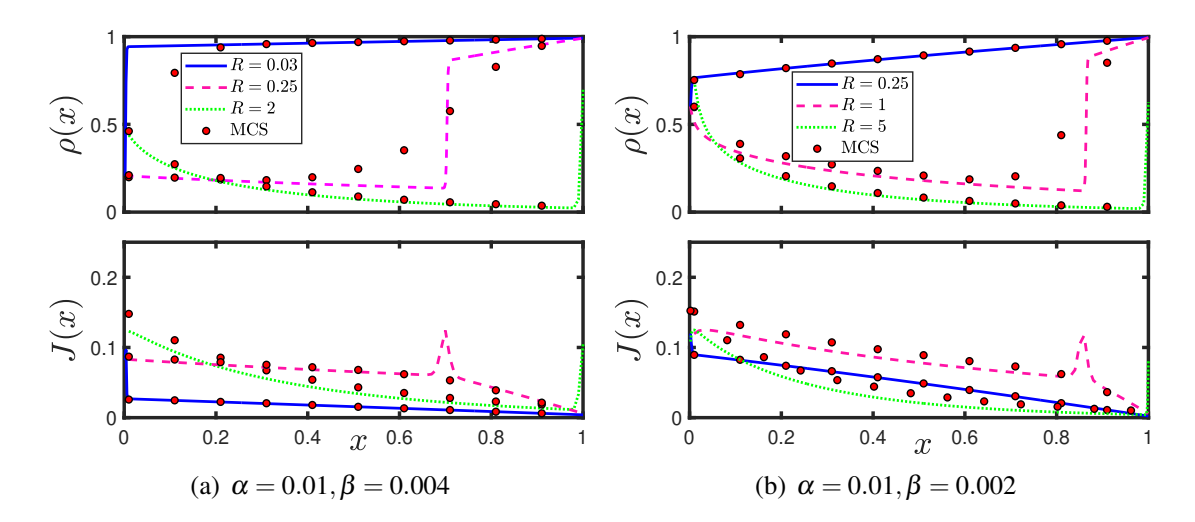


Figure 6.4: Transition in the stationary state density profile and current with respect to R for z = 0.5.

obstruction factor on them for relatively higher resetting rates, i.e., R = 1 and R = 5, depicted in FIG. 6.2 (c) and FIG. 6.2 (d), respectively

6.6.2 Influence of Obstruction Factor and Resetting Rate on Entry and Exit Densities

In an open system, the boundary densities play a crucial role in determining the stationary-state characteristics of the system. As observed in processes like mRNA translation, where the ribosome attaches and detaches at the boundary sites, its density is crucial for protein production and the effectiveness of binding and initiation mechanisms. Previous studies have shown that the average density at the entry (exit) site will increase (decrease) with the increase in the resetting rate considered in the proposed work [17]. In this section, we will examine the influence of the disorder as well as the resetting rate on the densities of these specific sites.

FIG. 6.3 (a) illustrates a monotonic increase in the density of the entry site with respect to R irrespective of the choice of z. Moreover, for $R \to \infty$, we have $\rho_1 \to 1$, and the rate of this convergence depends on the choice of the obstruction factor. It converges faster for a larger choice of the obstruction factor. This can be explained as follows: as the defects offer

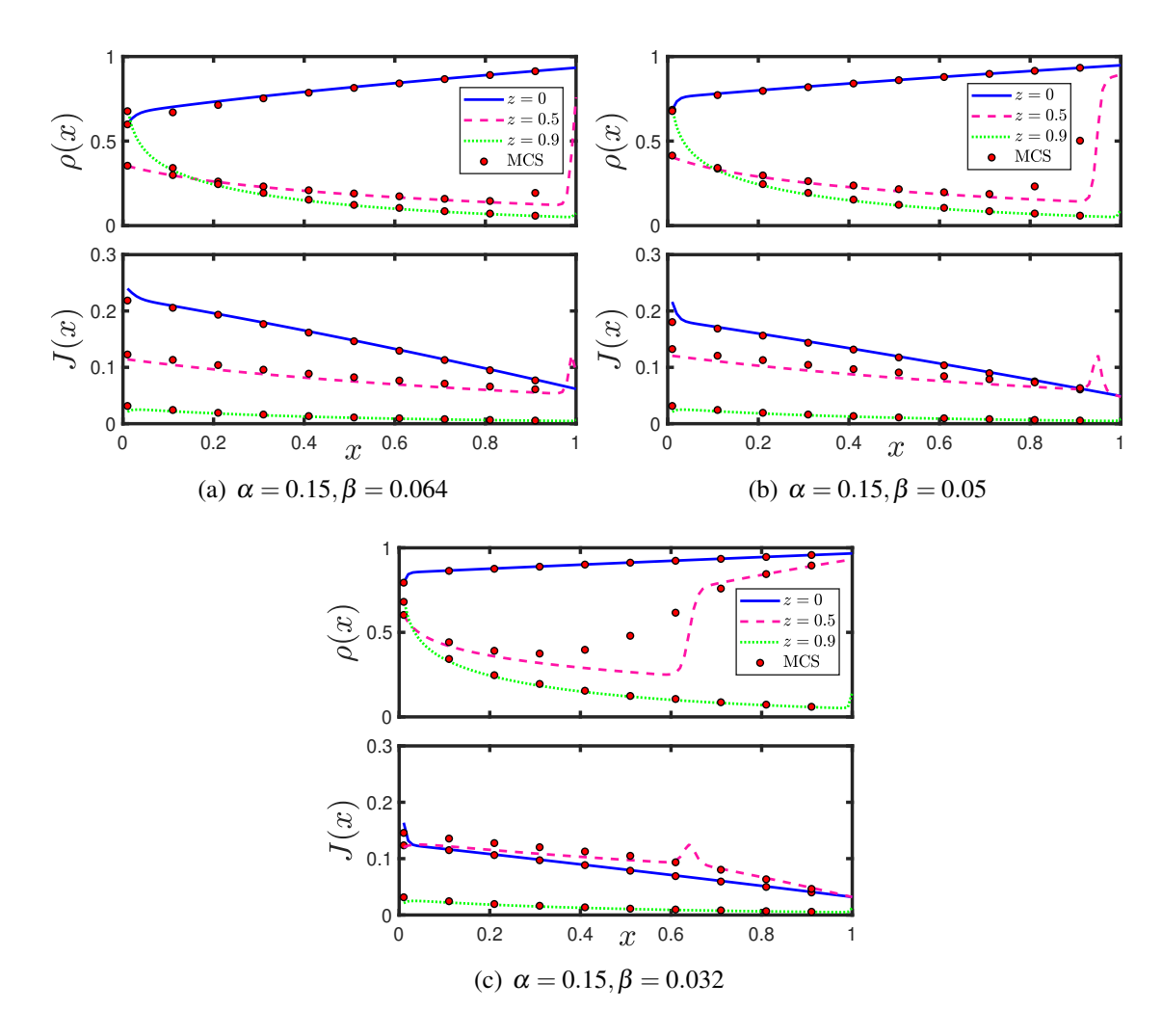


Figure 6.5: Transition in the stationary state density profile and current with respect to z for R = 0.5.

more obstruction to the particles on the lattice, their mobility across the lattice diminishes, allowing each particle to linger on the lattice for longer durations. Hence, it increases the chances of particles getting reset to the first site. In contrast, for any choice of the obstruction factor, the curve for exit site density shows a monotonic decrease with respect to R, as shown in FIG. 6.3 (a). In this scenario, as $R \to \infty$, we have $\rho_L \to 0$. The greater the obstruction factor, the faster the density at the exit site diminishes. This can also be understood in similar ways. We have also observed that in the limit $R \to \infty$ as well as $z \to 1$, the phase diagram is dominated by the MC phase; hence, it is easy to conclude that $\rho_1 \to 1$ and $\rho_L \to 0$ for a density profile in the MC phase.

Further, we have corroborated this trend via density profile for increasingly large and finite sizes of L, as shown in FIG. 6.3 (b). Here, the macroscopic rate R=rL escalates with the lattice size expansion, leading the system into a regime of large resetting for specific parameter configurations. The numerical examination depicted in FIG. 6.3 indicates that the density profile tends towards $\rho_1 \to 1$ and $\rho_L \to 0$, while the bulk density profile for $L \to \infty$ resembles that of the MC phase. To bolster this observation, we've also plotted the analytical expression of the stationary density profile for the MC phase derived within the mean-field framework using Eq. (6.8), reformulated as a function of a scaled position variable $\xi = \lambda i/L$. Consequently, Fig. 6.3(b) clearly illustrates that the analytically derived MC phase profile is in reasonable agreement with the Monte Carlo results. However, the discrepancy between the MCS and MFT results grows with increasing system size, highlighting the influence of finite-size effects on the stationary behavior.

6.6.3 Transition of stationary phases and steady-state current

Now, we aim to understand the potential phase transitions arising from changes in z and R using the stationary state density profiles. Additionally, plotting these profiles will aid in discerning alterations in the lattice current induced by these parameters. In FIG. 6.4, for a fixed choice of entry, exit rate, and obstruction factor, we vary the resetting rate to observe the transitions in the density profiles and the corresponding steady-state current in the lattice. Furthermore, the selection of α and β is made to ensure the observation of distinct possible phase transitions in the system.

The upper panel of FIG. 6.4 (a) depicts the density profiles during the systems' stationary phases transition from the HD phase to the LD-HD phase via the MC phase, and the corresponding lattice current is shown in the bottom panel. The lower panel in FIG. 6.4 (a) reveals that the current profile linked with the high-density phase hits its nadir, owing to the particle-packed lattice. FIG. 6.4 (b) shows the current in the lattice corresponding to the phase transitions observed. For a smaller choice of the exit rate, the top panel of FIG. 6.4 (b) illustrates the phase transitions from the HD phase to the MC phase through the MC-HD phase as the resetting rate increases. In contrast to the previous case, here the intermediate

phase i.e., the LD-HD phase, is replaced by the MC-HD phase, as indicated by the phase diagram: if a system persists in the LD-HD phase, lowering the exit rate will shift it into the MC-HD phase. In line with the earlier scenario, elevating the resetting rate augments the density at entry sites while diminishing it at exit sites, affirming the resetting process's effectiveness within the model. The lower panel in FIG. 6.4 (b) illustrates the current profiles. Note that the lattice current profile exhibits a nonlinear dependence on the density distribution, which governs both the emergence and detectability of discontinuity-induced peaks. Monte Carlo simulations (MCS) with increased spatial points will also exhibit these features.

Now, we examine the density profile concerning the phase transitions obtained by fixing the resetting rate and varying the obstruction factor. For a fixed choice of α and β , the upper panel of FIG. 6.5 (a) shows the transition from the HD phase to the LD phase and further to the MC phase with an increase in the obstruction factor. The upper panels of FIG. 6.5 (b) and 6.5 (c) also depict the phase transition concerning the obstruction factor, albeit for slightly lower exit rate selections. Here, the transitions still proceed from the LD phase to the MC phase, but the intermediate phases change to the LD-HD phase and the MC-HD phase, respectively. The lower panels of FIG. 6.5 illustrate the impact of increasing obstruction factors on the current profiles of respective stationary phases. Note that even if the density profile increases along the lattice length, the current in the bulk of the lattice and at the lattice exit decreases with respect to an increase in R or an increase in z. Physically, it can be interpreted as follows: As the resetting increases, the particles in bulk as well as at the exit quickly reset themselves at the entry site, leading to a decrease in the bulk as well as at the exit current; however, current at the entry site increases. On the other hand, if the obstruction factor increases, the chances of particle hopping to the next particle vacant site decreases, and hence, the current profile shows a decrease with an increase in the obstruction factor.

Similar to the TASEP-LK model [103], the proposed model shows a nonlinear pattern in the lattice current due to the non-linearity in the density. It is attributed to the source term of Eq. (6.17) due to the local resetting, not the dynamic disorder. One can map the proposed

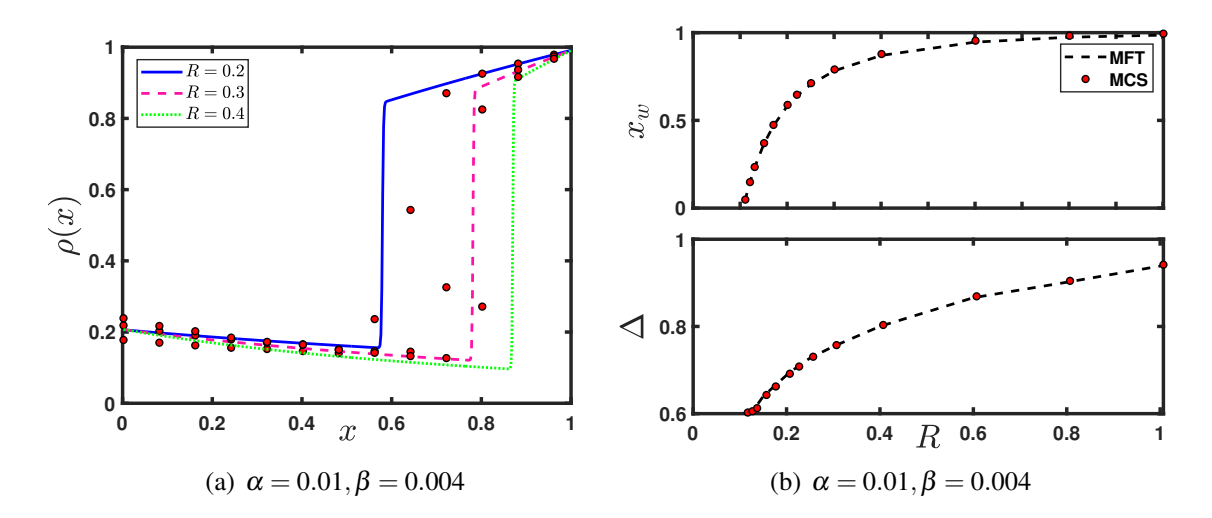


Figure 6.6: (a) Propagation and (b) change in the position and the height of the LD-HD shock profile with respect to R for z = 0.5.

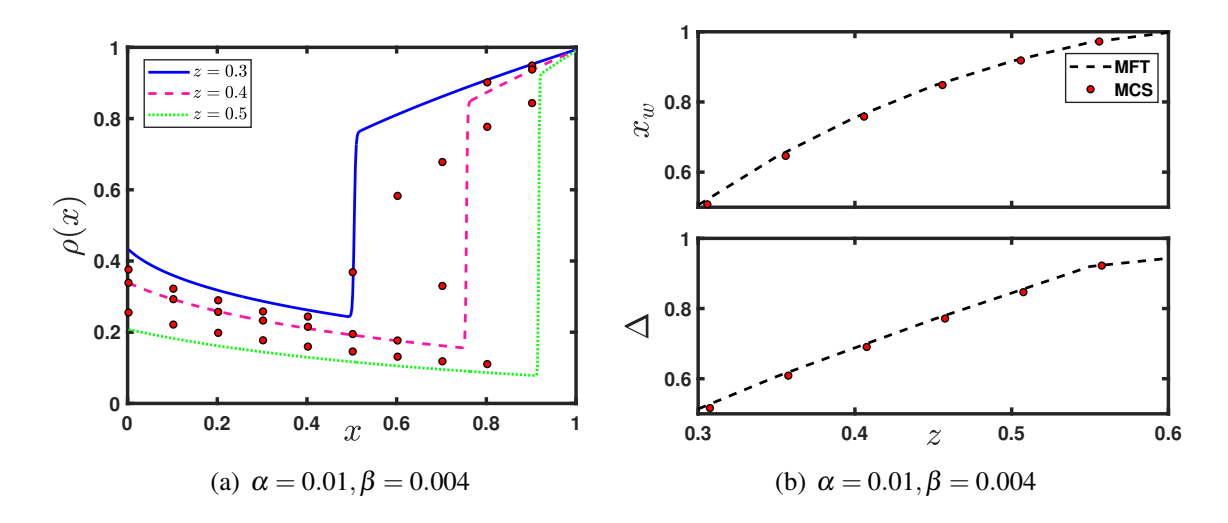


Figure 6.7: (a) Propagation and (b) change in the position and the height of the LD-HD shock profile with respect to z for R = 0.5.

model to the TASEP-LK model within mean-field approximations under certain conditions. The conditions are as follows: the obstruction must be zero, and the resetting process can be seen as a combination of the attachment/detachment process where the detachment and attachment occur in bulk as well as at the exit site with a rate $r(1-\rho_1)$ and 0, respectively. The attachment of particles occurs at the entire site only, thus giving rise to an effective entry rate.

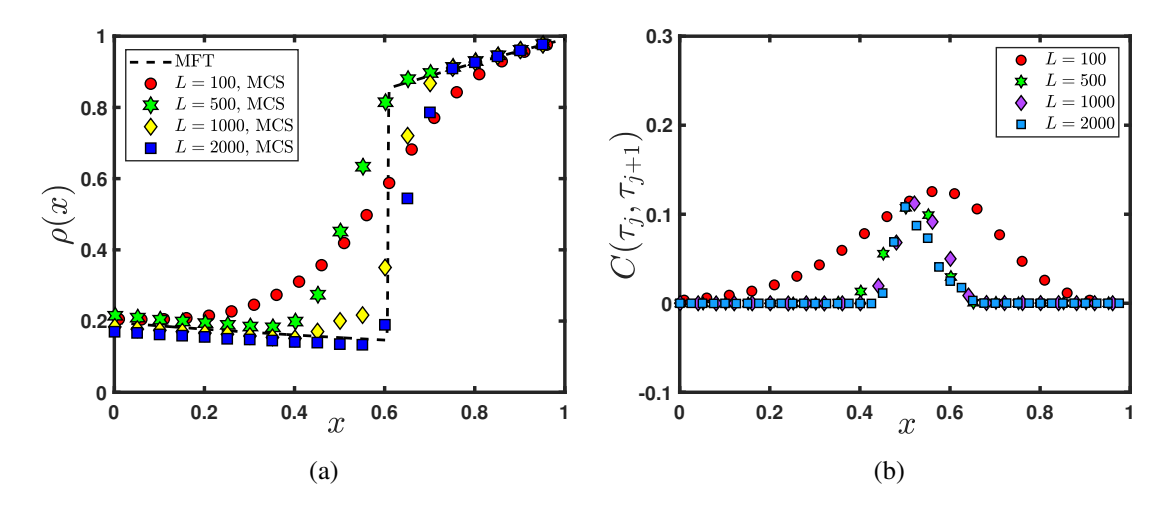


Figure 6.8: Finite-size effect on the LD-HD shock profile and (b) particle-particle correlations in the lattice with respect to R for $\alpha = 0.01$, $\beta = 0.004$, R = 0.2, and z = 0.5.

6.6.4 Domain Wall and Finite-size effect

A domain wall arises from the discontinuous conjunction of the density profiles of two stationary phases in the bulk. As discussed in the previous section, for $R \to 0$, a delocalized domain wall appears in the system in the form of the LD-HD phase, which remains confined to a line in the phase diagram [80]. An infinitesimal amount of resetting leads to not only the expansion of the LD-HD domain wall to a region but also makes it localized in the lattice. It also leads to the emergence of another shock profile, i.e., the MC-HD phase. The region containing both phases shows a non-monotonic behavior concerning the increase in the resetting rate; it initially expands and later diminishes with respect to R. Therefore, we aim to explore how the resetting rate and obstruction factor influence the shock's characteristics, such as position and height.

Initially, we focus on the impact of the resetting rate on the shock profiles by keeping the obstruction factor constant and varying the resetting rate, as illustrated in FIG. 6.6. FIG. 6.6 (a) depicts the position of the localized shock that shifts towards the right with an increase in R. For larger values of R, the shock reaches the right boundary, corroborating the system's transition from the LD-HD phase to the LD phase. Additionally, the height of the shock increases with respect to R, as shown in the lower panel of FIG 6.6 (b). It is also clear

from FIG 6.6 (b) that both the shock position as well as the shock height saturate for a larger value of R. The role of z is analogous to that of R, which is visible from FIG. 6.7. Furthermore, these results are validated via Monte Carlo simulations, which agree well in almost all situations except at the position of the shock.

To explore the finite-size effect in the proposed system, we depicted shock profiles and particle-particle correlations across the lattice for various system sizes L to mitigate the influence of finite system size on the stationary state outcomes, see FIG. 6.8. The findings demonstrate that while the shock position remains stable, the structure of its density profile, obtained via Monte Carlo simulations (MCS), depends on system size. Notably, the shock's inclination sharpens as the system size increases. For further analysis, we examined the particle-particle correlations, which reveal that as the system size increases, these correlations become increasingly confined to the vicinity of the shock position, as shown in FIG. 6.8 (b). Theoretical results obtained through mean-field approximations agree well with the Monte Carlo simulations for large system sizes. One can analyze the shock in the MC-HD phase similarly, where the effect of the resetting rate and the obstruction factor remain invariant on the shock's position and height.

6.7 Conclusion

Motivated by the transport during the biological process of mRNA transcription, we studied a single-channel dynamically disordered TASEP along with the local resetting. The analytical expressions of stationary state results, such as density profiles, currents, and phase boundaries, are derived under the mean-field approximations using the Lambert-W function. The parameters responsible for showcasing defect dynamics on the lattice, such as the affected hopping rate (p_d) and stationary-state defect density (ρ_d) , are integrated into a single parameter called the obstruction factor to reduce the parameter space.

To comprehensively grasp the influence of both the obstruction factor and the resetting rate on the configuration of the phase diagrams, various phase diagrams are generated for different combinations of these parameters. Irrespective of the choice of the obstruction

6.7 Conclusion 171

factor and resetting rate choices, the phase diagram always possesses five stationary phases: the LD phase, the MC phase, the HD phase, the LD-HD phase, and the MC-HD phase. For a fixed choice of obstruction factor and in the small resetting regime (or $R \to 0$), the phase diagram of the proposed model converges to that of a single-channel dynamically disordered TASEP (dd-TASEP). As the parameter R increases, the quadruple and triple point shifts anti-diagonally as R increases. As a result, the region encompassing the shock phases—namely, the LD-HD and the MC-HD phases—initially expands but subsequently contracts along with the other phases beyond a certain threshold. Finally, in the regime of large resetting (or as $R \to \infty$), the phase diagram is predominantly characterized by the MC phase, regardless of the chosen obstruction factor.

For a fixed choice of the resetting rate, in the limit $z \to 0$, the phase diagram of the proposed study reduces to that of the conventional open-TAEP with local resetting [105]. Increasing the obstruction factor induces a similar change in the topology of the phase diagram, i.e., shifting the quadruple and triple point anti-diagonally. This finding is actually in contrast to the dd-TASEP model [15], where the triple point shifts vertically downward with an increase in the obstruction factor. For a fixed entry and exit rate, we have also discussed the density profiles showcasing possible phase transitions that a system can undergo with the changes in the resetting rate and the obstruction factor. Further, their influence on the lattice currents corresponding to the distinct stationary phases is also explored. Similar to the TASEP-LK model [103], both the current and density profiles exhibit non-linear characteristics. Thus, a mapping has been established, subject to specific conditions, through which the proposed model can be reduced to the TASEP-LK model [103]. Lastly, we investigated the role of the resetting rate on the shock dynamics and examined the finite size effect on the stationary state properties.

Concluding the proposed theoretical framework opens up promising avenues for its application within the microscopic realm of biological systems, particularly in contexts where conventional TASEP models elucidate ribosome dynamics. Although the model is generic, it harbors versatile potential for utilization in scenarios involving particle attachment or detachment dynamics. For instance, it can effectively simulate dynamic phenomena like

premature transcription termination followed by subsequent rescue and recycling processes [103, 72, 50]. Further extensions of this work could incorporate more realistic features pertinent to diverse physical and biological systems.



Far from equilibrium transport on TASEP with pockets

Preamble

Inspired by the dynamics of densely packed colloidal particles flowing through narrow channels and their subsequent separation, this chapter explores a geometrically adapted TASEP model incorporating pocket-like structures. These structures, mimicking the asymmetric geometry and outspread areas of channels, serve as the key component in particle separation processes. Our investigation focuses on the stationary state characteristics of this model under both finite and infinite particle resource conditions. This approach aims to provide insights into the complex interplay between channel geometry, particle dynamics, and resource availability in colloidal separation phenomena.

7.1 Background

Mostly studied TASEP models to analyze the system dynamics are coupled to an infinite reservoir in spite of the fact that various real-life processes like mRNA translocation or vehicular flow have resources whose availability is limited in nature [26, 18, 29, 46, 19, 35]. Hence, a TASEP with the constraint on the total number of particles in the system is introduced to invoke the dynamics originated from the particle conservation in the system. The presence of a finite reservoir in these models affects the rate with which particles enter the lattice [1, 33, 32, 22, 57, 56, 54]. As a result, TASEP with limited resources apprehends distinct stationary state properties in comparison to the conventional open-TASEP, which is assumed to be connected to an infinite reservoir. It features characteristics such as formation of a localised domain wall, the extension of a shock phase to a region and the emergence of distinct phases is controlled by the reservoir capacity [66, 137, 138].

Another challenging task is to separate the particles of different sizes that we encounter in the above-discussed biological and physical processes. The usual length of motor protein varies from 10nm - 1 μ m and the similar range can be observed for the densely suspended colloidal particles in a narrow channel [130, 142, 127, 128]. Such a separation is useful to remove unwanted particles in the blood or to isolate different types of blood cells [39, 125, 14]. The structures of these narrow channels have an asymmetric geometry and the key component of separation comes from the outspread areas of the channel which are treated as pockets. To model it, the dynamics of a generalized Asymmetric Simple Exclusion Process was combined with a channel having array of pockets [62]. This model has been studied with periodic boundary conditions [63]. Motivated by the rich and dynamic behavior captured by the open boundary conditions and the stimulated use of TASEP in realistic situations, we propose a study of the single-channel TASEP model with pockets under the open boundary conditions. Both the ends of the lattice are either connected to an infinite or a finite reservoir. Further, each lattice site is connected to a pocket that can accommodate at-most q particles. Our model can describe the physical processes such as the traffic of vehicles on a one-way main road where vehicles enter and exit with dynamic behavior. The main road is connected to several parking spots/side streets on the lateral, where each 7.2 Model 175

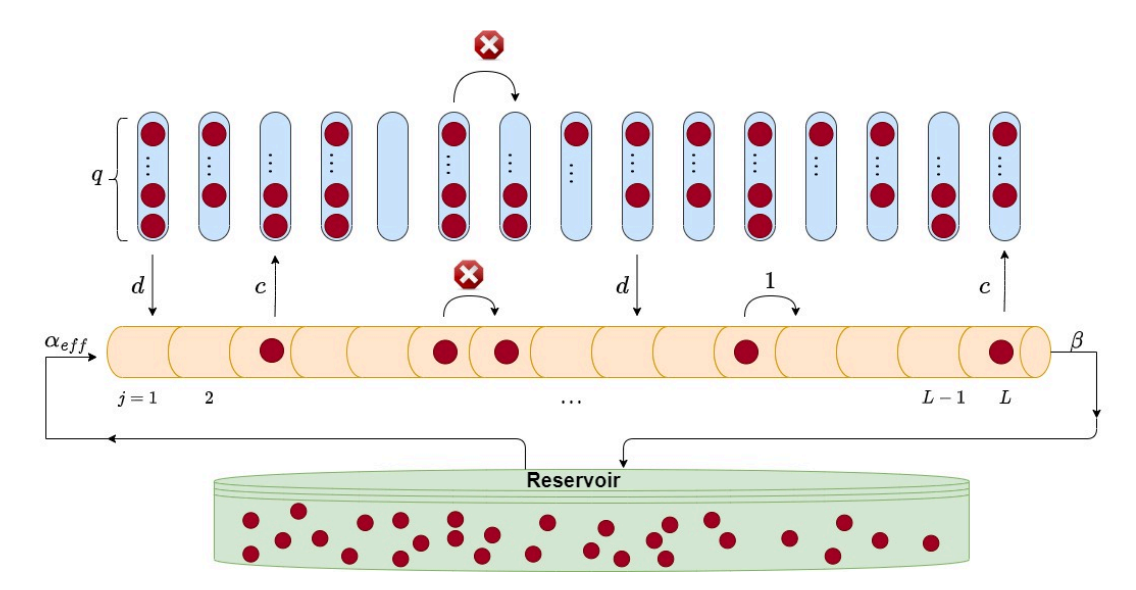


Figure 7.1: A schematic perspective of the pocket model, in which each pocket has the same capacity, say q. Particles (red) enter the first site of the lattice (j = 1) from the reservoir with the rate α_{eff} and depart the lattice from the last site (j = L) with the rate β . The particles migrate from various lattice sites to pockets or vice versa with rates c and d, respectively.

sideways space can withhold an equal and finite amount of traffic. The initial focus is to deal with the above model in the presence of an infinite reservoir and further to explore the overall dynamics of the system with limited resources. We provide a mean-field framework to capture the stationary state properties in the above model such as phase diagrams and density profiles. A prosperous phase behavior can emerge from several ingredients, such as the attachment-detachment rate, capacity parameter, and the number of particles in the finite reservoir. We will be interested in observing the significant changes that phase diagrams and density profiles undergo beneath these ingredients.

7.2 Model

We propose a model comprising a linear filament, which can also be conceived as a 1-D discrete lattice with L sites, each of which is coupled with a *pocket* structure (see FIG. 7.1). The lattice sites are labeled as $j=1,2,\ldots,L$, where j=1(L) represents the entry(exit), and the remaining sites $(j=2,\ldots,L-1)$ are referred to as the bulk of the lattice. The particles from the reservoir (finite or infinite) can only enter the lattice through its first site and rejoin

the reservoir through its last site. The particles on the lattice hop uni-directionally from left to right and can also move laterally to the pocket. Each lattice site is bounded by a hard-core exclusion principle, which states that each site can hold only one particle. However, all the pockets have a unique characteristic known as their capacity (q) which denotes the maximum number of particles that a pocket can accommodate. The particles attach (detach) to (from) lattice site from (to) the corresponding pocket stochcastically: a particle attaches to a vacant lattice site with rate d, whereas an occupied site detaches a particle with rate c. The pockets fail to meet the hard-core exclusion criterion for $q \neq 1$. For a finite choice of q, the pockets collectively can be considered as a finite non-diffusive reservoir as the particles are not allowed to hop between the pockets whereas a case of the model discussed in [29] deals with the particle attachment/detachment from a finite diffusive reservoir. The lateral movement of the particles from lattice to pockets or vice versa depends on the pockets' capacity; therefore, the above model may be thought of as a single channel TASEP with constrained LK dynamics.

The particle dynamics and associated rates that occur at different lattice sites (Entry, Exit, and Bulk) are as follows:

- 1. Entry: If the entry site is occupied, then the particle first tries to detach itself from this lattice site to the corresponding pocket with a rate c, provided the pocket can accommodate the incoming particle. If it fails, the particle hops to its adjacent empty lattice site on the right with a unit rate. For a vacant entry site, a particle in the corresponding pocket first tries to attach to this lattice site with a rate d, if the pocket contains at least one particle. In case it fails, then a particle from the reservoir enters the first site with a rate α .
- 2. *Exit*: If the exit site is occupied, then the particle first tries to detach itself from this lattice site to the corresponding pocket with a rate c, if the corresponding pocket can accommodate the incoming particle. In case it fails, the particle rejoins the reservoir with a rate β . For a vacant exit site, a particle in the corresponding pocket tries to attach to this lattice with a rate d, provided the pocket contains at least one particle.

3. *Bulk*: If the bulk site is occupied, then the particle first tries to detach itself from this lattice site to the corresponding pocket with a rate *c*, if the corresponding pocket can accommodate the incoming particle. If it fails, the particle hops to its adjacent empty lattice site on the right with a unit rate. For a vacant bulk site, a particle in the corresponding pocket attempts to attach to this bulk site with a rate *d*, provided the pocket has at least one particle.

The particle dynamics will be consistent across all pockets as each pocket is solely connected to its associated lattice site but not to the reservoir. Moreover, as pockets are not interconnected, the particles in the pockets can only communicate indirectly with the help of lattice sites.

Furthermore, the reservoir in the model can be treated as a special lattice site connected to both ends of the lattice. We define the modified effective entrance rate, $\alpha_{\rm eff}$ that depends on the number of particles in the reservoir (N_r) , which might be finite or infinite and follows the relation given by $\alpha_{\rm eff} = \alpha g(N_r)$. The choice of g controls the system dynamics, and the inflow rate of particles is proportional to the number of particles in the reservoir [1]. Therefore, g can be considered as a monotonically increasing function, defined as $g(N_r) = \frac{N_r}{N_{tot}}$. To explore the effect of N_{tot} on system dynamics, we define the filling factor [57] as

$$\mu = \frac{N_{tot}}{L}.\tag{7.1}$$

The limiting case, $\mu \to \infty$ corresponds to an infinite reservoir with a constant entry rate, i.e., $\alpha_{\rm eff} = \alpha$.

7.3 Master equations and mean-field analysis of lattice with single-capacity pocket

This section provides mathematical support for the process involved in the proposed model with single-capacity pockets only. For q=1, both lattice sites and pockets strictly follow the hard-core exclusion principle; therefore, we begin our investigation with this case. We

define τ_j and σ_j as the occupational numbers for the j^{th} lattice site and the corresponding pocket, respectively. The random variables τ_j , σ_j are binary since both the lattice and single-capacity pockets fulfill the exclusion criterion. If the site (pocket) is vacant, the corresponding random variable takes 0; if the site (pocket) is occupied, it takes 1. The master equation for the evolution of the average site occupation number in the bulk of the lattice $(2 \le j \le L - 1)$ is given by:

$$\frac{d\langle \tau_j \rangle}{dt} = \langle \tau_{j-1}(1 - \tau_j) \rangle + d\langle (1 - \tau_j)\sigma_j \rangle - \langle \tau_j(1 - \tau_{j+1}) \rangle - c\langle \tau_j(1 - \sigma_j) \rangle, \tag{7.2}$$

whereas at the lattice boundaries, the average site occupation number evolves according to the following equations:

$$\frac{d\langle \tau_1 \rangle}{dt} = \alpha_{\text{eff}} \langle (1 - \tau_1) \rangle + d\langle (1 - \tau_1) \sigma_1 \rangle - \langle \tau_1 (1 - \tau_2) \rangle - c\langle \tau_1 (1 - \sigma_1) \rangle, \tag{7.3}$$

$$\frac{d\langle \tau_L \rangle}{dt} = \langle \tau_{L-1}(1 - \tau_L) \rangle + d\langle (1 - \tau_L)\sigma_L \rangle - \beta \langle \tau_L \rangle - c\langle \tau_L(1 - \sigma_L) \rangle, \tag{7.4}$$

where $\langle \cdots \rangle$ denote the statistical average. Moreover, the evolution of the average site occupation number in pockets is only due to vertical transitions that induce the master equation for pockets given by:

$$\frac{d\langle \sigma_j \rangle}{dt} = c\langle \tau_j (1 - \sigma_j) \rangle - d\langle \sigma_j (1 - \tau_j) \rangle, \quad 1 \le j \le L. \tag{7.5}$$

The above system of equations cannot be solved directly due to the presence of one and two point correlators. So, we employ mean-field approximation that neglects all the possible correlations present in the above system of equations, i.e. $\langle \tau_i \tau_j \rangle = \langle \tau_i \rangle \langle \tau_j \rangle$ or $\langle \tau_i \sigma_j \rangle = \langle \tau_i \rangle \langle \sigma_j \rangle$. We define the average lattice density at site j as $\rho_j = \langle \tau_j \rangle$ and the corresponding average pocket density as $m_j = \langle \sigma_j \rangle$. Now, in order to derive the continuum limit of the model, we coarse grain the lattice by introducing a quasi-continuous variable $x = \frac{j}{L} \in [0, 1]$, the lattice constant as $\varepsilon = \frac{1}{L}$ and re-scaled time $t' = \frac{t}{L}$.

The following can explain the necessity of introducing the reduced kinetic rates. The number of sites $n \sim t$ visited by a particle during hopping depends on the time t it spends

on the lattice before detaching, where $t \sim \frac{1}{c}$. Hence, for fixed c, the fraction $\frac{n}{L} \sim \frac{1}{cL}$ of sites visited by a particle during its walk on the lattice would go to zero as $L \to \infty$. The struggle between bulk and boundary dynamics in large systems will only be evident if particles get enough time to spend on the lattice before detaching; therefore, a total detachment rate is introduced as,

$$\Omega_c = Lc, \tag{7.6}$$

which remains constant for $L \to \infty$. Similar arguments follow for a total attachment rate given by,

$$\Omega_d = Ld. \tag{7.7}$$

When c and d are considered independent of L, the effect of attachment and detachment is negligible for large but finite systems ($L \gg 1$). The consideration of spatial homogeneity on the lattice and pockets along with the application of Taylor series to eq. (7.2) and eq. (7.5) results in,

$$-\frac{\partial^{2}}{\partial x^{2}}\begin{pmatrix} \frac{\varepsilon\rho}{2} \\ 0 \end{pmatrix} + \frac{\partial}{\partial t'} \begin{pmatrix} \rho \\ m \end{pmatrix} + \frac{\partial}{\partial x} \begin{pmatrix} \rho(1-\rho) \\ 0 \end{pmatrix} = \begin{pmatrix} \Omega_{d}m - \Omega_{c}\rho + m\rho(\Omega_{c} - \Omega_{d}) \\ \Omega_{c}\rho(1-m) - \Omega_{d}m(1-\rho) \end{pmatrix}. \quad (7.8)$$

At stationary state, the system of equations given by eq.(7.8) in the limit of $\varepsilon \to 0$ yields a first order differential equation,

$$\frac{\partial \rho}{\partial x} = \frac{\Omega_d m - \Omega_c \rho + m \rho (\Omega_c - \Omega_d)}{1 - 2\rho},\tag{7.9}$$

whereas the boundary conditions are given as,

$$\rho(0) = \alpha_{\text{eff}} \text{ and } \rho(1) = 1 - \beta. \tag{7.10}$$

The differential equation given by the eq. (7.9) with two boundary conditions in eq. (7.10) is over-determined. However, the solution to eq. (7.9) can be found by utilizing only one boundary condition at a time. At a stationary state, we also obtain an essential relationship

between pocket density and lattice density given by,

$$m = \begin{cases} \frac{\Omega_c \rho}{\Omega_d + (\Omega_c - \Omega_d) \rho}; & \Omega_c \neq \Omega_d, \\ \rho; & \Omega_c = \Omega_d. \end{cases}$$
 (7.11)

The above-obtained relation helps in simplifying eq. (7.9), which further reduces to

$$(1 - 2\rho)\frac{\partial \rho}{\partial x} = 0, (7.12)$$

whose solution is readily available and is similar to that of standard TASEP with infinite resources. Furthermore, the pocket density entirely depends upon lattice density and the attachment and detachment rates as per eq. (7.11). The upcoming section will explore the steady-state features like density profiles and phase diagrams of lattice and single-capacity pockets. The lattice would initially be treated with an infinite reservoir, and later with a finite reservoir.

Table 7.1: Expressions for the existence conditions of the density phases in lattice and pocket for $\Omega_c = \Omega_d$.

Density	Phase	Lattice	Pocket
phases	region	density	density
		(ho)	(<i>m</i>)
LD	$\alpha < \min(\beta, \frac{1}{2})$	α	α
HD	$\beta < \min(\alpha, \frac{1}{2})$	$1-\beta$	$1-\beta$
MC	$\min(\alpha, \beta) \geq \frac{1}{2}$	1/2	1/2
S*	$\alpha = \beta, \alpha < \frac{1}{2}$	-	-

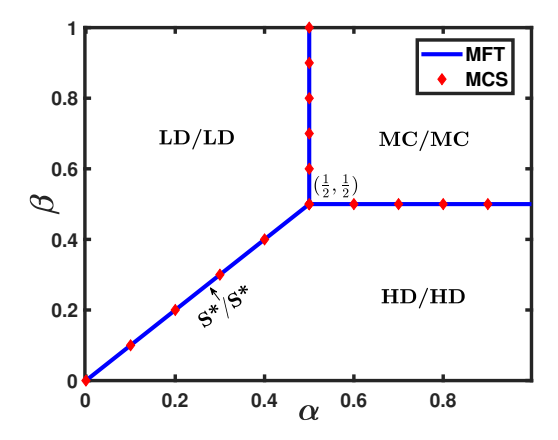


Figure 7.2: The phase diagram of lattice and pocket of any capacity q with infinite resources for $\Omega_c = \Omega_d$, where the first phase refers to the density phase in lattice and the second phase refers to the density phase in the pocket.

7.3.1 Phase plane analysis for infinite resources

For an infinite reservoir, the entry rate of particles becomes independent of the number of particles in the reservoir N_r i.e. $\alpha_{\rm eff} = \alpha$. In the previous section, we found that the first-order differential equation in lattice density given by eq. (7.12) only depends on the entry rate as well as the exit rate but is entirely independent of the pocket density as well as the attachment and detachment rates. Physically, we can interpret the situation with a refutable argument that when the system reaches the stationary state, the net flux between each lattice site and the corresponding pocket becomes zero. As a result, the mean-field equations governing the lattice in the system becomes necessarily equivalent to the standard open-TASEP and the expression for the lattice density in the model given as,

$$\rho(x) = \begin{cases} \alpha; & \alpha < \min\left(\beta, \frac{1}{2}\right), \\ 1 - \beta; & \beta < \min\left(\alpha, \frac{1}{2}\right), \\ \frac{1}{2}; & \min(\alpha, \beta) \ge \frac{1}{2}. \end{cases}$$
 (7.13)

However, the pocket density is entirely dependent on the particle density in the lattice and the attachment-detachment rates as per eq. (7.11). Furthermore, if particle attachment and detachment occur at the same rate ($\Omega_c = \Omega_d$), the pocket density exactly matches the lattice

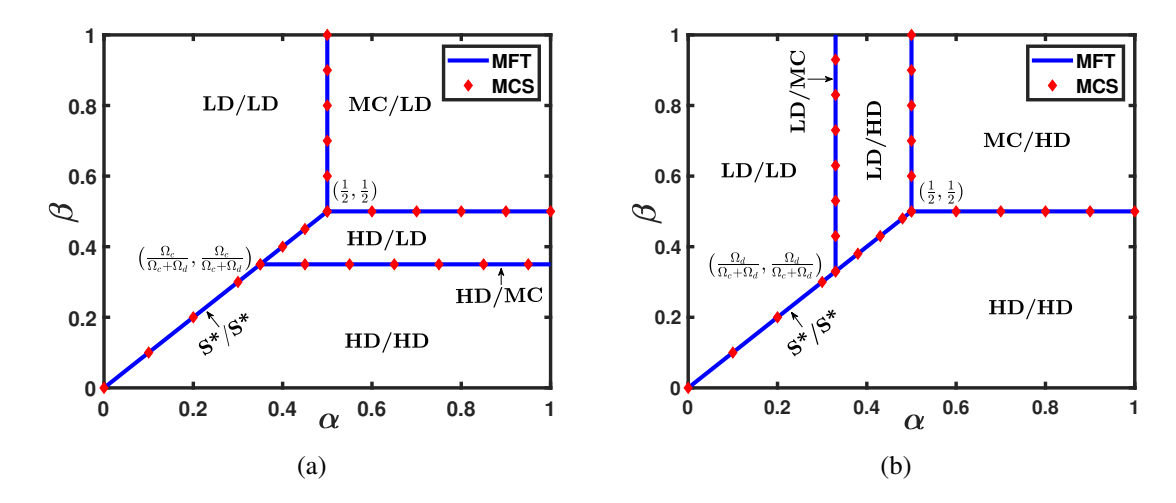


Figure 7.3: The phase diagram of lattice and pocket of any capacity q with infinite resources for $\Omega_c \neq \Omega_d$. (a) The phase diagram (on left) is for $\Omega_c = 0.35$ and $\Omega_d = 0.65$. (b) The phase diagram (on right) is for $\Omega_c = 0.65$ and $\Omega_d = 0.35$.

density. The lattice and pocket phase diagram for the case $\Omega_c = \Omega_d$ is given in FIG. 7.2 that contains each phase of the form A/B, where A and B correspond to the density phase in lattice and pocket, respectively. The set of potential phases, as well as their existential requirements, are summarized in Table 7.1. An important observation must be made in pockets: although there is an only vertical movement of particles and no horizontal movement, they still possess the same density profiles as the lattice. The two-channel TASEP with symmetric coupling also captures this sort of behavior, which implies that the pockets behave identically to the lattice despite not having any horizontal movement in them.

Now, we analyze the case $\Omega_c \neq \Omega_d$. The eq. (7.12) clearly suggests that the lattice phase diagram remains unchanged of the attachment-detachment rates. However, the pocket density varies depending on the lattice density as well as the rates Ω_c and Ω_d , and the phase diagram now includes the same set of phases for pockets which existed in lattices also, namely low-density (LD) phase, high-density (HD) phase, maximal-current (MC) phase, and a non-stationary shock (S*) phase, see FIG. 7.3. The LD (HD) phase in pockets dominates the phase diagram if particle attachment to the lattice occurs at a faster (slower) rate than particle detachment from the lattice. This phenomenon can be explained in a physical context as follows: The higher the attachment (detachment) rate, the more (less) particles

flow from pockets to the lattice, leading the pocket into a LD (HD) dominated phase. On the other hand, no such phase domination is observed for the lattice counterpart. Despite the non-linear relationship relation between m and ρ , the lattice phase diagram remains invariant and behaves just like a standard open-TASEP without pocket. The flow of an infinite number of particles across the lattice may have eliminated the phase domination due to unequal attachment and detachment rates. In contrast to the equal attachment and detachment rates, the MC phase appears only on a line in the pocket phase diagram rather than a region.

Table 7.2: Expressions for the existence conditions of the density phases in pocket for $\Omega_c \neq \Omega_d$.

Pocket phases	Phase region	Phase region	Pocket density
	$(\Omega_c > \Omega_d)$	$(\Omega_c < \Omega_d)$	(<i>m</i>)
LD	$lpha < rac{\Omega_d}{\Omega_c + \Omega_d}$	$eta > rac{\Omega_c}{\Omega_c + \Omega_d}$	$rac{\Omega_{c}lpha}{\Omega_{d}+(\Omega_{c}-\Omega_{d})lpha}$
HD	$lpha>rac{\Omega_d}{\Omega_c+\Omega_d}$	$eta < rac{\Omega_c}{\Omega_c + \Omega_d}$	$\frac{\Omega_c(1-\beta)}{\Omega_d + (\Omega_c - \Omega_d)(1-\beta)}$
МС	$lpha=rac{\Omega_d}{\Omega_c+\Omega_d}$	$eta = rac{\Omega_c}{\Omega_c + \Omega_d}$	$rac{\Omega_c}{\Omega_c + \Omega_d}$
S*	$\alpha=eta<rac{1}{2}$	$\alpha = \beta < \frac{1}{2}$	-

For $\Omega_c \neq \Omega_d$, the explicit and continuous relationship between the lattice density and pocket density in eq. (7.11) always induces a S* phase in the pocket whenever it is there in the lattice. A non-stationary shock (S*) phase appears on the line ($\alpha = \beta < \frac{1}{2}$). The Table 7.2 summarises the list of all conceivable pocket density phases and associated existential requirements for $\Omega_c \neq \Omega_d$. The conditions for the existence of the density phases in lattice remains invariant of Ω_c and Ω_d .

Motivated by the findings of the standard open-TASEP with LK dynamics which has produced a non-trivial effect on system properties like density profiles and phase diagrams

[103]. In contrast, the constrained LK dynamics in the proposed model failed to produce any new lattice phase or change in the density profiles. The constrained attachment and detachment caused by the pockets' limiting capacity might explain this finding. Later, we will also investigate the effect of the increase in pocket capacity on the lattice density profiles and phase diagram. Furthermore, we are also interested in finding whether the limiting case $q \to \infty$ converges to the LK model.

7.3.2 Lattice and pocket compete for finite resources

In the case of limited resources, the entry rate of particles becomes dependent on the number of particles in the reservoir, N_r , i.e., $\alpha_{\text{eff}} = \alpha g(N_r)$. In contrast, the exit rate of particles is assumed to be independent of N_r . It is believed that the free particles in the reservoir are not correlated and homogeneously distributed within the reservoir. Since the number of particles in the system is conserved, the total number of particles N_{tot} can be written as,

$$N_{tot} = N_r + Lm + L\rho, \tag{7.14}$$

Both lattice and pockets can accommodate at most L particles; therefore, the standard open-TASEP limit is approached when $N_{tot} \gg 2L$. The interplay between the finite reservoir and phase diagrams comes into effect when the total number of particles (N_{tot}) in the system is of the order of $N_{tot} \sim 2L$ or smaller.

The phase behavior of a given lattice is entirely determined by its effective entry rate and the exit rate, according to the rules for a standard open-TASEP given in eq. (7.13). The relation between the total number of particles and the number of particles in the reservoir is provided by,

$$N_{tot} = \begin{cases} N_r + L\alpha_{\text{eff}} + L\psi(\alpha_{\text{eff}}); & \alpha_{\text{eff}} < \min(\beta, \frac{1}{2}), \\ N_r + L(1-\beta) + L\psi(1-\beta); & \beta < \min(\alpha_{\text{eff}}, \frac{1}{2}), \\ N_r + \frac{L}{2} + L\psi(\frac{1}{2}); & \min(\alpha_{\text{eff}}, \beta) \ge \frac{1}{2}, \end{cases}$$
(7.15)

where the first, second, and third relations refer to the LD, HD, and MC phase, respectively, and $\psi(\rho) = \frac{\Omega_c \rho}{\Omega_d + (\Omega_c - \Omega_d) \rho}$.

To explore the effect of total number of particles on the system dynamics, we define the filling factor $\mu = \frac{N_{tot}}{L}$ and the reservoir density as $\rho_r = \frac{N_r}{L}$. The equation showing the relationship in terms of reservoir density and filling factor is given by,

$$\mu = \begin{cases} \rho_r + \frac{\alpha \rho_r}{\mu} + \psi(\frac{\alpha \rho_r}{\mu}); & \rho_r < \min(\frac{\beta \mu}{\alpha}, \frac{\mu}{2\alpha}), \\ \rho_r + 1 - \beta + \psi(1 - \beta); & \beta < \min(\frac{\alpha \rho_r}{\mu}, \frac{1}{2}), \\ \rho_r + \frac{1}{2} + \psi(\frac{1}{2}); & \min(\frac{\alpha \rho_r}{\mu}, \beta) \ge \frac{1}{2}. \end{cases}$$
(7.16)

The phase boundaries corresponding to distinct phases can be computed by obtaining ρ_r in that particular phase for a fixed μ .

7.3.2.1 Theoretical calculations for phase existence and phase boundaries $(\Omega_c = \Omega_d)$

The relationship between lattice and pocket density in eq. (7.11) remains intact for the case of a finite reservoir as well. Hence, for an equal attachment and detachment rate, the lattice and pocket density remain the same as the phase diagrams. For the case ($\Omega_c \neq \Omega_d$), the pocket density non-linearly depend on lattice density, which further depend on μ through boundary conditions. Furthermore, to obtain the phase boundaries for both lattice and pocket, it is ideal to split the analysis into two cases, (i) $\Omega_c = \Omega_d$ and (ii) $\Omega_c \neq \Omega_d$. In this case, the density profiles of pockets are exact matches to the lattice of a standard open-TASEP. As a result, the proposed model reduces to the competition of finite resources between two lattices, with horizontal movement restricted among pockets. Due to the same density profiles in both lattice and pockets, the system will possess only symmetric density phases: LD/LD, HD/HD, MC/MC, and S/S, depending upon the total number of particles in the system. This section obtains the possible density phases in the system and their existential conditions for lattice and pocket with equal attachment and detachment rates. The phase boundaries are determined by computing the reservoir density ρ_r and its existential conditions in that phase.

LD/LD Phase

We assume both the lattice and pockets exhibit a low-density phase. Both the segments will be entry-dominated, for which the conditions of existence are given in eq. (7.16). Now, the reservoir density (ρ_r) in this phase is computed as,

$$\rho_r = \frac{\mu^2}{\mu + 2\alpha}.\tag{7.17}$$

The conditions for the existence of this phase utilizing the expression obtained above for reservoir density (ρ_r) are,

$$\alpha\mu < \min\left(\beta(\mu + 2\alpha), \frac{\mu + 2\alpha}{2}\right).$$
 (7.18)

In addition, the constraints on μ (for fixed α and β) for the existence of this phase are obtained as,

$$\mu \begin{cases} < \min\left(\frac{2\alpha\beta}{\alpha-\beta}, \frac{2\alpha}{2\alpha-1}\right); & \alpha > \beta, \alpha > \frac{1}{2} \\ > \max\left(\frac{2\alpha\beta}{\alpha-\beta}, \frac{2\alpha}{2\alpha-1}\right); & \alpha < \beta, \alpha < \frac{1}{2} \end{cases}$$

$$(7.19)$$

Furthermore, the LD/LD phase will always exist in the phase plane irrespective of the choice of μ .

HD/HD Phase

For this phase, the lattice and pockets are assumed to exhibit a high-density phase, where both these segments are exit-dominated and satisfy the existence condition given in eq. (7.16). The density of particles in the reservoir (ρ_r) in the HD phase is,

$$\rho_r = \mu - 2(1 - \beta). \tag{7.20}$$

Similarly, the conditions for the existence of this phase are given as,

$$\alpha\left(\mu - 2(1-\beta)\right) > \beta\mu, \quad \beta < \frac{1}{2},\tag{7.21}$$

whereas the constraints on μ (for fixed α and β) is given by,

$$\mu > \frac{2\alpha(1-\beta)}{|\alpha-\beta|}.\tag{7.22}$$

As a result of the above constraint, we can conclude that the HD/HD phase will exist for $\mu \in (1, \infty)$, whereas it cease to exist in the phase plane for $\mu \leq 1$.

S/S phase

The conservation of particle number in the lattice leads to a localized shock denoted by S. The explicit relation given by eq. (7.11) between lattice and pocket density produces a shock in the pocket whenever it exists in the lattice. Furthermore, the shock can completely be characterized by obtaining its location and height in the lattice and pockets. Since we are dealing with the case $\Omega_c = \Omega_d$, therefore, the position s and the height of the shock Δ on both the lattice and pockets remain the same. The expression for shock position can be obtained using the particle number conservation and given as,

$$s = \frac{\mu(\alpha - \beta) - 2\alpha(1 - \beta)}{2\alpha(\beta - 1)},\tag{7.23}$$

whereas the height of the shock is given as,

$$\Delta = 1 - 2\beta. \tag{7.24}$$

Clearly, the shock height only depends on the parameter β , but not upon μ and α . In contrast, its position is a function of all three parameters α , β and μ . The S phase exists for 0 < s < 1, and using the fact that the transition from LD to S phase occurs when s = 1 and the transition from HD to S phase occurs when s = 0 [57]. The conditions for the existence of S/S phase are,

$$2\alpha\beta < \mu(\alpha - \beta) < 2\alpha(1 - \beta). \tag{7.25}$$

For a fixed α and β , the eq. (7.25) suggests that there always exist a range of μ for which the S/S phase arises.

MC/MC Phase

In this case, the lattice and pocket are assumed to have a maximal-current phase. The reservoir density (ρ_r) in the MC/MC phase is given as,

$$\rho_r = \mu - 1. \tag{7.26}$$

The conditions for the existence of this phase are given as,

$$2\alpha(\mu - 1) \ge \mu, \ \beta \ge \frac{1}{2},\tag{7.27}$$

and the constraint on μ for the existence of MC/MC phase (for fixed α and β) is computed as,

$$\mu \ge \frac{2\alpha}{|2\alpha - 1|}.\tag{7.28}$$

In conclusion, the MC/MC phase only exist for $\mu \in (1, \infty)$.

Phase plane analysis

For smaller values of μ in FIG. 7.4, only LD/LD and S/S phases appear in the phase diagram. Physically, at this stage, the scarcity of the particles in the system leads to a reduced effective arrival, resulting in low density. The presence of the S/S phase suggests the negligible effect of the attachment-detachment process on system dynamics. In contrast, an expansion in the S/S phase and a shrinking in the LD/LD phase can be observed when the value of μ is further increased but kept less than 1.

Additionally, upon further increasing μ and disrupting its critical value of $\mu=1$, the MC/MC and HD/HD phases begin to emerge in the phase diagram. No significant topological change has been observed in the phase diagrams beyond $\mu=1$, except for a shift in the phase boundaries, resulting in the expansion of HD/HD and MC/MC phases but shrinkage of LD/LD and S/S phases. For a system of an infinite number of particles $\mu \to \infty$, we can clearly see that the phase diagram of both lattice and pocket converges to the standard open-

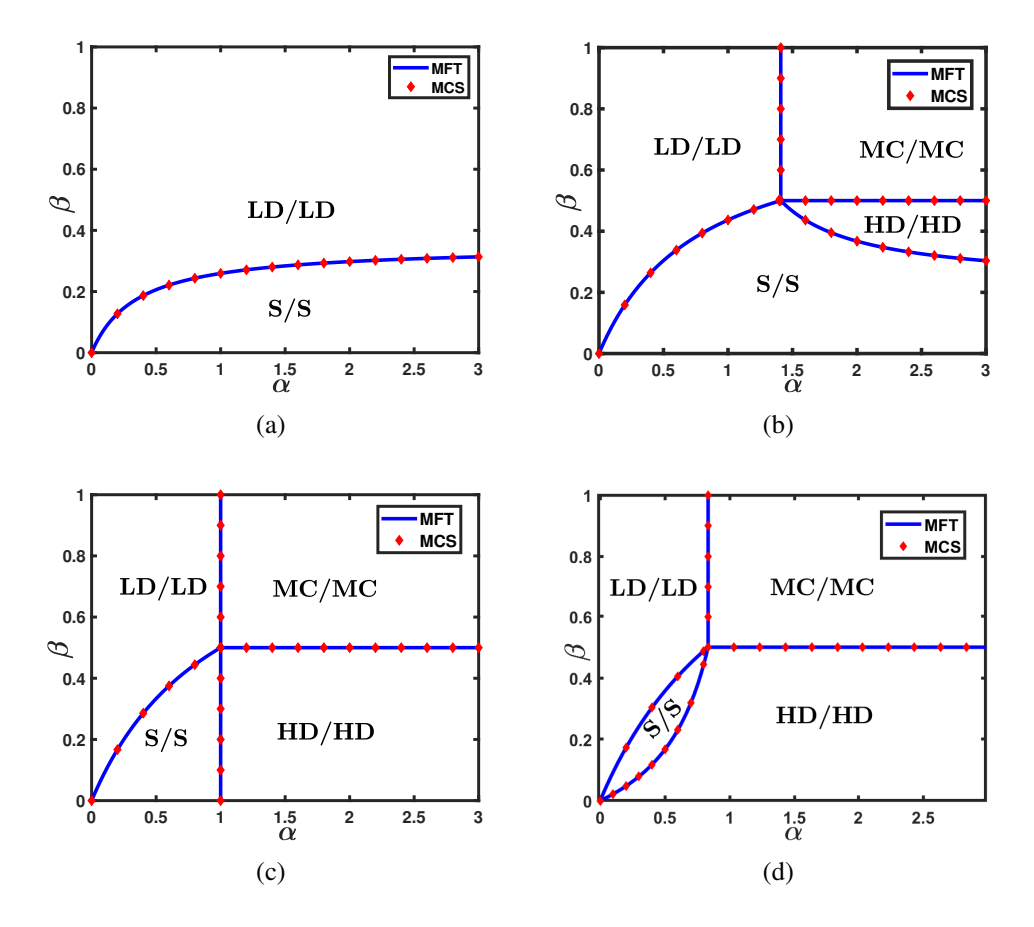


Figure 7.4: The effect of μ on the phase diagram of lattice and single-capacity pocket phase for the case $\Omega_c = \Omega_d$. (a) $\mu = 0.7$, (b) $\mu = 1.55$, (c) $\mu = 2$, (d) $\mu = 5$.

TASEP. The steady-state dynamics of the proposed system produce the conditions for the existence of phases that precisely match the model of two homogeneous TASEP coupled to a finite reservoir [54]. This implies that, despite the lack of horizontal movement, the pockets here also behave similarly to that of a lattice.

7.3.2.2 Theoretical calculations for phase existence and phase boundaries $(\Omega_c \neq \Omega_d)$

The discussion of phase diagrams of lattice and pockets for the case $\Omega_c \neq \Omega_d$ is further divided into two sub-cases: $\Omega_c > \Omega_d$ and $\Omega_c < \Omega_d$. For the sake of simplicity, we discuss the case $\Omega_c > \Omega_d$, and the other case can simply be explained through the particle-hole symmetry. Parallel to the case of infinite resources, the non-linear relationship between lattice and pocket density may give rise to the existence of non-symmetric phases along with the

symmetric phases. As lattice is explicitly connected to the reservoir, we first obtain the conditions for the existence of four different phases (LD, HD, MC, or S) in lattice depending upon the availability of resources. Further, we utilize this information to discuss the possibility of pocket density in any of the four possible phases.

i) Lattice in LD Phase:

In this case, we assume the lattice to be in the LD phase, and the reservoir density (ρ_r) in that case can be obtained from eq. (7.16) and provided as,

$$A\rho_r^2 + B\rho_r + C = 0, (7.29)$$

where $A=\alpha(\mu+\alpha)$, $B=\frac{\mu\left(\alpha(\Omega_c+\Omega_d)-\mu\alpha(\Omega_c-\Omega_d)+\mu\Omega_d\right)}{\Omega_c-\Omega_d}$ and $C=-\frac{\mu^3\Omega_d}{\Omega_c-\Omega_d}$. The conditions for the existence of LD phase in the lattice utilising the above obtained reservoir density is given as,

$$\alpha(-B \pm \sqrt{B^2 - 4AC}) < \min(2\beta\mu A, \mu A). \tag{7.30}$$

The attachment and detachment rates decide the choice of the sign in the above equation, where the + and - signs correspond to the cases $\Omega_c > \Omega_d$ and $\Omega_c < \Omega_d$, respectively. The expression for lattice density in LD phase is obtained as,

$$\rho_{\rm LD} = \frac{\alpha(-B \pm \sqrt{B^2 - 4AC})}{2A\mu} \tag{7.31}$$

Now, assuming the lattice to be in LD phase, the existence conditions for different density phases that a pocket can possess by utilising eq. (7.11) are given as,

$$m = \frac{\Omega_c \alpha_{\text{eff}}}{\Omega_d + (\Omega_c - \Omega_d) \alpha_{\text{eff}}} \begin{cases} < \frac{1}{2}; & \text{Pockets in LD,} \\ > \frac{1}{2}; & \text{Pockets in HD,} \\ = \frac{1}{2}; & \text{Pockets in MC.} \end{cases}$$
(7.32)

which are equivalent to,

$$\frac{\Omega_d}{\Omega_c + \Omega_d} \begin{cases}
> \alpha_{\text{eff}}; & \text{Pockets in LD,} \\
< \alpha_{\text{eff}}; & \text{Pockets in HD,} \\
= \alpha_{\text{eff}}; & \text{Pockets in MC.}
\end{cases}$$
(7.33)

While assuming the lattice is in the LD phase, the existence of HD and MC phases in pockets is only possible for the case $\Omega_c > \Omega_d$. In addition, the LD phase can also exist in pockets for any choice of Ω_c and Ω_d whenever the lattice is in the LD phase. Furthermore, the continuous relationship between lattice and pocket density and the assumption of lattice in the LD phase also neglects the possibility of the S phase in pockets.

ii) Lattice in HD Phase:

Now, assuming the lattice to be in HD phase, the (ρ_r) from eq. (7.16) can be computed as,

$$\rho_r = \frac{\left(\mu - (1 - \beta)\right)\left(\Omega_d + (\Omega_c - \Omega_d)(1 - \beta)\right) - \Omega_c\left(1 - \beta\right)}{\Omega_d + \left(\Omega_c - \Omega_d\right)\left(1 - \beta\right)}.$$
(7.34)

The conditions referring to a HD phase in lattice are,

$$\frac{\alpha \left(\mu - (1 - \beta)\right) \left(\Omega_d + (\Omega_c - \Omega_d)(1 - \beta)\right) - \Omega_c \left(1 - \beta\right)}{\beta \mu \left(\Omega_d + (\Omega_c - \Omega_d)(1 - \beta)\right)} > 1,\tag{7.35}$$

and

$$\beta < \frac{1}{2}.\tag{7.36}$$

The expression for the density of lattice in the HD phase is given by,

$$\rho_{HD} = 1 - \beta. \tag{7.37}$$

The existence conditions on the possible pocket phases assuming the lattice is in HD phase are,

$$\frac{\Omega_d}{\Omega_c + \Omega_d} \begin{cases}
> 1 - \beta; & \text{Pockets in LD,} \\
< 1 - \beta; & \text{Pockets in HD,} \\
= 1 - \beta; & \text{Pockets in MC.}
\end{cases}$$
(7.38)

It is pretty evident from the above relation that the HD phase exists in pockets for any choice of Ω_c and Ω_d whenever the lattice is in the HD phase. Additionally, the pockets can also possess the LD and MC phases whenever the lattice is in the HD phase, and the attachment rate is greater than the detachment rate. The reason for the non-existence of the S phase here follows the same explanation given in the previous case.

iii) Lattice in S Phase:

We assume the lattice in a S phase and attempt to find the possible phases that a pocket can have. Again it is evident from eq. (7.11) that the pocket will have a shock phase only whenever it exists in the lattice. To further characterize the shock, we compute its location and height in the lattice and pocket. As a result of eq. (7.11), the shock position in lattice and pocket remains the same and hence denoted by s_1 . Utilizing the particle number conservation, the expression for shock position is computed as,

$$s_1 = \frac{\mu(\alpha - \beta) - \alpha(1 - \beta) - \alpha\psi(1 - \beta)}{\alpha(2\beta - 1 + \psi(\beta) - \psi(1 - \beta))}.$$
(7.39)

With increase in μ , the shock position continuously shifts to the left for fixed α and β . The transition from LD phase to S phase occurs for $s_1 = 1$ whereas the HD-S phase transition occurs for $s_1 = 0$. For S phase to exist, $0 < s_1 < 1$ and hence the conditions for its existence in lattice and pocket are provided as,

$$\alpha \left(-B \pm \sqrt{B^2 - 4AC} \right) > 2\beta \mu A, \tag{7.40}$$

and

$$\frac{\alpha \left(\mu - (1 - \beta)\right) \left(\Omega_d + (\Omega_c - \Omega_d)(1 - \beta)\right) - \Omega_c \left(1 - \beta\right)}{\beta \mu \left(\Omega_d + (\Omega_c - \Omega_d)(1 - \beta)\right)} < 1. \tag{7.41}$$

Contrary to the shock position, the heights of the shock in lattice and pocket differ and are given as,

$$\Delta_1 = 1 - 2\beta$$
, and $\Delta_2 = \psi(1 - \beta) - \psi(\beta)$, (7.42)

respectively. This shows that the shock height in both the lattice and pocket remains invariant with respect to α , whereas it decreases with respect to β . Moreover, contrary to the shock height in the pocket, the shock height in the lattice is independent of attachment and detachment rates.

iv) Lattice in MC Phase:

For this case, the lattice is assumed in the MC phase with density its $(\rho_{MC} = \frac{1}{2})$ and the reservoir density correspond to this phase from eq. (7.16) can be computed as,

$$\rho_r = \mu - \frac{\left(3\Omega_c + \Omega_d\right)}{2\left(c + d\right)},\tag{7.43}$$

The conditions for the existence of MC phase in lattice are provided as,

$$\alpha \ge \frac{\mu\left(\Omega_c + \Omega_d\right)}{2\mu\left(\Omega_c + \Omega_d\right) - \left(3\Omega_c + \Omega_d\right)}, \quad \beta \ge \frac{1}{2},$$
(7.44)

The existence conditions of different density phases in pockets while assuming the lattice in a MC phase are,

$$\frac{\Omega_d}{\Omega_c + \Omega_d} \begin{cases}
> \frac{1}{2}; & \text{Pockets in LD,} \\
< \frac{1}{2}; & \text{Pockets in HD,} \\
= \frac{1}{2}; & \text{Pockets in MC.}
\end{cases}$$
(7.45)

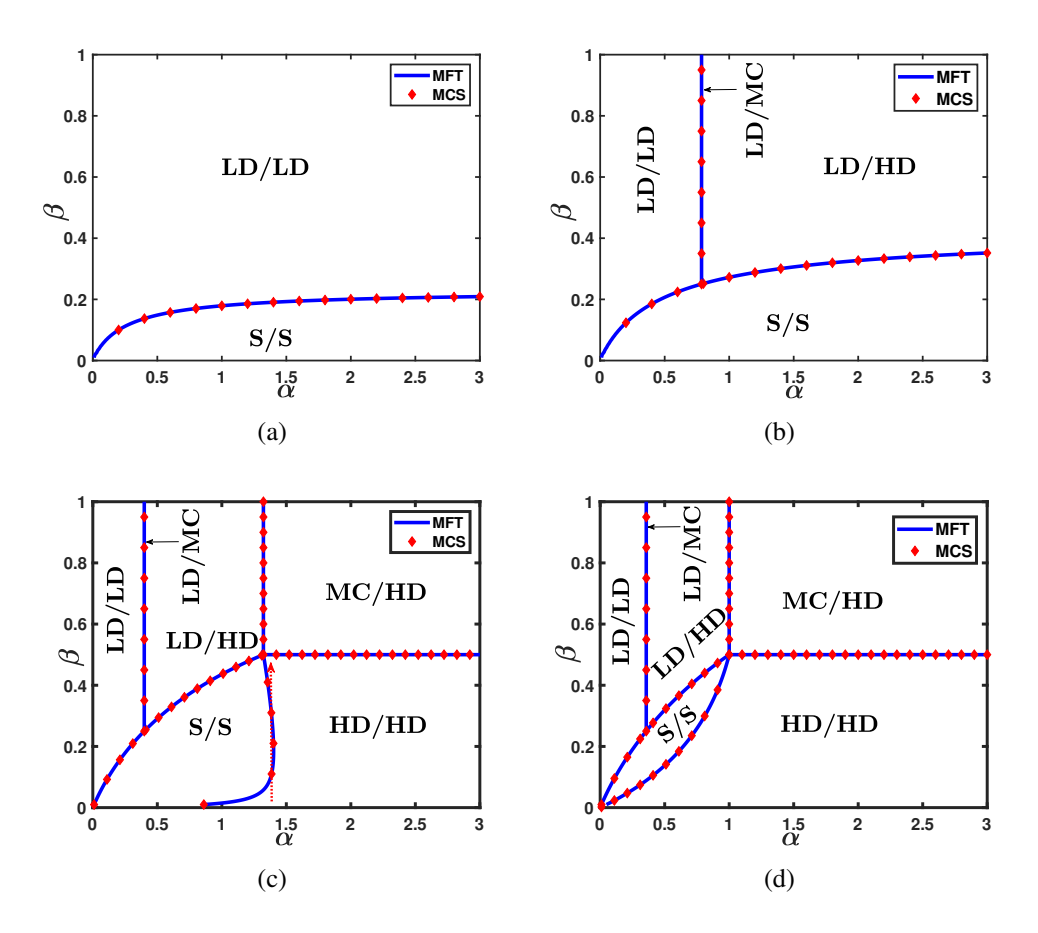


Figure 7.5: The effect of μ on phase diagrams of lattice and single-capacity pockets for the case $\Omega_c > \Omega_d$, where $\Omega_c = 0.3$ and $\Omega_d = 0.1$ (a) μ = 0.7, (b) μ = 1.1, (c) μ = 2.01, (d) μ = 2.5. The arrow (in black) refers to the region occupied by the corresponding density phase. The dotted arrow (in red) refers to the back and forth (reentrant) transition.

Therefore, the assumption of lattice in a MC phase concludes that the pockets can either be in a LD phase if $\Omega_c < \Omega_d$ or in a HD phase if $\Omega_c > \Omega_d$. Moreover, the S phase cannot appear in pockets whenever the lattice is in the MC phase following the same explanation provided in previous cases, whereas the above-obtained relation clearly neglects the possibility of the existence of the MC phase in pockets whenever the lattice is in MC phase.

Phase plane analysis

The effect of the filling factor (μ) on the phase diagrams of both lattice and pocket with unequal attachment and detachment rates is shown in FIG. 7.5. For smaller values of μ

i.e., $0 < \mu < \mu_1^* = \frac{\Omega_c + 3\Omega_d}{2(\Omega_c + \Omega_d)}$, both lattice and pockets can only possess a LD and a S phase; therefore the phase plane consists of only two phases that are LD/LD and S/S phases. The occurrence of only these two phases can be explained due to the lesser number of particles in the system. As soon as μ surpasses the value μ_1^* , the lattice will hold onto the LD and S phases only but now all the four phases (LD, HD, MC, and S) are observed for the pocket. This results in the existence of two additional phases, LD/MC and LD/HD, in the phase diagram along with the preexisting phases (LD/LD and S/S).

Moreover, the MC phase in pockets just occurs on a line, which is similar to that of the pockets in the case of the infinite reservoir. The further increase in the value of μ in the range $\mu_1^* < \mu < \mu_2^* = \frac{3\Omega_c + \Omega_d}{2(\Omega_c + \Omega_d)}$ doesn't add any new phases to either lattice or pocket, but shift in the phase boundaries are observed. The instant μ is chosen more than μ_2^* , the lattice begins to possess two more phases, HD and MC, whereas no new phase appears in the pockets. The addition of two more phases, HD/HD and HD/MC, concludes a total of six phases in the phase diagram.

The FIG. 7.5(c) illustrates that the further increase in the value of μ causes the phase boundaries to form such a peculiar structure and a phenomenon is captured in the form of back-and-forth transition [22, 138]. It can be observed that for a fixed α when β is increased, the phase transition occurs in the following manner: $HD/HD \rightarrow S/S \rightarrow HD/HD$. Finally, in the limit $\mu \to \infty$, the phase diagram converges to the one obtained for the infinite reservoir, see FIG. 7.3(b). After exploring the single-capacity pocket model, the next goal of our research is to enhance the capacity of the pockets and study dynamical changes occurring to the model at a stationary state.

7.4 Master equations and mean-field analysis of lattice with multiple-capacity pocket

In the previous sections, we studied a geometric adaptation of the standard TASEP whose each site is connected to a lateral pocket with a unit capacity. We computed their stationary state properties like density profiles and phase diagrams when both infinite and finite resources were made available in the reservoir. In real-life situations, most of the non-equilibrium stochastic transport systems may have dead-end-like structures with more than one capacity. For example, each pocket may be considered a parking place/side-road that can accommodate more than one vehicle. Therefore, we introduce a generalized version in the TASEP adaptation where each lateral pocket has an enhanced capacity. The particle dynamics and transition rates on the linear filament as well as pockets remain unchanged.

We are interested in analyzing the effects of the parameter capacity and attachment-detachment rates on the stationary state properties like density profiles and phase diagrams of the multiple-capacity pocket model. To do so, we retain the same notation τ_j for the lattice occupation number as it obeys the hard-core exclusion principle. In contrary to the lattice, now pocket fails to obey the hard-core exclusion therefore we define the probability mass function $m_{j,i}$ that denotes the possibility of having an i-many particle in the j^{th} pocket, where $1 \le j \le L$ and $0 \le i \le q$. The temporal evolution of particle density in pockets $(1 \le j \le L)$ are given by the modified system of master equations,

$$\frac{dm_{j,i}}{dt} = d\langle (1-\tau_j)\rangle m_{j,i+1} + c\langle \tau_j\rangle m_{j,i-1} - d\langle (1-\tau_j)\rangle m_{j,i} + c\langle \tau_j\rangle m_{j,i}; \ 1 \le i \le q-1,$$
(7.46)

$$\frac{dm_{j,0}}{dt} = d\langle (1-\tau_j)\rangle m_{j,1} - c\langle \tau_j\rangle m_{j,0},\tag{7.47}$$

$$\frac{dm_{j,q}}{dt} = c\langle \tau_j \rangle m_{j,q-1} - d\langle (1 - \tau_j) \rangle m_{j,q}. \tag{7.48}$$

The density evolution in the bulk of the lattice $(2 \le j \le L - 1)$ can be written as,

$$\frac{d\langle \tau_j \rangle}{dt} = \langle \tau_{j-1}(1-\tau_j) \rangle + d\langle (1-\tau_j) \rangle (1-m_{j,0}) - \langle \tau_j(1-\tau_{j+1}) \rangle - c\langle \tau_j \rangle (1-m_{j,q}), \quad (7.49)$$

whereas at the lattice boundaries, the density evolves according to the following equations:

$$\frac{d\langle \tau_1 \rangle}{dt} = \alpha_{\text{eff}} \langle (1 - \tau_1) \rangle + d\langle (1 - \tau_1) \rangle (1 - m_{1,0}) - \langle \tau_1 (1 - \tau_2) \rangle - c\langle \tau_1 \rangle (1 - m_{1,q}), \quad (7.50)$$

and,

$$\frac{d\langle \tau_L \rangle}{dt} = \langle \tau_{L-1}(1-\tau_L) \rangle + d\langle (1-\tau_L) \rangle (1-m_{L,0}) - \beta \langle \tau_L \rangle - c\langle \tau_L \rangle (1-m_{j,q}). \quad (7.51)$$

The above system of coupled equations involve one and two point correlators and hence cannot be solved analytically. Therefore, we deploy mean-field approximations that ignores all the possible correlations in the system. Similar to the single-capacity case, we drop the subscript j in the absence of spatial in-homogeneity and coarse grain the lattice to obtain the the continuum version of the eq. (7.49) given as,

$$-\frac{\varepsilon}{2}\frac{\partial^2 \rho}{\partial x^2} + \frac{\partial \rho}{\partial t'} + (1 - 2\rho)\frac{\partial \rho}{\partial x} = \Omega_d(1 - \rho)(1 - m_0) - \Omega_c \rho(1 - m_q). \tag{7.52}$$

In the limit $\varepsilon \to 0$, the master equation in the steady-state reduces to a non-linear first-order ordinary differential equation given as,

$$(1-2\rho)\frac{\partial\rho}{\partial x} = \Omega_d(1-\rho)(1-m_0) - \Omega_c\rho(1-m_q). \tag{7.53}$$

The density distribution in multiple-capacity pockets at the stationary state are obtained utilising eqs.(7.46)-(7.48) which further deduces a relation of the form,

$$m_i = A^i m_0; \ 1 \le i \le q,$$
 (7.54)

where $A = \frac{\Omega_c \rho}{\Omega_d (1-\rho)}$. Utilizing the Kolmogorov's second probability axiom on the density function m_i to get,

$$m_0 = \begin{cases} \frac{1-A}{1-A^{q+1}}; & A \neq 1, \\ \frac{1}{q}; & A = 1. \end{cases}$$
 (7.55)

The above relations reduce the eq. (7.53) into a more straightforward form provided as,

$$(2\rho - 1)\frac{\partial \rho}{\partial x} = 0, (7.56)$$

whereas the eq. (7.50) and eq. (7.51) reduce to the boundary conditions $\rho(0) = \alpha_{\rm eff}$, and $\rho(1) = 1 - \beta$, respectively. For multiple-capacity case, the governing equation for the lattice density at stationary state along-with the boundary conditions matches exactly with the expressions obtained for the single-capacity case, see eq. (7.13). Moreover, the attachment-detachment rates and capacity parameters do not affect the lattice density, which is solely determined by utilising the boundary conditions. Further, the average particle density for the pockets can be obtained as,

$$m^* = \frac{E(m_i)}{q} = \begin{cases} \frac{A - (1+q)A^{q+1} + qA^{q+2}}{q(1-A)(1-A^{q+1})}; & A \neq 1, \\ \frac{1}{2}; & A = 1, \end{cases}$$
(7.57)

where E refers to the expected value of the distribution function. As compared to the single-capacity case, an additional factor that affects the pocket density along with the attachment-detachment rates and lattice density is its capacity. In the limit $q \to 1$, the generalized expression for pocket density in eq. (7.57) reduces exactly to the one obtained for the single-capacity case in eq. (7.11). In the upcoming sections, the density expressions obtained for the lattice and pocket will further be utilised to construct the phase diagrams for infinite as well as finite resources. Additionally, we are interested in analysing the effects of the parameters q, Ω_c and Ω_d on the stationary state properties of the system.

7.4.1 Phase plane analysis for infinite resources

For an infinite reservoir, the expression for the lattice density remains intact to that of a standard open-TASEP, see eq. (7.13). Similar to the single-capacity case, the lattice density remains independent of the kinetic rates and the capacity parameter, resulting in no change in the topology of the phase diagram. The change in the pocket density with respect to the change in the lattice density for different choices of q can be seen in FIG. 7.6. For $\Omega_c = \Omega_d$, the FIG. 7.6(a) illustrates that both the lattice and pocket will possess only symmetric phases for different choices of q. Further, the increase in the value of q brings no qualitative change but only the quantitative change to the pocket densities. In the limit $q \to \infty$, the pocket

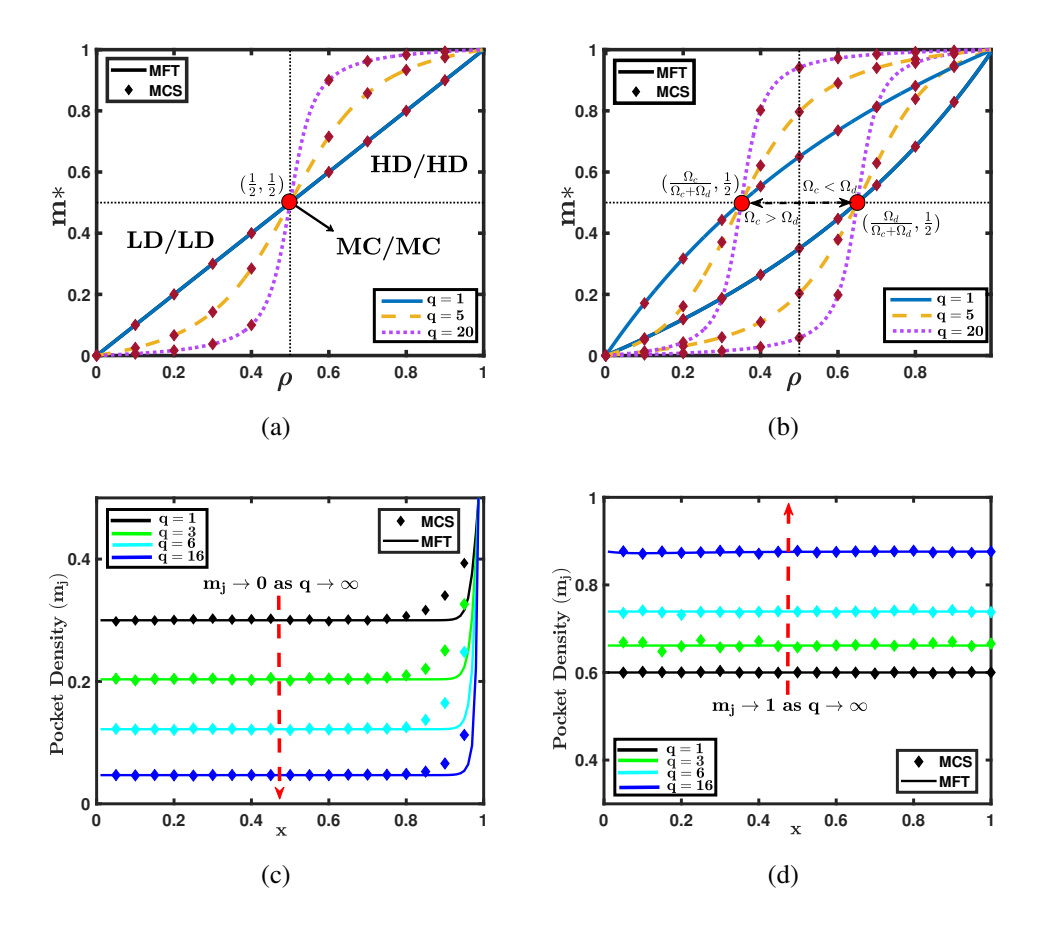


Figure 7.6: (a) Pocket density vs lattice density for different choices of q and $\Omega_c = \Omega_d$. (b) Pocket density vs lattice density for different choices of q and $\Omega_c \neq \Omega_d$, where $\Omega_c, \Omega_d \in \{0.35, 0.65\}$. The dashed arrow (in red) refers to the shift in the density profiles with increasing q. (c) The density profile in the LD phase (in pocket) approaches toward 0 in the limit $q \to \infty$. (d) The density profile in the HD phase (in pocket) approaches towards 1 in the limit $q \to \infty$.

density in the LD and HD phases approaches 0 and 1, respectively, as illustrated in FIG. 7.6(c) and 7.6(d). Hence, the phase diagram remains invariant of the parameter q.

For the case $\Omega_c
eq \Omega_d$ also, the phase diagram remains unaffected by the pocket's capacity. The justification for the case $\Omega_c < \Omega_d$ can be explained as follows. We argue from the FIG. 7.6(b) that the phase diagram will only contain the following six density phases: LD/LD, MC/LD, HD/LD, HD/MC, HD/HD, and S*/S*. The phase boundaries between LD/LD - MC/LD phases and MC/LD - HD/LD phases are completely characterized by the lattice density and hence remain invariant of q.

For q = 1, we can re-write the expression for pocket density in eq. (7.11) as,

$$m = \frac{A}{1+A},\tag{7.58}$$

where $A = \frac{\Omega_c \rho}{\Omega_d (1-\rho)}$. The transition from HD/LD to HD/HD phase (or vice-versa) occurs along the phase boundary capturing HD/MC phase. The pockets must possess the MC phase for the transition mentioned above to occur, and that happens for A=1 only. Further, for $q \neq 1$, we utilise m* in eq. (7.57) to obtain the condition of transition from HD/LD to HD/HD phase which is given as,

$$qA^{q+2} - (2+q)(A^{q+1} - A) - q = 0, (7.59)$$

while the pocket will have a S* phase as long as the lattice contains a S* phase. The above equation holds true only for A = 1, which is the same condition obtained for the single-capacity case. For any choice of q, the above equation holds true only for A = 1. This proves that all the phase boundaries for the multiple-capacity case are independent of the capacity parameter.

Surprisingly, despite being a function of q, the pocket density does not influence the phase diagram. The above findings conclude that the capacity parameter q brings no qualitative change in the topology of the phase diagram with infinite resources.

7.4.2 Lattice and multiple-capacity pockets compete for finite resources

Finally, we study the case where the lattice and multiple-capacity pocket competes for a finite number of particles in the reservoir. Like-wise to the single-capacity case, only the entry rate is affected by the number of particles in the reservoir. The actual interplay of the finite reservoir and phase diagrams can be observed for $N_{tot} \sim 2L$ or smaller. The number of particles in the system remains conserved; therefore N_{tot} can be written as,

$$N_{tot} = N_r + L\rho + Lm^*. (7.60)$$

As discussed in the previous section, the master equation governing the lattice density neither involves the attachment-detachment rates nor capacity but entirely depends on the boundary conditions. Therefore, we consider the same expression for the lattice density given in eq. (7.13), where only the entry rate is replaced with the effective entry rate. The pocket density follows the same relation in eq. (7.57), further we utilise the notation $\phi(\rho,q)$ for m^* and we get,

$$N_{tot} = \begin{cases} N_r + L\alpha_{\text{eff}} + L\phi(\alpha_{\text{eff}}, q); & \alpha_{\text{eff}} < \min(\beta, \frac{1}{2}), \\ N_r + L(1-\beta) + L\phi(1-\beta, q); & \beta < \min(\alpha_{\text{eff}}, \frac{1}{2}), \\ N_r + \frac{L}{2} + L\phi(\frac{1}{2}, q); & \min(\alpha_{\text{eff}}, \beta) \ge \frac{1}{2}, \end{cases}$$
(7.61)

where the first, second and third relation refer to the LD, HD, and MC phase respectively.

Utilising these relations, we obtain a relationship between the reservoir density ρ_r and the filling factor μ given as,

$$\mu = \begin{cases} \rho_r + \frac{\alpha \rho_r}{\mu} + \phi(\frac{\alpha \rho_r}{\mu}, q); & \rho_r < \min(\frac{\beta \mu}{\alpha}, \frac{\mu}{2\alpha}), \\ \rho_r + 1 - \beta + \phi(1 - \beta, q); & \beta < \min(\frac{\alpha \rho_r}{\mu}, \frac{1}{2}), \\ \rho_r + \frac{1}{2} + \phi(\frac{1}{2}, q); & \min(\frac{\alpha \rho_r}{\mu}, \beta) \ge \frac{1}{2}. \end{cases}$$
(7.62)

Further, the phase boundaries corresponding to the distinct phases can be computed by calculating ρ_r in that particular phase for a fixed μ .

7.4.3 Phase plane analysis

For the case of multiple-capacity under finite resources, the phase boundaries are computed numerically. For a fixed μ , the effect of q on phase diagrams is illustrated in FIG. 7.7. For $\Omega_c = \Omega_d$, the phase plane only possesses the symmetric phases, and the number of density phases remains intact, whereas the phase boundaries shift with q. Further, the FIG. 7.7(a) clearly shows that the increase in the capacity factor leads to the expansion in the region of S/S phase and the shrinkage in the LD/LD and HD/HD phase regions, whereas the region

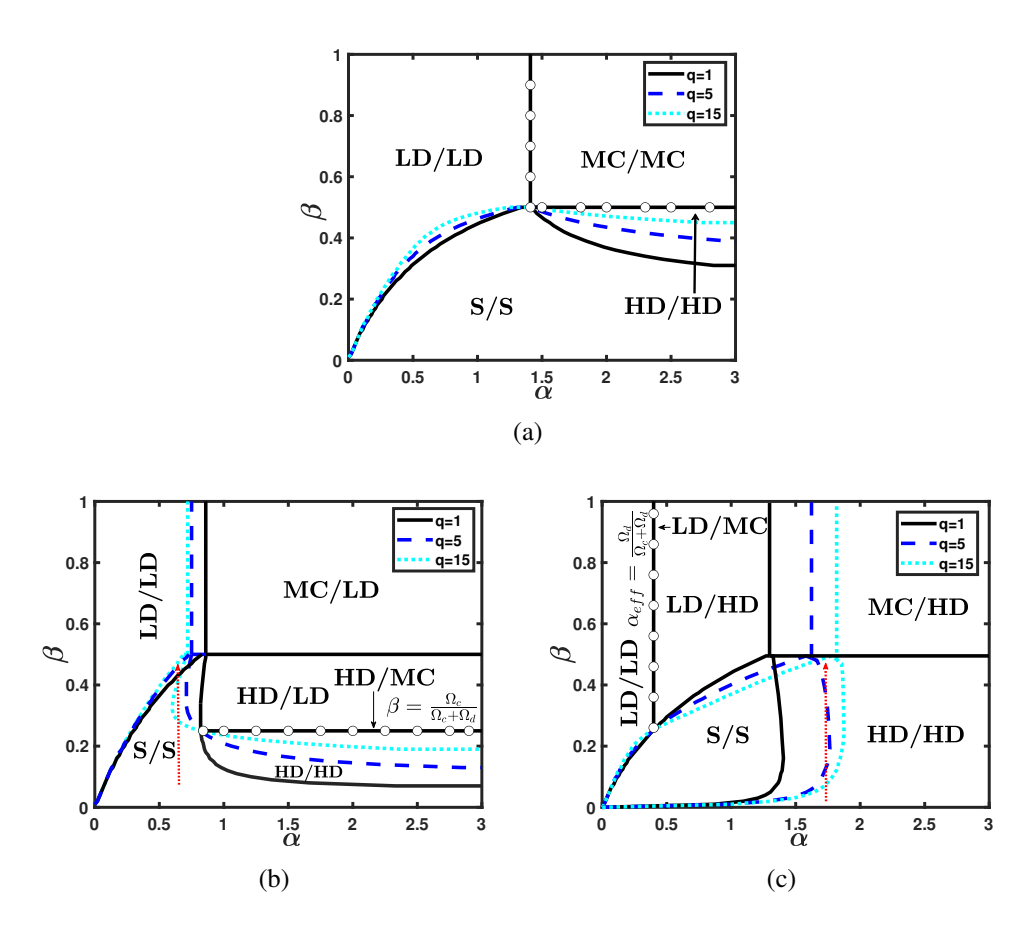


Figure 7.7: The effect of q on phase diagrams obtained for lattice and multiple-capacity pockets under finite resources. The phase boundaries with white circles remain intact with an increase in q. (a) $\mu=1.55$ and $\Omega_c=\Omega_d$. (b) $\mu=1.8$ and $\Omega_c=0.1, \Omega_d=0.3$. (c) $\mu=2.01$ and $\Omega_c=0.3, \Omega_d=0.1$. The dotted arrows (in red) refer to the back-and-forth (reentrant) transition for larger choices of q. The arrows (in black) refer to the region occupied by the corresponding density phase.

occupied by the MC/MC phase remains unaffected. For the case $\Omega_c \neq \Omega_d$ also, no new density phase emerges with q, but a shift in the phase boundaries can be seen in the FIG. 7.7(b) and 7.7(c). These figures also illustrate that not all phase boundaries shift, and the justification is provided only for the case $\Omega_c < \Omega_d$. The HD/MC phase just appears on the phase boundary, as discussed before. The only phase boundary that remains intact of changes in q is the one containing HD/MC phase. The pocket have a MC phase for A=1 and, together with the assumption of lattice being in HD phase, provides us with a condition $\beta = \frac{\Omega_c}{\Omega_c + \Omega_d}$. This shows that the phase boundary containing HD/MC phase remains invariant of q.

7.5 Conclusion 203

Moreover, the increase in q leads to the shrinkage in LD/LD and HD/HD phase regions, whereas the MC/LD, HD/LD, and S/S phase regions expand. Furthermore, the back and forth (reentrant) transition phenomena can also be seen for the larger values of q and some fixed choice of μ . For finite resources also, the pocket densities in the LD and HD phases approach 0 and 1, respectively, in the limit $q \to \infty$. As a result, the multiple-capacity model under finite resources produces no non-trivial effect on the density profiles and the phase diagrams.

7.5 Conclusion

In this work, we have proposed a study related to the geometric adaptation of the standard open-TASEP, whose each site is connected to a pocket. The attachment and detachment of particles are allowed between the lattice site and the corresponding pocket. The pockets may have varying capacities; therefore, we classified the study into two components: the lattice with unit-capacity pocket and the other with multiple-capacity pocket. The direct movement of particles from one pocket to another pocket is strictly prohibited. For both cases, the lattice is first treated with a reservoir having infinite resources and then with the one containing limited resources. Our model can be thought of as a pair of parallelly coupled TASEP where horizontal movement is restricted in one of the lattices. For q=1, both lattice and pocket strictly obey the hard-core exclusion principle and we employ mean-field approximation to study the steady-state properties of the system, such as density profiles, phase plane analysis, and phase transitions. The violation of the hard-core exclusion principle with the introduction of multiple-capacity pockets clearly shows that the mean-field theory cannot simply be generalized for this case. Therefore, we defined a probability mass function to compute the density of multiple-capacity pockets.

The theoretical results are obtained in support of our mathematical investigation. We found an explicit relationship between the lattice and pocket density in a stationary state. In the case of the infinite reservoir, the phase diagram remains invariant of the pocket capacity. For $\Omega_c = \Omega_d$, the phase diagram holds four symmetric phases, whereas three symmetric and

three asymmetric phases are observed for the case $\Omega_c \neq \Omega_d$. At stationary state, the lattice density remains independent of the attachment-detachment rates as well as the pocket's capacity due to the presence of net zero current between lattice site and the corresponding pocket. In contrast to the lattice density, the pocket density is affected by the attachment-detachment rates as well as the capacity parameter.

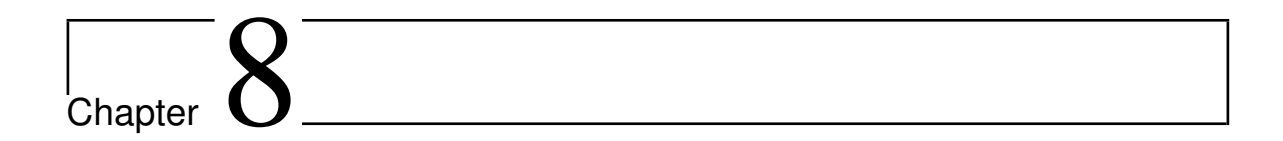
Analogous to the case of infinite resources, the phase diagrams for finite resources also possess symmetric phases for $\Omega_c = \Omega_d$ and both symmetric and asymmetric phases are observed for $\Omega_c \neq \Omega_d$. The number of the phases appearing in the phase diagram depends on the value of μ . For q=1 and $\Omega_c=\Omega_d$, there exists only two symmetric phases in the phase diagram for $\mu < 1$ whereas two more symmetric phases appear for $\mu \ge 1$. The increase in the value of μ observes no topological changes in the phase diagram. For the case of $\Omega_c > \Omega_d$ and q=1, the phase diagram observes two symmetric phases for $\mu < \frac{\Omega_c + 3\Omega_d}{2(\Omega_c + \Omega_d)}$ and two asymmetric phases join the phase diagram as soon as μ goes beyond this critical value. In addition to these four phases, a new symmetric phase and an asymmetric phase appear for $\mu \geq \frac{3\Omega_c + \Omega_d}{2(\Omega_c + \Omega_d)}$. Furthermore, the phenomena of back-and-forth transition are also observed for unequal attachment-detachment rates and a fixed choice of μ . Compared to the single-capacity case, the capacity parameter brings no topological changes in the phase diagram. A shift in some of the phase boundaries is observed with respect to q. We retrieve the phase diagrams obtained for the infinite resources in the limit $\mu \to \infty$. Additionally, the pocket densities in the LD and HD phases approaches to 0 and 1, respectively, in the limit $q \to \infty$.

For symmetric coupling, the single-capacity pockets in the proposed model behave identically to the lattice despite having no horizontal movement of particles. Notably, the proposed model's limiting case $q \to \infty$ does not converge to the TASEP-LK model. This is justified with the argument that the particles in the TASEP-LK model are always readily available to attach on the vacant lattice sites, whereas simply increasing the capacity of each pocket does not ensure the availability of particles in them.

Our model serves a more realistic purpose by studying the vehicular traffic on highways with several drive-ins (a place where a finite number of vehicles would wait for any specific

7.5 Conclusion **205**

purpose). The capacity of each drive-in to accommodate the vehicles is assumed to be equal. Moreover, the traffic of vehicles in these drive-ins has a non-linear dependence on the highways. It would be interesting to investigate an extension by keeping different capacity for different drive-ins in the above model.



Conclusion and Future work

This thesis demonstrates the versatility and power of the Totally Asymmetric Simple Exclusion Process (TASEP) as a fundamental framework for modeling complex dynamics in diverse physical and biological systems. Throughout our investigations, we have consistently shown that TASEP, far from being a mere toy model, serves as an effective tool for capturing intricate transport phenomena in a remarkably accessible manner.

A key strength of our approach lies in the application of mean-field theory, which provides a robust approximation method for deriving stationary state results across various model adaptations. This technique has proven invaluable in elucidating critical features such as particle flux, phase boundaries, phase transitions, and boundary densities for a wide range of scenarios.

To validate our theoretical findings, we have employed extensive Monte Carlo simulations, which consistently corroborate the results obtained through mean-field approximations. In instances where standard mean-field theory falls short, as exemplified in Chapter 2, we have successfully developed enhanced approaches. By incorporating correlations between different species (particles and defects) on the lattice, we have extended the applicability of mean-field methods to more complex systems.

Our work underscores the adaptability of theoretical frameworks in statistical physics. When conventional techniques prove insufficient, innovative modifications can account for additional complexities, such as inter-particle correlations, thereby expanding the scope of

analytical approaches.

In conclusion, this thesis reaffirms the TASEP's significance as a powerful yet accessible model for studying stochastic transport processes. Despite its apparent simplicity, TASEP-based models demonstrate remarkable efficacy in capturing the steady-state characteristics of complex systems. This research not only advances our understanding of non-equilibrium phenomena but also paves the way for future investigations into increasingly sophisticated transport mechanisms in both natural and engineered systems.

8.1 Future Scope

This thesis investigates fundamental physical characteristics exhibited by diverse transportation systems. While the proposed models have provided valuable insights, there remains significant potential for further development and expansion. Future research directions aim to address several complex features of transport systems that were not incorporated in the current models.

One promising avenue for future investigation is the incorporation of time-varying or particle-dependent hopping rates in the bulk of the lattice, as opposed to the constant rates examined in the current study. This extension could offer valuable insights into heterogeneous transport systems and more accurately simulate real-world scenarios, such as traffic flow regulated by time-dependent signals.

Another area of potential expansion is the transition from single-lane to multi-lane or multi-dimensional TASEP models. This development would enable the exploration of more complex transport phenomena, including dynein-inspired multilane exclusion processes. Such extensions could provide a more comprehensive understanding of intricate transportation networks and their dynamics.

Furthermore, the integration of machine learning algorithms presents an exciting opportunity to enhance the predictive capabilities of TASEP models. These advanced computational techniques could be employed to forecast phase transitions in various TASEP generalizations, potentially yielding more sophisticated and accurate results. 8.1 Future Scope 209

These proposed research directions aim to bridge the gap between theoretical models and real-world transportation systems, ultimately contributing to a more nuanced understanding of complex transport processes and their applications.

- [1] D. ADAMS, B. SCHMITTMANN, AND R. ZIA, Far-from-equilibrium transport with constrained resources, Journal of Statistical Mechanics: Theory and Experiment, 2008 (2008), p. P06009.
- [2] B. Alberts, A. Johnson, J. Lewis, M. Raff, K. Roberts, and P. Walter, *Molecular Biology of the Cell*, Garland Science, New York, 4th ed., 2002.
- [3] C. APPERT-ROLLAND, M. EBBINGHAUS, AND L. SANTEN, *Intracellular transport driven by cytoskeletal motors: General mechanisms and defects*, Physics Reports, 593 (2015), pp. 1–59.
- [4] C. ARITA, *Phase transitions in the two-species totally asymmetric exclusion process with openboundaries*, Journal of Statistical Mechanics: Theory and Experiment, 2006 (2006), p. P12008.
- [5] P. F. ARNDT, T. HEINZEL, AND V. RITTENBERG, First-order phase transitions in one-dimensional steady states, Journal of statistical physics, 90 (1998), pp. 783–815.
- [6] A. AYYER, C. FINN, AND D. ROY, Matrix product solution of a left-permeable two-species asymmetric exclusion process, Physical Review E, 97 (2018), p. 012151.
- [7] A. AYYER, J. L. LEBOWITZ, AND E. R. SPEER, *On the two species asymmetric exclusion process with semi-permeable boundaries*, Journal of Statistical Physics, 135 (2009), pp. 1009–1037.
- [8] A. AYYER, J. L. LEBOWITZ, AND E. R. SPEER, On some classes of open two-species exclusion processes, arXiv preprint arXiv:1008.4721, (2010).
- [9] M. BARMA, *Driven diffusive systems with disorder*, Physica A: Statistical Mechanics and its Applications, 372 (2006), pp. 22–33.
- [10] U. BASU, A. KUNDU, AND A. PAL, Symmetric exclusion process under stochastic resetting, Physical Review E, 100 (2019), p. 032136.

- [11] R. J. BAXTER, Exactly solved models in statistical mechanics, Elsevier, 2016.
- [12] V. BELITSKY, J. KRUG, E. J. NEVES, AND G. SCHÜTZ, *A cellular automaton model for two-lane traffic*, Journal of Statistical Physics, 103 (2001), pp. 945–971.
- [13] D. BEN AVRAHAM AND J. KÖHLER, *Mean-field (n, m)-cluster approximation for lattice models*, Physical Review A, 45 (1992), p. 8358.
- [14] A. A. S. Bhagat, H. Bow, H. W. Hou, S. J. Tan, J. Han, and C. T. Lim, *Microfluidics for cell separation*, Medical & biological engineering & computing, 48 (2010), pp. 999–1014.
- [15] N. BHATIA AND A. K. GUPTA, *Modified version of open tasep with dynamic defects*, in International Conference on Traffic and Granular Flow, Springer, 2022, pp. 257–264.
- [16] N. BHATIA AND A. K. GUPTA, Role of dynamic defects in a resource-constrained exclusion process, Chaos, Solitons & Fractals, 167 (2023), p. 113109.
- [17] N. BHATIA AND A. K. GUPTA, *Totally asymmetric simple exclusion process with lo*cal resetting in a resource-constrained environment, Physical Review E, 109 (2024), p. 024109.
- [18] T. L. BLASIUS, N. REED, B. M. SLEPCHENKO, AND K. J. VERHEY, *Recycling of kinesin-1 motors by diffusion after transport*, PloS one, 8 (2013), p. e76081.
- [19] M. BOJER, I. R. GRAF, AND E. FREY, Self-organized system-size oscillation of a stochastic lattice-gas model, Physical Review E, 98 (2018), p. 012410.
- [20] L. BOLTZMANN, *Lectures on gas theory, trans*, Stephen G. Brush (Berkeley: University of California Press, 1964), 90 (1964).
- [21] P. BONNIN, N. KERN, N. T. YOUNG, I. STANSFIELD, AND M. C. ROMANO, *Novel mrna-specific effects of ribosome drop-off on translation rate and polysome profile*, PLoS computational biology, 13 (2017), p. e1005555.
- [22] C. A. BRACKLEY, L. CIANDRINI, AND M. C. ROMANO, Multiple phase transitions in a system of exclusion processes with limited reservoirs of particles and fuel carriers, Journal of Statistical Mechanics: Theory and Experiment, 2012 (2012), p. P03002.
- [23] L. CANTINI, Asymmetric simple exclusion process with open boundaries and koorn-winder polynomials, in Annales Henri Poincaré, vol. 18, Springer, 2017, pp. 1121–1151.
- [24] D. CHANDLER, *Introduction to modern statistical*, Mechanics. Oxford University Press, Oxford, UK, 5 (1987), p. 11.

[25] S.-K. Choi and M. H. Saier Jr, Regulation of sigl expression by the catabolite control protein ccpa involves a roadblock mechanism in bacillus subtilis: potential connection between carbon and nitrogen metabolism, Journal of bacteriology, 187 (2005), pp. 6856–6861.

- [26] T. CHOU AND G. LAKATOS, *Clustered bottlenecks in mrna translation and protein synthesis*, Physical review letters, 93 (2004), p. 198101.
- [27] D. CHOWDHURY, Stochastic mechano-chemical kinetics of molecular motors: a multidisciplinary enterprise from a physicist's perspective, Physics Reports, 529 (2013), pp. 1–197.
- [28] D. CHOWDHURY, L. SANTEN, AND A. SCHADSCHNEIDER, Statistical physics of vehicular traffic and some related systems, Physics Reports, 329 (2000), pp. 199–329.
- [29] L. CIANDRINI, I. NERI, J. C. WALTER, O. DAULOUDET, AND A. PARMEGGIANI, *Motor protein traffic regulation by supply-demand balance of resources*, Physical biology, 11 (2014), p. 056006.
- [30] L. CIANDRINI, I. STANSFIELD, AND M. C. ROMANO, Ribosome traffic on mrnas maps to gene ontology: genome-wide quantification of translation initiation rates and polysome size regulation, PLoS computational biology, 9 (2013), p. e1002866.
- [31] M. CLINCY, M. EVANS, AND D. MUKAMEL, Symmetry breaking through a sequence of transitions in a driven diffusive system, Journal of Physics A: Mathematical and General, 34 (2001), p. 9923.
- [32] L. J. COOK, J. DONG, AND A. LAFLEUR, Interplay between finite resources and a local defect in an asymmetric simple exclusion process, Physical Review E, 88 (2013), p. 042127.
- [33] L. J. COOK AND R. ZIA, Feedback and fluctuations in a totally asymmetric simple exclusion process with finite resources, Journal of Statistical Mechanics: Theory and Experiment, 2009 (2009), p. P02012.
- [34] R. M. CORLESS, G. H. GONNET, D. E. HARE, D. J. JEFFREY, AND D. E. KNUTH, *On the lambert w function*, Advances in Computational mathematics, 5 (1996), pp. 329–359.
- [35] O. DAULOUDET, I. NERI, J.-C. WALTER, J. DORIGNAC, F. GENIET, AND A. PARMEGGIANI, *Modelling the effect of ribosome mobility on the rate of protein synthesis*, The European Physical Journal E, 44 (2021), pp. 1–15.
- [36] B. DERRIDA, E. DOMANY, AND D. MUKAMEL, An exact solution of a one-dimensional asymmetric exclusion model with open boundaries, Journal of statistical physics, 69 (1992), pp. 667–687.

[37] B. DERRIDA, M. R. EVANS, V. HAKIM, AND V. PASQUIER, *Exact solution of a 1d asymmetric exclusion model using a matrix formulation*, Journal of Physics A: Mathematical and General, 26 (1993), p. 1493.

- [38] B. DERRIDA AND J. L. LEBOWITZ, *Exact large deviation function in the asymmetric exclusion process*, Physical review letters, 80 (1998), p. 209.
- [39] D. DI CARLO, D. IRIMIA, R. G. TOMPKINS, AND M. TONER, *Continuous inertial focusing, ordering, and separation of particles in microchannels*, Proceedings of the National Academy of Sciences, 104 (2007), pp. 18892–18897.
- [40] J. Elf, G.-W. Li, AND X. S. Xie, *Probing transcription factor dynamics at the single-molecule level in a living cell*, Science, 316 (2007), pp. 1191–1194.
- [41] V. EPSHTEIN, F. TOULMÉ, A. R. RAHMOUNI, S. BORUKHOV, AND E. NUDLER, Transcription through the roadblocks: the role of rna polymerase cooperation, The EMBO journal, (2003).
- [42] D. W. ERICKSON, G. PRUESSNER, B. SCHMITTMANN, AND R. K. ZIA, *Spurious phase in a model for traffic on a bridge*, Journal of Physics A: Mathematical and General, 38 (2005), p. L659.
- [43] M. R. EVANS, D. P. FOSTER, C. GODRÈCHE, AND D. MUKAMEL, Asymmetric exclusion model with two species: spontaneous symmetry breaking, Journal of statistical physics, 80 (1995), pp. 69–102.
- [44] M. R. EVANS, D. P. FOSTER, C. GODRÈCHE, AND D. MUKAMEL, Spontaneous symmetry breaking in a one dimensional driven diffusive system, Physical review letters, 74 (1995), p. 208.
- [45] M. R. EVANS, R. JUHÁSZ, AND L. SANTEN, *Shock formation in an exclusion process with creation and annihilation*, Physical Review E, 68 (2003), p. 026117.
- [46] M. R. EVANS, Y. KAFRI, K. E. SUGDEN, AND J. TAILLEUR, *Phase diagrams of two-lane driven diffusive systems*, Journal of Statistical Mechanics: Theory and Experiment, 2011 (2011), p. P06009.
- [47] M. R. EVANS AND S. N. MAJUMDAR, *Diffusion with stochastic resetting*, Physical review letters, 106 (2011), p. 160601.
- [48] M. R. EVANS AND S. N. MAJUMDAR, Run and tumble particle under resetting: a renewal approach, Journal of Physics A: Mathematical and Theoretical, 51 (2018), p. 475003.
- [49] R. FALCAO AND M. R. EVANS, *Interacting brownian motion with resetting*, Journal of Statistical Mechanics: Theory and Experiment, 2017 (2017), p. 023204.

[50] S. FRANCKENBERG, T. BECKER, AND R. BECKMANN, Structural view on recycling of archaeal and eukaryotic ribosomes after canonical termination and ribosome rescue, Current opinion in structural biology, 22 (2012), pp. 786–796.

- [51] S. GARG AND I. DHIMAN, Particle creation and annihilation in a dynamically disordered totally asymmetric simple exclusion process, Physical Review E, 103 (2021), p. 052120.
- [52] J. W. GIBBS, Elementary principles in statistical mechanics: developed with especial reference to the rational foundations of thermodynamics, C. Scribner's sons, 1902.
- [53] D. T. GILLESPIE, *Exact stochastic simulation of coupled chemical reactions*, The journal of physical chemistry, 81 (1977), pp. 2340–2361.
- [54] P. GREULICH, L. CIANDRINI, R. J. ALLEN, AND M. C. ROMANO, *Mixed population of competing totally asymmetric simple exclusion processes with a shared reservoir of particles*, Physical Review E, 85 (2012), p. 011142.
- [55] A. GUPTA, B. PAL, A. JINDAL, N. BHATIA, AND A. K. GUPTA, *Modelling of transport processes: Theory and simulations*, MethodsX, 10 (2023), p. 101966.
- [56] M. HA AND M. DEN NIJS, *Macroscopic car condensation in a parking garage*, Physical Review E, 66 (2002), p. 036118.
- [57] A. HALDAR, P. ROY, AND A. BASU, Asymmetric exclusion processes with fixed resources: Reservoir crowding and steady states, Physical Review E, 104 (2021), p. 034106.
- [58] N. HAO, S. KRISHNA, A. AHLGREN-BERG, E. E. CUTTS, K. E. SHEARWIN, AND I. B. DODD, *Road rules for traffic on dna—systematic analysis of transcriptional roadblocking in vivo*, Nucleic acids research, 42 (2014), pp. 8861–8872.
- [59] N. HIROKAWA, Kinesin and dynein superfamily proteins and the mechanism of organelle transport, Science, 279 (1998), pp. 519–526.
- [60] N. HIROKAWA, Y. NODA, Y. TANAKA, AND S. NIWA, *Kinesin superfamily motor proteins and intracellular transport*, Nature reviews Molecular cell biology, 10 (2009), pp. 682–696.
- [61] J. HOWARD AND R. CLARK, *Mechanics of motor proteins and the cytoskeleton*, Appl. Mech. Rev., 55 (2002), pp. B39–B39.
- [62] Y. A. HUMENYUK, M. KOTRLA, K. NETOČNÝ, AND F. SLANINA, Separation of dense colloidal suspensions in narrow channels: A stochastic model, Physical Review E, 101 (2020), p. 032608.

[63] Y. A. HUMENYUK, M. KOTRLA, AND F. SLANINA, *Continuous and discontinuous waves in an asep with pockets*, Journal of Statistical Mechanics: Theory and Experiment, 2021 (2021), p. 033209.

- [64] H. ITO AND K. NISHINARI, *Totally asymmetric simple exclusion process with a time-dependent boundary: Interaction between vehicles and pedestrians at intersections*, Physical Review E, 89 (2014), p. 042813.
- [65] V. JAKSIC, *Linear response theory in quantum statistical mechanics*, HAL Open Science, (2006).
- [66] S. A. JANOWSKY AND J. L. LEBOWITZ, Finite-size effects and shock fluctuations in the asymmetric simple-exclusion process, Physical Review A, 45 (1992), p. 618.
- [67] E. T. JAYNES ET AL., *Gibbs vs boltzmann entropies*, American Journal of Physics, 33 (1965), pp. 391–398.
- [68] A. JINDAL, A. B. KOLOMEISKY, AND A. K. GUPTA, *The role of dynamic defects in transport of interacting molecular motors*, Journal of Statistical Mechanics: Theory and Experiment, 2020 (2020), p. 043206.
- [69] R. Jose, C. Arita, and L. Santen, *Bidirectional non-markovian exclusion processes*, Journal of Statistical Mechanics: Theory and Experiment, 2020 (2020), p. 033207.
- [70] R. Juhász, L. Santen, and F. Iglói, *Partially asymmetric exclusion processes with sitewise disorder*, Physical Review E—Statistical, Nonlinear, and Soft Matter Physics, 74 (2006), p. 061101.
- [71] Y. KAFRI, E. LEVINE, D. MUKAMEL, G. SCHÜTZ, AND R. WILLMANN, *Phase-separation transition in one-dimensional driven models*, Physical Review E, 68 (2003), p. 035101.
- [72] K. KAMIENIARZ-GDULA AND N. J. PROUDFOOT, *Transcriptional control by pre-mature termination: a forgotten mechanism*, Trends in Genetics, 35 (2019), pp. 553–564.
- [73] M. KARDAR, Statistical physics of fields, Cambridge University Press, 2007.
- [74] S. KARTHIKA AND A. NAGAR, *Totally asymmetric simple exclusion process with resetting*, Journal of Physics A: Mathematical and Theoretical, 53 (2020), p. 115003.
- [75] S.-Y. KIM, J. H. CHO, E. MURRAY, N. BAKH, H. CHOI, K. OHN, L. RUELAS, A. HUBBERT, M. MCCUE, S. L. VASSALLO, ET AL., *Stochastic electrotransport selectively enhances the transport of highly electromobile molecules*, Proceedings of the National Academy of Sciences, 112 (2015), pp. E6274–E6283.

[76] S. KLUMPP AND R. LIPOWSKY, *Traffic of molecular motors through tube-like compartments*, Journal of Statistical Physics, 113 (2003), pp. 233–268.

- [77] A. B. KOLOMEISKY, Exact solutions for a partially asymmetric exclusion model with two species, Physica A: Statistical Mechanics and its Applications, 245 (1997), pp. 523–533.
- [78] A. B. KOLOMEISKY, Asymmetric simple exclusion model with local inhomogeneity, Journal of Physics A: Mathematical and General, 31 (1998), p. 1153.
- [79] A. B. KOLOMEISKY, Motor proteins and molecular motors, CRC press, 2015.
- [80] A. B. KOLOMEISKY, G. M. SCHÜTZ, E. B. KOLOMEISKY, AND J. P. STRALEY, *Phase diagram of one-dimensional driven lattice gases with open boundaries*, Journal of Physics A: Mathematical and General, 31 (1998), p. 6911.
- [81] T. KRETZ, A. GRÜNEBOHM, AND M. SCHRECKENBERG, Experimental study of pedestrian flow through a bottleneck, Journal of Statistical Mechanics: Theory and Experiment, 2006 (2006), p. P10014.
- [82] J. KRUG, *Boundary-induced phase transitions in driven diffusive systems*, Physical review letters, 67 (1991), p. 1882.
- [83] R. KUBO, M. TODA, AND N. HASHITSUME, *Statistical physics II: nonequilibrium statistical mechanics*, vol. 31, Springer Science & Business Media, 2012.
- [84] W. H. LAM, J. Y. LEE, AND C. CHEUNG, A study of the bi-directional pedestrian flow characteristics at hong kong signalized crosswalk facilities, Transportation, 29 (2002), pp. 169–192.
- [85] D. LANDAU AND K. BINDER, A guide to Monte Carlo simulations in statistical physics, Cambridge university press, 2021.
- [86] R. B. MACCIONI AND V. CAMBIAZO, *Role of microtubule-associated proteins in the control of microtubule assembly*, Physiological reviews, 75 (1995), pp. 835–864.
- [87] C. T. MACDONALD AND J. H. GIBBS, *Concerning the kinetics of polypeptide synthesis on polyribosomes*, Biopolymers: Original Research on Biomolecules, 7 (1969), pp. 707–725.
- [88] C. T. MACDONALD, J. H. GIBBS, AND A. C. PIPKIN, *Kinetics of biopolymerization on nucleic acid templates*, Biopolymers: Original Research on Biomolecules, 6 (1968), pp. 1–25.
- [89] P. MEAKIN, 4.2 ballistic deposition on surfaces p. meakin, p. ramanlal, lm sander, and rc ball, Dynamics of Fractal Surfaces, 34 (1991), p. 151.

[90] S. MILLECAMPS AND J.-P. JULIEN, Axonal transport deficits and neurodegenerative diseases, Nature Reviews Neuroscience, 14 (2013), pp. 161–176.

- [91] N. MIRIN AND A. B. KOLOMEISKY, Effect of detachments in asymmetric simple exclusion processes, Journal of statistical physics, 110 (2003), pp. 811–823.
- [92] A. MIRON AND S. REUVENI, *Diffusion with local resetting and exclusion*, Physical Review Research, 3 (2021), p. L012023.
- [93] A. MONTANARI AND R. ZECCHINA, *Optimizing searches via rare events*, Physical review letters, 88 (2002), p. 178701.
- [94] S. MUHURI AND I. PAGONABARRAGA, *Phase segregation and transport in a two-species multi-lane system*, Journal of Statistical Mechanics: Theory and Experiment, 2011 (2011), p. P11011.
- [95] S. MUKHERJI, Fixed points and boundary layers in asymmetric simple exclusion processes, Physical Review E—Statistical, Nonlinear, and Soft Matter Physics, 79 (2009), p. 041140.
- [96] K. NAGEL, *Particle hopping models and traffic flow theory*, Physical review E, 53 (1996), p. 4655.
- [97] M. NANGAKU, R. SATO-YOSHITAKE, Y. OKADA, Y. NODA, R. TAKEMURA, H. YAMAZAKI, AND N. HIROKAWA, *Kif1b, a novel microtubule plus end-directed monomeric motor protein for transport of mitochondria*, Cell, 79 (1994), pp. 1209–1220.
- [98] J. OLMSTED, *Microtubule-associated proteins*, Annual review of cell biology, 2 (1986), pp. 421–457.
- [99] O. O'LOAN, M. EVANS, AND M. CATES, Spontaneous jamming in one-dimensional systems, Europhysics Letters, 42 (1998), p. 137.
- [100] B. PAL AND A. K. GUPTA, *Non-conserving exclusion process with a dynamic obstacle*, Chaos, Solitons & Fractals, 162 (2022), p. 112471.
- [101] B. PAL AND A. K. GUPTA, Reservoir crowding in a resource-constrained exclusion process with a dynamic defect, Physical Review E, 106 (2022), p. 044130.
- [102] A. PARMEGGIANI, T. FRANOSCH, AND E. FREY, *Phase coexistence in driven one-dimensional transport*, Physical review letters, 90 (2003), p. 086601.
- [103] A. PARMEGGIANI, T. FRANOSCH, AND E. FREY, *Totally asymmetric simple exclusion process with langmuir kinetics*, Physical Review E—Statistical, Nonlinear, and Soft Matter Physics, 70 (2004), p. 046101.

[104] B. M. PASCHAL, R. A. OBAR, AND R. B. VALLEE, *Interaction of brain cytoplasmic dynein and map2 with a common sequence at the c terminus of tubulin*, Nature, 342 (1989), pp. 569–572.

- [105] A. PELIZZOLA AND M. PRETTI, *Totally asymmetric simple exclusion process with local resetting and open boundary conditions*, Journal of Physics A: Mathematical and Theoretical, 55 (2022), p. 454001.
- [106] A. PELIZZOLA, M. PRETTI, AND M. ZAMPARO, Simple exclusion processes with local resetting, Europhysics Letters, 133 (2021), p. 60003.
- [107] V. POPKOV, M. R. EVANS, AND D. MUKAMEL, *Spontaneous symmetry breaking in a bridge model fed by junctions*, Journal of Physics A: Mathematical and Theoretical, 41 (2008), p. 432002.
- [108] V. POPKOV AND I. PESCHEL, Symmetry breaking and phase coexistence in a driven diffusive two-channel system, Physical Review E, 64 (2001), p. 026126.
- [109] V. POPKOV AND G. M. SCHÜTZ, Steady-state selection in driven diffusive systems with open boundaries, Europhysics Letters, 48 (1999), p. 257.
- [110] V. PRIVMAN, *Nonequilibrium statistical mechanics in one dimension*, Cambridge University Press, 1997.
- [111] E. PRONINA AND A. B. KOLOMEISKY, Spontaneous symmetry breaking in twochannel asymmetric exclusion processes with narrow entrances, Journal of Physics A: Mathematical and Theoretical, 40 (2007), p. 2275.
- [112] N. RAJEWSKY, L. SANTEN, A. SCHADSCHNEIDER, AND M. SCHRECKENBERG, The asymmetric exclusion process: Comparison of update procedures, Journal of statistical physics, 92 (1998), pp. 151–194.
- [113] S. REUVENI, M. URBAKH, AND J. KLAFTER, *The role of substrate unbinding in michaelis-menten enzymatic reactions*, Biophysical Journal, 106 (2014), p. 677a.
- [114] É. ROLDÁN, A. LISICA, D. SÁNCHEZ-TALTAVULL, AND S. W. GRILL, *Stochastic resetting in backtrack recovery by rna polymerases*, Physical Review E, 93 (2016), p. 062411.
- [115] S. ROY, B. ZHANG, V. M.-Y. LEE, AND J. Q. TROJANOWSKI, *Axonal transport defects: a common theme in neurodegenerative diseases*, Acta neuropathologica, 109 (2005), pp. 5–13.
- [116] M. SAHOO, J. DONG, AND S. KLUMPP, *Dynamic blockage in an exclusion process*, Journal of Physics A: Mathematical and Theoretical, 48 (2014), p. 015007.

[117] M. SAHOO AND S. KLUMPP, Asymmetric exclusion process with a dynamic roadblock and open boundaries, Journal of Physics A: Mathematical and Theoretical, 49 (2016), p. 315001.

- [118] L. SANTEN AND C. APPERT, The asymmetric exclusion process revisited: fluctuations and dynamics in the domain wall picture, Journal of statistical physics, 106 (2002), pp. 187–199.
- [119] R. SATO-HARADA, S. OKABE, T. UMEYAMA, Y. KANAI, AND N. HIROKAWA, *Microtubule-associated proteins regulate microtubule function as the track for intracellular membrane organelle transports*, Cell structure and function, 21 (1996), pp. 283–295.
- [120] G. SCH ET AL., *Phase transitions in an exactly soluble one-dimensional exclusion process*, Journal of Statistical Physics, 72 (1993), pp. 277–296.
- [121] A. SCHADSCHNEIDER, D. CHOWDHURY, AND K. NISHINARI, Stochastic transport in complex systems: from molecules to vehicles, Elsevier, 2010.
- [122] M. SCHLIWA AND G. WOEHLKE, *Molecular motors*, Nature, 422 (2003), pp. 759–765.
- [123] B. SCHMITTMANN AND R. ZIA, *Driven diffusive systems. an introduction and recent developments*, Physics reports, 301 (1998), pp. 45–64.
- [124] G. SCHÜTZ, Generalized bethe ansatz solution of a one-dimensional asymmetric exclusion process on a ring with blockage, Journal of statistical physics, 71 (1993), pp. 471–505.
- [125] J. SEO, M. H. LEAN, AND A. KOLE, Membrane-free microfiltration by asymmetric inertial migration, Applied Physics Letters, 91 (2007), p. 033901.
- [126] N. SHARMA AND A. GUPTA, Phase segregation and spontaneous symmetry breaking in a bidirectional two-channel non-conserving model with narrow entrances, Journal of Statistical Mechanics: Theory and Experiment, 2017 (2017), p. 043211.
- [127] F. SLANINA, *Inertial hydrodynamic ratchet: Rectification of colloidal flow in tubes of variable diameter*, Physical Review E, 94 (2016), p. 042610.
- [128] F. SLANINA, Movement of spherical colloid particles carried by flow in tubes of periodically varying diameter, Physical Review E, 99 (2019), p. 012604.
- [129] M. A. SØRENSEN, C. KURLAND, AND S. PEDERSEN, *Codon usage determines translation rate in escherichia coli*, Journal of molecular biology, 207 (1989), pp. 365–377.

[130] T. M. SQUIRES AND S. R. QUAKE, *Microfluidics: Fluid physics at the nanoliter scale*, Reviews of modern physics, 77 (2005), p. 977.

- [131] J. Q. TOLEDO-MARIN, D. BOYER, AND F. J. SEVILLA, *Predator-prey dynamics: Chasing by stochastic resetting*, arXiv preprint arXiv:1912.02141, (2019).
- [132] G. TRIPATHY AND M. BARMA, Steady state and dynamics of driven diffusive systems with quenched disorder, Physical review letters, 78 (1997), p. 3039.
- [133] F. TURCI, A. PARMEGGIANI, E. PITARD, M. C. ROMANO, AND L. CIANDRINI, *Transport on a lattice with dynamical defects*, Physical Review E—Statistical, Nonlinear, and Soft Matter Physics, 87 (2013), p. 012705.
- [134] M. UCHIYAMA, *Two-species asymmetric simple exclusion process with open bound-aries*, Chaos, Solitons & Fractals, 35 (2008), pp. 398–407.
- [135] R. B. VALLEE, J. C. WILLIAMS, D. VARMA, AND L. E. BARNHART, *Dynein: An ancient motor protein involved in multiple modes of transport*, Journal of neurobiology, 58 (2004), pp. 189–200.
- [136] A. VALLERIANI, Z. IGNATOVA, A. NAGAR, AND R. LIPOWSKY, *Turnover of messenger rna: Polysome statistics beyond the steady state*, Europhysics Letters, 89 (2010), p. 58003.
- [137] A. K. VERMA AND A. K. GUPTA, *Limited resources in multi-lane stochastic transport system*, Journal of Physics Communications, 2 (2018), p. 045020.
- [138] A. K. VERMA AND A. K. GUPTA, Stochastic transport on flexible lattice under limited resources, Journal of Statistical Mechanics: Theory and Experiment, 2019 (2019), p. 103210.
- [139] A. K. VERMA, N. SHARMA, AND A. K. GUPTA, Far-from-equilibrium bidirectional transport system with constrained entrances competing for pool of limited resources, Physical Review E, 97 (2018), p. 022105.
- [140] B. WACLAW, J. CHOLEWA-WACLAW, AND P. GREULICH, *Totally asymmetric exclusion process with site-wise dynamic disorder*, Journal of Physics A: Mathematical and Theoretical, 52 (2019), p. 065002.
- [141] Y.-Q. WANG, X.-P. NI, C. XU, AND B.-H. WANG, *Physical mechanisms of the dynamical patterns and non-equilibrium processes of self-driven particles in an asep network affected by a finite external particle source*, Chaos, Solitons & Fractals, 151 (2021), p. 111192.
- [142] G. M. WHITESIDES, *The origins and the future of microfluidics*, nature, 442 (2006), pp. 368–373.

[143] R. WILLMANN, G. SCHÜTZ, AND D. CHALLET, *Exact hurst exponent and crossover behavior in a limit order market model*, Physica A: Statistical Mechanics and its Applications, 316 (2002), pp. 430–440.

List of Publications

- 1. Bhatia, Nikhil, and Arvind Kumar Gupta. "Site-wise dynamic defects in a non-conserving exclusion process." *SciPost Physics Core* 8.1 (2025): 009.
- 2. Bhatia, Nikhil, and Arvind Kumar Gupta. "Local resetting in a dynamically disordered exclusion process." *Physica A: Statistical Mechanics and its Applications* (2025): 130280.
- 3. Bhatia, Nikhil, and Arvind Kumar Gupta. "Local Resetting in a Bidirectional Transport System." *Journal of Statistical Physics* 191.7 (2024): 79.
- 4. Bhatia, Nikhil, and Arvind Kumar Gupta. "Totally asymmetric simple exclusion process with local resetting in a resource-constrained environment." *Physical Review E* 109.2 (2023): 024109.
- 5. Bhatia, Nikhil, and Arvind Kumar Gupta. "Role of site-wise dynamic defects in a resource-constrained exclusion process." *Chaos, Solitons & Fractals* 167 (2023): 113109.
- 6. Bhatia, Nikhil, and Arvind Kumar Gupta. "Far from equilibrium transport on TASEP with pockets." *The European Physical Journal Plus* 137.8 (2022): 892.
- 7. Gupta, Ankita, Bipasha Pal, Akriti Jindal, Nikhil Bhatia, and Arvind Kumar Gupta. "Modelling of transport processes: Theory and Simulations." *MethodsX* (2022): 101966.
- 8. Jindal, Akriti, Nikhil Bhatia, Anatoly B. Kolomeisky, and Arvind Kumar Gupta. "The effect of local reversible dissociation of particles in interactive driven diffusive system." *Physica A: Statistical Mechanics and its Applications* 588 (2021): 126555.

Conference Proceeding

1. Bhatia, Nikhil, and Arvind Kumar Gupta. "Modified version of open TASEP with dynamic defects." *Traffic and Granular Flow* -22 (2024): 257-264.

Extended abstracts in National/International conferences Oral/Poster presentations

- 1. Bhatia, Nikhil, and Arvind Kumar Gupta. "Far from equilibrium non-conserving exclusion process with site-wise dynamic defects" at "10th International Congress on Industrial and Applied Mathematics", held in August 2023 in Tokyo, Japan.
- 2. Bhatia, Nikhil, and Arvind Kumar Gupta. "Modified version of open TASEP with dynamic defects" at "International Conference on Traffic and Granular Flow", held in October 2022 at the Indian Institute of Technology Delhi.
- 3. Bhatia, Nikhil, and Arvind Kumar Gupta. "A geometric adaptation of TASEP" at "07th Warsaw School of Statistical Physics", held in June, 2022 at Sandomeirz, Poland.